Available online at www.sciencedirect.com
SCIENCE DIRECT®
Fusion Engineering and Design 73 (2005) 189–327
Fusion Engineering and Design
www.elsevier.com/locate/fusengdes

# The ITER toroidal field model coil project

A. Ulbricht[a], J.L. Duchateau[b], W.H. Fietz[a,*], D. Ciazynski[b], H. Fillunger[c], S. Fink[a], R. Heller[a], R. Maix[c], S. Nicollet[b], S. Raff[f], M. Ricci[g], E. Salpietro[d], G. Zahn[a], R. Zanino[h], M. Bagnasco[h], D. Besette[j], E. Bobrov[a], T. Bonicelli[d], P. Bruzzone[i], M.S. Darweschsad[a], P. Decool[b], N. Dolgetta[b], A. della Corte[g], A. Formisano[g], A. Grünhagen[n], P. Hertout[b], W. Herz[a], M. Huguet[j], F. Hurd[d], Yu. Ilyin[l], P. Komarek[a], P. Libeyre[b], V. Marchese[a], C. Marinucci[i], A. Martinez[b], R. Martone[o], N. Martovetsky[e], P. Michael[m], N. Mitchell[j], A. Nijhuis[l], G. Nöther[a], Y. Nunoya[k], M. Polak[p], A. Portone[d], L. Savoldi Richard[h], M. Spadoni[g], M. Süßer[a], S. Turtú[g], A. Vostner[d], Y. Takahashi[j], F. Wüchner[a], L. Zani[b]

[a] *Euratom Association Forschungszentrum Karlsruhe, Institut für Technische Physik, Herman-Helmholtz-Platz 1, D-76366 Eggenstein-Leopoldshafen, Germany*
[b] *DRFC, Euratom Association CEA Cadarache, France*
[c] *ATI, Euratom Association ÖAW, Technische Universität Wien, Austria*
[d] *EFDA/CSU, Euratom Association IPP, Garching, Germany*
[e] *Lawrence Livermore Laboratory, Livermore, USA*
[f] *Euratom Association Forschungszentrum Karlsruhe, Institut für Reaktorsicherheit, Germany*
[g] *Dip. Ing. Informazione, Seconda Università di Napoli, I-81031 Aversa (CE), Italy*
[h] *Dipartimento di Energetica, Politecnico, Torino I-10129, Italy*
[i] *CRPP, Euratom Association, Villigen, Switzerland*
[j] *ITER JWS, Naka, Japan*
[k] *JAERI, Naka, Japan*
[l] *Faculty of Science & Technology, University of Twente, Enschede, The Netherlands*
[m] *Plasma Science & Fusion Center, MIT, Boston, MA, USA*
[n] *Euratom Association Forschungszentrum Karlsruhe, Institut für Medizintechnik u. Biophysik, Germany*
[o] *Dipartimento di Ingegneria della Informazione Seconda Università di Napoli, Italy*
[p] *Institute of Electrical Engineering, Bratislava, Slovak Republic*

Received 17 June 2005; received in revised form 17 June 2005; accepted 14 July 2005
Available online 26 September 2005

**Abstract**

The ITER toroidal field model coil (TFMC) was designed, constructed and tested by the European Home Team in the framework of the ITER research and development program of the Engineering Design Activities (EDA). The project was performed under

* Corresponding author. Tel.: +49 7247 82 3911; fax: +49 7247 82 2849.
*E-mail address:* walter.fietz@itp.fzk.de (W.H. Fietz).

0920-3796/$ – see front matter 
doi:10.1016/j.fusengdes.2005.07.002

the leadership of European Fusion Development Activity/Close Support Unit (EFDA/CSU), Garching, in collaboration with the European superconductor laboratories and the European industry. The TFMC was developed and constructed in collaboration with the European industry consortium (AGAN) and Europa Metalli LMI supplied the conductor. The TFMC was tested in the test phase I as single coil and in phase II in the background field of the EURATOM LCT coil in the TOSKA facility of the Forschungszentrum Karlsruhe. In phase I, the TFMC achieved an ITER TF coil relevant current of about 80 kA and further representative test results before the end of the EDA. In the more complex test phase II, the coil was exposed to ITER TF coil relevant mechanical stresses in the winding pack and case. The tests confirmed that engineering design principles and manufacturing procedures are sound and suitable for the ITER TF full size coils. The electromagnetic, thermo hydraulic and mechanical operation parameters agree well with predictions. The achieved Lorentz force on the conductor was about 800 kN/m. That has been equivalent to the Lorentz forces in ITER TF coils.


*Keywords:* ITER; TFMC; EDA

## 1. Introduction

The oil crises in the beginning of the 1970's stimulated the research for energy sources outside the combustion of coal and natural gas. Besides nuclear fission, which was already an available energy source, the magnetic confinement for the controlled fusion reaction has been looked on as a promising energy source for the future with an inexhaustible fuel source. The first conceptual designs of fusion reactors of the tokamak type were developed [1]. The dimensions of their large magnet systems showed soon that the magnets have had to be superconducting if the reactor should have a positive energy balance. Since the next generation of large plasma physics experiments (JET, TFTR, JT-60) were planned at that time with normal conducting magnets the necessity was recognised that, in parallel, the development of superconducting magnet technology for such types of magnets is indispensable. A technology experiment for the toroidal field coil system of the tokamak magnet system was initiated under the auspices of the International Energy Agency (IEA). This was the construction and test of a superconducting six-coil torus (Large Coil Task, LCT), with coil technology scalable to reactor coils, within an international collaboration of EURATOM, European Community; JAERI, Japan; SIN/BBC, Switzerland; ORNL, USA [2]. The LCT was successfully completed in 1987. In that project various forced-flow-cooled conductor concepts as well as basic design principles and components for large superconducting coils were developed and tested. In 1983, the NET team was established in Garching (Germany) with the aim to coordinate the European fusion activities and to develop a European design of a device to be built after JET [3,4]. The NET design has clearly demonstrated the need of high magnetic field ($Nb_3Sn$) and high current carrying conductors; therefore, cables in conduit with forced-flow-cooled conductors has been the choice for application in the future. Several $Nb_3Sn$ and NbTi conductors were fabricated in short lengths and tested successfully in the SULTAN facility (Switzerland) [5].

In two medium size experiments POLO at Research Center Karlsruhe, Germany, in collaboration with CEA Cadarache, France, and DPC JAERI, Japan, in collaboration with MIT, USA, the superconducting technology for the poloidal field tokamak coils that had to withstand higher magnetic field transients and electrical losses than the TF coils, were successfully developed [6–9]. In addition, the necessary high voltage technology that has been indispensable for handling the tens of GJ of stored energy in large superconducting magnet systems, was developed in the POLO project [10].

Simultaneously with the developments of large superconducting tokamak magnets several medium size tokamaks with superconducting toroidal field coils for plasma physics experiments were constructed and successfully operated (T10, T15 [11], TORE SUPRA [12], TRIAM-1M [13]). The reliable operation of the medium size superconducting tokamaks has contributed to convincing the plasma physics community of the advantages and reliability of superconducting magnet technology.

The application and continuation of these developments were initiated by the ITER Conceptual (CDA) and Engineering Design Activity (EDA) in the 1990s. There were no more doubts that the ITER magnet system had to be constructed with superconducting coils [14]. In the beginning of the EDA in 1992, this led to the superconducting model coils of the ITER magnet system in the ITER research and development program. It was decided to construct and test a central solenoid model coil (CSMC) and a toroidal field model coil (TFMC). The necessary magnetic field levels between 11 and 13 T required use of the strain sensitive $Nb_3Sn$ as the superconducting material and this was a great challenge for the conductor and winding fabrication technology [15]. This resulted in the development of new structural materials that had to be compatible with the heat treatment and modified construction principles of the winding pack and coil structure. All that needed the confirmation in an overall test, which was covered by the ITER model coil program.

The CSMC was constructed and tested by the ITER partners Japan, Russian Federation, USA, and European Union in JAERI, Naka (Japan) [16].

The TFMC was constructed by the European Union alone and tested in FZK Karlsruhe (Germany) with the participation of the ITER partners.

Both tests were successfully completed in 2002. The CSMC project was concluded with the test of two three insert coils [17]. The first one was JAERI's CS conductor insert coil (CSCI) followed by RF's TFCI (TF conductor insert coil) demonstrating the pulse field capability of the ITER conductor concepts [18]. The third one was the JAERI's ALI ($Nb_3Al$ conductor insert coil), an alternative material to $Nb_3Sn$ but with a more sophisticated fabrication technology [19]. In test Phase 1 (2001), the TFMC achieved with 80 kA the highest current in a large superconducting coil [20] and in test Phase 2, ITER TF coil equivalent Lorentz forces of about 800 MN/m.

The subject of this contribution is an overview of the TFMC project within the European Union with the international ITER collaboration. The main features of design, construction of the TFMC and finally the TFMC test results in the TOSKA facility are described to guide the interested reader in more detailed publications of different areas.

## 2. Project objectives and management

The ITER design foresees to use for the TF coils a $Nb_3Sn$ cable in a circular thin walled conduit, insulated and completely enclosed in a groove in steel plates [21]. These are then stacked together to form the winding pack and supported by a steel case. The concept is demonstrated by two large industrial actions. The first one is the fabrication of a racetrack shaped model coil (TFMC), with outer dimensions of 2.8 m × 3.9 m, a peak field of 9.97 T (in pancake 2.2 in the 80/16 kA load case, 8.8 T in the 70/16 kA load case) and a total number of Ampere turns of 7.84 MA (6.86 MA for 70 kA) including an overall test. The second one is the fabrication of two full size sections of a case and a radial plate [22,23]. The racetrack shape for the TFMC was selected simplifying the fabrication and reducing the costs. The bending free D-shape is a specific property of the torus operation, which has no importance in a two coil test configuration. On the other hand, relevant stress levels (radial pressure, shear stresses) and Lorentz body forces on the conductor comparable to those of the full size ITER TF coils were achieved by this configuration (see Section 8). The specific problems of the fabrication of full size TF coils (radial plates and case components) was assigned in the second task mentioned before.

The objectives of the TFMC are as follows:

(a) To develop and verify the full scale TF coil manufacturing techniques, in particular the following features:
   - plate manufacturing (forming the grooves);
   - fitting the conductor in the groove after heat treatment and insulation (i.e., predictable geometry change);
   - closing the groove with a cover plate and plate insulation;
   - fitting the winding into the case, gap filling and case closure.

(b) To establish realistic manufacturing tolerances.

(c) To bench-mark methods for the ITER TF coil acceptance tests, including insulation and impregnation process monitoring, welding quality of closure welds for cover plates and case, and conductor joint electrical quality.

(d) To gain information on the coil's mechanical behaviour, operating margins and in-service mon-

itoring techniques, particularly for the insulation quality.

The TFMC and its test arrangement were designed to be representative for the ITER TF coil in respect of layout and electrical and mechanical stresses [24–27]. The layout of the TFMC overtook as many as possible features of the ITER TF coil design on a scale nearly 1:1. Only the overall dimensions had to be chosen in a way that the TFMC assembled together with the already existing EURATOM LCT coil fitted into the TOSKA facility of the FZK/ITP at Karlsruhe [28].

The construction and test of the TFMC was the main part of one of the seven large R&D projects of the ITER EDA [29]. The TFMC has been conceptually designed by the EURATOM Associations CEA Cadarache, ENEA Frascati and Forschungszentrum Karlsruhe (ITP) under the coordination of EFDA-CSU Garching (the former NET Team). The work sharing between the laboratories was adapted according to their experimental facilities as well as their expertise in the different fields and special skills for assistance during the construction and the preparations for the test [20].

A consortium of European companies, called AGAN (Accel, Alstom, Ansaldo, Noell) developed and performed the engineering design and manufacture of the TFMC under the surveillance of the EFDA-CSU Garching on behalf of EURATOM, in tight collaboration with the mentioned associations. The conductor was manufactured by Europa Metalli in separate contract and provided by EFDA-CSU to the AGAN consortium.

The work sharing within AGAN was as follows:

Accel Instruments: Design calculations, technical project and quality management.
Alstom: Winding pack assembly, manufacturing of coil case and superconducting bus bars, final coil assembly and instrumentation.
Ansaldo Superconduttori: Double pancake module fabrication.
Babcock Noell Nuclear: Design calculations, commercial management, structural components (radial plates, intercoil structure), related instrumentation, and assembly of the test configuration at TOSKA site.

The TFMC construction phase was accompanied by seven review meetings over 5 years within the international ITER collaboration.

The test of the TFMC was conducted by the Coordination Group consisting of the EU project manager as chairman, delegates of the ITER partners, ITER International Team and the test-hosting laboratory. The Group was supported by two experts groups (Test & Analysis and Operation Group), consisting of association staff, which prepared, performed and evaluated the test.

The testing in TOSKA facility at FZK Karlsruhe was supported by participation of scientists representing all ITER partners (EU, JA, RF, US) and ITER central team.

## 3. Toroidal field model coil layout and manufacture

### 3.1. Layout of the TF model coil

#### 3.1.1. TFMC Project objectives and layout

The special coil design (Fig. 3.1) with a circular $Nb_3Sn$ cable in conduit conductor placed into the spiral grooves of the 316LN stainless steel (SS) radial plates required the development of new manufacturing methods including the associated tooling. This has been described in several publications [30–34]. The design, manufacture and quality assurance (QA) results are described in detail in [35].

The ITER TF Model Coil design parameters and the main operating data are shown in Tables 3.1 and 3.2 in comparison with the ITER TF coils.

Table 3.1
ITER TF model coil design parameters

| Properties | ITER TF | TFMC |
|---|---|---|
| Conductor diameter [mm] | 43.4 | 40.7 |
| Nominal turn insulation thickness [mm] | 1.25–2.0 | 2.5 |
| Nominal DP module insulation | 1.0 | 1.5 |
| Total insulation between DP modules [mm] | ∼5.0 | ∼4.0 |
| Ground insulation thickness [mm] | 8 | 8 |
| Number of DP modules | 7 | 5 |
| Total number of turns | 134 | 98 |
| Winding min. radius [mm] | 500 | 600 |
| Case thickness [mm] | 75–240 | 70–80 |
| Overall dimensions [m] | $14.7 \times 8.5 \times 1.4$ | $3.8 \times 2.7 \times 0.77$ |
| Mass per coil [t] | ∼340 | ∼40 |

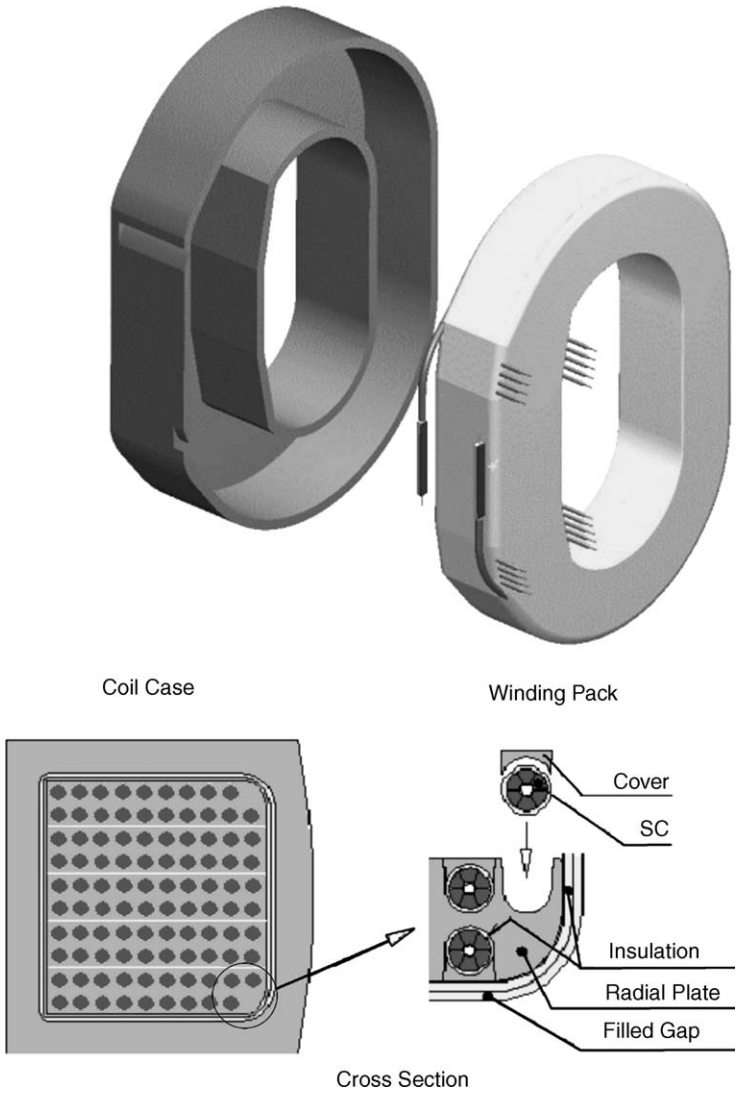


Fig. 3.1. Layout of the TF model coil (TFMC).

### 3.2. Conductor manufacture

#### 3.2.1. Strand

A total of 3.9 t of internal tin $Nb_3Sn$ strand (ITER HP1 specifications) have been used to fabricate about 900 m of conductor for the five double pancakes of the TFMC by the Europa Metalli Company. The production has demonstrated good reproducibility of the conductor performance. Table 3.3 shows the main parameters of the TFMC $Nb_3Sn$ filamentary strand (Fig. 3.2) and the NbTi filamentary strand of the bus bars.

#### 3.2.2. Cable

The cable, composed of 1080 wires one-third of which are Cu wires, has a 304 stainless steel central spiral, and an Inconel wrap for the last-but-one cable stage (10% gap) and for the final cable (half overlapped). The

Table 3.2
Main operating data of the TFMC in comparison with the ITER TF coils

| Operating data | ITER TF | TFMC alone/ TFMC + (LCT) |
|---|---|---|
| Operating current (LCT) [kA] | 68 | 80/80(16) |
| Ampere turns (LCT) [MA] | 9.1 | 7.8/7.8 (9.4) |
| $B_{max}$ in ITER TF/TFMC [T] | 11.8 | 7.78/9.97 |
| Max. compression stresses on coil [MPa] | −130 | −/−180 |
| Max. inter-DP shear stresses [MPa] | 30 | −/50 |
| Max. Tresca stresses in case [MPa] | 527 | −/470 |
| Max. Lorentz force [kN/m] | 780 | 622/797 |

cable build-up and the cross-section of the conductor are shown in Fig. 3.3 with the main parameters listed in Table 3.4.

### 3.2.3. Jacket and jacketing

Seamless 316LN SS tubes, with 1.6 mm wall thickness, were butt-welded to the final unit length (TIG orbital welding). After pulling the cable into the jacket the conductor was brought to the final specified dimensions by a set of rollers and calendered onto a 2.5 m diameter drum.

The manufacturing process has shown the importance of maintaining proper tuning of the cabling system as one cable had a slight undulation causing difficulties during introduction into the jacket. It also turned out that the use of a center spiral of a different supplier caused a significant change in the flow resistance (Section 6.2.1).

Table 3.3
Main parameters of the strands for the TFMC conductor and the bus bars

| Properties | TFMC | Bus bar |
|---|---|---|
| Sc. material | $Nb_3Sn$ | NbTi |
| Diameter [mm] | $0.810 \pm 0.003$ | $0.810 \pm 0.003$ |
| Twist pitch [mm] | ≤10 | ≤10 |
| Twist direction | RHH[a] | RHH[a] |
| Cu/nonCu ratio | $1.50 \pm 0.05$ | $2.4 \pm 0.05$ |
| Barrier | 2 μm Cr coating | 10 μm CuNi int. barrier |
| Average $I_C$ | 153 A at 12 T and 4.2 K | 440 A at 5 T and 4.2 K |
| RRR | >100 | >120 |

[a] Right hand helix.

The conductor design and manufacture has been described in several publications [36,37].

The NbTi bus bar conductor was fabricated according to a similar method. Instead of a tube a thick-walled stainless steel jacket (316LN) was used developed for the central solenoid conductor within a task of the European Fusion Technology Program.

## 3.3. Double pancake (DP) module manufacturing

### 3.3.1. Pancake winding

An automatically controlled calendering system was built and integrated into the winding line consisting of a roll-off jack, guiding rollers, straightening unit, cleaning and sand blasting unit, and calendering device. Stainless steel plates with spiral grooves served as winding templates, reaction moulds and references to position the conductor terminations.

During winding (Fig. 3.4), the conductor diameter was reduced from 40.9 mm on the spool to about 40.5 mm after straightening and further to an oval shape of $40.4 \pm 0.1$ mm in the curved regions of the racetrack. The as built TFMC double pancake data are listed in Table 3.5.

### 3.3.2. Manufacturing of the terminations

The terminations consist of an explosion bonded copper/stainless steel box, in which the cable ends were pressed by a cover with a force of about 2 MN. The Inconel over-wrap of the cable, the surface section of the petal wrap and the Cr-coating of the strands were removed before inserting the cable ends into the box. The cover was fixed by TIG welding and kept in a rigid tool fixed to the reaction mould during the whole heat treatment cycle. This type of terminations developed by CEA was qualified with full-size joint samples (FSJS) showing very low resistance as described in Section 7 [38,39]. A cross-section of such a termination is shown in Fig. 3.5.

### 3.3.3. Reaction heat treatment

The reaction heat treatment (210 °C/100 h, 340 °C/24 h, 450 °C/24 h, 650 °C/200 h) was performed in a special oven using high purity Argon as an inert gas flowing inside the conductor and with slight overpressure in the oven (Fig. 3.6). Some of the heat

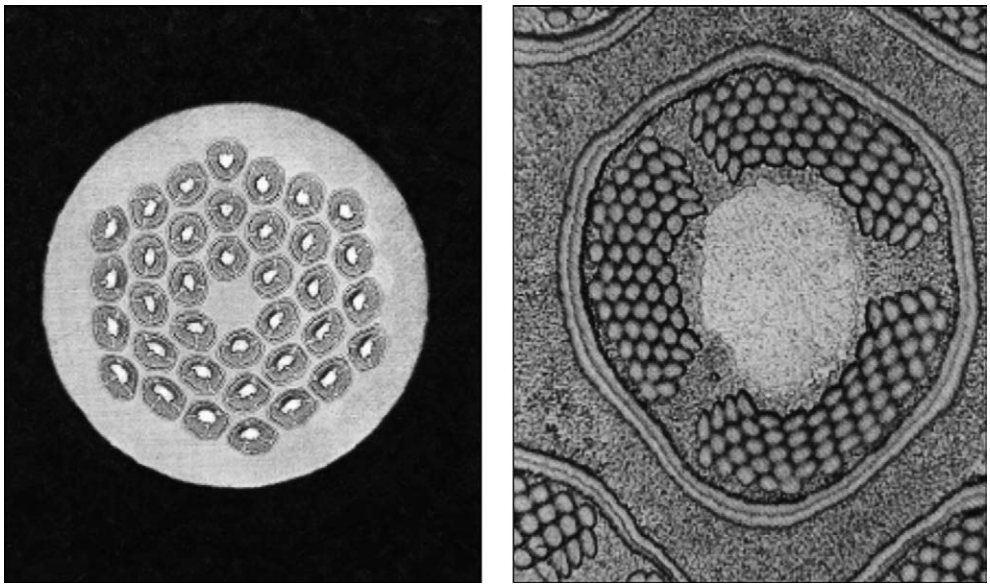

Fig. 3.2. Cross-section of the Europa Metalli $Nb_3Sn$ internal tin strand.

Fig. 3.3. Cross-section and build-up of the TFMC conductor.

Table 3.4
Parameters of the TFMC and bus bar conductor

| Properties | TFMC | Bus bar |
|---|---|---|
| Cable build-up (see Fig. 3.3) | (2 sc + 1 Cu) × 3 × 5 × 4 × 6 (MC2) | 3 × 4 × 4 × 4 × 6 |
| Cabling direction at all stages | Right hand | Right hand |
| No. of s/c strands | 720 | 1152 |
| No. of Cu strands | 360 | 0 |
| Central tube diameter | 12.0 mm × 1.0 mm | 12.0 mm × 1.0 mm |
| Central spiral gap | 35 and 50% | 50% |
| Wrapping of last-but-one stage | 0.1 mm thick Inconel tape; gap 10% | 0.1 mm thick Inconel tape; gap 10% |
| Wrapping of last stage | 0.1 mm thick Inconel tape; half overlapped | 0.1 mm thick Inconel tape; half overlapped |
| Compacted cable diameter | 37.4 mm | 38.2 mm |
| Jacket material | 316 LN | 316 LN |
| Conductor dimensions | 40.7 mm circular | 51 mm square |
| Twist pitches [mm] | | |
| Stage 1 (first triplet) | 45 ± 5 | 45 ± 5 |
| Stage 2 | 85 ± 5 | 85 ± 5 |
| Stage 3 | 125 ± 5 | 125 ± 5 |
| Stage 4 (LBO, last-but-one) | 160 ± 10 | 160 ± 10 |
| Stage 5 (full size) | 400–425 | 400–425 |

treatments were interrupted due to oven failures, and were continued after repairs. Witness strands reacted with the pancakes showed no degradation.

During heat treatment the conductor expanded in length by about 0.05%. This was overcome by increasing the width of the groove of the reaction mould leaving the conductor some freedom to move.

After heat treatment a dimensional check and leak test were carried out on all pancakes. All the pancakes including terminations were leak tight to better than $1 \times 10^{-10}$ mbar l/s.

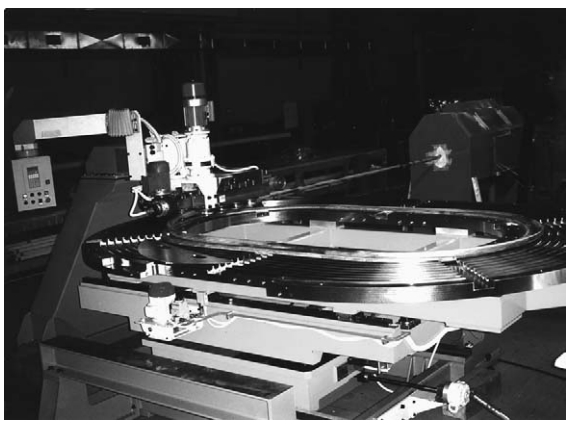

Fig. 3.4. Winding of a pancake into a reaction mould.

### 3.3.4. Turn insulation and transfer

The pancakes were spread in a fixture that ensured that the reacted conductor was not strained more than 0.2%. In this position, the glass–Kapton turn insulation and the co-wound voltage taps were applied manually as shown in Fig. 3.7. Subsequently, the pancake was transferred into the grooves of the radial plate using reference marks on conductor and plate. The turns were held in the grooves by covers spot welded in ∼200 mm distances. After turning the plate over the second pancake of a DP module was transferred in the same way.

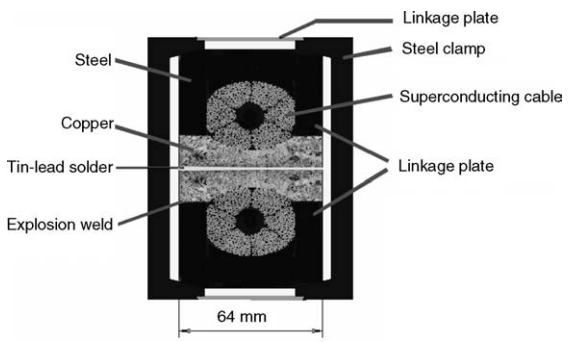


Fig. 3.5. Cross-section of a conductor termination. The terminations of two adjacent pancakes were soft soldered (inner pancake and winding end joints) or electron beam welded (outer pancake joints) and finally clamped together.

Table 3.5
TFMC double pancake data as fabricated

| Properties | Specified | DP1 | DP2 | DP3 | DP4 | DP5 |
|---|---|---|---|---|---|---|
| Length of pancakes 1/2 [m] | | 73/83 | 83/83 | 83/83 | 83/83 | 83/73 |
| No. of turns in pancake 1/2 | | 9/10 | 10/10 | 10/10 | 10/10 | 10/9 |
| Average conductor dimensions of pancake | | | | | | |
| Straight [mm] | 40.7 × 40.7 | 40.3 × 40.4 | 40.3 × 40.4 | 40.5 × 40.5 | 40.5 × 40.5 | 40.5 × 40.5 |
| Bent [mm] | | 40.3 × 40.4 | 40.0 × 40.2 | 40.4 × 40.2 | 40.4 × 40.3 | 40.5 × 40.3 |
| Local void fraction calculated for pancake | | | | | | |
| Straight [%] | 35.4% | 34.1 | 34.1 | 34.7 | 34.7 | 34.7 |
| Bent [%] | | 34.1 | 33.4 | 34.0 | 34.0 | 34.3 |
| Last cabling pitch in termination | | | | | | |
| Pancake 1 | | | | | | |
| Inner[a] [mm] | | 435 | 440 | 425 | 440 | 435 |
| Outer[a] [mm] | | 440 | 430 | 435 | 445 | 440 |
| Pancake 2 | | | | | | |
| Inner[a] [mm] | | 440 | 445 | 440 | 435 | 440 |
| Outer[a] [mm] | | 435 | 440 | 440 | 432 | 440 |
| Terminations void fraction calculated [%] | | ∼23 | ∼23 | ∼23 | ∼23 | ∼23 |
| Central tube in the terminations [mm × mm] | 12 × 3 | 12 × 3 | 12 × 3 | 12 × 3 | 12 × 3 | 12 × 3 |
| Heat treatment and incidents | 100 h, 210 °C; 24 h, 340 °C; 24 h, 450 °C; 200 h, 650 °C | Interrupted due to oven failure at 340 °C | Interrupted due to oven failure at 340 °C | Ok; none | Interrupted due to oven failure at 340 °C | Ok; none |

[a] Termination.

Fig. 3.6. Two pancakes in the reaction moulds in front of the furnace.

The radial plates (RP) and covers are made of 316LN stainless steel by forging and machining. Thanks to intermediate heat treatments at 950 °C the flatness of the finally machined radial plates was within ∼0.2 mm distinctly better than originally expected by industry.

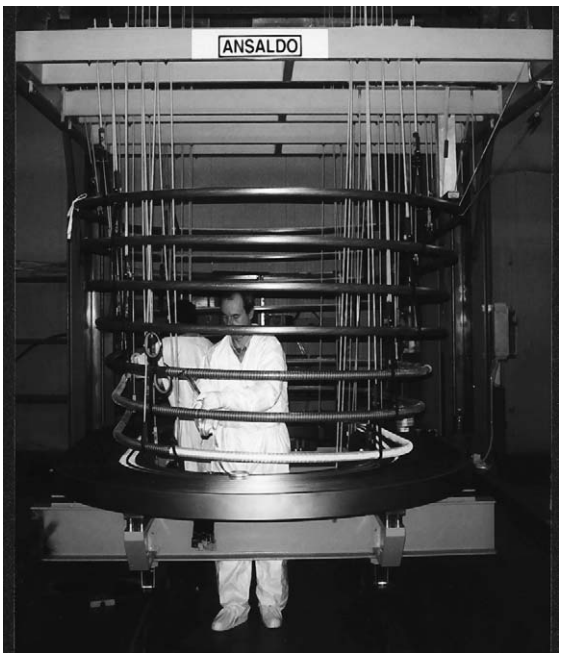


Fig. 3.7. Insulation of the turns including the installation of the co-wound stainless steel tape voltage taps and transfer into the grooves of the radial plate.

*3.3.5. Soldering and clamping of the inner joints*

It turned out that after heat treatment and removal of the fixture all terminations deformed into a banana-like shape, the copper sole being on the convex side. This posed some problems in the assembly of the terminations into the inter-pancake joints, but has been solved by precise machining of the two adjacent copper soles before connecting them. Because the necessity of such a machining was expected, some extra copper thickness was provided. The resulting joints were in agreement with the expectations (see Section 7).

The procedure to soft-solder the inner terminations to form the inter-pancake joint caused a 2 mm thermal expansion, which was taken up by the not yet impregnated turn insulation. After soldering, the joints were fitted with rigid clamps as shown schematically in Fig. 3.5.

*3.3.6. Laser welding of the covers*

To give the DP modules the right stiffness**,** the covers had to be welded with a penetration of 2.5 mm. Nd–YAG laser welding (2 kW/(0.6 m min), automatic tracking) was chosen to keep the heat input at a minimum (Fig. 3.8). Optimum flatness of the DP modules of less than 2 mm was achieved by several turnovers of the plate during the operation. With an eddy current test method developed by ENEA it was possible to check the weld quality and penetration.

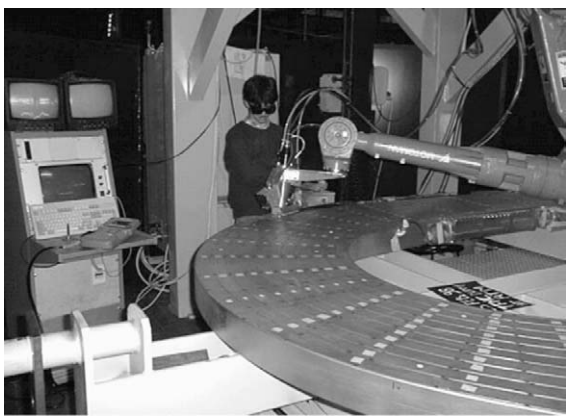

Fig. 3.8. Laser welding of the covers onto the conductor grooves of the radial plate with automatic tracker system.

*3.3.7. Module ground insulation and impregnation*

The modules were wrapped by 1.3 mm glass/Kapton insulation followed by an impregnation with DGEBA epoxy resin at about 75 °C followed by a curing cycle at about 125 °C. The resin could penetrate through holes in the covers into the turn insulation. Some of the good flatness of the radial plates was lost due to a too low stiffness of the impregnation mould.

*3.3.8. Final tests on the DP modules*

Before shipment, all DP modules passed insulation resistance tests (500 V DC conductor to radial plate), dielectric test (3 kV DC and $AC_{peak\text{-}to\text{-}peak}$ conductor to radial plate and 1.5 kV DC radial plate to ground), continuity and mutual insulating test on all voltage taps, gas flow test and a leak test at 30 bar helium internal pressure in a vacuum vessel to a level of $1 \times 10^{-10}$ mbar l/s. The test results are compiled in Table 3.6.

*3.4. Winding pack manufacture*

*3.4.1. DP stacking and winding pack impregnation*

A special stacking device was developed to align and stack the DP's to form the winding pack, as shown in Fig. 3.9. Glass felt was introduced between the DP modules in order to get good impregnation and bonding between the DP's and to adjust the height of the winding pack. During impregnation with epoxy resin a further setting of the glass felt took place**,** namely between the higher compressed lower DP's. The total height of the winding pack was decreased by about 2 mm. The impregnated winding pack can be seen in Fig. 3.10.

Fig. 3.9. Stacking of the DP modules with glass felt inter layer to equalize tolerances and to adjust the height of the winding pack.

*3.4.2. Outer joint manufacturing*

The gap between adjacent terminations had to be bridged by copper shims to secure a good contact.

Unlike the inner joints**,** it was not possible to connect the terminations of two adjacent double pancakes by soldering because of the 2 mm thermal expansion during heating. This would have caused unacceptably high stresses in the jacket.

These two technical constraints led the supplier to a solution using copper pins as shims (9–10 mm diameter) that were introduced into holes drilled between two

Table 3.6
Data of final tests of the DP modules at Ansaldo works

| Flow test | Pressure drop [bar] | DP1 [N m$^3$/h] | DP2 [N m$^3$/h] | DP3 [N m$^3$/h] | DP4 [N m$^3$/h] | DP5 [N m$^3$/h] |
|---|---|---|---|---|---|---|
| $N_2$ mass flow through pancake DP*X*.1 (*X* = 1–5) | 2 | 11.5 | 9.7 | 10.0 | 9.4 | 11.5 |
| | 4 | 21.0 | 18.3 | 18.7 | 17.5 | 21.0 |
| $N_2$ mass flow through pancake DP*X*.2 (*X* = 1–5) | 2 | 11.5 | 9.0 | 10.2 | 9.5 | 11.0 |
| | 4 | 21.0 | 16.5 | 18.9 | 17.0 | 20.0 |
| High voltage tests | | | | | | |
| 3 kV DC between turns and RP, 1 min [GΩ] | | 13 | 9.2 | 8.35 | 7.6 | 7.75 |
| 3 $kV_{peak–peak}$ AC between turns and RP, 1 min [mA] | | 91 | 99 | 102 | 101 | 92 |
| 1.5 kV DC between RP and ground, 1 min [GΩ] | | 9.7 | 9.5 | 3 | 10 | 10.9 |

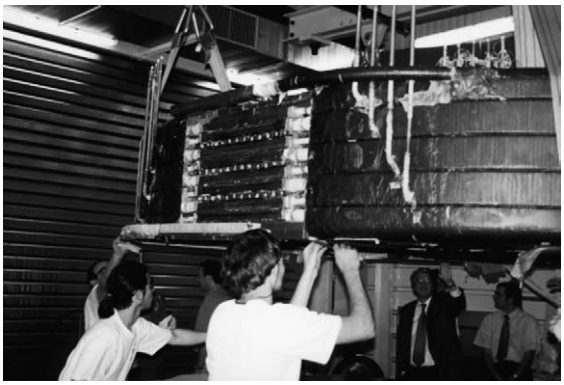

Fig. 3.10. The impregnated winding pack. The Helium outlet tubes protrude and the outer joint area is still left free.

adjacent terminations and protruding into both copper soles. These pins were electron beam welded in such a way that the bulk temperature of the terminations did not reach more than 60 °C. This method has been validated with a full-size joint sample as described in Section 7.

*3.4.3. Ground insulation and impregnation*

After having provided the outer joints with welded clamps of aluminium alloy they were wrapped by the required sliding layer (Tedlar tape) and a combined glass–Kapton insulation. Then 8 mm of combined glass–Kapton insulation was built up on the whole surface in order to form the ground insulation, which was then impregnated with DGEBA epoxy resin.

After impregnation and before assembly with the coil case dielectric tests (10 kV DC and $AC_{peak\text{-}to\text{-}peak}$) and flow/pressure/leak tests were performed successfully.

*3.4.4. Stainless steel case*

The case of the TFMC was made of 70–90 mm thick 316LN stainless steel sheet. The thickness was defined after FE calculations for the worst load case.

The pieces were MAG welded together by qualified procedures to a U-shaped structure. All welds were ultrasonically tested. Defects had to be repaired, which were unacceptable according standards for highly loaded austenitic welds.

The tightly toleranced shape was obtained by machining and local heating, partially in combination with the applied force of hydraulic jacks.

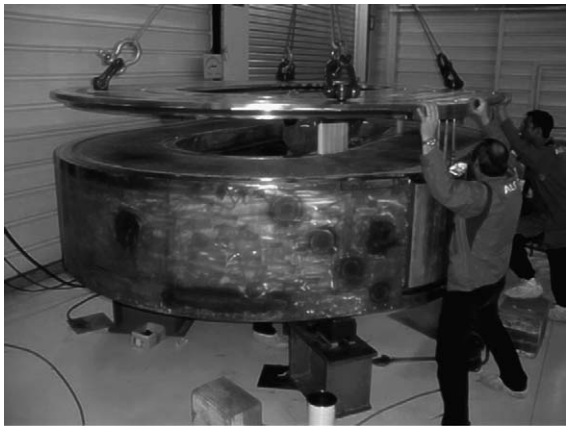

Fig. 3.11. The winding pack in the stainless steel case. After filling the gap between the two with silica sand the cover was placed on top and subsequently welded.

The welding chamfers on top of the U-shape and on the cover plate were copy milled. A fit within a few tenth of mm was achieved.

*3.4.5. Winding pack/case assembly*

For the winding pack/case assembly**,** both were in reversed position (i.e., bottom up). After having brought up the glass felt layers on the bottom of the winding pack the case was put on. A special tool fixed the assembly and allowed a turn over without slipping out of place.

After having the gap filled with silica sand and placing glass felt on top**,** the case cover was positioned on top (Fig. 3.11). The first three passes of the root were TIG welded and inspected using dye penetrant. The remaining 70–90 mm deep seam was MAG welded. Ultrasonic testing on all welding seams was performed by the French Institut de Soudure. All located defects larger than those agreed had to be repaired, particularly in highly stressed areas of the case.

After cover welding the case openings were sealed to make it vacuum tight for impregnation with the same type of epoxy resin and the same curing procedure, as used for the previous impregnations (see Section 3.3.7). For impregnation, the same mould was used again as a heating vessel.

*3.4.6. Final machining and surface finish*

The final machining of the interfaces and cooling channels on the outer circumference was done after

impregnation of the coil in the case and sand blasting of the outer surface. After the final machining the covers were welded on the cooling channels of the outer circumference and pressure and leak tested. The final surface finish was achieved by degreasing with agreed solvents.

### 3.4.7. Headers and bus bars

The inlet and outlet header assemblies have been built up on assembly frames. After having been pressure and leak tested they were transferred onto the TFMC.

A number of sensors (strain gauges, rosettes, displacement, temperature, etc.) as described in Section 3.7 were mounted onto the TFMC. The Kapton insulated high voltage cables have been equipped with the warm vacuum tight feed throughs by FZK and provided by industry with the cold end pieces that were connected with the voltage taps coming from the pancakes and the radial plates.

The bus bars have been manufactured from a CS1 type conductor using NbTi strands and a stainless steel square jacket. The bus bar terminations are of the same type as the EU FSJS's [40,38].

Two types of bus bars were manufactured: Bus bars type 1 were mounted on the TFMC connected to the coil terminations (see Fig. 3.12). After assembly in the TOSKA facility they were connected to the terminations of bus bars type 2 forming part of the TOSKA current lead system (so-called cryostat extension). The busbars were insulated by multi-layer wrapping with glass-Mica tapes wetted with ambient temperature curing epoxy resin.

### 3.4.8. Intermediate and final tests at suppliers works

Intermediate tests (dielectric, pressure/flow/leak, geometrical, etc.) were performed on DP modules, winding pack in different stages and subassemblies.

A final 30 bar helium internal pressure and leak test of the TFMC with all headers and instrumentation was carried out in a vacuum tank built by modifying the impregnation mould. The total leak rate had to be: $<10^{-7}$ mbar l/s. After this the four main He inlet and outlet tubes were welded on and tested separately.

Other final tests at the supplier's works comprise: resistance, inductance and dielectric (10 kV DC and $AC_{peak\text{-}to\text{-}peak}$) tests, dimensional check of interfaces and envelop, pressure drop on all hydraulic circuits, check of all voltage taps and sensors, etc. Table 3.7 gives an overview on the tests performed and the results.

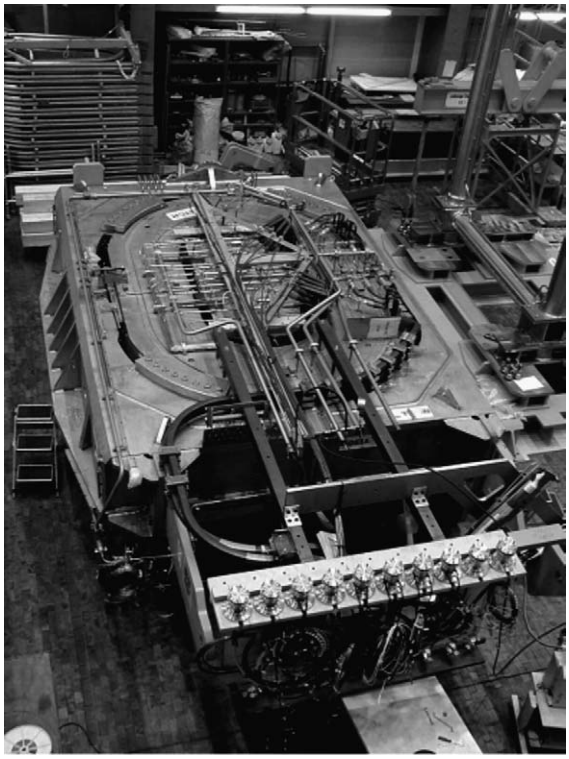

Fig. 3.12. The TFMC in the inter-coil structure (ICS) at TOSKA facility of FZK Karlsruhe. Above of the bore of the coil are the coil headers arranged. The Kapton insulated high voltage cables are guided to the 10 feed throughs (in front of the picture) to be mounted later on in the TOSKA connection box. Coming from the coil terminals are the S-shaped type 1 bus bars, which are pained with black conductive paint.

## 3.5. The inter-coil structure (ICS)

The ICS is a large welded and machined structure. It was needed to support the TFMC and connect it to the LCT coil. During joint operation of the two coils attracting forces of up to 82.6 MN were acting. Therefore, the ICS had to be designed very carefully and the design had to be validated by complex FE calculations (see Section 8). For the manufacture only high strength 316LN austenitic steel was used. The cooling channels on the surface are TIG welded. All weld-

Table 3.7
TFMC Data measured at Alstom Works

| Properties | Test condition | Result |
|---|---|---|
| Insulation resistance coil to ground | 500 V DC | 13 GΩ |
| Joints/radial plates to ground | 10 kV DC 1 min | <1 μA (>10 GΩ) |
| Impedance | 3.55 $kV_{rms}$ AC 1 min | 149 mA (∼24 kΩ) |
| Turn insulation test up to 100 V/turn | Impulse up to 9800 V | Ok |
| Inductance measurement on TFMC | at 100 Hz | 4.56 μH; Q-factor: 0.07 |
| | at 1 kHz | 153 μH; Q-factor: 0.25 |
| Global resistance of coil at 19 °C | 0.0352 Ω | $I$ = 98.4 A/$U$ = 3.471 V |
| Instrumentation and quench detection wires | | All ok except: temperature sensor; TI832 and strain gauge rosette GRI830 |

ing was qualified and tested to recognised standards. Subassemblies were leak tested in a special vacuum tank ($<1 \times 10^{-9}$ mbar l/s). The surface cooling channels were checked using locally mounted vacuum cups.

During welding and machining the ICS deformed by up to 30 mm. Partially it was possible to correct this. The remaining discrepancies were overcome by finding a modified best fit of the TFMC in the ICS and corresponding correction machining.

The overall leak rate of the ICS at 1 bar pressure difference was $<1 \times 10^{-9}$ mbar l/s. Also the ICS was equipped with mechanical and temperature sensors as listed in Section 3.7.

### 3.6. Final assembly at FZK/ITP Karlsruhe

The final assembly of the test rig and its installation into the TOSKA facility was a joint action of the AGAN consortium and FZK/ITP. After cool down the final acceptance test of the TFMC was successfully performed [41]. A quality inspection assembly plan agreed by all parties determined the sequence of operations and controls. Fig. 3.12 shows the TFMC in the ICS.

Before delivery of the TFMC to FZK both the TFMC and ICS were measured using a Leica Tracker System by ENEA (Frascati). In addition to the main interface dimensions of the two components the positions of the bus bar interfaces in TOSKA and the TFMC were checked. By remote analysis of the data from the different locations it was possible to assess the various components and interfaces and resolve detected problems.

The Leica Tracker System was also used after both test campaigns to establish whether any distortion had occurred. No permanent distortion of either component was recorded.

### 3.7. Instrumentation of the TF model coil

The TFMC and its structure were equipped with numerous sensors for protection, control and diagnostics: voltage taps, temperature, pressure, flow rate and magnetic field sensors as well as strain gauges and displacement transducers. The sensors were checked, characterised and/or calibrated prior to their installation. Each sensor was given a number for identification and relation to the calibration data. An overview on the TFMC instrumentation is given in [42,43]. Fig. 3.13 shows the electrical and cooling flow scheme of the TFMC with the schematic position of the related sensors.

#### 3.7.1. Voltage taps

A series of voltage taps were installed to monitor the superconducting state of the coil and to measure the resistance of the internal joints (Fig. 3.14). The voltage taps are made of stainless steel tapes that were connected to the superconductor at the terminations of the pancakes and routed parallel to the conductor embedded in the turn insulation. The signals are transmitted to the control room via specifically developed high voltage (HV) cables that are running from the inner joints of the individual double pancakes to the vacuum vessel wall of the TOSKA facility. The HV cables were fabricated to the same design as used for the POLO coil experiment [9,10], but were insulated by coated and baked Kapton tapes as insulation material instead of Teflon. Therefore, the HV cables could be directly

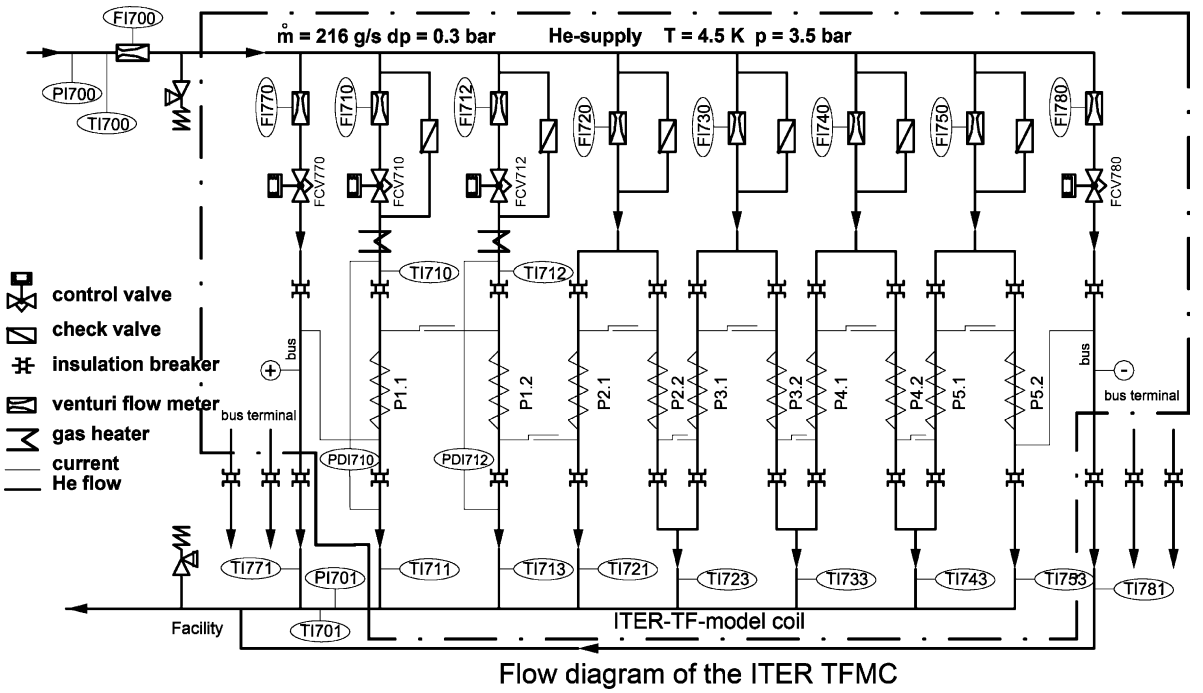


Fig. 3.13. TFMC flow and instrumentation scheme for winding and bus bars.

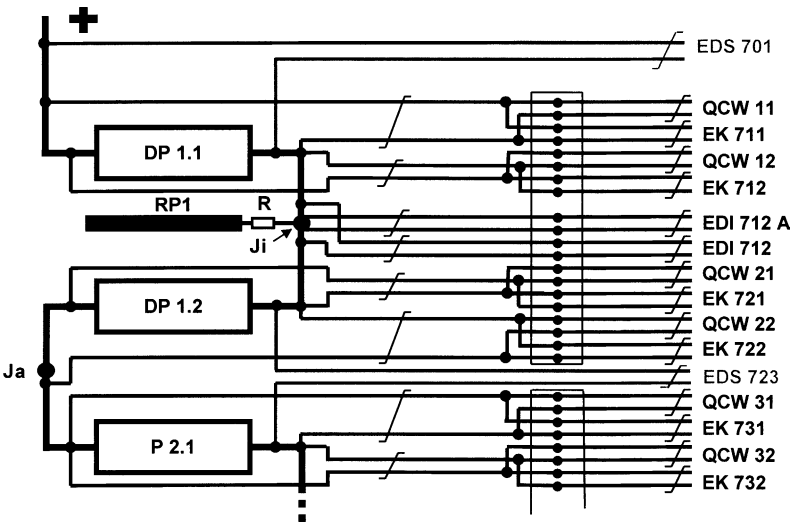


Fig. 3.14. Voltage tap instrumentation scheme for the first double pancake DP1 as example. EDI: short (A), respectively, long voltage taps (including 600 mm of conductor on each side) for joint resistance measurement; EDS: voltage taps for measurement of pancake, respectively, double pancake voltage; EK: compensated voltage taps for diagnostic; Ja: outer pancake joint; Ji: inner pancake joint; P: pancake; QCW: compensated voltage for quench detection; R: ohmic resistor (for simplification the radial plate RP is directly connected across a resistor to the inner joint. In reality the resistor is outside the vacuum vessel at room temperature; RP: radial plate.

bonded to the ground insulation of the coil so that the insulation was electrically tight in case of a vacuum breakdown and passing through the Paschen minimum pressure.

*3.7.2. Temperature sensors*

Three types of temperature sensors were used to monitor the temperature of the coolant of the coil, the case and the ICS. Due to the high magnetic field the cheaper TVO sensors could not be used in certain positions. For measuring the helium temperature, 13 CERNOX sensors (11 for the winding and 2 for the ICS) were placed directly in the helium flow inside the cooling pipes at the inlet and outlet points of the flow scheme. However, 31 TVO sensors were installed for monitoring and controlling the cool down process. They were positioned on the surface of the coil case, the surface of the ICS and on cooling pipes. Additional 4 Pt100 sensors were used to monitor the hot spots of the coil case and the ICS during cool down.

*3.7.3. Strain gauges, rosettes and displacement transducers*

The Lorentz forces deformed the overall and cross-sectional shape of the coil case and the ICS. Thirty-four individual strain gauges and 11 rosettes were installed to measure the surface strains at the main symmetry planes of TFMC, at the highly stressed wedges of the ICS and at the contact areas of TFMC, ICS and LCT. Twenty-four displacement transducers monitored the elongation of the joint area connecting adjacent double pancakes of the winding and the overall distortion of the shape of TFMC and the change of mutual position (details are presented in Section 8).

*3.7.4. Flow rate and pressure drop sensors*

The helium flow rate was measured by Venturi tube flowmeters Pancake DP1.1 and pancake DP1.2 were provided with individual Venturi flowmeters and pairs of capillaries for pressure drop measurements, because these were the pancakes foreseen for the heat slug injection to investigate the operation limits of the TFMC. There were another six Venturi flowmeters installed at the inlet points of the remaining double pancakes and bus bars.

*3.7.5. Magnetic field sensors*

In the geometrical center of TFMC, a pair of Hall probes and pick-up coils were installed to measure the magnetic field of the coil.

*3.7.6. Heaters at the inlet pipes of the DP's 1.1 and 1.2*

In order to make it possible to heat the helium flowing into the two pancakes adjacent to the LCT coil the corresponding inlet pipes were equipped with resistive heaters with a maximum power of 1000 W.

*3.8. Summary*

The specific manufacturing technology for the ITER TF coil design was successfully developed by the construction of the ITER TFMC. The main effort was put in the fabrication of the radial plates and the specific manufacturing technologies related to heat treatment and the brittleness of the $Nb_3Sn$ conductor. The milling of the groves as well as radial plate flatness within the small tolerances was a challenging task, which was solved. The "wind–react–insulate–transfer" method was the solution for handling the sensitive conductor without causing any degradation. Tolerance problems between the reacted conductor spiral and the groove of the radial plate were solved. All joints had to be fabricated with the reacted conductor. This was no problem with the applied joint technology. Soldering and EB welding techniques were used joining the special prepared conductor end of the pancakes with each other. The insulation system was based on fibreglass–Kapton tapes wrapping with a three step vacuum impregnation including the fixture of the winding pack in the thick-walled stainless steel coil case. The assembling of the TFMC with the inter-coil structure, which was manufactured by another company, was performed at the TOSKA site. The coil was equipped with an electrical, thermal-hydraulic, and mechanical instrumentation, which was integrated in the manufacturing steps of the TFMC.

The whole manufacturing process was accompanied by quality assurance procedures guaranteeing the quality of the product in respect of its electrical, thermal-hydraulics and mechanical properties.

The manufacturing of the TFMC was a coordinated task under the leadership of EFDA between the indus-

trial consortium AGAN and the European superconducting magnet laboratories.

## 4. TOSKA facility

The TOSKA facility was constructed in the early 1980s for the testing of large superconducting magnets for the magnetic confinement of nuclear fusion. The first test was the acceptance test of the LCT coil (1984) before shipment to the international test facility of "The Large Coil Task" at the Oak Ridge National Laboratory, USA [44,2]. After the conclusion of the test of the poloidal field model coil POLO (1995) [9], the cryogenic and electrical supply systems, the measuring and control equipment including data acquisition as well as the lifting capacity of the crane system were extended and modernised in the frame of a task agreement with ITER Director for the test of the ITER TFMC. The extension was performed in two steps including the intermediate test operation of the LCT coil with superfluid forced-flow helium II cooling (1996–1997) [45] and the acceptance test of the W 7-X DEMO coil in the background field of the LCT coil (1999) [46,47]. The TFMC was tested in 2000 as a single coil (Phase 1) [20] and in 2002 in the background field of the LCT coil (Phase 2) [52].

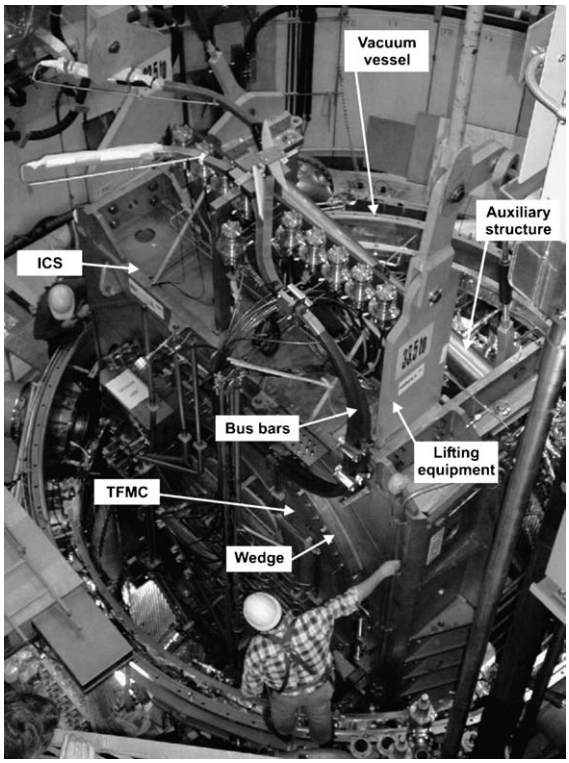


Fig. 4.1. First installation of the TFMC without the LCT coil for test Phase 1.

### *4.1. Installation of the test configuration in the TOSKA facility*

#### *4.1.1. Installation*

In Phase 1, the LCT coil was replaced by a frame, the so-called auxiliary structure. The complete assembled test rig with a total weight of 61 t was lifted into the vacuum vessel with only one crane (Fig. 4.1). After the exact positioning of the test rig and the installation of the two cryostat extensions containing the 80 kA current leads and superconducting bus bars type 2 (BB2), the electrical joints of the bus bars BB1 and BB2 (see Figs. 4.22 and 4.23) were assembled. For the He and $LN_2$ cooling system, the piping was already prepared in advance, as far as possible, but it had to be extended and connected to the TFMC coil, inter coil and auxiliary structure and the cryostat extensions.

Also the high and low voltage instrumentation wiring and the capillaries had to be installed, connected to the data acquisition system (DAS) and/or programmable logic controller (PLC) system and tested as explained below. After the final leak testing the entire He piping and the whole test configuration was covered with multi layer insulation (reduction of thermal radiation losses as low as possible) before closing the lid of the $LN_2$ shield and the vacuum vessel.

After completion of Phase 1, the test arrangement was disconnected from the facility and extracted from the vacuum vessel.

For test Phase 2, the auxiliary structure was removed and the LCT coil assembled beside the TFMC. Now the test arrangement had a weight of 108 t and both cranes (50 + 80 t) with an added special lifting beam for the distribution of the load were required for the installation (Fig. 4.2). This beam was equipped with the appropriate lifting tools to adjust the test rig in an absolutely vertical position (over a height of 4.6 m the maximum acceptable tilting was only 5 mm). This was

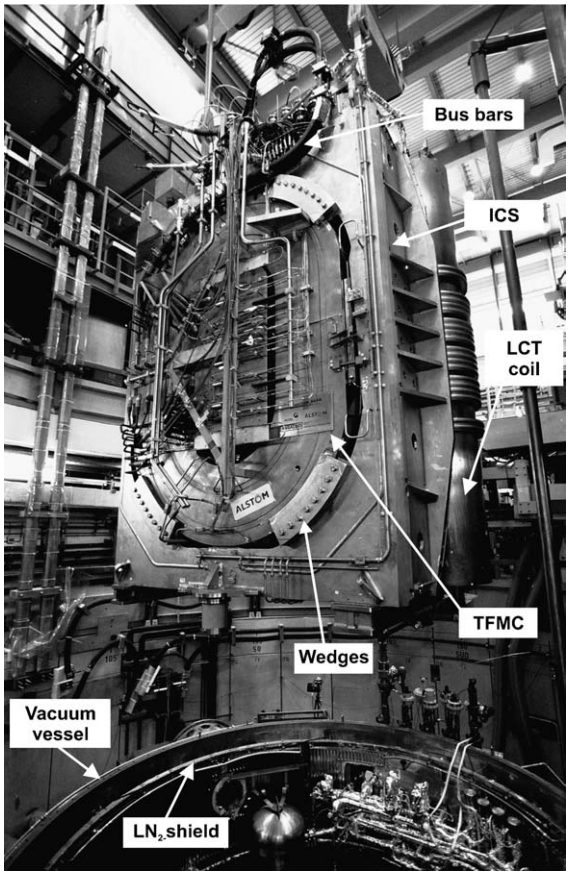


Fig. 4.2. Second installation of the TFMC with the LCT coil for test Phase 2. The total weight including the lifting beam was 115 t therefore both cranes were used simultaneously.

necessary for the installation into the vacuum vessel because of the small clearance between the $LN_2$ shield and the test arrangement.

All the connections of the He- and $LN_2$-cooling system as well as for the current and measuring systems were manufactured now for both of the coils. All the tests mentioned below (Section 4.1.2) were performed successfully in advance and after the evacuation of the vacuum vessel and the start of the cool down. This was the installation of the largest test arrangement up to now into this facility.

After completion of test Phase 2, the rig was again disconnected from the facility, extracted from the vacuum vessel and placed onto the assembly frame in the TOSKA experimental area.

### *4.1.2. Accompanying test strategy during installation*

The installation of large test arrangements requires a well-defined series of acceptance and accompanying tests. Acceptance tests are needed for unique transfer of responsibility and the reference state of the interfaces. Accompanying tests assure the quality of the installation work during the single steps and monitor the properties during test operation. During installation the accompanying tests are arranged in such a sequence that in case of faults a repair with a reasonable effort is possible. For the TFMC installation, these are mainly leak and pressure tests, instrumentation tests and tests of the dielectric insulation. In case of acceptance tests, geometrical and flow measurements are added.

For the leak tests, the coolant circuit is pressurised to the maximum operation pressure. A bag made of a plastic foil or a temporary local vacuum chamber is then placed around weld seams or flange seals after completion of piping work. The volume of the bag must be small to obtain a high sensitivity in case of measurement of the leak according to the concentration increase method. The leak test by the local vacuum chamber has the same sensitivity as an overall vacuum leak test. The methods described above are indispensable as an accompanying test and for the localisation of leaks. The last and most reliable leak test is performed with the coil in the vacuum vessel at a pressure level $<10^{-3}$ mbar.

The instrumentation checks assure the continuity of the wiring, correct polarity and the sufficient insulation to ground.

The dielectric tests assure soundness of dielectric insulation system. They are extensively treated in Section 9.

The accompanying tests performed during installation are summarised in Table 4.1. In principle the sequence of the accompanying tests is the same procedure for test Phase 1 or 2. The number of several tests is nearly doubled in case of the two-coil test configuration. The achieved leak rates are presented in Table 4.2. In test Phase 1, a small leak was discovered after cool down, and in test Phase 2, at the end of the test campaign. Both leaks had no impact on the operation.

The dielectric insulation system had a fault at the Paschen minimum. Fortunately, these faults did not represent a limitation for the high current test operation.

Table 4.1
Overview of performed acceptance test and accompanying test during installation

| Step | Leak test | Sensor continuity | Dielectric insulation test | Mechan. dimensions | Flow test |
|---|---|---|---|---|---|
| After assembly TFMC/ICS/Aux. structure | +[a] | + | + | + | – |
| After installation in the TOSKA vac. vessel | +[a,b] | + | + | – | + |
| After evacuation of the TOSKA vac. vessel | +[c] | + | + | – | – |
| Fault localisation work | +[a,b] | + | + | – | – |
| After cool down, acceptance test | +[c] | + | + | – | + |
| Before warm up | +[c] | + | + | – | + |
| After warm up at room temperature | +[c] | + | + | – | + |
| Fault localisation work | +[a,b] | + | + | – | – |

[a] Bagging and concentration increase.
[b] Local vacuum chamber.
[c] Vacuum leak test.

### 4.2. Test procedure

The test procedure is the agreed sequence of test steps to achieve the desired results in an optimised way in time and risk. The test procedure of the single coil is given in [49].

The test procedure for the TFMC test in the background field of the LCT coil was determined by the following boundary conditions:

(1) each coil has to be operated first as a single coil;
(2) for currents > 12 kA the LCT coil has to be operated at 3.5 K, which is a more sophisticated operation mode of the cryogenic system (Section 4.3.2.2).

The single steps of the summarised test procedure of Phase 2 are presented in Table 4.3 [49]. The test procedure is characterised by defined cool down, cooling and ramping procedures to certain current levels.

According to the FEM analysis performed by the coil manufacturer AGAN, the TFMC current has to be limited to 70 kA in order to avoid overstressing of the outer joint region. The FEM analysis showed that a current combination (TFMC 80 kA, LCT 14 kA) had nearly the same attractive forces between the coils but increased the Lorentz body (volume) force on the TFMC conductor. The assessment of the measured mechanical data and the upscaling to a current combination (TFMC 80 kA, LCT 16 kA) should create no mechanical problem, which was confirmed in the experiment. In this case, the achieved load is 100% of the peak Lorentz body force (∼800 kN/m) expected on the ITER TF coil conductor in nominal operating conditions.

The fast high voltage discharge test was cancelled in Phase 1 after the discovery of the insulation fault. The careful dielectric investigations at the end of Phase 1 and their assessments have shown that a fast high voltage discharge with reversed polarity and a reduced voltage (≤4 kV) can be performed without risk.

All tests of the procedure were performed successfully in the given time frame of about 4.5 months.

### 4.3. Cryogenic system and operation experience

A 2 kW He refrigerator was used for cool down of the test configuration, steady state operation at 4.5 K and for the cooling of the four current leads (Fig. 4.3) in both of the tests phases [48,50]. An additional available 500 W refrigerator, which is designed for an operation temperature between 4.5 und 1.8 K, was used for

Table 4.2
Measured overall helium leak tightness in test Phase 1/2 by performing a vacuum leak test

| Test phase | Helium leak rate [mbar l/s] (pressure [$bar_{abs.}$]) | | | |
|---|---|---|---|---|
| | Before cool down (300 K) | After cool down (4.5 K) | Before warm up (4.5 K) | After warm up (300 K) |
| Phase 1 | $1 \times 10^{-7}$ (21) | $2 \times 10^{-5}$ (3.5) | $2 \times 10^{-5}$ (4) | $1 \times 10^{-7}$ (21) |
| Phase 2 | $5 \times 10^{-7}$ (8) | $7 \times 10^{-7}$ (4.8) | $3 \times 10^{-4}$ (3) | $1 \times 10^{-6}$ (18) |

Table 4.3
The test procedure for Phase 2 (TFMC + LCT coil)

| Position number | Procedure |
|---|---|
| 1 | Checkouts at RT |
| 2 | Cool down |
| 3 | Checkouts at operation temperature (∼4.5 K) |
| 4 | Single coil test TFMC analog to [20], no cycling |
| 5 | Single coil test LCT coil up to 11.3 kA at 4.5 K analog [20], no cycling, no current sharing measurements |
| 6 | TFMC + LCT coil, low current checkouts ($I_T$ = 3.5 kA, $I_L$ = 0.8 kA, $F = 0.0025 \times F_0$[a]) at 4.5 K<br>Ramp up–hold–ramp down (ramp rate TFMC: 22 A/s, LCT: 5 A/s)<br>Ramp up–hold–inverter mode discharge (max. power supply voltage) (ramp rate TFMC: 79 A/s, LCT: 18 A/s)<br>Ramp up–hold–safety discharge (exponential current decay) (ramp rate TFMC: 22 A/s, LCT: 5 A/s) |
| 7 | TFMC + LCT coil, ramping up in selected currents steps in fractions of $F_0$ at 4.5 K<br>{$I_T$ [kA], $I_L$ [kA], $F/F_0$ [1]}: {10, 2.3, 0.021}, {20, 4.6, 0.082}, {30, 6.9, 0.18}, {35, 8, 0.25}, {49.5, 11.3, 0.5}<br>For each step: repeat procedure of position 6[b] |
| 8 | LCT single coil test up to 16 kA at 3.5 K analog to [20], no cycling, no current sharing measurements |
| 9 | TFMC at 4.5 K + LCT coil at 3.5 K, ramping up in selected currents steps in fractions of $F_0$<br>{$I_T$ [kA], $I_L$ [kA], $F/F_0$ [1]}: {60.6, 13.9, 0.75}, {66.4, 15.2, 0.9}, {70, 16, 1.0}<br>For each step: repeat procedure of position 6[b] |
| 10 | TFMC at 4.5 K + LCT coil at 3.5 K, optimisation of the heating procedure without current |
| 11 | TFMC at 4.5 K + LCT coil at 3.5 K, determination of the operation limits ($T_{CS}$) by stepwise increase of the heating power of inlet helium of two pancakes at $F_0$<br>{$I_T$ [kA], $I_L$ [kA], $F/F_0$ [1]}: {70, 16, 1.0} till trans. into normal conducting state occurs |
| 12 | TFMC at 4.5 K + LCT coil at 3.5 K, TFMC cycling by a total of 28 triangular current pulses at four current levels with a ramp rate 140 A/s and LCT coil at 16 kA steady state operation<br>{$I_T$ [kA], $I_L$ [kA], $F/F_0$ [1]}: {35, 16, 0.5}, {52, 16, 0.75}, {63, 16, 0.90}[c], {70, 16, 1.0}[c] |
| 13 | Repeat Pos. 9 for {70, 16, 1.0}: ramp up–hold–ramp down, check mechanics |
| 14 | Repeat Pos. 10 + 11 for {80, 14, 1.0} |
| 15 | Repeat Pos. 10 + 11 for {80, 16, 1.14} |
| 16 | TFMC fast high voltage discharge[d]: $I_T$ = 6 kA, $U_T$ = 4.8 kV, $\tau$ = 26.5 ms |
| 17 | Standardised 25 kA safety discharge for measurement of electrical losses performed at suitable positions in the test procedure |
| 18 | High voltage (HV) tests: DC, AC, partial discharge, pulse voltage<br>These tests are performed in the relevant position numbers of the test procedure, e.g., 1, 3, 15–17 |
| 19 | Daily tests before starting testing: DC HV test, low current safety discharge |
| 20 | Final checkout at operation temperature |
| 21 | Warm up |
| 22 | Checkout at room temperature |

[a] Rated attractive Lorentz forces $F_0 \sim I_T \times I_L$; $I_T = I_{TFMC}$; $I_L = I_{LCT}$; $F_0$ is defined for the reference load case TFMC 70 kA/LCT 16 kA.
[b] The inverter mode discharge was omitted for $I_T > 35$ kA because the faster achieved $I_T \sim 0$ led to undefined power supply operation, which caused excessive electric losses in the TFMC. The reason is the magnetic coupling between TFMC and LCT coil, which has for same inverter voltage a smaller ramp rate caused by much higher inductance ($L_{LCT}$ = 1.57 H, $L_{TFMC}$ = 0.027 H).
[c] During cycling at these current levels two quenches of the LCT coil occurred. The reason was a too low temperature margin. After lowering the inlet temperature to 3.0 K no more quenches occurred.
[d] The LCT coil is shorted by its safety discharge resistor.

the operation of the LCT coil winding in the temperature range between 3 and 3.5 K. This was necessary to operate the NbTi coil up to a current of 16 kA. For the cool down, the He was supplied directly from the 2 kW refrigerator to the test configuration in a separate transfer line, whereas during operation at the temperature level of 4.5 K, the 2 kW refrigerator liquefied He into the control dewar (B250), while both coils and

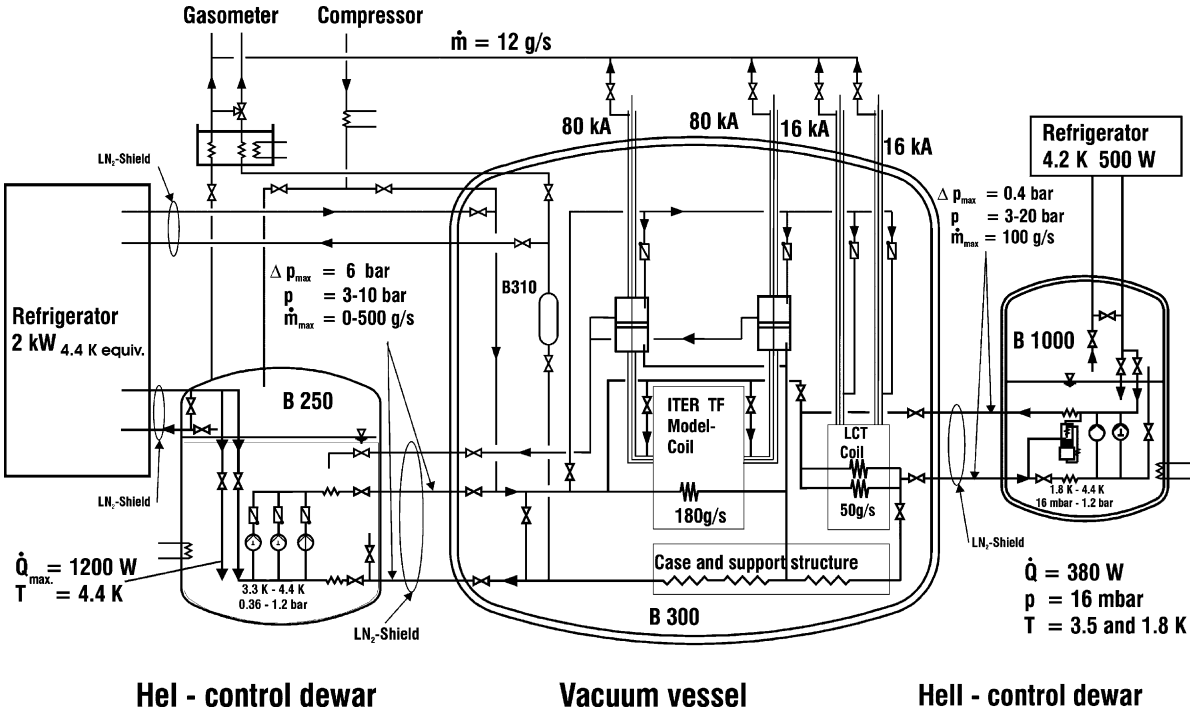


Fig. 4.3. Flow diagram of the He cooling system of the TFMC test including the LCT coil in TOSKA.

all structures were forced-flow-cooled in a secondary cooling loop. The He in this loop was circulated by means of two piston pumps and one centrifugal pump. The secondary cooling loop was filled and pressurised from the refrigerator at the inlet side of the pumps and also the He mass flow rate for the four current leads was supplied from the refrigerator through the pumps and heat exchangers in the secondary loop, in order to achieve the same low inlet temperature to the current leads as for the coils. For operating the LCT coil winding at a temperature level between 3.0 and 3.5 K, the winding was cooled in a separate forced-flow loop, which was connected to the control dewar B1000 as shown in Fig. 4.3. In this dewar the LHe was supplied from the second refrigerator which allows operation in the temperature range between 1.8 and 4.5 K because of its low pressure heat exchanger path and a set of vacuum pumps for an operation pressure down to 16 mbar. In the forced-flow-cooling loop, the He was circulated by a three-cylinder piston or a centrifugal pump.

In standby mode, during nights and weekends, the whole configuration was directly cooled by the 2 kW refrigerator with a reduced He mass flow rate.

For collecting the expelled He of the coils after a safety discharge or quench, a cold storage vessel of 1.8 $m^3$ and a maximum pressure of 18 bar (B310 in Fig. 4.3) was installed into the vacuum vessel B300. The collected He was later on warmed up to ambient temperature in a water/He heat exchanger, stored in a low pressure gasometer, purified and than stored in high pressure (200 bar) containers.

### *4.3.1. Cool down and warm up*

In both test phases the cool down was performed by a computer controlled inlet temperature from room temperature to about 20 K. Below this temperature the cool down was manually controlled. The temperature difference limits of 45 K across both coils and of 65 K across the ICS were never exceeded except at the outermost corner of the ICS (because of the local low thermal conduction). The extension of the temperature difference limit by 10 K was accepted by the manufacturer in this area of the ICS.

For the cool down, 2 weeks were required in Phases 1 and 2. Main temperatures and resistance recorded during the second one are shown as example in Fig. 4.4.

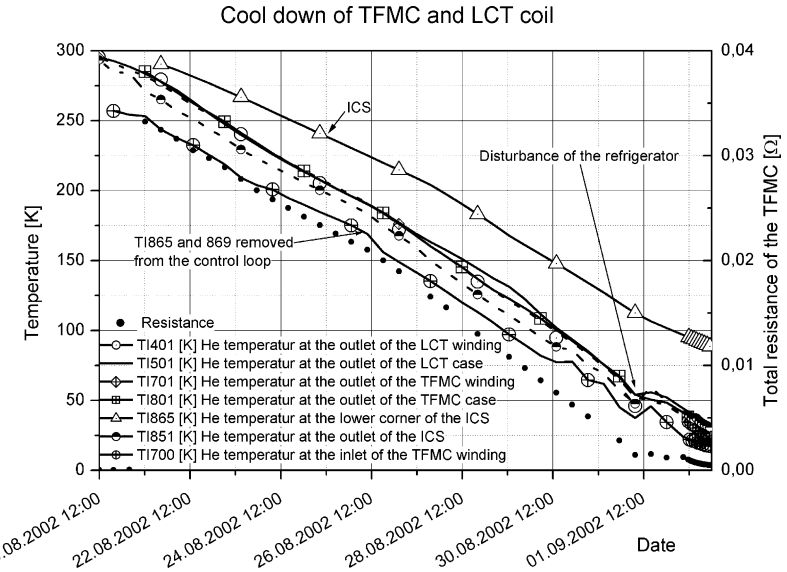


Fig. 4.4. Cool down of the TFMC test configuration for test Phase 2.

The smooth and safe cool down, as shown in this Fig. 4.4, was limited by the thermal conduction not by the refrigerator cooling capacity.

All components were cooled in parallel with the mass flow rate coming directly from the 2 kW refrigerator. The mass flow rates of the individual components were adjusted manually in order to minimize the temperature differences in the test arrangement. The total mass flow rate was in the range between 75 and 95 g/s. At the start of the cool down the cooling power was around 7 kW and decreased at the end to 2 kW. The cool down was stopped for 6 h at 77 K as shown in Fig. 4.4 for a calibration of the current distribution measurement.

The vacuum pressure in B300 was $9 \times 10^{-4}$ mbar at room temperature and reached $5.6 \times 10^{-6}$ mbar at LHe Temperature. During the cool down, and also during operation, the leak rate was checked frequently and no indication of a significant leak was found (see Table 4.2).

The warm up was also computer-controlled above 20 K, like the cool down, and the time needed was 2 weeks in both test phases.

### *4.3.2. Cryogenic operation*

The control dewar B250 was filled with LHe in parallel at the end of the cool down. When the cool down was finished the secondary cooling loop was pressurised to supercritical conditions. By means of the He piston pumps, the supercritical He was then circulated in the cooling loop of the coils. For the extended operation with a required mass flow rate up to 280 g/s, both piston pumps were operated in parallel. The mass flow rate of the different components was adjusted to the values as listed in Table 4.4. Also the heat load of the various components was investigated carefully before current operation and the results are included in Table 4.4 as standby values. The measured values were in good agreement with the calculated ones except of the heat load of the bus bars types 1 and 2. This heat load of 36 W for the negative and 40 W for the positive bus bar required a high He mass flow rate in order to keep the outlet temperature of the bus bars below 6 K and avoid a quench of the NbTi conductor during current operation. The reason for this unexpected high heat load could not be clarified up to now.

An advantage of the conductor and TFMC winding design is the relatively low pressure drop that was measured at room temperature as well as at LHe temperature (see Section 6.2.1) [51] and the relatively uniform mass flow distribution in the TFMC winding without an active control as shown in Fig. 4.5. The maximum deviation from the average mass flow rate was around −10% in DP4 and around +10% in DP5. These

Table 4.4
Cooling conditions of the TFMC coil

| Operation | Coil | $I_{coil}$ [kA] | $T_{Inlet}$ winding [K] | $T_{Outlet}$ winding [K] | $P_{Inlet}$ [bar] | $\dot{m}$ winding [g/s] | $\dot{m}$ bus bar [g/s] | $\dot{m}$ case [g/s] | $\dot{m}$ ICS [g/s] | $\dot{Q}$ winding [W] | $\dot{Q}$ bus bar [W] | $\dot{Q}$ case [W] | $\dot{Q}$ ICS [W] |
|---|---|---|---|---|---|---|---|---|---|---|---|---|---|
| Phase 1 | | | | | | | | | | | | | |
| Standby | TFMC | | 4.74 | 4.88 | 4.15 | 20 | <1 | 5 | 8 | 15 | 40/36 | 4 | 45 |
| Rated | TFMC | 80 | 4.51 | 4.93 | 4.75 | 74 | 10/9.7 | 13 | 14 | 134 | 61/55 | 9 | 30 |
| Extended | TFMC | 80 | 4.51 | 4.75 | 6.15 | 140 | 20/20 | 11 | 12 | 131 | 73/70 | 8 | 34 |
| Phase 2 | | | | | | | | | | | | | |
| Standby | TFMC | | 4.82 | 4.89 | 3.16 | 35 | <1 | 4 | 20 | 16 | 40/36 | 2 | 42 |
| | LCT coil | | 4.85 | 4.96 | 3.17 | 20 | | 10 | | 15 | | 18 | |
| Rated | TFMC | 49.5 | 4.52 | 4.88 | 3.67 | 49 | 5.8/5.5 | 10 | 19 | 80 | 45/40 | 4 | 42 |
| | LCT coil | 11.3 | 4.53 | 4.67 | 3.74 | 50 | | 16 | | 30 | | 12 | |
| Rated[a] | TFMC | 70 | 4.57 | 5.01 | 3.65 | 50 | 6/6 | 12 | 15 | 130 | 48/41 | 2 | 50 |
| | LCT coil | 16 | 3.49 | 3.78 | 3.77 | 50 | | 17 | | 42 | | 15 | |
| Extended[a] | TFMC | 80 | 4.52 | 4.82 | 5.92 | 138 | 21/21 | 33 | 21 | 147 | 77/72 | 13 | 55 |
| | LCT coil | 16 | 3.03 | 3.55 | 5.54 | 51 | | 50 | | 57 | | 15 | |

Phase 1, test without LCT coil; Phase 2, test with LCT coil.
The extended operation parameter were used before the heating for the $T_{CS}$ measurement was started.
$I$, coil current; $T$, temperature; P, pressure; $\dot{m}$, mass flow rate; $\dot{Q}$, heat load.
[a] Operation at different temperature levels.

deviations are similar to those measured in most of the tested coils up to now with parallel cooling channels, e.g., around 15% in case of the LCT coil. The thermal-hydraulic analysis of the TFMC itself is presented in Sections 6.2.1 and 6.2.2 and in [52]. Before finally starting the current operation an extensive check out of the interlock system of the cryogenic facility as well as for the link to power supplies and quench detection system was performed.

*4.3.2.1. Operation with one temperature level at 4.5 K.* In test Phase 1 (without the LCT coil), all components were cooled at the same temperature level of 4.5 K with the 2 kW refrigerator whereas the 500 W refrigerator was connected to the facility for redundancy reasons only.

The TFMC was energised in steps up to 80 kA and a safety discharge was initiated at each step. Beside the electrical and mechanical reasons for the energising in steps also the reaction of the cryogenic system after the safety discharge with a high heat load has to be investigated. Up to a coil current of 30 kA during the single coil test (Phase 1) and 25 kA during the Phase 2 (including the LCT coil) the cooling system could handle the heat load without valving off the secondary cooling loop. In case of a safety discharge or a quench above this value, the pumps were switched off, the valves to the control dewar closed and the valves to the cold storage vessel B310 (see Fig. 4.3) opened. The expelled He from the coils was collected in the cold storage vessel, warmed up later, and slowly transferred to the recovery system at room temperature. In Fig. 4.6, the typical cryogenic behaviour for the operation as a single coil during ramp up and down as well as during ramp up followed by a safety discharge is recorded. Re-cooling after a safety discharge without and with switching off the cooling system is shown in Figs. 4.7 and 4.8, respectively.

In the testing Phase 2, the windings of TFMC and LCT coil were cooled in series with cases and ICS in order to reduce the overall mass flow rate and, as consequence, also the pumping power in B250. A typical test run at the maximal current of both coils at a temperature level of 4.5 K is shown in Fig. 4.9 including inlet and outlet temperature and the heat load of both windings.

According to the test procedure an inverter mode discharge was foreseen at each step but the heat load

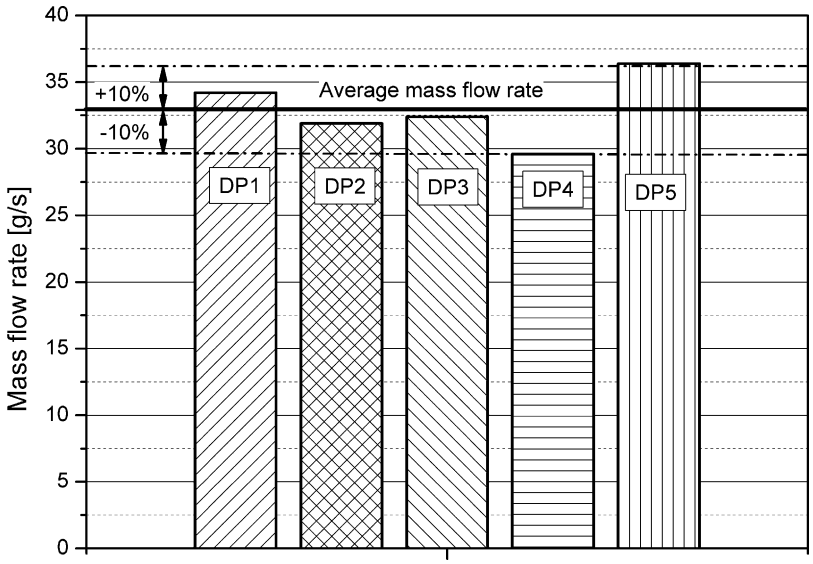


Fig. 4.5. Measured mass flow distribution in the TFMC winding during operation.

to the cooling system was unexpectedly high after an inverter mode discharge of both coils together. As shown in Fig. 4.10, the cooling energy reached 660 kJ for re-cooling after an inverter mode discharge from only 10 kA (TFMC)/2.3 kA (LCT) which is almost 10% of the stored energy and twice the cooling energy after a safety discharge from 25 kA (TFMC)/5.75 kA (LCT) as shown in Fig. 4.7. The reason for this could not be clarified during the test but it was decided to avoid in the remaining tests an inverter mode discharge of both coils in order to save testing time. An explanation of this behaviour was

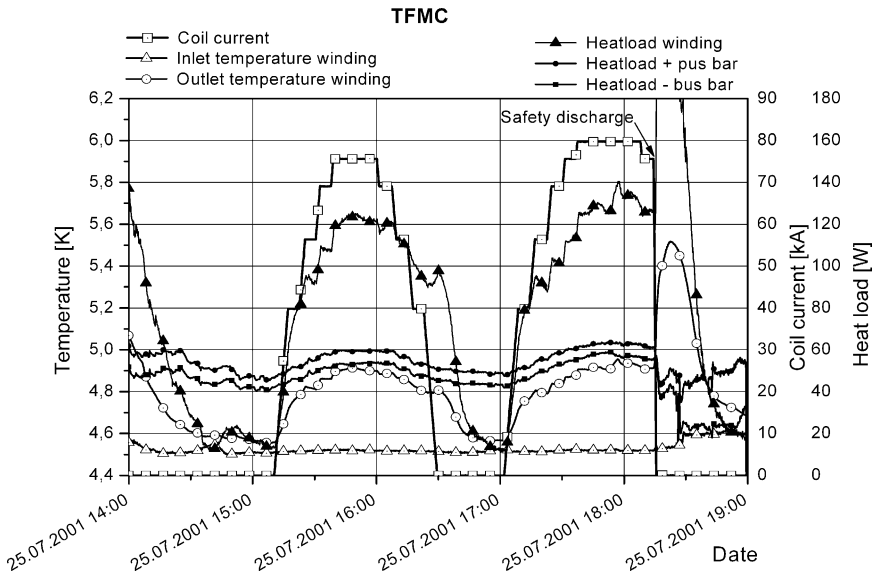


Fig. 4.6. Heat load during rated current operation in test Phase 1.

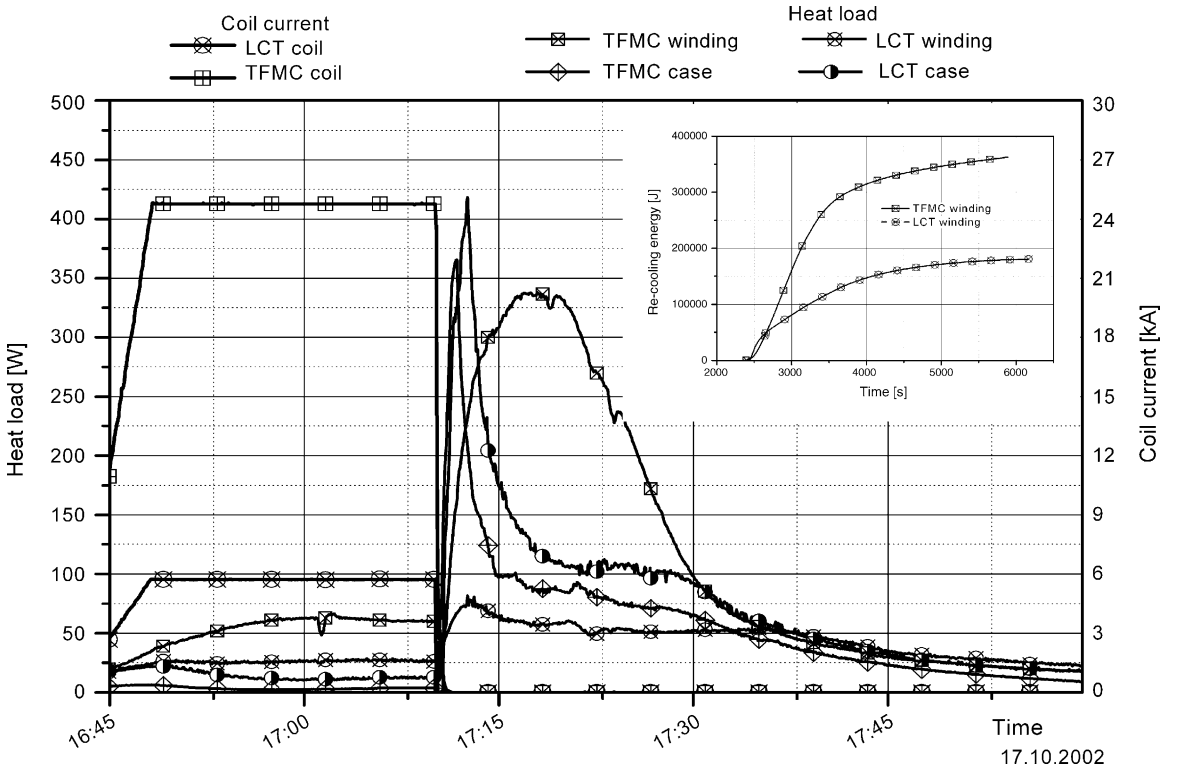


Fig. 4.7. Re-cooling after a safety discharge from 25 kA in the TFMC and 5.75 kA in the LCT coil and continuous running cooling system.

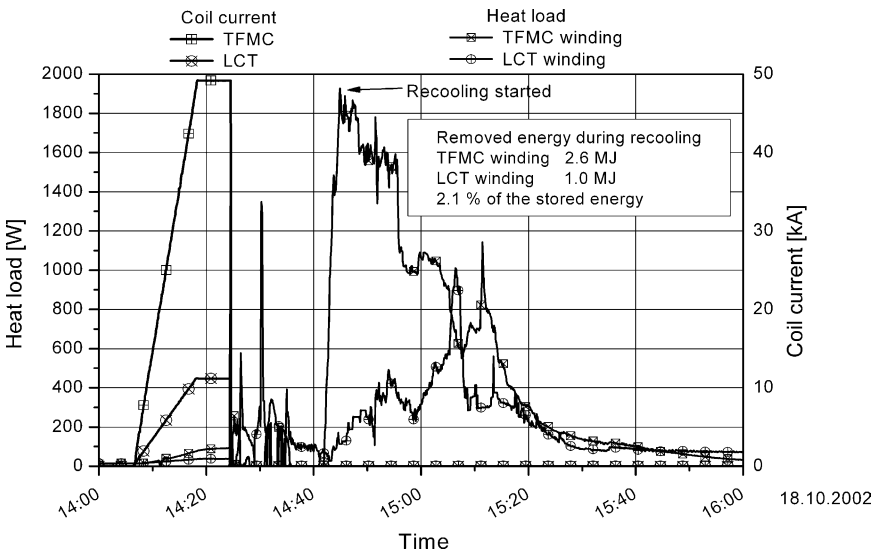


Fig. 4.8. Re-cooling after a safety discharge from 49.5 kA in the TFMC and 11.3 kA in the LCT coil. This was the maximum possible coil current for operation of both coils at 4.5 K. The cooling system had to be stopped with the initiation of the safety discharge.

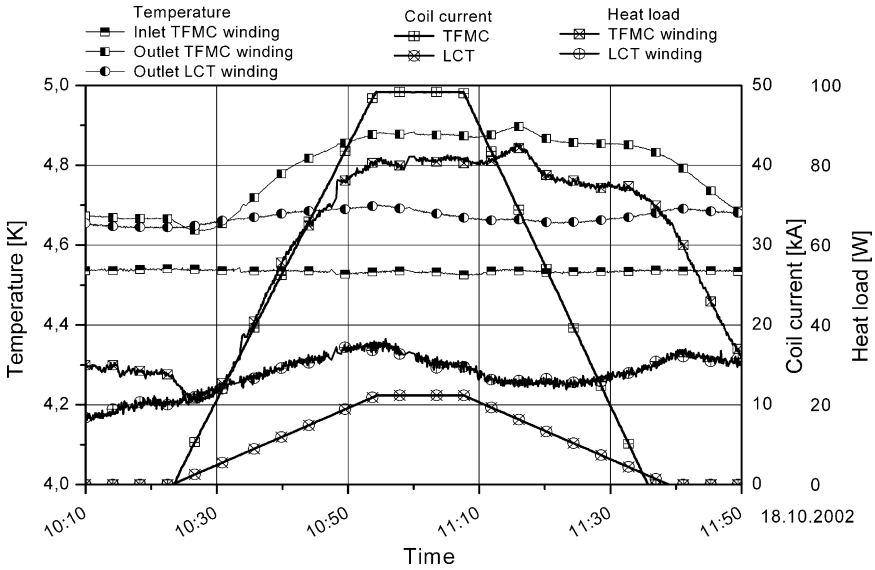


Fig. 4.9. Energising both coils to the maximum current of 49.5 kA in the TFMC and 11.3 kA in the LCT coil with a LCT coil winding operation temperature of 4.5 K.

found during the evaluation phase and is included in Section 4.5.2.

After a high voltage discharge from 6.3 kA, the re-cooling energy was 403 kJ, which is 75% of the stored energy (Fig. 4.11). In this case the efficiency of the energy extraction is poor because the time constant of the discharge circuit (∼27 ms) is much lower than the time constant of the structure (radial plates and case ∼100 ms).

*4.3.2.2. Simultaneous operation at two temperature levels, 3 and 4.5 K.* At the temperature level of 4.5 K, the LCT coil could be energised up to 11.3 kA only, but according to the test program an operation up to 16 kA was required and for this a cooling temperature of the LCT coil winding down to 3.5 K was necessary. Steady state operation up to 16 kA was performed without problems at 3.5 K but two quenches occurred in the LCT coil during cycling current operation of the TFMC. It was found that the temperature margin was too small and as a consequence the operation temperature was reduced to 3 K for the further test runs. For an operation at reduced temperature (3 K), the 500 W refrigerator was used as mentioned above and explained in [53]. The operation in this mode is not automated and it was therefore only possible during daytime with operators present. The consequence was that the cool down from 4.5 to 3.5 K, respectively, 3 K as seen in Fig. 4.12 had to be repeated every morning. In Fig. 4.13, temperature, coil current and heat load profile during the test at the rated coil current of 70 kA in the TFMC and 16 kA in the LCT is shown. The cooling conditions are listed also in Table 4.4. In Fig. 4.14, the re-cooling after a safety discharge from the same coil current level can be seen including the energy required for the re-cooling. Only 2–3% of the stored energy was transferred to the cryogenic system after all the safety discharges and quenches of both coils together and could be handled without problems. Most of the energy (97–98%) could be extracted and transferred to the dump resistor. The cooling requirements of the TFMC winding versus the coil current are shown in Fig. 4.15. In this diagram, it can be clearly seen that there is an additional heat load to the resistive and standby losses, which is explained in Section 6.1.3 as AC losses in the radial plates caused by the ripple of the current.

*4.3.2.3. Handling of $T_{CS}$ measurement and safety discharge.* In preparation of the $T_{CS}$ measurements a feasible heating scenario had to be investigated with the following constraints:

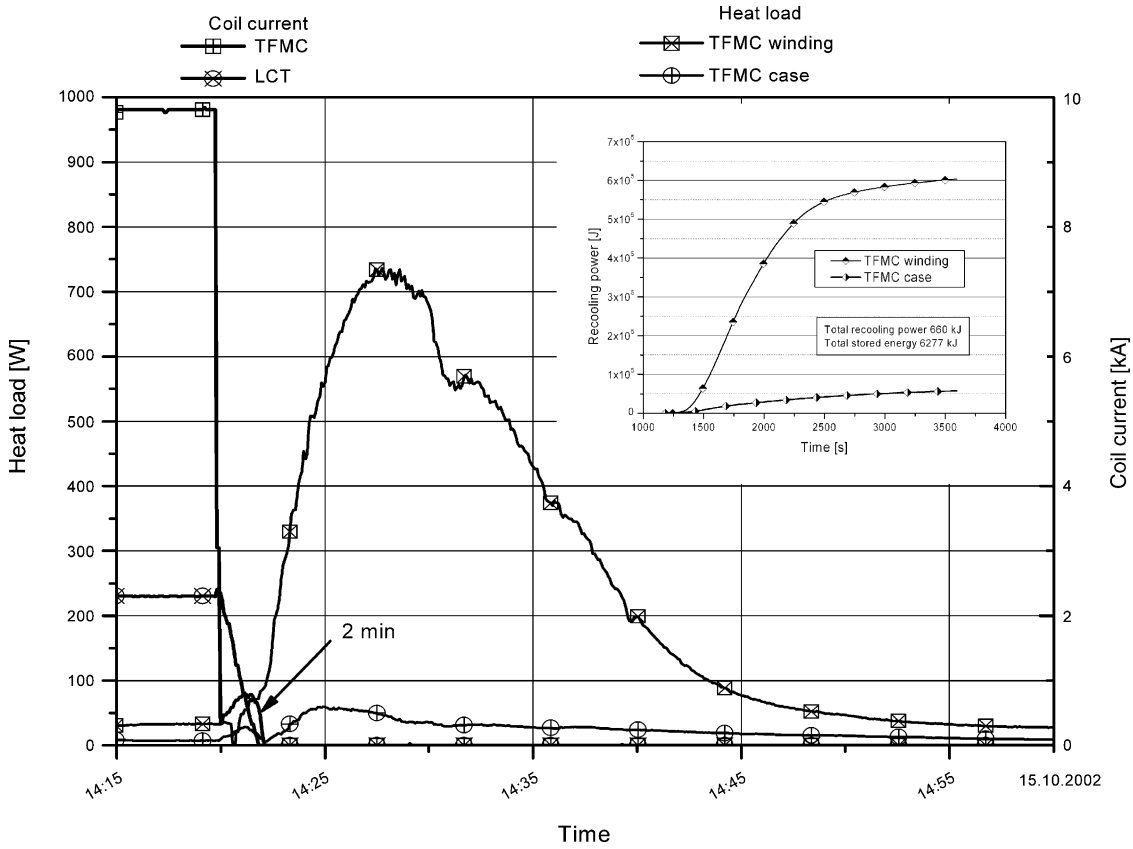


Fig. 4.10. Re-cooling after an inverter mode discharge from 10 kA in the TFMC and 2.3 kA in the LCT coil.

The current sharing temperature in the range between 8.5 and 11 K in double pancake one (P1.1 and P1.2) had to be realised in small steps and as stable as possible without or with only minor oscillations.

The cooling system of the facility had to be able to tolerate the overloading for a certain time without a shut down and handle the additional heat load after a safety discharge without He gas losses to the atmosphere.

In order to achieve this, a so-called multi-step heating scenario was proposed, calculated (see Section 5) [54] and tested for the coil current of 80 kA with an expected $T_{CS}$ of 8.5 K, a coil current of 69.3 kA with an expected $T_{CS}$ of 9.7 K and a coil current of 56.5 kA with an expected $T_{CS}$ of 11 K. One example of these numerous calibration runs without current is shown in Fig. 4.16. For a reliable repetition of this multi step heating, the heater power supply was computer controlled.

During all these tests the required cooling capacity was far outside the operation limits of the refrigerator (Fig. 4.17). This heat load could be handled only by evaporating the LHe stored in the control dewar B250, warming it up to room temperature and feeding it into the recovery system. The limiting factors were the pressure in the control dewar (B250) and the refrigerator power. The limit on the time duration of the test depended on the capacity of the stored LHe and the capacity of the recovery system.

After an appropriate heating scenario was found, the current sharing tests were started in the test Phase 1 without the LCT coil at 80 kA, followed by tests at 70, 69.3 and 56.5 kA (see Section 5) [54].

In the test Phase 2, calibration tests were started again, now with two coils with a total mass of 108 t. The single coil $T_{CS}$ measurements were repeated at 80 and 69.3 kA.

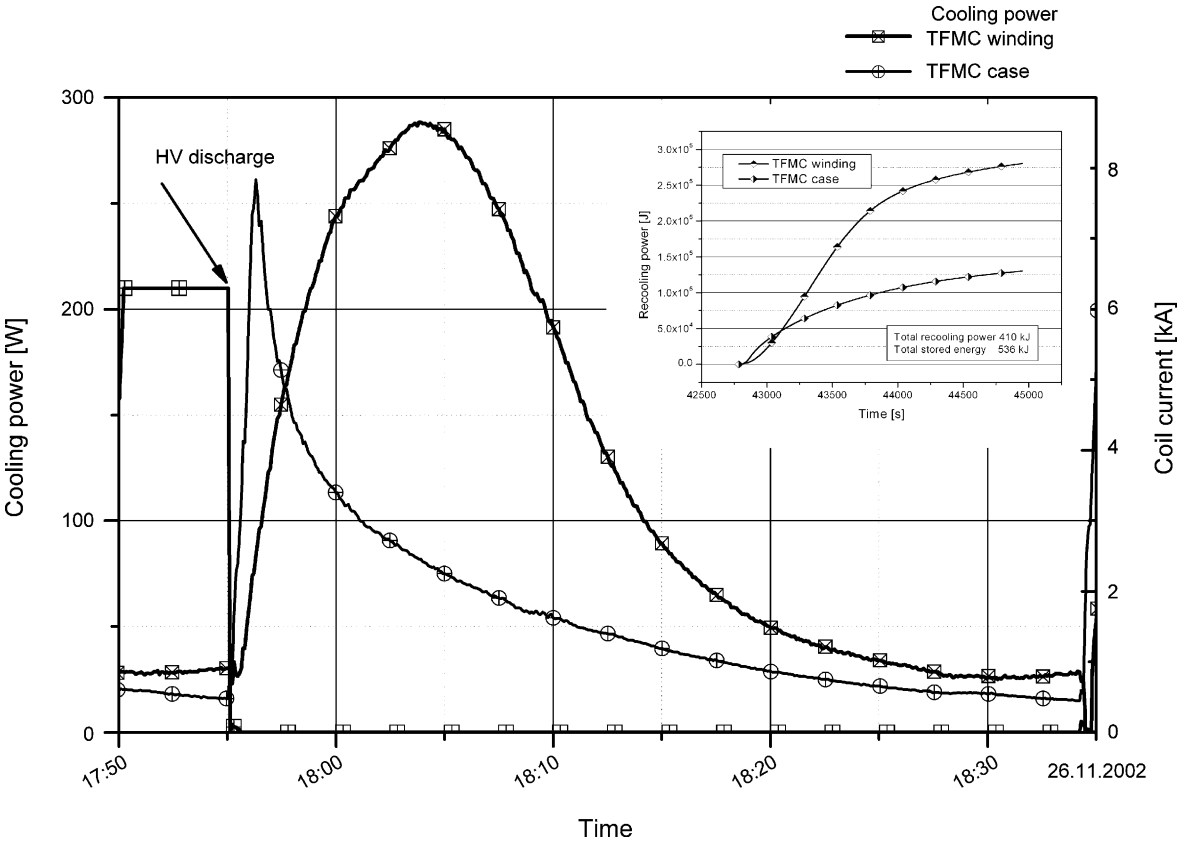


Fig. 4.11. Re-cooling of the TFMC coil after a high voltage discharge from 6 kA.

The first $T_{CS}$ measurements with two energised coils were performed with a coil current of 70 kA in the TFMC and 16 kA in the LCT coil with the following result from the cryogenic point of view.

Shortly before the expected $T_{CS}$ temperature of 7.9 K was reached almost all boundary conditions of the cooling system were exceeded. The pressure in the control cryostat and the suction pressure of the compressor were too high and as a consequence the power consumption of the compressor was at the limit. The liquid level of the control dewar was below the upper end of the heat exchangers and also the pumps. The cold gas return flow to the refrigerator was too high and as consequence the temperature of the turbines of the refrigerator was at the lower limit. After this, a quench in pancake P1.2 occurred followed by a safety discharge of both coils and a very high additional heat load. The consequence was a high He mass flow rate from the winding, which could not be handled completely by the recovery system. A small part of the He (∼5%) was lost through the relief valves for the first time. At the same time, the refrigerator was switched off because of too low temperature of one of the turbines. Also the re-cooling after this overloading was difficult and time consuming. This is not surprising because the cooling system was operated far outside the capacity before the quench as shown in Fig. 4.17.

In the further $T_{CS}$ test runs at 60.6/13.9 kA, repetition of 80, 70/16 and 80/16 kA (Fig. 4.18), the heating power was ramped down after the compensated voltage in pancake P1.2 reached ∼250 μV, in order to avoid again such problems with the cooling system and save testing time. This ramp down before running into a quench or safety discharge was much easier to handle for the cooling system and also the recovery time was much shorter.

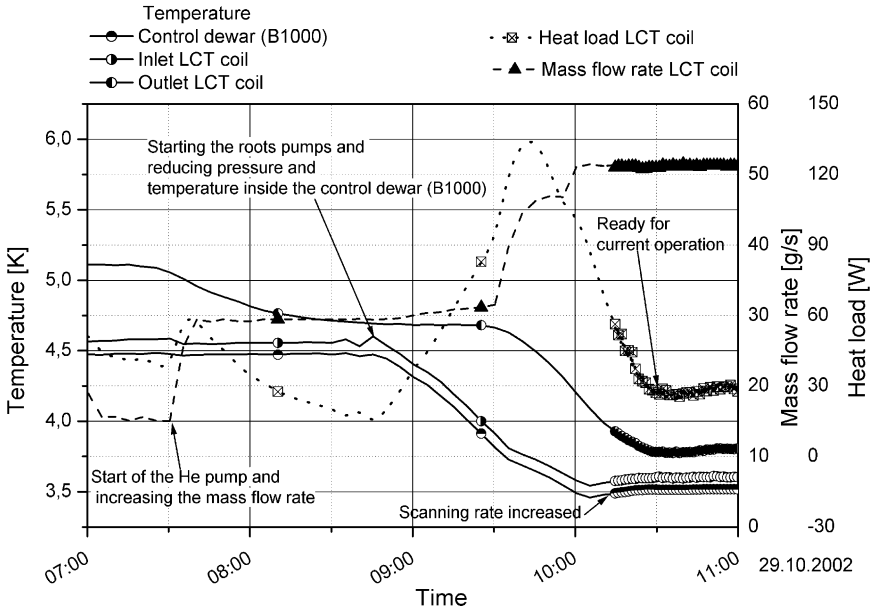


Fig. 4.12. Cool down the LCT coil winding to 3.5 K.

*4.3.2.4. Standby operation over night and weekends.* As already mentioned above, during nights and weekends all components of the test arrangement were cooled with the Joule–Thomson (JT) mass flow rate of the refrigerator, and the He pumps were switched off. This He was sub-cooled in the control dewar (B250) as shown in Fig. 4.3 and after cooling the test configuration, expanded in a JT valve and liquefied into the

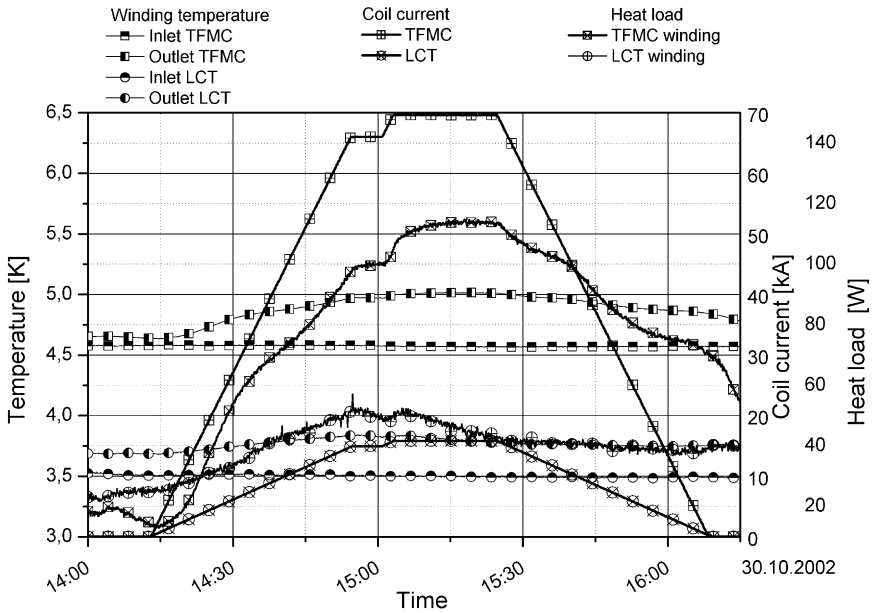


Fig. 4.13. Operation at rated current of 70 kA in the TFMC and 16 kA in the LCT coil for test Phase 2.

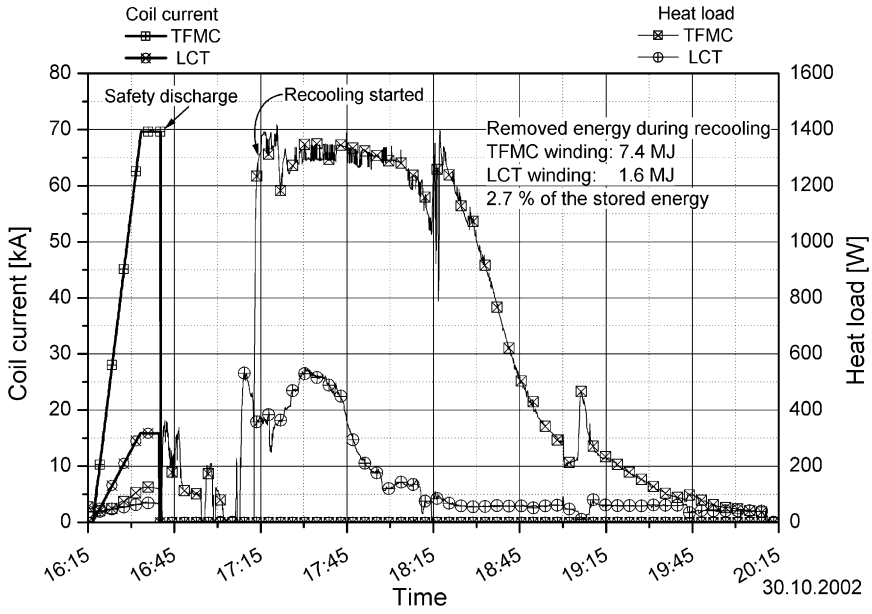


Fig. 4.14. Re-cooling after a safety discharge from rated currents.

control dewar (B250). With this method, the coils were kept cold, the control dewar (B250) was filled, and the running time of the He pumps was reduced by about 60%. An unattended operation during nights and weekends was possible and the change from standby mode to the operation mode with the full mass flow rate was done every morning in about 2 h (Fig. 4.19). The mass flow rates were adjusted to rated values after the daily high voltage and interlock tests at low currents, which did not require a high mass flow rate.

An overview of the complete test Phase 2 is given in Fig. 4.20. The cool down started August the 20th and the warm up finished December the 19th, 2002 without significant problems. The availability of the TOSKA facility was larger than 98%.

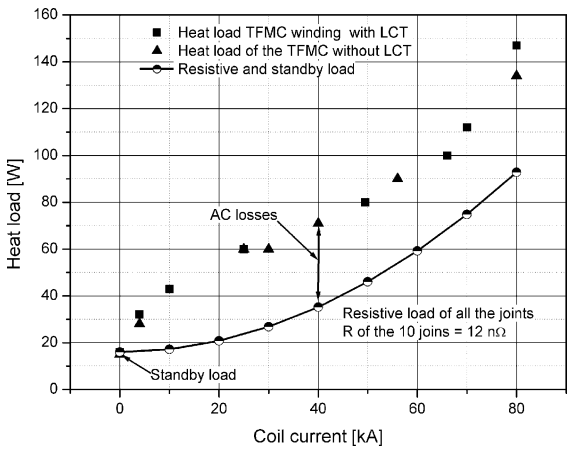


Fig. 4.15. Heat load of the TFMC winding vs. coil current in test Phases 1 and 2. The difference between the measured losses and the calculated resistive losses are the AC losses caused by the current ripple of about 40 W (see Section 6.1.3).

## 4.4. 80 kA current leads performance

### 4.4.1. Design of the 80 kA current leads

For the test of the TFMC in TOSKA, two 80 kA current leads were designed and manufactured based on the design principles developed within the last 15 years [55], see Fig. 4.21.

A significant experience was acquired from the construction and the performance tests of the 30 kA forced-flow-cooled current leads used for the POLO model coil experiment, the LCT coil 1.8 K test, the W 7-X conductor tests in the STAR facility, and the W 7-X DEMO coil test. The 80 kA current leads were designed based on that experience and according to the design principles worked out in the course of construction of forced-flow-cooled current leads and testing of those devices.

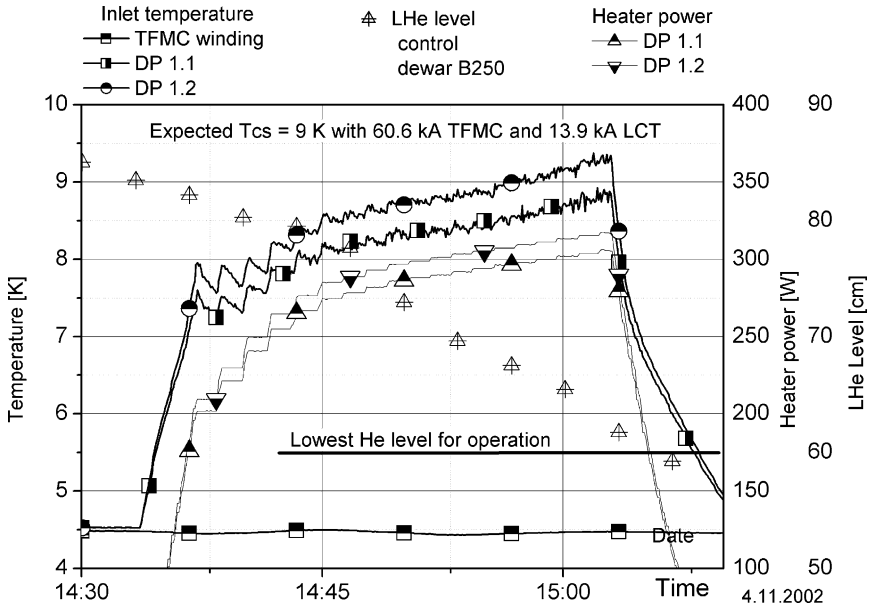


Fig. 4.16. Calibration test for the $T_{CS}$ measurement and the decreasing He level in the control dewar B250.

The design principles are described in [56] and will only be briefly reviewed here. The main features are:

- Forced-flow-cooling with 4.5 K supercritical helium.
- The heat exchanger (see Fig. 4.21) consists of a central copper conductor made of phosphorous deoxidised copper (SF-Cu) to increase the stability, the mass and also the heat capacity of the current lead

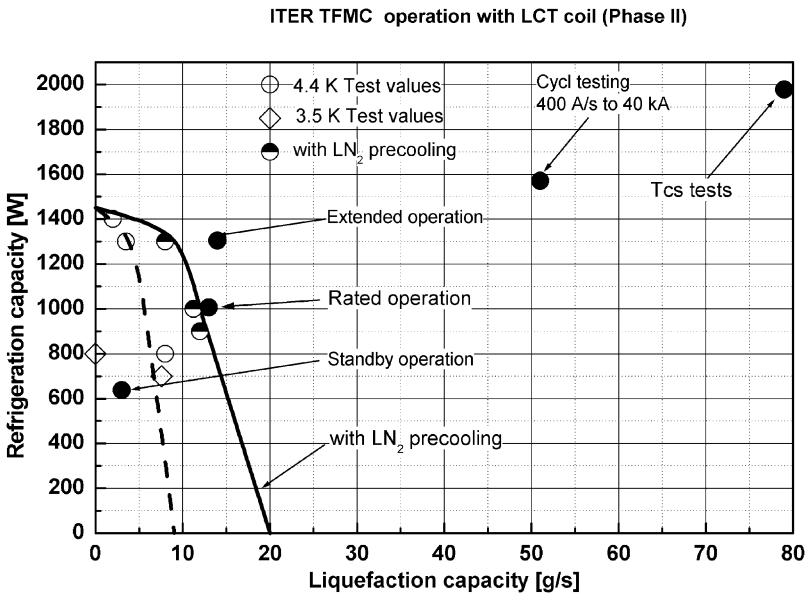


Fig. 4.17. Cooling capacity of the 2 kW refrigerator operation modes (without and with $LN_2$ pre-cooling) and cooling requirements for testing the TFMC.

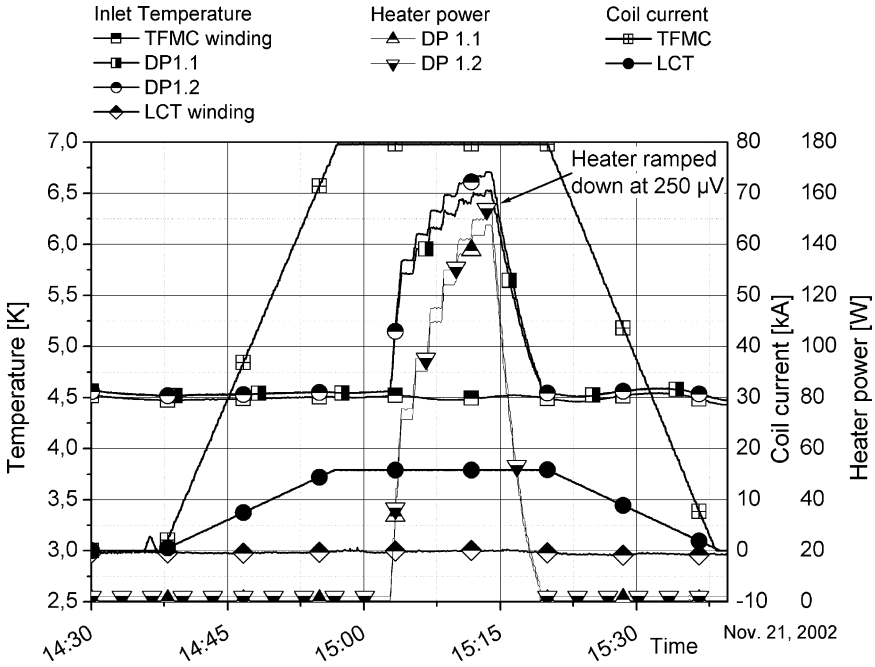


Fig. 4.18. $T_{CS}$ measurement at the maximum current (TFMC 80 kA, LCT 16 kA) in both coils with ramping down the heaters after 250 µV resistive voltage was reached in P1.2.

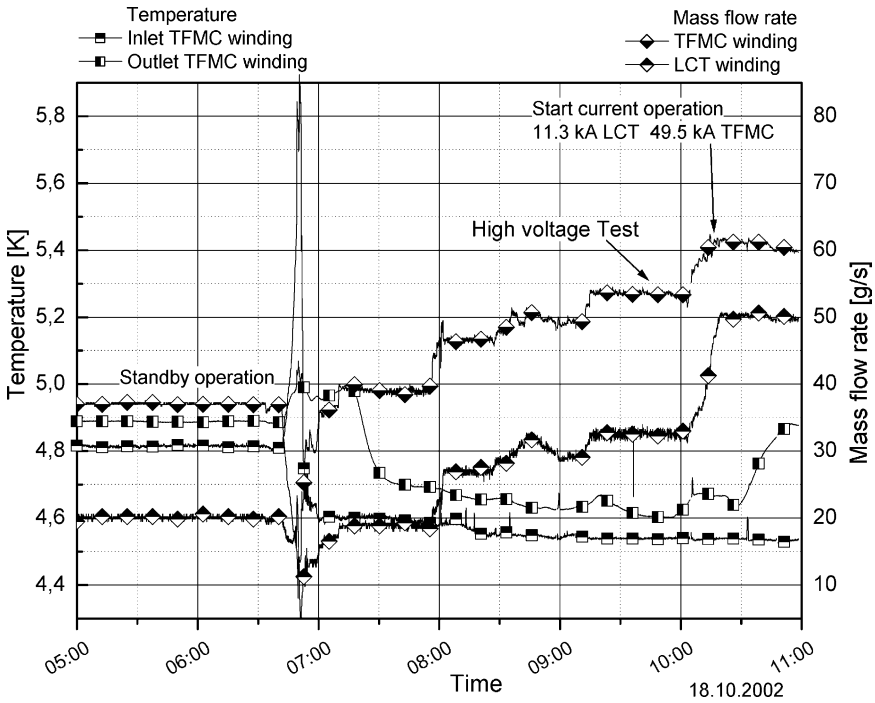


Fig. 4.19. Changing from standby operation to current operation.

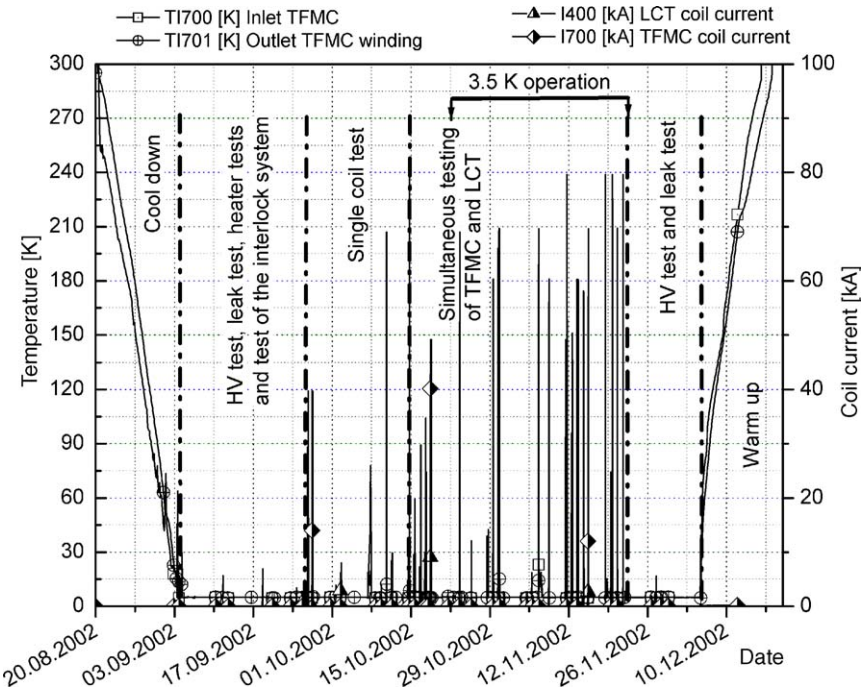


Fig. 4.20. Overview of the complete test Phase 2 including the LCT coil.

and circular perforated copper plates made of Electrolytic Tough Pitch copper (ETP-Cu), which are brazed to the central conductor as cooling fins. In order to compensate the differential shrinking of the central copper conductor and the outer stainless steel container, several axial bellows are added along the length of the lead. So, two different outer diameters of the cooling disks have to be used in the heat exchanger.

- Use of $Nb_3Sn$ inserts in the contact area and the low temperature region of the heat exchanger for adjusting the resistive length of the current lead and operating the lead at optimum mass flow rate over a wide current range [57].

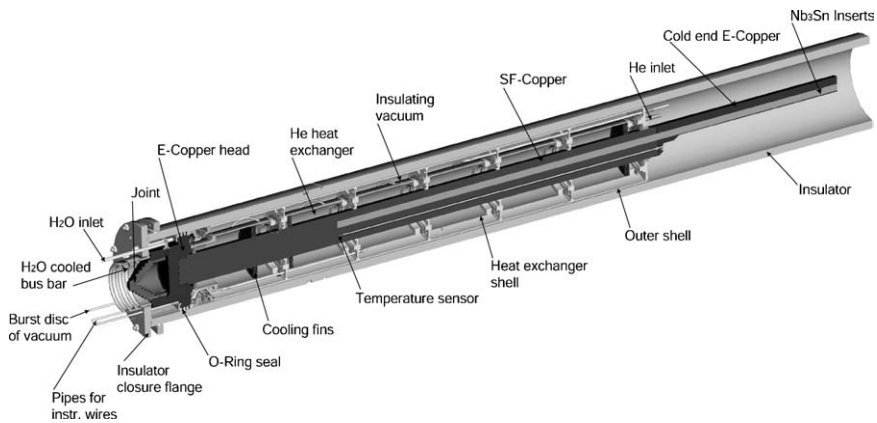


Fig. 4.21. Illustrative drawing of the helium cooled heat exchanger including the cold end clamp contact to the superconducting bus bar and the screw connection to the flexible copper bus bars.

- Use of SE-Cu in the contact area and in the room temperature region to reduce the Joule heating.
- Use of clamp contact between the cold end of the current lead and the bus bar connection.
- Implementation of the so-called “cold gas return” circuit, which allows to operate the first segment of the heat exchanger with a higher mass flow rate than the rest of the heat exchanger.
- Integration of a water cooled flexible jumper cable at the room temperature end of the current lead to connect the current lead to the water cooled aluminium bus bars of the TOSKA facility.

The electrical insulation system of the current lead is described in detail in [10]. In Fig. 4.22, a photograph of the two 80 kA current leads installed in their cryostat extensions during assembly in the TOSKA facility is presented. Fig. 4.21 shows an illustrative drawing of the helium-cooled heat exchanger, including the cold end clamp contact to the superconducting bus bar and the screw connection to the flexible copper bus bars. Due to the vertical installation of the current leads, the superconducting bus bar has to be divided in two parts (bus bars 1 and 2) for assembly reasons having a clamp contact in between. The cooling scheme is illustrated in Fig. 4.23.

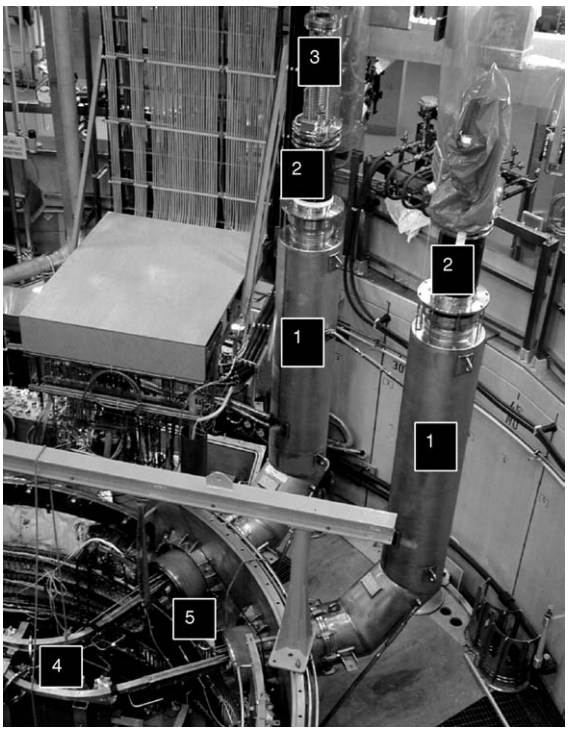


Fig. 4.22. Photograph of the 80 kA current leads installed in their cryostat extensions during assembly in the TOSKA facility (1, cryostat extension; 2, current lead; 3, flexible copper bus bars; 4, bus bar type 1; 5, bus bar type 2).

### *4.4.2. Overall performance of the current leads during TFMC operation*

As the first aim of the TFMC experiment was to reach the nominal current of 80 kA, the current leads were not operated in an optimum way. This was due to the fact that the experimental optimised operation parameters of the leads were unknown because no separate test was possible due to time constraints.

During Phase 1 of the TFMC experiment, and especially at its end, some parameter studies were made to find the minimum helium mass flow rates and to identify the reasons for the higher heat load introduced in the BB-1/2 system.

### *4.4.3. Electrical resistances of the clamp contacts*

The voltage taps used for quench detection were used to determine the resistances of the bus bar (+) and (−) systems. Each of them consisted of one full joint and two half joints of which one was the clamp contact to the current lead (Fig. 4.23). Each of the clamped joints was manufactured in a different way: for joint 2, indium wires were arranged in the longitudinal direction and pressed flat by tightening of clamping bolts for

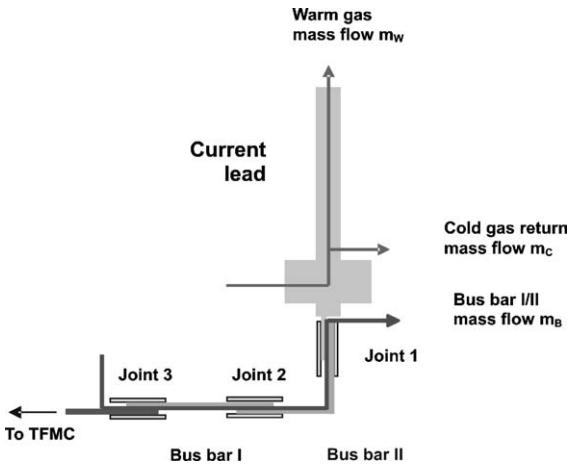


Fig. 4.23. Cooling scheme of the 80 kA current lead bus bar system (bus bar I = bus bar 1; bus bar II = bus bar 2).

2 weeks (JAERI method); for joint 1, a single indium foil was used and the clamping bolts were tightened in 3 days (FZK method). Also, the applied contact pressure was different: 11 MPa for joint 2 and 25 MPa for joint 1 (see Section 7.1.3). In addition, the copper surfaces of both the bus bar 2 and the current lead contact areas were plated with gold whereas the bus bar 1 contact areas were plated with silver. The resultant resistances were 1.5 nΩ for the bus bar joints and 1 nΩ for the bus bar current lead contact. It can be concluded that the resistance does not depend on the method of applying the indium. Moreover it is also not very dependent on the clamp pressure in the contact. But a very promising method was the surface plating of the copper by a noble metal (Au, Ag). Obviously, the plating reduces the contact resistance compared to bare copper because copper becomes oxidized. Comparing these resistances with former values, there is an improvement of about one order of magnitude.

*4.4.4. Optimisation of the current lead operation*

For both terminals, a helium mass flow optimisation was performed. First, an optimisation was performed at zero current. The conclusion of these tests was that the nominal helium mass flow through the heat exchanger of both terminals should be fixed to 0.8 g/s. A cold gas return mass flow rate of about 1–1.5 g/s should be adjusted, too, in order to reduce the heat load to the superconducting bus bars.

For 40 kA, only the (+)-terminal performance was studied whereas for 80 kA, both terminals were investigated. A reduction of the helium mass flow rate below the optimum one results in a more rapid increase of the temperature at the upper end of the superconductor inserts although this increase is not so fast (less than 1 K in about 10 min).

The computer code CURLEAD was used to predict the performance of the heat exchanger of the 80 kA current lead [58]. Fig. 4.24 shows the measured and calculated temperature distributions for both the (+) and the (−)-terminals. The difference in helium mass flow rates required to cool the heat exchangers of both leads can be explained by different RRR of the copper: the (+)-terminal would have an RRR of 4.7, the (−)-terminal an RRR of 5.5. This would lead to different optimum lengths of the heat exchangers, which of course could not be realised. It can also be concluded that the experimental results confirm the design calculations, which were done for an RRR of about 5.5.

In Table 4.5, the main operation parameters are summarised for 0, 40 and 80 kA.

*4.4.5. Search for possible sources of the heat load to the bus bar system*

As already mentioned, the thermal load to the bus bar system was so high that it was absolutely necessary to operate the current leads with a rather large helium mass flow rate through both the bus bar system and the cold gas return. This applies to both zero and non-zero current operations. During the optimisation studies, different parameters were varied and the effect on the heat load was evaluated.

Fig. 4.25 shows average heat load values with and without current. Clearly, the dependence on current is negligible (about 20 W) although the mass flow rate through the heat exchanger is quite different.

From this, it may be concluded that the high heat load at the 4.5 K level that has to be removed by the bus bar and cold gas return circuits is not mainly due to the heat exchanger.

To look more carefully for the possible sources, which may contribute to the heat load, some qualitative investigations were done. Using the geometrical and material data, the total of the various contributions to radiation and conduction losses was estimated at about 13 W, which is approximately a factor of 10 lower than the measured heat load.

In addition, heat may be transferred via conduction from the cold end of the heat exchanger to the bus bar region. To evaluate this, two temperature sensors were positioned below the inlet of the heat exchanger and at the lower end of the copper bar. Looking to the results, the heat load is below 10 W except the runs where the cold gas return circuit is switched off. Moreover, the heat load is rather independent on the heat exchanger mass flow rate as already discussed earlier. The opinion is that this is again a clear hint that the origin of the high heat load cannot be found in an ineffective heat exchanger but in the cold end region. However, the source is not identified yet. It can only be stated that in all coil experiments in TOSKA, a rather high heat load has been observed, which has only to be balanced by either a rather high mass flow rate through the heat exchanger or a high mass flow rate in the cold end region.

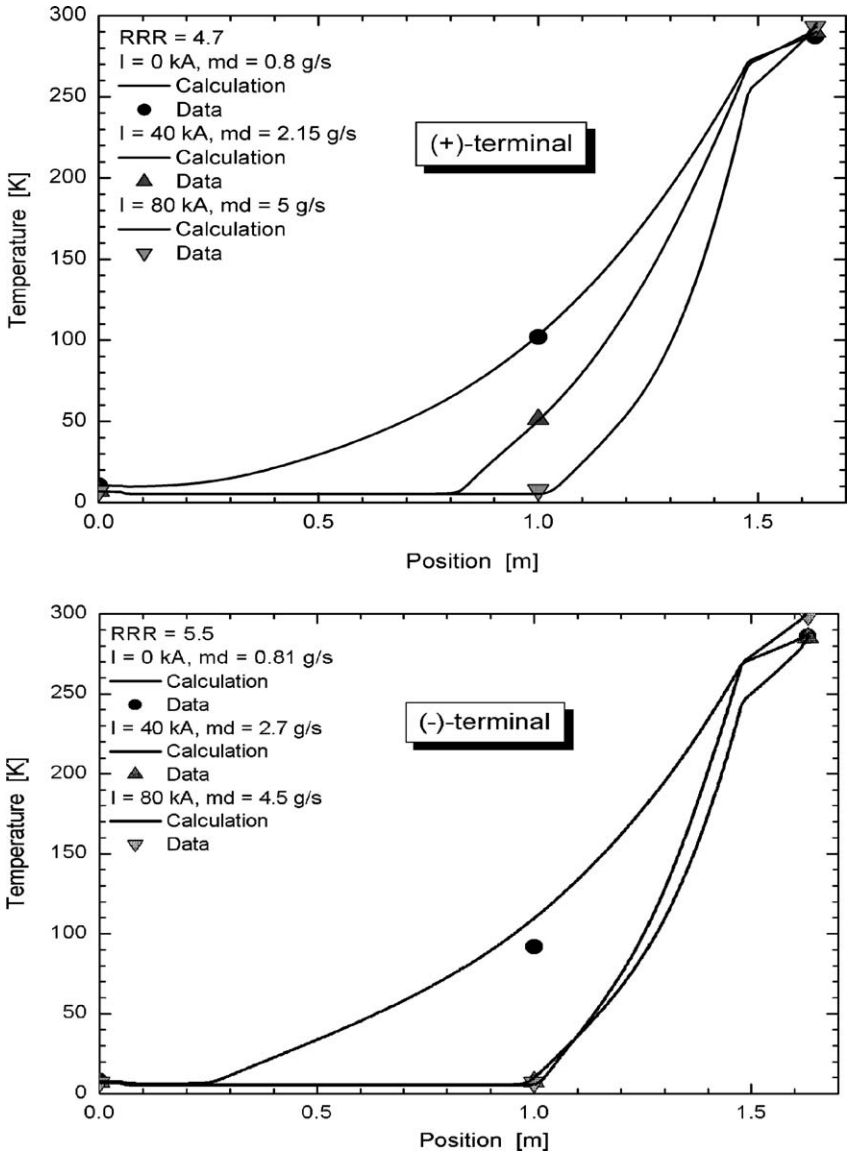


Fig. 4.24. Measured and calculated temperature profiles of (+)-terminal (top) and (−)-terminal (bottom) for 0, 40 and 80 kA.

*4.4.6. Summary*

The 80 kA current leads including the water-cooled flexible jumper cables were operated successfully during both test phases of the TFMC in 2001 and 2002.

Various optimisation runs were performed at zero current as well as at 40 and 80 kA, respectively. It could be demonstrated that the current leads were operated with the design mass flow rates through the heat exchanger. The slightly different mass flow rates of both terminals can be explained by different RRR of the copper of the heat exchanger.

The water-cooled flexible jumper cables were operated reliably up to 80 kA in steady state with a copper current density of up to 43 A/mm$^2$. Maximum outlet temperatures of the cooling water of about 60 °C were obtained resulting in a total cooling power of up to 240 kW for both legs.

Table 4.5
Main operation parameters of the 80 kA current leads

| | Current [kA] | | |
|---|---|---|---|
| | 0 | 40 | 80 |
| $T_{He,in}$ [K] | 5.62 | 4.83 | 4.79 |
| $T_{Cu,cold}$ [K] | 10.64 | 7.1 | 7.03 |
| $T_{Cu,SC}$ [K] | 102 | 51.3 | 6.86 |
| $T_{Cu,warm}$ [K] | 287 | 290 | 299 |
| $m_W$ [g/s] | 0.8 | 2.15 | 4.5 |
| $m_C$ [g/s] | 0 | 5.78 | 6.24 |
| $\Delta p_{heat\ exchanger}$ [mbar] | 75 | 165 | 420 |
| $Q_{sum}$ [W] | 112 | 166 | 168 |

Cu, copper conductor; He, helium; SC, superconductor.

The steady state heat load of the current lead superconducting bus bar system at the 4.5 K level was very high even at zero current (110 W per terminal). Detailed investigations showed that the heat exchangers could not be responsible for this high heat load because changes in the heat exchanger helium mass flow rate did not change the heat load significantly. Up to now, there is no final conclusion.

### *4.5. Power supply system and safety discharge performance*

For the test of the ITER TFMC, the electrical power supply system has been extended in the following way [59]:

(1) The existing 50 and 30 kA thyristor AC/DC converters were switched in parallel by means of a new control unit in order to obtain a maximum output current of 80 kA.
(2) An 80 kA safety discharge switching circuit of about 100 MJ energy capacity at a voltage level of 1 kV was installed.
(3) A new 20 kA thyristor AC/DC converter had to be installed and connected with the existing 20 kA safety discharge circuit of about 300 MJ energy capacity at a voltage level of 2.5 kV for the operation of the LCT coil.

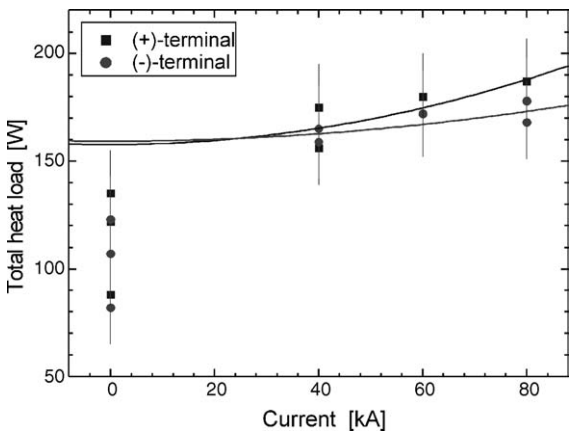


Fig. 4.25. Total heat load vs. coil current for (+) and (−)-terminals.

For the 80 kA supply system the main problem, that had to be solved, was the nearly simultaneous current commutation of both power supplies on the short circuit path also under fault conditions. Besides this, a sufficient low resistance and inductance of the short circuit path had to be achieved in order to have a voltage drop across it was remarkably lower than the nominal voltage of the rectifiers in inverter mode of operation.

The 20 kA thyristor rectifier had some specific problems in the balance control of the two 10 kA rectifiers. They were mastered in a way that there was practically no impact on the progress of the test procedure.

The POLO switching circuit was applied for the fast high voltage discharge of the TFMC (Section 9).

Early testing of the 30 and 50 kA power supplies with the POLO and a copper coil, steamed out the need of detailed analysis of current sharing during the safety discharge sequence and the optimisation of the feedback loop. This has been achieved with the help of computer models built using SIMULINK and Power System Blockset (PSB) developed both for MATLAB®. Several models of different complexity have been built for the two power systems to perform separate circuit analysis and predictions after validation with experimental data [60].

The first problem of the 80 kA power supply system, that had to be solved at the beginning of Phase 1, was the simultaneous commutation of the power supply currents into the short circuit path during a safety discharge. For this purpose, a sufficiently low resistance and inductance of the short circuit path was necessary in order to have a voltage drop across the short circuit lower than the voltage of the rectifiers in inverter mode of operation. This has been achieved connecting in parallel a second short circuit path (i.e., made of a make switch S1.2 and circuit breaker S2.2 connected

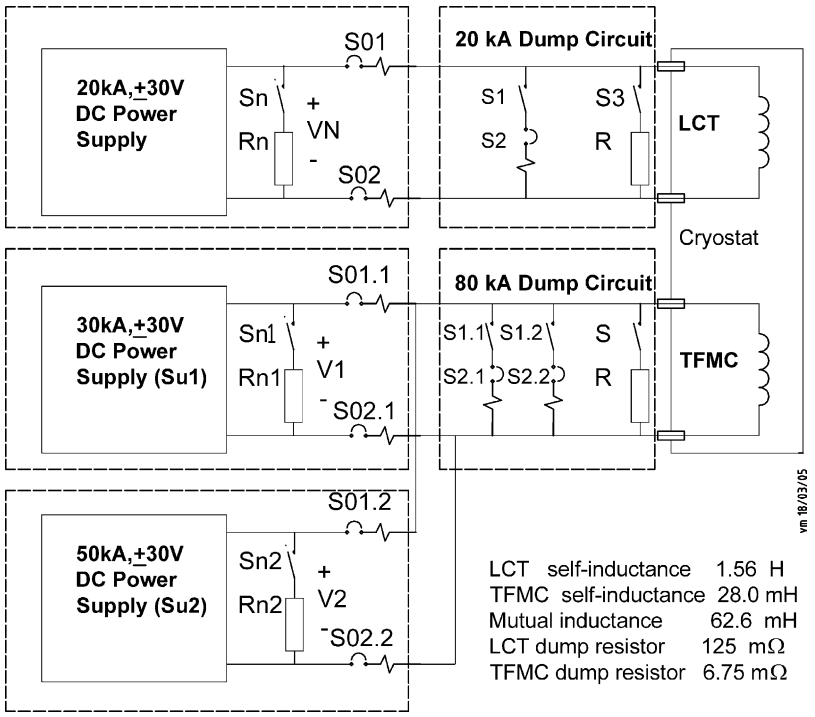


Fig. 4.26. TOSKA power supply system functional diagram.

in series as shown in Fig. 4.26, thus reducing the total resistance of the short circuit from 327 to 227 μΩ.

A second problem, which was solved also during Phase 1, was the shift of current from the 30 kA power supply to the 50 kA power supply during fast ramp down. This abnormal behaviour, which was due to an error in the current sharing controller, would have been particularly dangerous during the early phase of a safety discharge at 80 kA when the two power supplies operate in inverter mode [61].

Like the 30 and 50 kA power supplies, the 20 kA power supply is a thyristor rectifier, made of two 6-pulse bridge converters (Δ and Y) of 10 kA each connected in parallel to yield a 12-pulse converter. Also, this power supply had a specific problem in the balance control of the two 10 kA rectifiers, which was implemented with a μ-processor operating at the fixed sampling rate of 300 Hz. The problem was solved using an analogue circuit for the current sharing controller and leaving the dump resistor (125 mΩ) permanently connected in parallel with the LCT coil.

The circuit analysis presented in Section 4.5.1 deals with the normal ramp up and ramp down of the currents in the two circuits, with the inverter mode discharge and with the safety discharge in the configuration for Phase 2. The high voltage discharge of the TFMC coil, performed with the POLO switching circuit, is described in detail in Section 9.

### *4.5.1. Circuit analysis and comparison with measurement*

The analysis presented hereafter, performed with a computer model, will be limited to the DC side of the LCT coil and the TFMC power circuits. A plan view showing the position of the two coils in the vacuum vessel is given in Fig. 4.27 (dimensions are given in millimeters). The horizontal axes of the two coils are not parallel to each other but they form an angle of 4.5°. The magnetic coupling between the two coils is not too high (e.g., only 20% between coil windings). The absence of ferromagnetic materials in close proximity and the hypothesis that the two coils do not move justify the use of a linear time-invariant model for the two coils. The two power circuits, magnetically coupled through the LCT coil and the TFMC themselves, are shown in Fig. 4.28. Denoting with:

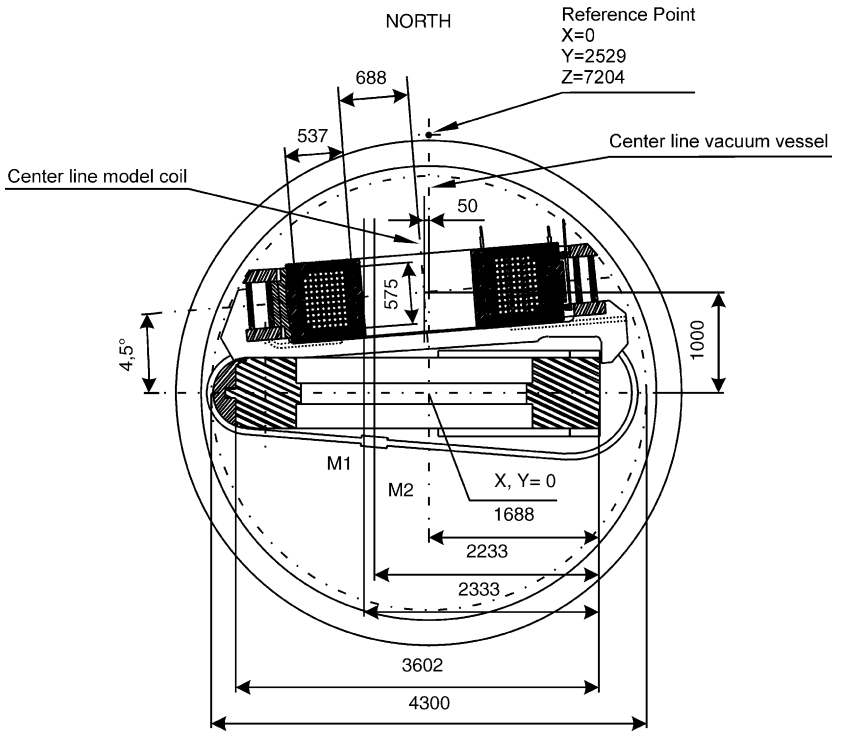


Fig. 4.27. LCT coil and TFMC arrangement in TOSKA.

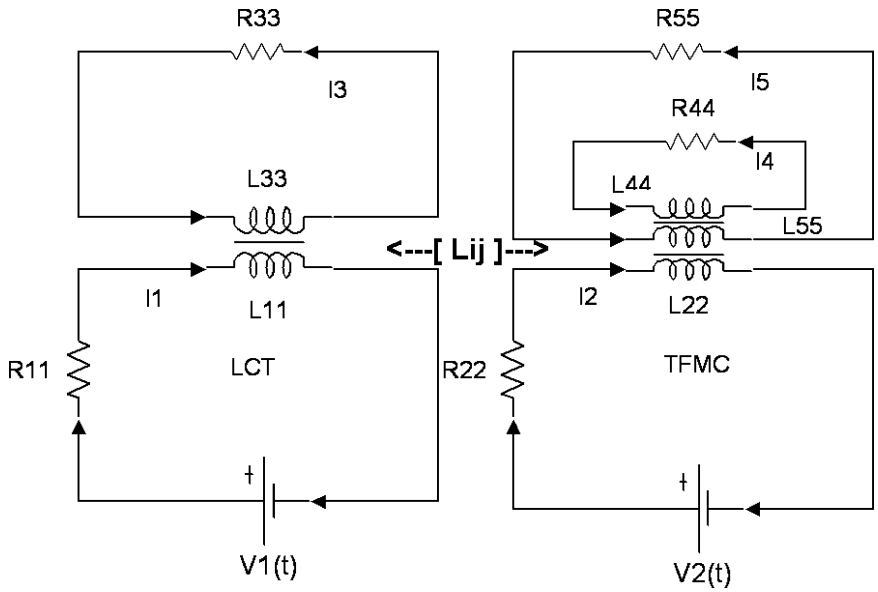


Fig. 4.28. LCT coil and TFMC circuit diagram (1, LCT coil winding circuit; 2, TFMC winding circuit; 3, LCT case; 4, TFMC radial plates; 5, TFMC case).

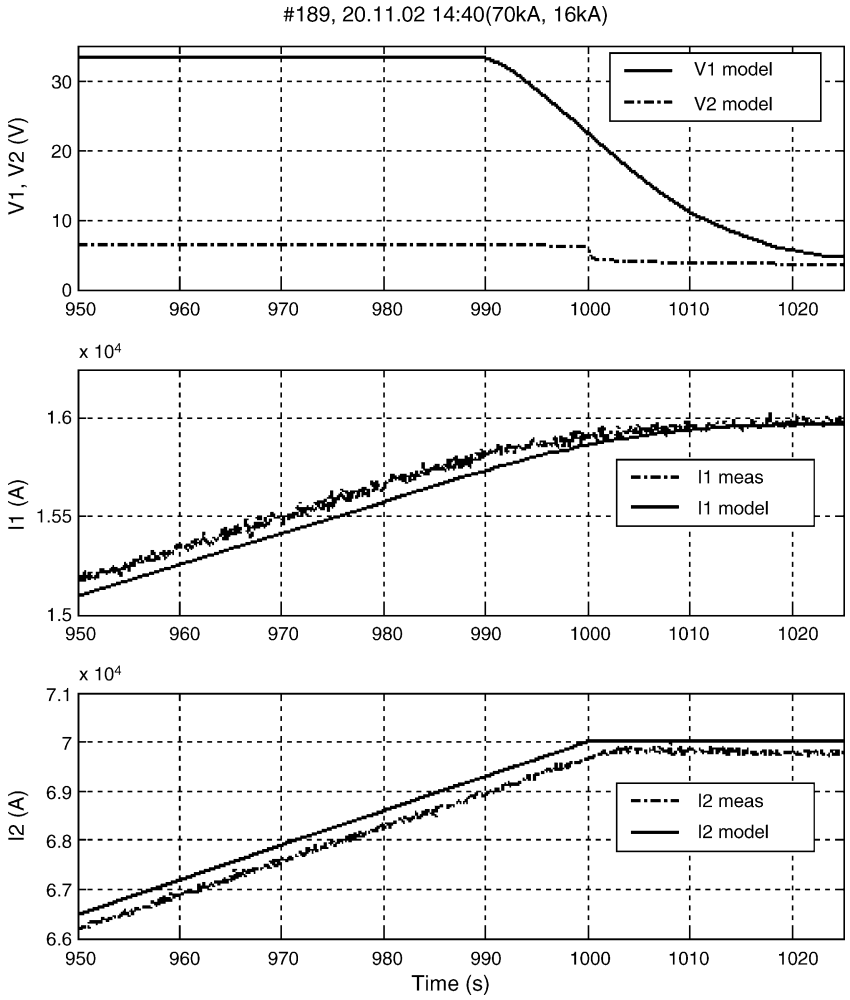


Fig. 4.29. LCT coil and TFMC current ramp up ($V_1$ and $I_1$ LCT coil circuit voltage and current, $V_2$ and $I_2$ TFMC circuit voltage and current. Measured voltages not available).

$I(t) = [I_1(t)I_2(t)I_3(t)I_4(t)I_5(t)]^T$, the $5 \times 1$ vector of currents, representing the currents in the LCT coil and TFMC windings, the eddy currents in the LCT coil case, in the TFMC radial plates and in the TFMC case, respectively; $V(t) = [V_1(t)V_2(t)]^T$, the vector of the two forcing voltages of the two winding circuits, $L$ the inductance matrix and $R$ the resistance matrix, the currents in the five circuits can be computed by integrating the following linear differential equation:

$$L\frac{dI(t)}{dt} + RI(t)V(t) \tag{4.1}$$

The method used for the calculation of the inductance matrix $L$ and resistance matrix $R$, both $5 \times 5$, is reported in Appendix A. The resistances of the LCT coil and TFMC windings (i.e., $R_{11} = 250\ \mu\Omega$ and $R_{22} = 50\ \mu\Omega$) have been validated experimentally and they are mostly due to the conventional bus bar system external to the vacuum vessel (i.e., Al bus bar and flexible cables).

The computer model (developed with SIMULINK) includes, in addition to the Eq. (4.1), a simplified model of the thyristor converters with their current transducers and current feedback modules (see Appendix A for more details). The model computes the power losses

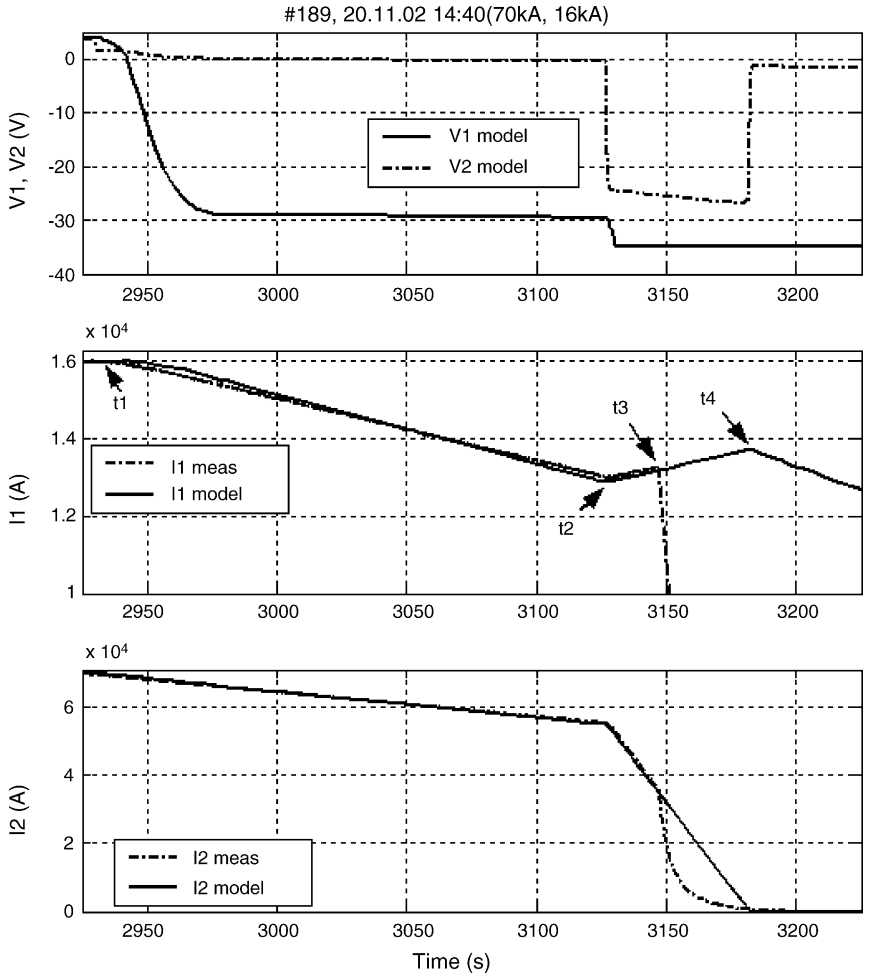


Fig. 4.30. Current ramp down followed by an inverter mode and a safety discharge ($V_1$ and $I_1$ LCT coil circuit voltage and current, $V_2$ and $I_2$ TFMC circuit voltage and current).

$P_i(t)$ due to Joule effect in the bus bar system and to the eddy currents in the coil passive structures, induced by time-varying excitation, as follows:

$$P_i(t) = R_{ii} \cdot I_i^2(t), \quad i = 1, \ldots, 5 \tag{4.2}$$

where $R_{ii}$ is the equivalent resistance and $I_i(t)$ the total current of the $i$-th circuit. The energy losses of each circuit $E_i(t)$ are obtained by simple integration of the power losses:

$$E_i(t) = \int_{t_0}^{t} P_i(\tau)\,\mathrm{d}\tau, \quad i = 1, \ldots, 5 \tag{4.3}$$

In case of AC voltage excitation the instantaneous currents $I_i(t)$ in Eq. (4.2) are replaced by their rms values.

A comparison between model outputs and current measurements in the LCT coil and TFMC during a typical current ramp to 16 and 70 kA, respectively, is shown in Fig. 4.29. The discrepancies between model outputs and measurements are within 0.5%. In the same figure are shown also the DC voltage signals computed with the model. Fig. 4.30 shows instead a comparison between computed and measured current during current decay. The ramp down of the current in the two coils is initiated 2930 s after the start of

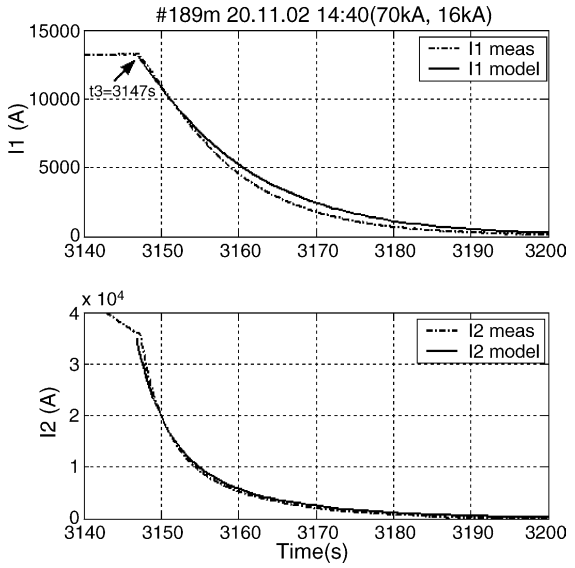


Fig. 4.31. LCT coil and TFMC safety discharge ($I_1$ and $I_2$ LCT coil and TFMC winding currents).

the pulse (time $t_1$) with the controlled ramp down of the current in the TFMC coil at the rate of 70 A/s, followed almost immediately by the LCT coil with a ramp down rate of 18 A/s. After 197 s (time $t_2$) a fault in the 20 kA dump circuit initiated an inverter mode discharge. This can be seen also in the TFMC current whose ramp down rate changes suddenly from 70 to 1000 A/s. The ramp rate for the LCT coil remains unchanged. After 20 s (time $t_3 = 3147$ s) the operator, having noticed an increase of current in the LCT coil, induced by TFMC current transient, pressed the emergency stop thus initiating a safety discharge of the two coils. If the operator had not pressed the emergency stop, the overshoot in the current of the LCT coil, which occurs at time $t_4$ when the current in the TFMC reaches zero, would have been only 850 A with no problem for the coil. The following Fig. 4.31 shows a comparison between computed winding currents and experimental data during the typical exponential decay of the safety discharge. In this condition, the power supplies are disconnected and the coil energy is discharged in the dumping resistors $R_{d1} = 125\,\text{m}\Omega$ for the LCT coil and $R_{d2} = 6.75\,\text{m}\Omega$ for TFMC. The current transient in this case is obtained by simple integration of the circuit Eq. (4.1) with initial conditions given by the previous run and zero forcing voltage. Taking into account the resistance of the conventional bus bar system mentioned before, the resistance $R_{11}$ in series with the LCT coil winding in this configuration for the safety discharge is 125.25 mΩ. Similarly, summing the resistance of the dump resistor ($R_{d2} = 6.75\,\text{m}\Omega$), the resistance of the Al bus bar and flexible cables mentioned before (0.05 mΩ) and the resistance of an additional Cu bus bar system that connects the dump resistor itself (227 μΩ) the resistance $R_{22}$ of the circuit for the TFMC is equal to 7.027 mΩ. The resulting time constants of the two windings, respectively, of 12.5 s for the LCT coil and 4 s for the TFMC coil, have been validated experimentally in several safety discharges.

### *4.5.2. Power losses in steady state, inverter mode and safety discharges*

This paragraph deals with the evaluation of the power losses due to Joule effect in the bus bar system and to the eddy currents in the coil passive structures, induced by time-varying excitation, which represent almost 90% of the total losses of the coils.

A pulse with flat top current in the LCT coil of 5.7 kA and in TFMC of 25 kA, referred in Section 6 as "standard safety discharge", has been taken as a reference. The typical ramp up rate used for this type of pulse is 16 A/s for the LCT coil and 70 A/s for the TFMC (see Fig. 4.32).

In addition to the currents in the LCT coil and the TFMC windings, Fig. 4.32 shows the following measurements: heat load on the LCT coil case; heat load on the TFMC windings and heat load on the TFMC case. The associated energies, also shown in the figure, are obtained by signal integration. The heat loads of the two coil cases, with the exception of a small transient due to eddy currents induced during the current rise, remain practically constant. The heat load on the TFMC windings instead increases by 40 W. This heat is generated in the TFMC radial plates by the eddy currents induced by the power supply voltage ripple[1] and

[1] A 12-pulse thyristor converter can be represented by a DC controlled voltage source of amplitude $V_d = V_{d0}\cos(\alpha)$ with superimposed a voltage ripple made of sinusoidal contribution of amplitude $\sqrt{2}V_n$ and frequency multiple of 50 Hz (where the harmonic number $n = k \times p$, with $p = 12$ and $k = 1, 2, \ldots$). At 25 kA flat top the DC voltage level in the TFMC power circuit is 1.25 V which correspond to 4% of $V_{d0}$. An $\alpha$-angle close to 90° is the worse condition from the point of view of the voltage ripple. For a 12-pulse thyristor converter,

Table 4.6
Computed energy losses of each circuit for two inverter modes and a standard safety discharge

| Run | $dI_1/dt$ (or $\tau_1$) | $dI_2/dt$ (or $\tau_2$) | $E_1$ [kJ] | $E_2$ [kJ] | $E_3$ [kJ] | $E_4$ [kJ] | $E_5$ [kJ] |
|---|---|---|---|---|---|---|---|
| IMD1 | −18 A/s | −1000 A/s | 1100 | 260 | 14.9 | 66.3 | 49.3 |
| IMD2 | −18 A/s | −79 A/s | 980 | 3320 | 12.5 | 12.6 | 12.1 |
| SSD | 12.5 s | 4 s | 31800 | 10510 | 156.3 | 265.5 | 232.4 |

IMD1, inverter mode discharge 1 (typical); IMD2, simultaneous current ramp down (never performed); SSD = standard safety discharge.
$E_1$, energy losses in the LCT coil winding circuit; $E_2$, energy losses in the TFMC winding circuit; $E_3$, energy losses in the LCT case; $E_4$, energy losses in the TFMC radial plates; $E_5$, energy losses in the TFMC case.

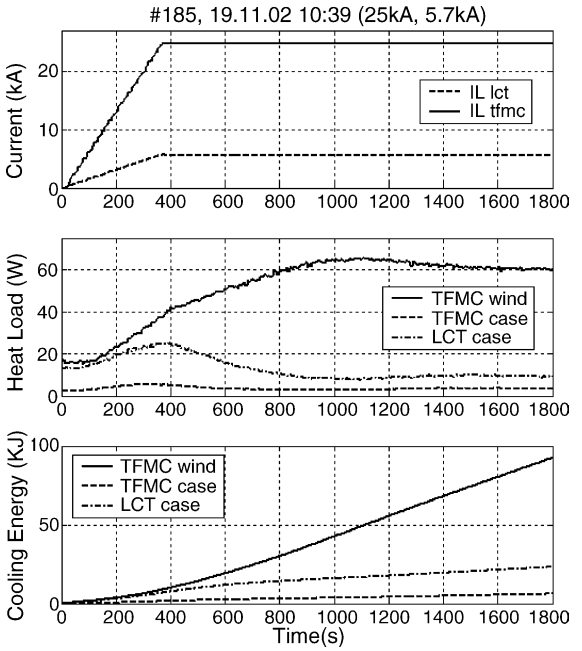


Fig. 4.32. Winding currents, measured heat loads and cooling energies during current rise and flat top of LCT coil and TFMC.

it is transferred to the conductor by a long heat diffusion process [63]. The value of the power losses in the TFMC steel plates computed with the model, using as voltage input $V_2$ a 600 Hz sinus waves with 5 V amplitude, is 47 W (rms) which is in good agreement with the measured heat load on the TFMC windings (see Section 6.1.3).

Fig. 4.33 shows a standard safety discharge performed about 30 min after the start of the pulse, when the cryogenic system is in steady state. For this specific case the integrated heat load of the cryogenic system due to the safety discharge is about 650 kJ, which represents about 1.5% of the magnetic energy stored in the coils (i.e., 43.02 MJ).

Table 4.6 summarises the energy losses in the five circuits computed with the model for three different pulse terminations starting at time $t_0$ with initial currents 5.7 kA in the LCT coil and 25 kA in TFMC: the first (IMD1) is a typical inverter mode discharge, performed several times during Phase 2; the second (IMD2) is a simultaneous current ramp down, never performed, and the third is a standard safety discharge (SSD) which was performed several times.

The sum of the energy loss in the LCT coil case, in TFMC radial plates and in TFMC case ($E_3 + E_4 + E_5$)

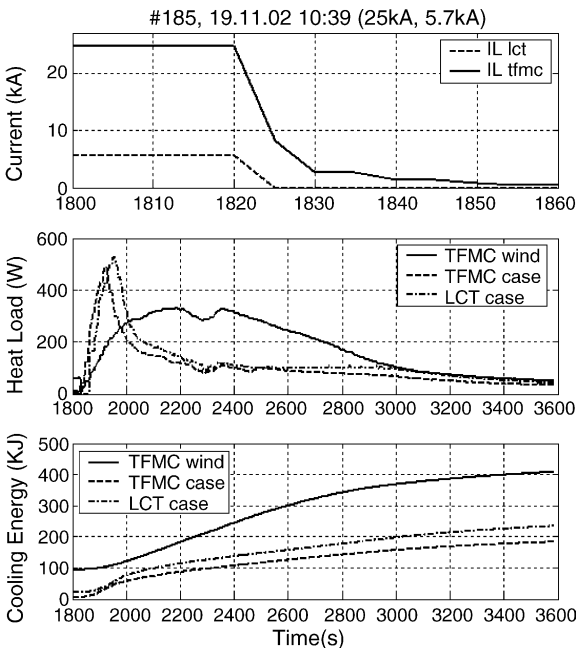


Fig. 4.33. Winding currents, measured heat loads and cooling energies during a safety discharge of LCT coil and TFMC.

such as the ones used for the TFMC tests, at $\alpha = 90^\circ$ the amplitude of the first harmonic, at 600 Hz, is $0.12V_{d0}$, which correspond to a peak of 5 V.

Table 4.7
Computed energy losses (grouped) for two inverter mode and a standard safety discharge

| Run | $\Sigma E_i$, $i = 1, \ldots, 5$ | | $E_1 + E_2$ | | $E_3 + E_4 + E_5$ | |
|---|---|---|---|---|---|---|
| | [kJ] | [%] | [kJ] | [%] | [kJ] | [%] |
| IMD1 | 1490 | 3.46 | 1360 | 3.16 | 130.5 | 0.30 |
| IMD2 | 4337 | 10.08 | 4300 | 10.00 | 37.2 | 0.08 |
| SSD | 42964 | 99.88 | 42310 | 98.36 | 654.3 | 1.52 |

$\Sigma E_i$, total energy losses; $E_1 + E_2$, energy losses outside the cryostat; $E_3 + E_4 + E_5$, energy losses inside the cryostat.

for the safety discharge is 654.3 kJ and this is in very good agreement with the experimental values of the integrated heat load shown in Fig. 4.33. Also for the safety discharge, the biggest contribution to the energy losses inside the vacuum vessel is generated in the TFMC radial plates (i.e., 265.5 kJ) and it is transferred to the conductor by the heat diffusion process [63] described in Section 6.

The first two columns of Table 4.7 show the total energy losses for the three cases—in kJ and in % of the total energy stored in the coil. At first sight, the inverter mode discharge (IMD1), where the total energy losses are at the minimum, appears as the most convenient. But, if one analyses separately the losses in the external bus bar system and the losses in the cryostat, the simultaneous ramping down strategy (IMD2) appears to be more convenient for the cryogenic plant (i.e., energy losses of 0.08% of the total stored magnetic energy in the coil against 0.30% of IMD1). The safety discharge is the more severe for the operation of the cryogenic plant (i.e., total energy losses 1.52%), but has to be retained as backup protection in case of failure of the inverter mode discharge.

An additional advantage of simultaneous ramping down of the currents in magnetically coupled circuits has to do also with the behaviour of the thyristor converter during switching off of the firing pulses. Usually this action is performed by the thyristor firing pulses controller when the current in the circuit is below a minimum threshold. When the thyristor firing pulses are turned off, induced currents from magnetically coupled circuit, although of modest amplitude, might inhibit the last active pair of thyristor to switch off. In this case the AC input voltage (i.e., 50 V peak at 50 Hz) is applied directly to the load present at the DC side.

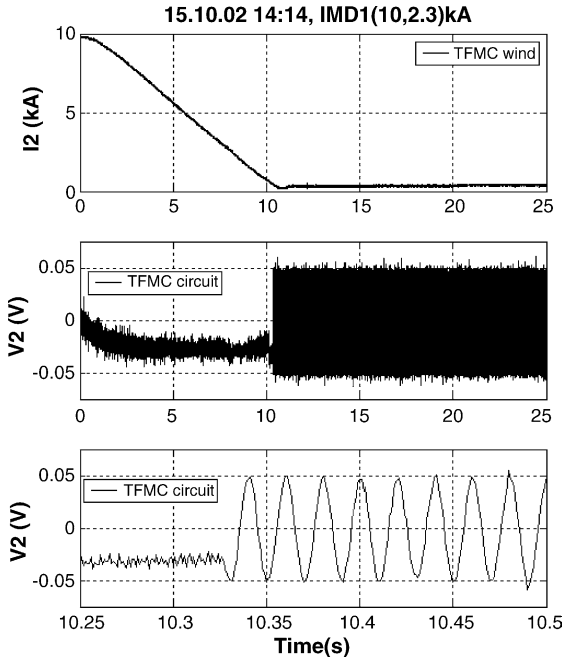


Fig. 4.34. TFMC AC/DC converter failure to switch off during an inverter mode discharge in combined operation of LCT coil and TFMC.

The fault just described occurred a few times during the power system set up Phase 2 (see Fig. 4.34). As mentioned in Section 4.3.2.1, during an inverter mode discharge (i.e., $dI_1/dt = -18$ A/s and $dI_2/dt = -1000$ A/s), with initial current flows in the LCT coil at 2.3 kA and in TFMC at 10 kA, the integrated heat load for the TFMC windings, shown in Fig. 4.10, reached about 600 kJ which is of the same order of magnitude as the energy losses of the standard safety discharge. The computed current in the TFMC windings with a sinusoidal voltage source of 50 V and 50 Hz, as shown in Fig. 4.35, is 123 A (rms) which produces, for 2 min, 5.13 kW (rms) of losses in the radial plates due to the eddy currents. The quench detectors, based on compensated voltages, and integration over 0.5 s period, did not intervene. Unfortunately, due to the tight time schedule of the tests, it was not possible to change the control software of the 30 kA and 50 kA power supplies to allow a simultaneous ramp down during an inverter mode discharge and therefore most of the protective actions had to be implemented with the safety discharge.

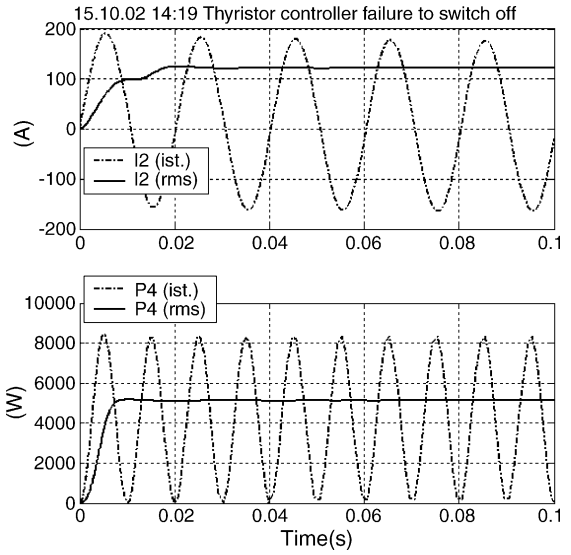


Fig. 4.35. Computed TFMC windings current and radial plate's losses during a converter failure to switch off.

### *4.6. Signal conditioning, data acquisition and protection performance*

#### *4.6.1. Signal conditioning and data acquisition*

The ITER TFMC has been equipped with sufficient number of sensors for protection and diagnostic as described in Section 3.7. All sensors are connected to the signal conditioning and the data acquisition system of the TOSKA facility including also the sensors of the facility (Fig. 4.36) [59,64].

There are two electrical isolation classes: sensors that are at the high voltage potential of the winding, and sensors, which are at or near ground potential. The signal conditioning path for the sensors at high voltage potential contains isolation amplifiers for a rated voltage of 10 kV.

The data acquisition system of TOSKA facility has been composed by reliable hardware and software components available in the first half of the 1990s. All components are linked by the TOSKA ETHERNET SEGMENT. The task of the TOSKA data acquisition system has been as follows:

(1) Acquisition of the sensor data with various scan rates, changing them to engineering units, making them directly available for process control including monitoring and archiving them in a database.
(2) The process control and handling of the cryogenic system including the visualisation of the flow schemes and the operation of valves and controllers via displays by the operators.
(3) Calculation of new values in engineering units by combining of different sensor values in a function for getting a new parameter for process control and monitoring (e.g., mass flow, cooling power, principal strain, von Mises stresses).
(4) Connection to the local area network (LAN) and access to the database by World Wide Web (WWW).

All signals collected by the slow scanners (subsystems: 1, 3, 5) within a time gap, that is <5 s, are provided with the identical time stamp and archived in the database.

Fast procedures are collected by a transient system (subsystem 4). They are divided in three trigger groups, which can be independently triggered with different scan rates. In this way, the acquisition of different experimental procedures could be handled successfully.

The whole system achieved its full performance in steps by previous tests (test of LCT coil with superfluid forced-flow-cooling up to 11 T, acceptance test of the W 7-X DEMO coil).

The main problem arose due to the high requirements needed for the compensated voltage signals for the determination of the resistive take-off voltage in order to measure the current sharing temperature $T_{CS}$. Fig. 4.37 represents the arrangement of the voltage taps (compensated voltages, pancake voltages, voltage drop across the joints). The compensated voltage signals were very noisy because of the 12-pulse thyristorised power supplies. The problem was successfully solved by filtering and calibration work of the signal conditioning lines. The needed signals (compensated voltage, temperature) were assigned to an available scanner, which was operated outside the existing data acquisition system. It improved simultaneously the time synchronisation. Details are described in Section 5.

#### *4.6.2. Protection*

The cryogenic and the electrical system are protected according to the state-of-the-art. For the quench protection of the TFMC, a modified quench detection

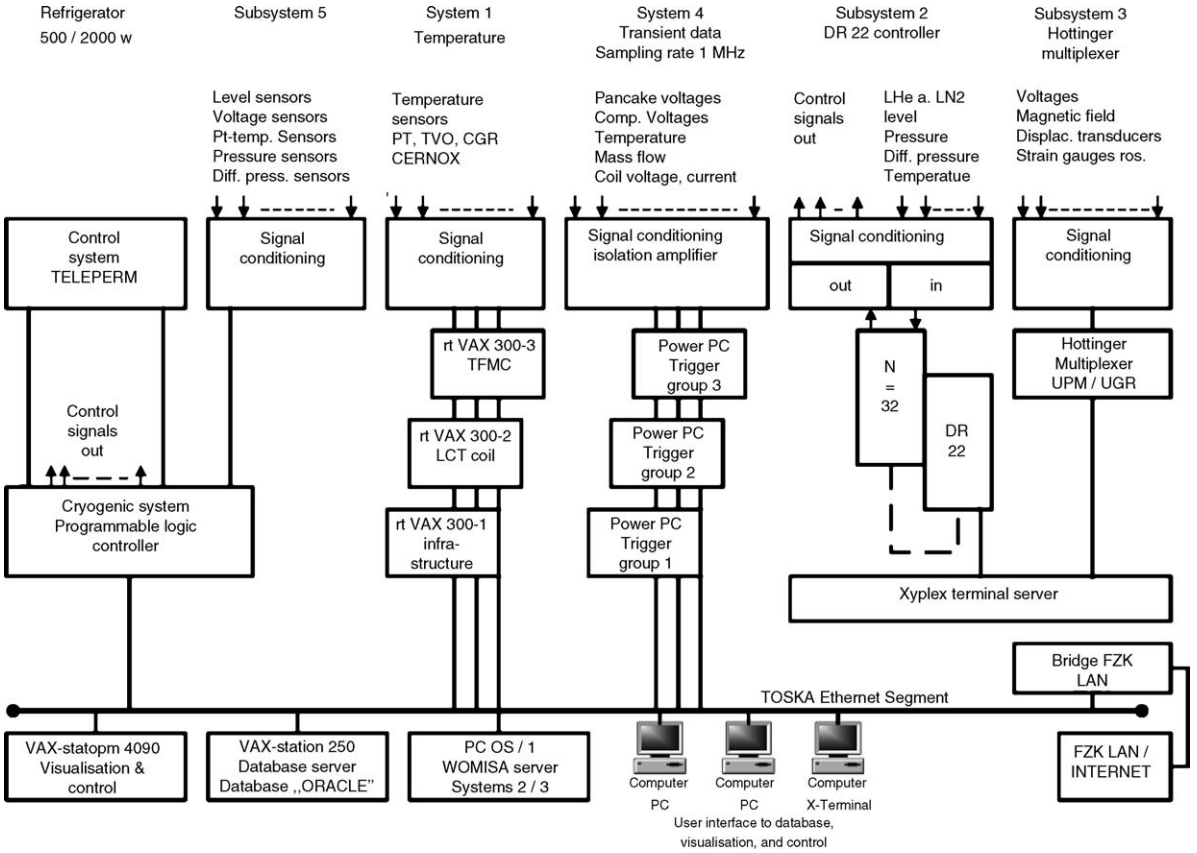


Fig. 4.36. The signal conditioning and data acquisition system of the TOSKA facility for the test of the ITER TFMC. All components of the system communicate across the TOSKA ETHERNET SEGMENT.

system has been used similar to those of the LCT coil [65]. The bridge circuit for the compensation of the inductive voltage was replaced by co-wound tapes. For redundancy, two co-wound tapes were integrated in the conductor insulation of each pancake (Section 3.7). Each co-wound tape of a pancake is connected to its own quench detector. The electronic function of each quench detector and its wiring is continuously monitored. In case of a fault in the electronic circuit (e.g., break of wire, malfunction of an amplifier) an alarm is immediately set. The logical output of both quench detectors is linked by an "and" gate. In this way, a fault or disturbance in one of the two quench detector does not lead to the triggering of a safety discharge. This increases the operation reliability, which is indispensable for the operation of large superconducting magnet systems. The outputs of all "and" gates are linked by an "or" gate. The quench detection system of the TFMC is represented in Fig. 4.38. The quench detection level and a delay time were adjustable in steps, respectively. The actual level used was 100 mV for the TFMC, and 10 mV for the superconducting bus bars. The adjusted delay time was in both cases 0.5 s. The achieved residual inductance was about 14 μH for the TFMC quench detection system and 0.5 μH for the bus bars.

The integrity of the electronic circuit of the quench detector is monitored by a small current running permanently through the co-wound tapes as mentioned above. This leads to an additional voltage drop, which has to be taken into account by the adjustment of the quench detection level.

The system worked very reliably over the whole TFMC test in both phases. All quenches were detected. No safety discharge was triggered by a fault of

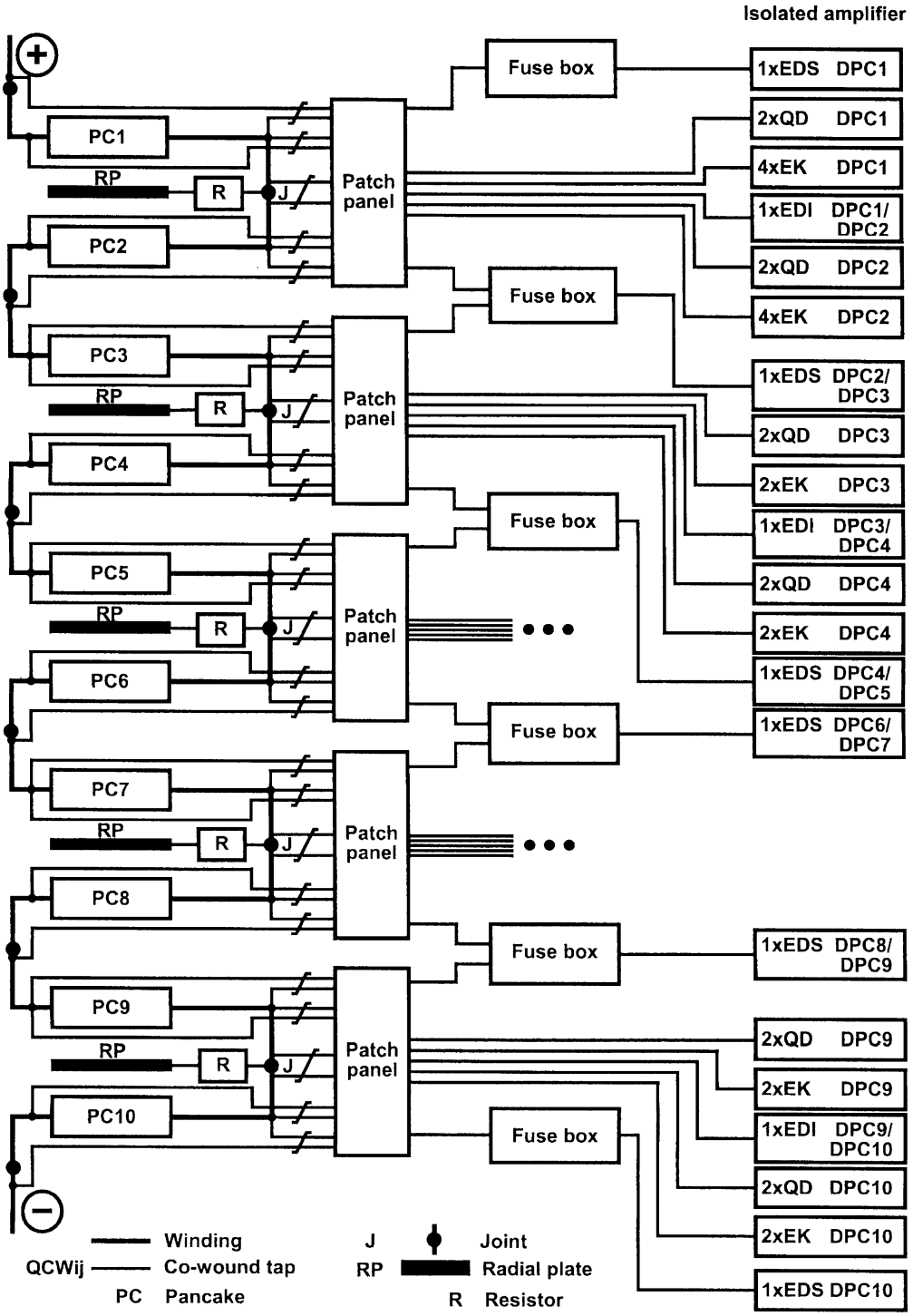


Fig. 4.37. The arrangement of the voltage taps across the TFMC winding (EDS, pancake voltages; QD, quench detectors; EK, compensated voltages; EDI, voltage drop across the joints).

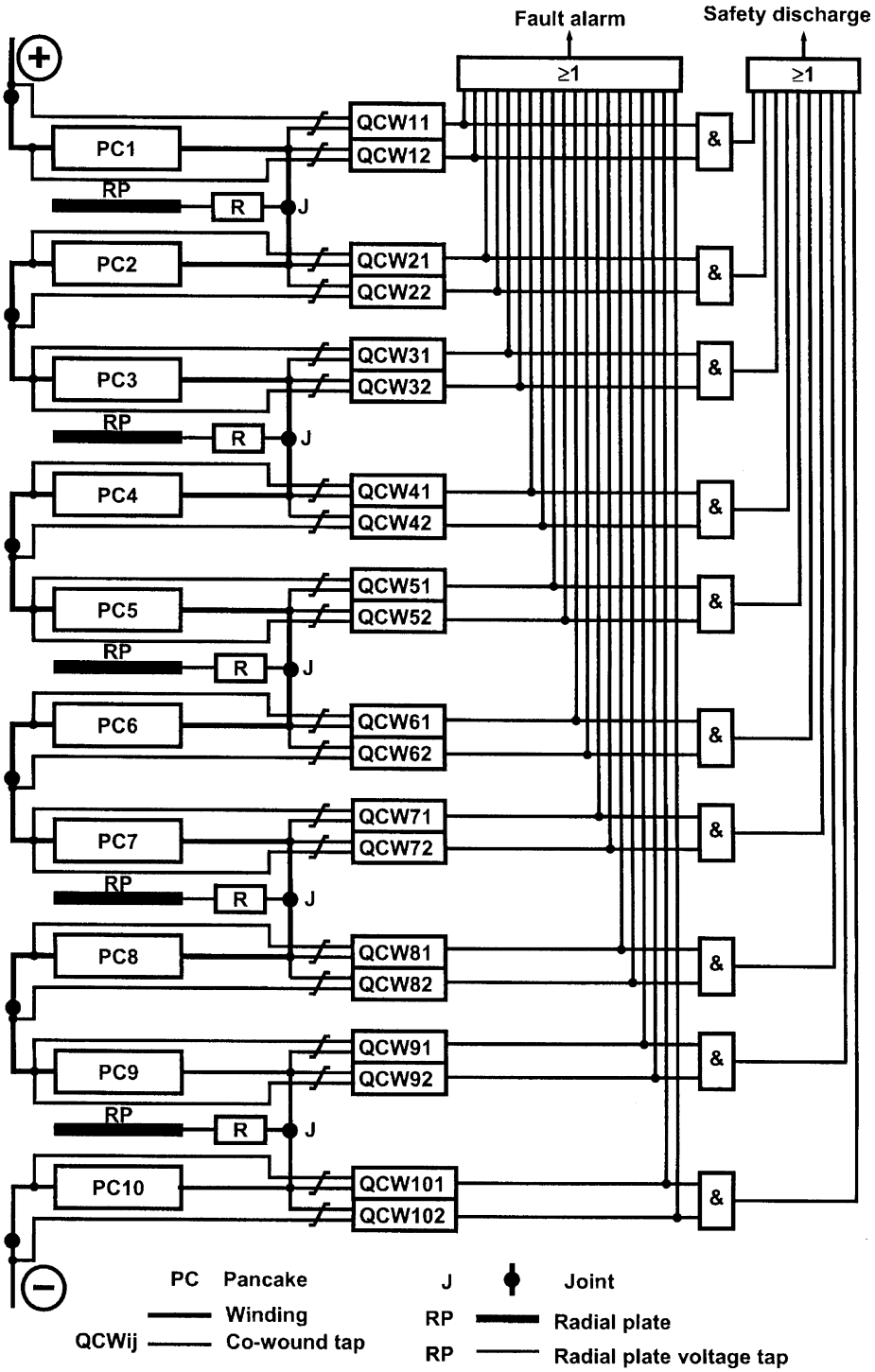


Fig. 4.38. The quench detection system of the TFMC winding and the logical links of the quench detectors. The logical output of two quench detectors of a pancake are linked by an “and” gate. All outputs of the “and” gates are linked by an “or” gate.

the quench detection system. The logic links of the quench detectors and the function monitoring allow the exchange of a faulty quench detector during current operation with no risk for the coil.

### 4.7. Behaviour of the LCT coil

The LCT coil was systematically prepared by investigations and experimental tests to extend the current operation from 16 kA up to 20 kA [66]. The goal was achieved by forced-flow-cooling with supercritical He II and by a mechanical reinforcement [45,53,67]. Careful FEM analysis was performed by means of a global model of the TFMC test configuration and detailed model of the LCT coil (Section 8) [68].

The highest in-plane (circumferential) forces on the LCT coil were achieved in the single coil test. This is demonstrated in Fig. 4.39, where the overall horizontal deformation for both load cases, LCT single coil and (LCT coil + TFMC), are presented. During the testing with the TFMC the LCT coil experienced the highest out-of-plane load, which was an overall attractive force of 82 MN between the coils. The measured von Mises stresses of the coil case were within 20% in fair agreement with the calculations.

No instabilities of the LCT coil conductor were observed during the operation of the most loaded case (TFMC: 80 kA, LCT: 16 kA).

### 4.8. Summary

- The TOSKA facility was operated very reliably with an availability of 98% thanks to the experience gained and improvements performed in the preceding tests (1996/1997: LCT coil at 1.8 K; 1999: W 7-X DEMO coil including the facility).
- For short times the cryogenic system can work far outside its rated capability by the optimised use of stored LHe.
- The two newly developed forced-flow-cooled 80 kA current leads and their high current density water-cooled flexible bus bars worked very well at the first attempt.
- The electrical supply system up to 80 kA including: power supply, safety discharge circuit, normal and superconducting bus bars, current leads, is unique

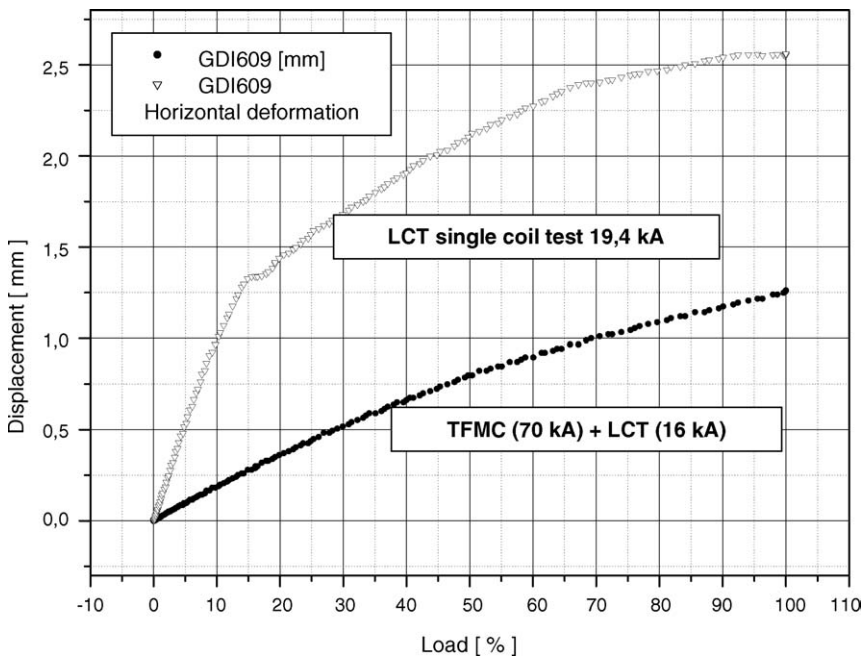


Fig. 4.39. Comparison of the horizontal deformation measured across the aperture of the LCT coil for the single coil test and the test with adjacent to the TFMC vs. percent of load.

around the world and meets ITER TF coil current levels.
- High voltage test equipment and a cryogenic high voltage laboratory are available for further developments of the ITER magnet dielectric insulation system.

Symbols used in equations:

| Symbol | Explanation |
|---|---|
| $E_i(t)$ | Energy losses of circuit $i$, $i = 1, 2, \ldots, 5$ |
| $I(t)$ | $5 \times 1$ vector of circuit currents |
| $I_i(t)$ | Circuit current of circuit $i$, $i = 1, 2, \ldots, 5$ |
| $L$ | Inductance matrix ($5 \times 5$) |
| $P_i(t)$ | Power losses circuit $i$, $i = 1, 2, \ldots, 5$ |
| $R$ | Resistance matrix ($5 \times 5$) |
| $R_{11}$ | LCT coil circuit resistance (mainly Al bus bars and water cooled flexible cables) |
| $R_{22}$ | LCT coil circuit resistance (mainly Al bus bars and water cooled flexible cables) |
| $R_{d1}$ | Discharge resistor circuit 1 (LCT coil) |
| $R_{d2}$ | Discharge resistor circuit 2 (TFMC) |
| $V(t)$ | $2 \times 1$ vector of circuit voltages |
| $V_i$ | Circuit voltage of circuit $i$, $i = 1, 2$ |

General acronyms, abbreviations, and initialisms are explained in Glossary.

## 5. Current sharing tests and assessment of the performance/operating limits of the TFMC conductor

### 5.1. Introduction and general properties

The classical measurement of the current sharing temperature $T_{CS}$ on a single strand requires to operate under a constant and uniform magnetic field $B$, with a DC current $I$ flowing through the wire. Then the operating temperature $T$ is slowly increased while the voltage drop $V$ over a given length $L$ (preferably equal to a multiple of the strand twist pitch length) is recorded to extract an average electric field $E = V/L$. By definition, the current sharing temperature $T_{CS}(B, I)$ is the value of $T$ for which $E = E_c = 10\ \mu V/m$. The accuracy of this measurement relies on the uniformity of $B$, $T$ and other determining parameters (such as the strain in $Nb_3Sn$ strands), over the length $L$.

The measurement of the current sharing temperature on a multistrand twisted cable as a whole should follow the same rules, except the length $L$ is a multiple of the last cabling twist pitch length. However, the comparison of the cable performance with the original strand one turns out to be rather complex because of all the heterogeneities encountered by the strands inside the cable. One major source of non-uniformity is the magnetic field gradient in the cable cross-section due to the so-called self-field (which can be generally neglected in the case of the single strand), but other sources exist such as non-uniformities of temperature (at least along the cable in the case of a cable-in-conduit), strain (for $Nb_3Sn$ strands), current distribution among strands (depending on the joints), and angle between strand and magnetic field (depending on the cabling pattern) [69]. In a general way, for $Nb_3Sn$ cables, the comparison leads to estimate the strain state of the filaments in the conductor [70,71], however it can be easily understood that this final result will depend on the level of modelling of all the heterogeneities in the cable, and that the use of refined computer codes becomes rapidly compulsory.

The measurement of the current sharing temperature in the TFMC still reached a higher level of complexity. First from an intrinsic point of view, because of the evolutions of field, temperature, and strain along the conductor length, and second from a practical point of view, because only the overall voltage drop across one full pancake (including the joints) and the helium inlet temperature were measured [72].

The tested pancake was the P1.2 pancake, which is located close to the LCT coil. This pancake is submitted to the maximum magnetic field when the LCT coil current is set at 16 kA. Fig. 5.1 gives the distributions along the pancake length (1st inner turn) of the maximum magnetic field modulus $B_{max}$, the magnetic field on conductor center $B_{center}$ [73], and the applied longitudinal strain on the conductor (called operating strain $\varepsilon_{op}$) [74] (see also Section 8.4), for 80 kA in the TFMC and 0 kA in the LCT coil. The same distributions are plotted in Fig. 5.2 for 80 kA in the TFMC and 16 kA in the LCT coil. The abscissa origins in Figs. 5.1 and 5.2 correspond to the beginning of the inner joint, which is therefore fully included in the curve. It can be seen that the peak field is not far from the inner joint (about 1.6 and 2.0 m from the center of the joint in Figs. 5.1 and 5.2, respectively).

Looking first at Fig. 5.1, one can see a significant but almost constant transverse field variation

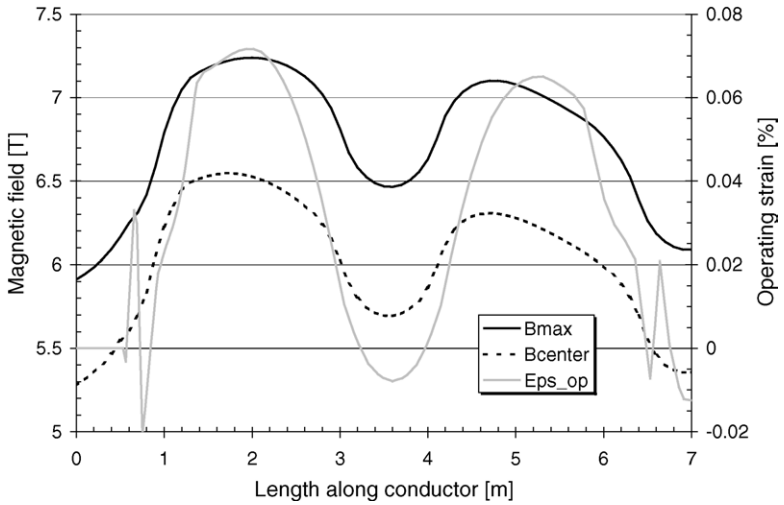


Fig. 5.1. Maximum and center magnetic field moduli $B_{max}$ and $B_{center}$, and operating strain Eps_op (=$\varepsilon_{op}$) along P1.2 length for 80 kA in TFMC and 0 kA in LCT coil.

($B_{max} - B_{center} \approx 0.70$ T) over the first turn. The evolution of $B_{max}$ and $\varepsilon_{op}$ are not fully correlated although the peak field corresponds well to the maximum of $\varepsilon_{op}$. Since the cable twist pitch length is 450 mm, one can see that, at least at peak field, field and strain can be considered as uniform over such a length (at ±0.2% on $B$, and ±4% on $\varepsilon_{op}$). Looking then at Fig. 5.2, one can see again an almost constant transverse field variation ($B_{max} - B_{center} \approx 0.80$ T) over the first turn. However, in that case, strain and field look quite non-correlated due to off-plane stress (see Section 8.2), and particularly at peak field, the maximum of field corresponds to a high longitudinal gradient of strain (variation of ±0.7% on $B$, and ±23% on $\varepsilon_{op}$ over 450 mm). These results show that the operating conditions in the TFMC were far from the ideal case as concerns conductor current sharing temperature measurements, particularly when the LCT coil was powered.

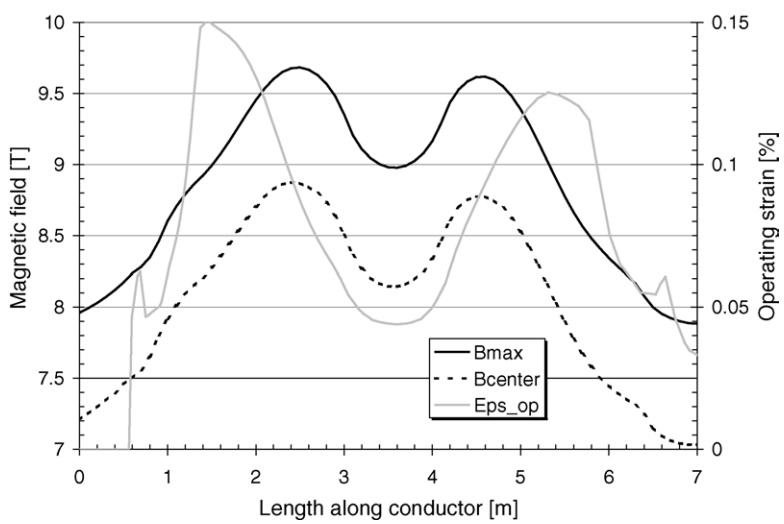


Fig. 5.2. Maximum and center magnetic field moduli $B_{max}$ and $B_{center}$, and operating strain Eps_op (=$\varepsilon_{op}$) along P1.2 length for 80 kA in TFMC and 16 kA in LCT coil.

The knowledge of the strand electrical properties is compulsory for comparing conductor performance to the single strand one. The non-copper critical current density $J_c$ of the TFMC strand as function of magnetic field $B$, of temperature $T$, and of longitudinal strain $\varepsilon$, has been described using the following formulas derived from the Summers model [75–77]:

$$J_c = C_0\left(1-\left(\frac{T}{T_{c0}}\right)^2\right)^2 B^{-0.5}\left(1-\frac{B}{B_{c2}}\right)^2 \quad (5.1)$$

$$B_{c2} = B_{c20}\left(1-\frac{T}{T_{c0}}^2\right)\left(1-\frac{T}{3T_{c0}}\right) \quad (5.2)$$

$$B_{c20} = B_{c20m}(1-a|\varepsilon|^{1.7}) \quad (5.3)$$

$$T_{c0} = T_{c0m}(1-a|\varepsilon|^{1.7})^{1/3} \quad (5.4)$$

$$C_0 = C_{00}(1-a|\varepsilon|^{1.7})^{1/2} \quad (5.5)$$

with $a = 900$ when $\varepsilon < 0$ (i.e., compression on $Nb_3Sn$ filaments), and $a = 1250$ when $\varepsilon > 0$ (i.e., tension on $Nb_3Sn$ filaments).

From the first measurements performed on a TFMC type strand, the following values of parameters were derived (using Eq. (5.2) instead of Eq. (5.2b)) [75]:

$$B_{c20m} = 29.1\,\mathrm{T} \quad (5.6a)$$

$$T_{c0m} = 16.9\,\mathrm{K} \quad (5.6b)$$

From the measurements performed on the TFMC strands and witness samples, the value of $C_{00}$ was estimated to be for a copper/non-copper ratio of 1.51, and for the P1.2 pancake conductor (again using Eq. (5.2) instead of Eq. (5.2b)) [76]:

$$C_{00} = 1.10\times10^{10}\,\mathrm{A\,m^{-2}\,T^{1/2}} \quad (5.7)$$

The electric field $E_s$ developed along a strand carrying a current $I_s$ is calculated using the usual semi-empirical $n$ power law:

$$E_s = E_c\left(\frac{J_s}{J_c(B_\perp, T, \varepsilon)}\right)^n \quad (5.8)$$

where $E_c = 10\,\mu\mathrm{V/m}$, $J_s = I_s/A_{nc}$, with $A_{nc}$, the non-copper area of the strand, and $B_\perp$ is the component of the magnetic field perpendicular to the strand, $n$ is called the $n$ index.

Several problems are related with the $T_{CS}$ measurements in the TFMC. Starting with the voltage drop, one has first to cope with the accuracy of this measurement which is extracted from the voltage drop along about 80 m of conductor, using a compensating co-wound strip to balance the inductive voltage. Moreover, this voltage drop $V$ includes contributions of the two joints at pancake ends. The magnetic field and strain are not enough "peaked" to be able to associate this voltage drop (after joint resistive voltages removal) with a local electric field at peak magnetic field, i.e., the length $L$ as defined above is not known and may be not a constant. As a consequence, the local electric field at peak magnetic field cannot be extracted directly from the measured voltage drop. As concerns the temperature, the problem does not look simpler because only the inlet temperature $T_{in}$ is measured and there is Joule heating in the inner joint as well as along conductor when the electric field is not negligible. Moreover, the conductor is a dual channel cable-in-conduit, in which the annular area and the central channel are not isothermal, and in addition the heat transfer through the joint between jointed conductors (P1.1 and P1.2 pancakes) may be not negligible.

Finally, in order to extract the current sharing temperature from the measurements, one is led to build coupled thermal-hydraulic and electric models, in which the strands are modelled using the preceding formulas. The unknowns in these models are the strand $n$ value and the $Nb_3Sn$ strain $\varepsilon$. These parameters are adjusted in order to fit with computing curves the experimental curves $V(T_{in})$. Then the local (along conductor length) strand temperature and electric field can be extracted from the computation, and a local current sharing temperature can be estimated as the value of the (local) strand temperature when the (local) electric field reaches for the first time 10 μV/m in the conductor. Therefore, the current sharing temperature "measurement" is only indirect and relies on model and code accuracies. All this work will be depicted in the following sections.

In a first approach, assuming that the mechanical strain applied to the jacket is fully transmitted to the filaments, the effective strain $\varepsilon$ in $Nb_3Sn$ filaments can be written as the sum of three different terms as follows:

$$\varepsilon = \varepsilon_{th} + \varepsilon_{op} + \varepsilon_{extra} \quad (5.9)$$

where $\varepsilon_{th}$ is the so-called thermal strain which can be simply defined as the value of $\varepsilon$ at zero current, $\varepsilon_{op}$

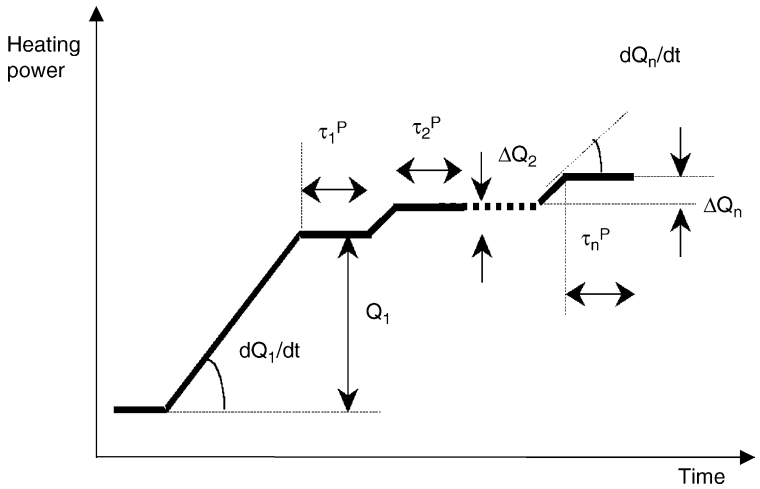


Fig. 5.3. Multi-step strategy: schematic view of the heating power waveform. The generic ($n$-th) step is defined by the slope ($dQ_n/dt$), and by the duration ($\tau_n^P$) and height ($Q_n = Q_1 + \sum \Delta Q_k$) of the plateau.

has been defined previously and $\varepsilon_{extra}$ is an additional contribution (see below) at a given combination of LCT coil and TFMC currents. From a rigorous point of view, one should call ($\varepsilon_{op} + \varepsilon_{extra}$) the real operating strain.

At first glance, $\varepsilon_{extra}$ should be zero, but it will be shown in the following that it was not the case. It will be also shown how $\varepsilon_{th}$ can be estimated from the experimental results.

### 5.2. *Set-up and heating strategies for the measurement of the current sharing temperature*

Essentially all the measurements of the current sharing temperature were performed according to the multi-step heating strategy,[2] which had been successfully applied to the $T_{CS}$ tests of other ITER coils (e.g., the CSMC [79]). For the TFMC, the strategy was developed during the Phase 1 tests, based on the M&M code [80] analysis presented in [81], and then it was used also during Phase 2.

Resistive heaters were available on the conductor inlets (upstream of the joint) of P1.1 and P1.2, and they were controlled to inject hot helium in the two conductors, according to a suitable heating scenario, see e.g., Fig. 5.3. During all Phase 1, and the first tests of Phase 2, the inlet helium temperature was increased step-wise until a quench of the coil occurred. The heat load on the facility turned out to be very high, i.e., at the outermost operation limit of the cryogenic plant, especially for the $T_{CS}$ measurements at low currents. Eventually, after a severe quench that caused a significant release of helium to the atmosphere, a careful monitoring of the voltage across the heated pancakes, and in particular P1.2 where the quench was expected first, allowed ramping down the heater power as soon as a suitable portion of the $V$–$T_{in}$ characteristic was available for analysis (i.e., as soon as voltages of, say, 200–300 μV were measured, with a bit more of thrill the higher the bet was). Once back at zero heater power, the ramp down of the current followed, and this approach allowed avoiding the quench in all of the $T_{CS}$ tests where it was applied during Phase 2, with a significant reduction of the load on the facility. Of course, at each combination of currents in the TFMC and in the LCT coil, a different $T_{CS}$ could be foreseen, and correspondingly a different heater scenario (=succession of steps of different power followed by plateaus of given duration) had to be designed and tested beforehand without current. The scenario for the last test (80 kA in the TFMC, 16 kA in the LCT coil) could not be checked experimentally because of lack of time, so that it was fully based, for the first and only time, on the predictive

[2] A single $T_{CS}$ test at 80 kA in the TFMC was performed during phase 1 according to a *single* step strategy, but it turned out to be quite difficult to analyse due to lack of reliable $V$–$T_{in}$ signals and to the fully transient nature of this strategy [78]. It will not be further discussed here.

Table 5.1
Summary of $T_{CS}$ tests performed on the TFMC

| Date | $I_{TFMC}$ [kA] | $I_{LCT}$ [kA] | Comments |
|---|---|---|---|
| August 8, 2001 | 80 | 0 | See [84] |
| September 10, 2001 | 80 | 0 | [a] |
| September 11, 2001 | 80 | 0 | [a,b] |
| September 12, 2001 | 69.3 | 0 | [a] |
| September 13, 2001 | 56.6 | 0 | [a] |
| September 14, 2001 | 80 | 0 | [a] |
| September 17, 2001 | 80 | 0 | [a] |
| September 27, 2001 | 56.6 | 0 | |
| September 28, 2001 | 80 | 0 | |
| October 14, 2002 | 80 | 0 | Repetition after Phase 1 |
| October 23, 2002 | 69.3 | 0 | |
| November 6, 2002 | 70 | 16 | First combined test and nominal peak load conditions |
| November 8, 2002 | 60.6 | 13.9 | Two-coil current scan |
| November 11, 2002 | 49.1 | 11.3 | Two-coil current scan |
| November 18, 2002 | 80 | 14 | Extended operation |
| November 19, 2002 | 80 | 0 | Repetition after cycling |
| November 20, 2002 | 70 | 16 | Repetition after cycling |
| November 21, 2002 | 80 | 16 | Extended operation to peak mechanical load on cable comparable to ITER TF coils (∼800 kN/m) |

[a] No reliable $V$–$T_{in}$ characteristic available.
[b] Single step heating strategy.

capability of the M&M code, which proved to be reliable. In general, it can be said that a careful operation of the cryogenic facility brought it to operate, during these tests, far above its expected nominal capacity (see Section 4.3.2.3; Fig. 4.17) [48].

### 5.3. Experimental results

The full set of $T_{CS}$ tests performed on the TFMC during Phases 1 and 2 is summarised in Table 5.1. It may be noticed that, although the test of the conductor critical properties was initially beyond the scope of the TFMC test campaign, 17 $T_{CS}$ measurements could be performed. The 80/0 kA scenario was tested five times in the Phase 1 campaign, in order to assess if any degradation due to quenches had occurred, and two additional times during Phase 2 to check first the effect of the warm-up and cool-down, and then the effect of cycling on the conductor properties. The first tests at 69.3/0 and 56.6/0 kA, performed during Phase 1, were repeated for different reasons: the former (repeated in Phase 2) in order to have a reliable $V$–$T_{in}$ characteristic, while the latter (during Phase 1) in order to reduce the temperature difference between P1.2 and P1.1, thus reducing the heat exchange in the inlet joint and the corresponding uncertainties in the analysis [83]. The test at 70/16 kA, corresponding to the nominal peak load conditions during Phase 2, was repeated twice in order to assess the effect of cycling on the conductor. The TFMC was also tested extending the operation beyond the nominal values, so that the two tests at 80/14 and 80/16 kA could be carried out according to the extrapolation of the mechanical test results without overstressing of the coils and structures.

Below some details are given on the major direct outcomes of these tests, namely electrical and thermal-hydraulic signals, which are then used to reconstruct the voltage–inlet temperature $V$–$T_{in}$ characteristic most useful for the analysis.

#### 5.3.1. Electrical signals

As already mentioned before, the total voltage drop across the whole P1.2 pancake (including the joints) was measured. This measurement, which was used for quench detection and diagnostics, turned out to be rather noisy (for an accurate measurement of current sharing) and to have a large offset. As a matter of fact, the offset was in the order of −16 mV, the joint voltage drops in the order of 0.1 mV, and the noise within ±0.3 mV, while the useful range for the signal was 0–0.25 mV. The major source of low frequency noise was suspected to come from the power sup-

ply current regulation. This situation required a strong post-processing of the signal. The offset and the joint voltage drop were removed by subtracting the value of the signal at full current, before raising the inlet temperature (i.e., at 4.5 K). By using moving averaging over 50 pts, the noise could be reduced to ±20 μV on the (standard) transient data acquisition system and to ±10 μV on the so-called "SPARTAN" data acquisition system. Nevertheless, in spite of this data post processing, the accuracy of this measurement, although good, remains not satisfactory when dealing with start of voltage increase and fine transient analyses. Particularly under concern are the accurate level of the offset (<10 μV accuracy is required, which means a few $10^{-4}$ times the offset value), its variation with time, and the rather long integration time (5 s) associated with the averaging process. One can note that during heating to reach $T_{CS}$, the increase of voltage due to the increase of joint resistance is about 5–10 μV, which makes the constancy of the offset only approximated during the whole run. Regarding the averaging process, one can check that the integration time remains low enough not to perturb the dynamics of the voltage evolution (see Section 5.3.3), although from a hydraulic point of view, the travel of helium through the central channel during 5 s is quite large (3–7 m range, see Sections 5.3.2 and 5.4.2). Examples of electric signals can be seen in Section 5.3.3 and following.

### 5.3.2. Thermal-hydraulic signals

The schematic location of the most relevant thermal-hydraulic sensors, all outside of the coil, is already given in Fig. 3.13 (see Section 3). Temperature measurements were available at the common inlet manifold and at the outlet of each pancake (or couple of pancakes on adjacent radial plates) and of each busbar. Pressure sensors were available at the common inlet and outlet manifolds, while Venturi flowmeters were located at the inlet of each double pancake. On the heated pancakes, additional sensors were available and namely of the mass flow rate before the heater, of the temperature after the heater but upstream of the inlet joint, and of the pressure drop along the conductor. Control valves were used to regulate the flows in the heated pancakes.

The measurements of $T_{CS}$ required a careful control of the thermal-hydraulic parameters of the circuit, in order to ensure:

1. Operating pressure ∼0.5–0.6 MPa, to avoid thermal-acoustic oscillations [81,83].
2. Adequate mass flow rate in the heated pancakes, such as to reach the target temperature (close to the expected $T_{CS}$) during the heating scenario with the available heating power but without overloading the facility.

Before the start of the $T_{CS}$ measurement, a careful regulation of the control valves allowed to establish the target pressure drop (more reliable than the mass flow rate measurement) in the heated pancakes. When the heaters were switched on (Fig. 5.4a), the temperature at the joint inlet evolved at the same time as shown in Fig. 5.4b. The control valves were maintained in the same position, so that the pressure drop (Fig. 5.5a) across, and the mass flow rate (Fig. 5.5b) through the heated pancakes evolved according to a dynamics driven by the heater and by the parallel paths of the different double pancakes [85].

Concerning the accuracy of the thermal-hydraulic signals:

- the mass flow rate, derived from the pressure drop measurement across the Venturis, is computed with an accuracy of ±5% of the full range (∼20 g/s for P1.1 and P1.2);
- the pressure drop on the heated pancakes is known with an accuracy of ±100 Pa;
- the temperature sensors have an accuracy of ±3 mK;
- the absolute pressure is known with an accuracy of ±1.2 kPa.

### 5.3.3. Voltage–inlet temperature ($V$–$T_{in}$) characteristics

During Phase 1 it was difficult to extract a $V$–$T_{in}$ characteristics from the experimental data, since voltage and temperature signals were taken from different data acquisition systems [83]. This analysis is concentrated on the $V$–$T_{in}$ characteristics for $T_{CS}$ measurements of Phase 2. Both temperature and voltage signals are taken from either the transient DAS or the so-called SPARTAN data [85], post-processed. The resulting characteristic is plotted in Fig. 5.6a for the case at 70/16 kA (November 20, 2002). Note that the voltage has been base-lined to zero. Finally, the evolution of the inlet temperature and the corresponding evolution of the resistive voltage are shown in Fig. 5.6b for the case at 80/16 kA.

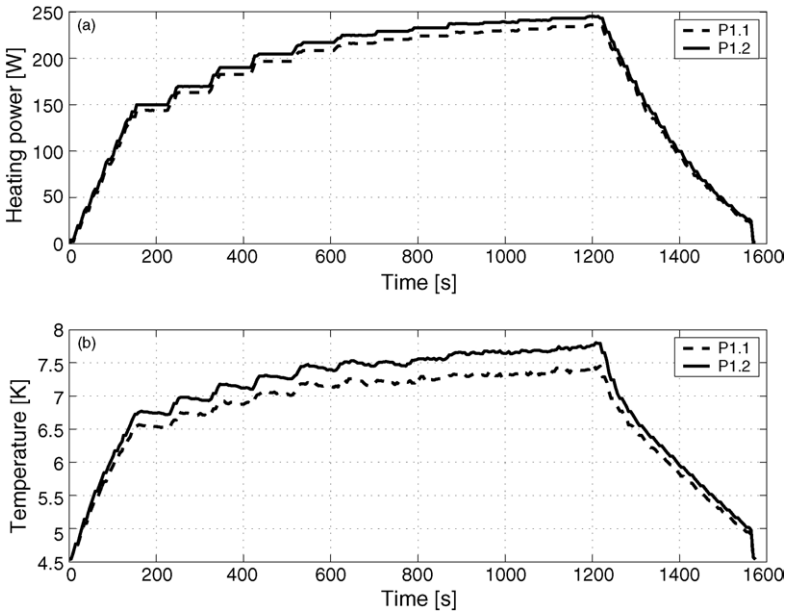


Fig. 5.4. $T_{CS}$ measurement at 70/16 kA (November 20, 2002). (a) Evolution of the heating power during $T_{CS}$ measurement; (b) evolution of the inlet temperature in P1.1 (dashed) and P1.2 (solid) during the heating.

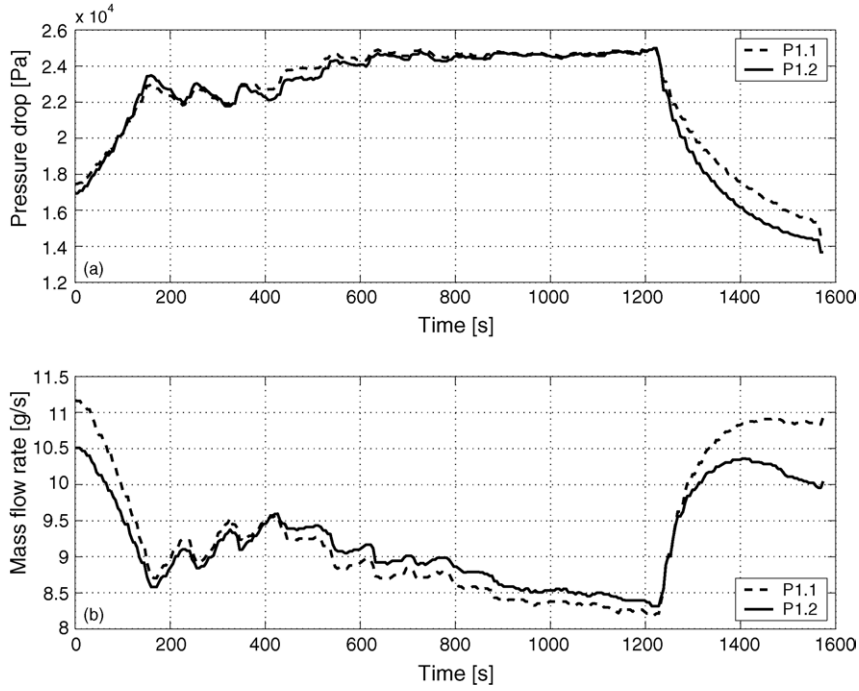


Fig. 5.5. $T_{CS}$ measurement at 70/16 kA (November 20, 2002). (a) Evolution of the pressure drop across P1.1 (dashed) and P1.2 (solid) during the heating; (b) Evolution of the mass flow rate in P1.1 (dashed) and P1.2 (solid) during the heating.

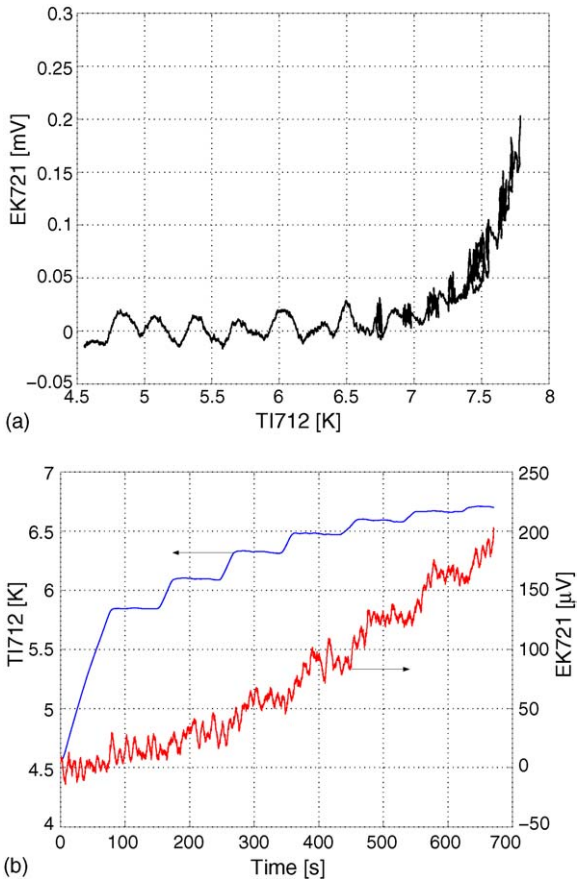


Fig. 5.6. (a) $V$–$T_{in}$ characteristics (SPARTAN data) for $T_{CS}$ measurement at 70/16 kA (November 20, 2002). (b) Evolution of $T_{in}$ (left axis) and V (right axis), SPARTAN data, for $T_{CS}$ measurement at 80/16 kA.

### 5.4. Evaluation of the current sharing temperature from the experimental results

#### 5.4.1. M&M analysis

The results and analysis of the $T_{CS}$ tests of Phase 1 were already presented in Ref. [85].

The strategy for the M&M [80] analysis of the $T_{CS}$ tests has been already established in previous work [78], so that it will only be briefly reviewed here. An "average" strand is considered representative of the conductor performance (uniform current distribution among strands is assumed in the model). The strain on the average strand is assumed given by Eq. (5.9), where $\varepsilon_{th} = -0.61\%$ is taken as the thermal strain [76], and $\varepsilon_{extra}$ as a fitting parameter. M&M computes the strand temperature profile $T_{st}(x, t)$ along the conductor, for a given measured inlet temperature evolution of the helium $T_{in}(t)$. Using the computed profile $B(x)$ of the average and maximum magnetic field along P1.2, an average electric field $\langle E_s \rangle (x, t)$ on the conductor cross-section is computed by M&M, using Eq. (5.8) and a value for the second fitting parameter, the exponent or index "$n$". The resistive voltage $V(t)$ along the conductor is then computed integrating $\langle E_s \rangle$ $(x, t)$ along P1.2, and one attempts to fit the measured $V$–$T_{in}$ characteristic with the computed one, using the two fitting parameters ($\varepsilon_{extra}$, $n$), taken independently one of each other. From this fit, one deduces:

(a) the possible "degradation" $\varepsilon_{extra}$ of the conductor performance with respect to the strand;
(b) the conductor $n$;
(c) the "measured" $T_{CS}$, defined here as the value of $T_{st}$ *computed* at the first time and location when $\langle E_s \rangle (x, t) = E_c$. Except for the two fitting parameters, the rest of the input is the same for all simulations. The simulations are performed using the (cyclic) inlet temperatures as well as outlet pressure and pressure drop as time-dependent boundary conditions.

It should be also noted here that Eq. (5.2) in Section 5.1 is only an approximation of the original Summers formula, which is in fact [77]:

$$B_{c2} = B_{c20}\left(1 - \left(\frac{T}{T_{c0}}\right)^2\right) \times \left\{1 - 0.31\left(\frac{T}{T_{c0}}\right)^2 (1 - 1.77 \ln\left(\frac{T}{T_{c0}}\right)\right\} \quad (5.2b)$$

This latter formula is used in M&M, however associated with the values of $B_{c20m}$ and $T_{c0}$ given in Eqs. (5.6a) and (5.6b), respectively.

A collection of the results of the M&M analysis of *all* $T_{CS}$ tests of Phase 2, using the actual Summers scaling [77] (see Section 5.1), is reported in Figs. 5.7–5.14. It may be noted that no significant changes were observed in the coil performance in Phase 2 with respect to Phase 1, nor after cycling with respect to that before cycling (compare Fig. 5.9 with Fig. 5.8, and Fig. 5.13 with Fig. 5.12, respectively) [87]. The corresponding values of the computed current sharing

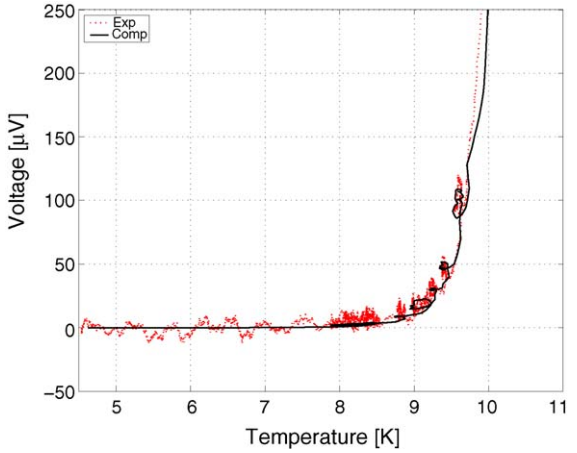


Fig. 5.7. M&M best-fit of the characteristic for the 69.3/0 kA.

temperature $T_{CS}$ and the conductor $n$ value are reported in Table 5.2.

For almost all cases, the analysis was performed simulating at the same time P1.1 and P1.2, in order to properly reproduce the heat transfer in the inlet joint. In the case 80/16 kA, during the heating a normal voltage developed also along P1.1. The M&M simulation for this case allows also the computation of the voltage drop along P1.1, which has been performed using the same $n$ but a slightly smaller $\varepsilon_{extra}$ ($-0.175$ instead of $-0.18$) compared to P1.2 (see Section 5.5.1. for a possible explanation). In Fig. 5.15, the experimental

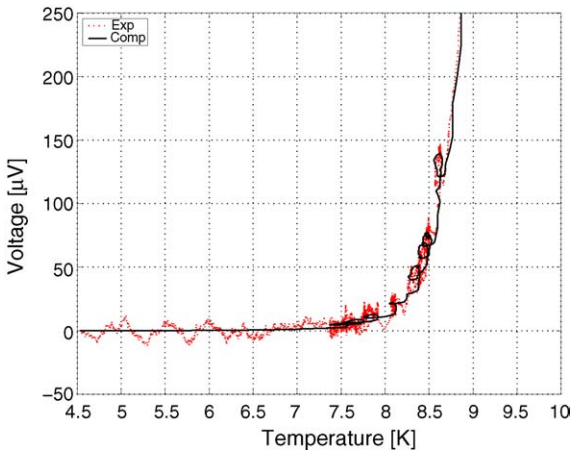


Fig. 5.8. M&M best-fit of the characteristic for the 80/0 kA (before cycling).

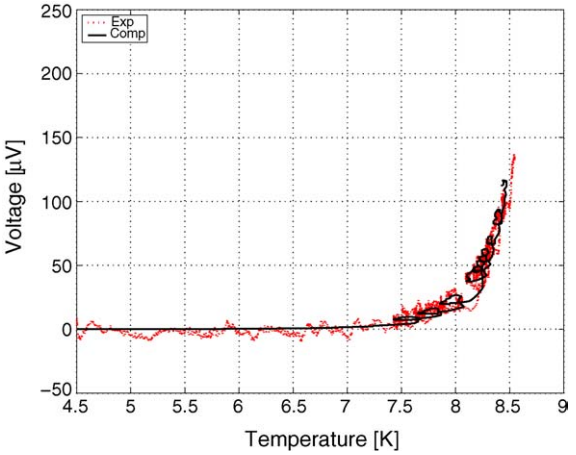


Fig. 5.9. M&M best-fit of the characteristic for the 80/0 kA (after cycling).

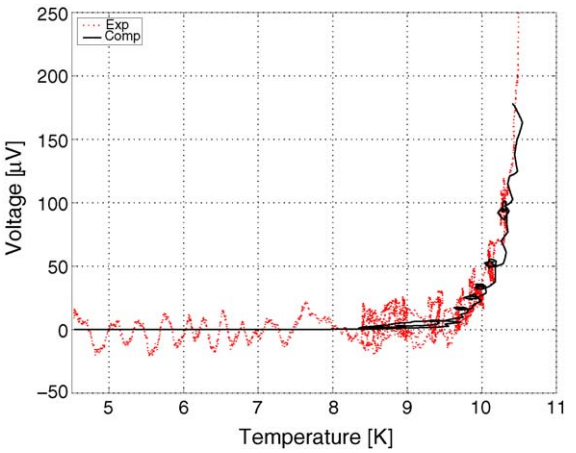


Fig. 5.10. M&M best-fit of the characteristic for the 49/11 kA.

and the computed voltage drop along P1.1 are reported, showing a very good agreement.

### 5.4.2. *ENSIC analysis*

*5.4.2.1. ENSIC model.* An electrical network DC model has been developed at CEA to represent the whole P1.2 pancake. This network model includes a realistic modelling of the joints, leading to an uneven current distribution among the strands inside each petal, but uniform among the petals[3] [69]. Because of this

[3] A deviation of ±10% among petals currents can be expected from geometrical measurements, which has no significant impact on the final result.

Table 5.2
Summary of M&M and ENSIC results (Phases 1 and 2) for the conductor $n$ and strand $n$, respectively, and $T_{CS}$ at different combinations $I_{TFMC}/I_{LCT}$

| Date | $I_{TFMC}$ [kA] | $I_{LCT}$ [kA] | M&M + Summers | | M&M (Summers) | | ENSIC (Summers[b]) | |
|---|---|---|---|---|---|---|---|---|
| | | | $\varepsilon_{op}$ [%][a] | $\varepsilon_{extra}$ [%] | $T_{CS}$ [K] | $n_{cond}$ | $T_{CS}$ [K] | $n_{strand}$ |
| 28/09/2001 | 80 | 0 | 0.042 | –0.14 | 8.3 | 7 | 8.43 [86] | 10 [86] |
| 12/09/2001 | 69.3 | 0 | – | – | – | – | – | – |
| 27/09//2001 | 56.6 | 0 | 0.030 | −0.0045 | 10.9 | 7 | – | – |
| 14/10/2002 | 80 | 0 | 0.042 | −0.11 | 8.4 | 7 | – | – |
| 23/10/2002 | 69.3 | 0 | 0.036 | −0.09 | 9.6 | 6 | – | – |
| 6/11/2002 | 70 | 16 | 0.065 | −0.16 | 7.2 | 7 | – | – |
| 9/11/2002 | 60.6 | 13.9 | 0.056 | −0.14 | 8.6 | 6 | $8.62 \pm 0.5$ | $6 \pm 0.05$ |
| 11/11/2002 | 49.5 | 11.3 | 0.046 | −0.10 | 10.0 | 5 | $10.07 \pm 0.5$ | $5 \pm 0.05$ |
| 18/11/2002 | 80 | 14 | 0.067 | −0.185 | 6.3 | 7 | – | – |
| 19/11/2002 | 80 | 0 | 0.042 | −0.14 | 8.3 | 7 | $8.38 \pm 0.5$ | $8 \pm 0.05$ |
| 20/11/2002 | 70 | 16 | 0.065 | −0.17 | 7.2 | 7 | $7.27 \pm 0.5$ | $10 \pm 0.05$ |
| 21/11/2002 | 80 | 16 | 0.074 | −0.18 | $6.0 \pm 0.03$ | $8 \pm 1$ | $6.10 \pm 0.5$ | $10 \pm 0.05$ |

The values of $\varepsilon_{op}$ at the computed $T_{CS}$ location and of the best-fitting $\varepsilon_{extra}$ from M&M are also reported.
[a] At the computed $T_{CS}$ location.
[b] Summers with $B_{c2}$ from Eq. (5.2) instead of (5.2b).

uneven current distribution, the conductor index $n$ will be different (i.e., lower) from the strand index $n_{strand}$. In fact, the code calculates (indirectly) the conductor index $n$, at variance with M&M in which it is entered as an input. The magnetic field map across the conductor, as well as the angular inclination between field and strand (see Eq. (5.8)) due to the multistage twisting structure of the cable are taken into account [69]. This model has been validated using experimental results on full size conductor samples [70]. The ENSIC code also includes a simplified steady state thermal-hydraulic model, calculating the temperature profile along the conductor length from the inlet temperature, taking into account the Joule heating in the joints as well as in the regular conductor. This model has been recently upgraded from [86] since it is now considering heat exchange in the inner joint (with pancake P1.1), and a dual channel thermal-hydraulics (i.e., temperatures are different in central channel and strand region) through a characteristic heat transfer length $\lambda_{th}$ between the two hydraulic channels. The heat exchange with the adjacent pancake (along the conductor) can also be

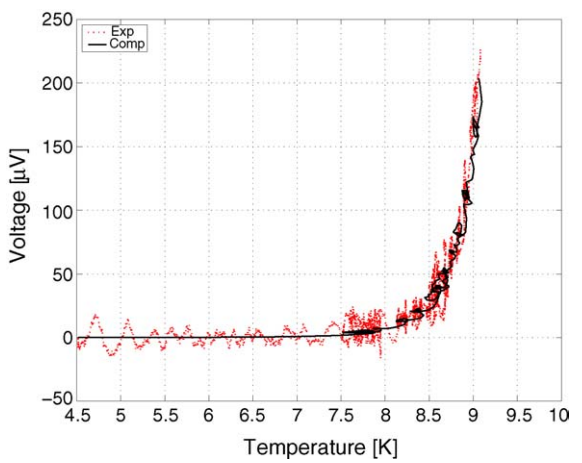


Fig. 5.11. M&M best-fit of the characteristic for the 60.6/13.9 kA.

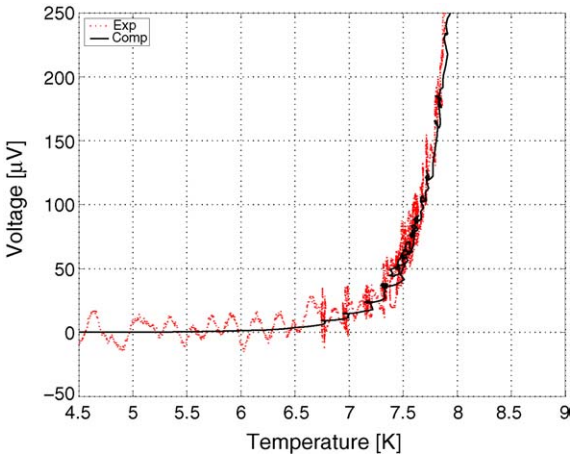


Fig. 5.12. M&M best-fit of the characteristic for the 70/16 kA (before cycling).

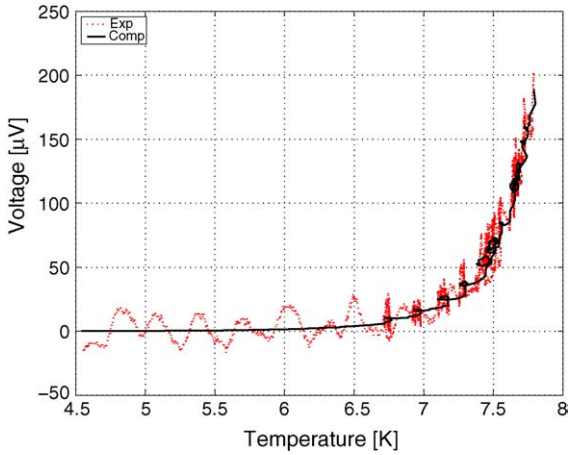


Fig. 5.13. M&M best-fit of the characteristic for the 70/16 kA (after cycling).

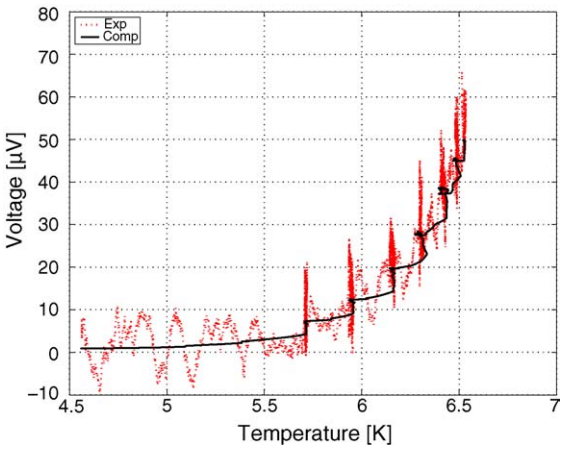


Fig. 5.15. M&M best-fit of the characteristic of DP1.1 for the 80/16 kA.

taken into account but has been neglected in this case. The heat exchange in the joint has been extrapolated from the value measured on the PF–FSJS joint (i.e., 20% of the enthalpy difference at helium inlets) [88]. The values of $\lambda_{th}$ have been extrapolated from direct measurements performed on the PF–FSJS conductor [88,89], they range from 0.6 to 1 m, depending on the test. For the sake of consistency with the strand experiments, the strand properties are described using the simplified Summers model (i.e., using Eq. (5.2) and not Eq. (5.2b), see Section 5.1).

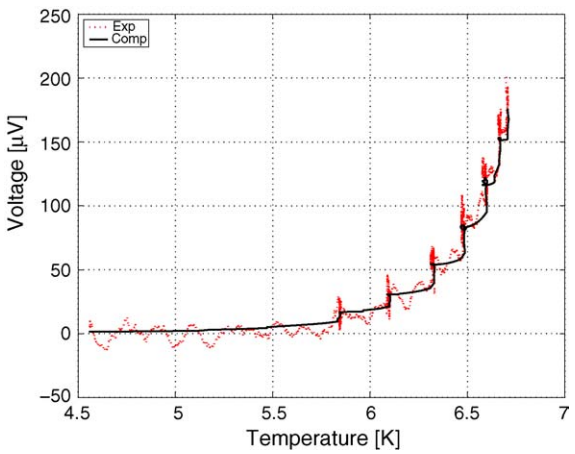


Fig. 5.14. M&M best-fit of the characteristic of DP1.2 for the 80/16 kA.

In addition, to cope with the divergence of Eq. (5.1) as $B$ tends towards zero (see Section 5.1), an empirical corrected formula (valid for the ITER strands) was introduced by the ITER Team as follows:

$$J_c = \frac{1}{1/J_{c1} + 1/J_{co}} \tag{5.11}$$

where $J_{c1}$ is the value of $J_c$ given by Eq. (5.1) and:

$$J_{c0} = J_{c00}\left(1 - \left(\frac{T}{T_{c0}}\right)^2\right)^2 \tag{5.12}$$

with $J_{c00} = 3.355 \times 10^{10}$ A/m$^2$.

The high value of $J_{c00}$ shows that such a correction is only active at low field, particularly it was found to give better results when compared to TFMC strand experimental values at 4.2 K and low field ($B \leq 8$ T) [90]. Note that this correction is also used in the ITER conductors design [91], but the high level of field (12–13 T) makes it negligible because of a lower $J_{c1}$.

The minimum length step of the mesh has been set to 400 mm, which is roughly equal to the cable twist pitch. Average values are taken over this length, which means that no distinction between main subcables (petals) inside the cable is made. This is consistent with the assumption of equal sharing of current among petals.

The tests results analysis will lead to estimate $\varepsilon$ and so to know $(\varepsilon - \varepsilon_{op}) = (\varepsilon_{th} + \varepsilon_{extra})$. Therefore, another way to deal with this strain is to consider that $\varepsilon_{th}$ is not

known, which is partly true (see Section 5.5), and so to write $\varepsilon$ in the following form:

$$\varepsilon = \varepsilon_o + \varepsilon_{op} \quad (5.10)$$

where $\varepsilon_o = (\varepsilon_{th} + \varepsilon_{extra})$ contains the unknown part of $\varepsilon$.

Note that ENSIC results are directly comparable to M&M results as soon as one takes the same value for $\varepsilon_{th}$ (=−0.61% in M&M).

There are only three free parameters in the model: the strand index $n_{strand}$ in Eq. (5.8), the interstrand resistivity in the conductor $\rho_{t\_cond}$ [70], and $\varepsilon_o$ in Eq. (5.10). However, from AC losses consideration, test results analysis on full-size conductor samples [70], and preliminary analysis of TFMC results [86], the value of $\rho_{t\_cond}$ could be fixed to 25 μΩ m and kept constant for all runs. The remaining two free parameters ($\varepsilon_o$, $n_{strand}$) are then adjusted to best fit the experimental voltage drop measured across the P1.2 pancake as function of the inlet temperature (see Section 5.3.3). Note that the code is also computing the evolution of the voltage drop across the inner joint, which is included in the measured voltage. Thus, not kept constant (i.e., equal to its value at 4.5 K) and corresponding roughly to the measured value.

*5.4.2.2. Data processing.* The ENSIC code performing a steady state calculation is not fully adapted to simulate a time varying experiment as the TFMC $T_{CS}$ measurement, except during temperature plateaus or when the evolutions of temperature are slow enough. As a matter of fact, since only the helium inlet temperature is measured, one can see that the $V(T_{in})$ curves are not single value functions (i.e., different $V$ correspond to the same $T_{in}$), which is mainly due to a much faster decrease than increase of inlet temperature, when no quench occurs (see Fig. 5.4) since during the ramp-down of the heaters the conductor temperature cannot follow instantaneously the fast decrease of $T_{in}$, so that for the same $T_{in}$ a higher voltage is seen along the conductor than during the heater ramp-up. There is however a way to cope partially with this problem and so to improve the relevance of the model, taking advantage of the peculiar case of the TFMC winding. Indeed, the major part of the voltage drop occurs along the first (inner) turn of the P1.2 pancake (see Figs. 5.1 and 5.2), then one can assume that roughly the "useful" inlet temperature $T_{inc}(t)$ associated with a measured voltage drop $V(t)$ at time $t$, correspond to the value of $T_{in}$ at time $(t - t_d)$, where $t_d$ can be assimilated to the time needed by helium to reach the high electric field region. Although this assumption first looks rough, the results turn to be rather unexpectedly good, i.e., using a single value of $t_d$ per test, a single-value function $V(T_{inc})$ can be recovered, including all experimental points within the interesting range of temperature (i.e., over about 1 K, see Fig. 5.18 for example). Note that such a function is thus typical of what could be found in the steady state regime (i.e., elimination of the time variable). Depending on the run (mass flow, temperature), the delay time $t_d$ is ranging from 10 to 20 s, which corresponds to distances of about 4–5 m at the average helium velocity. Besides the previous argument, such an apparent good result using a constant $t_d$ per run is helped by the averaging of $V$ and $T_{in}$ signals over 5 s, by the decrease of the mass flow as $T_{in}$ increases (see Fig. 5.6), and by the noise of the signal (see Fig. 5.16).

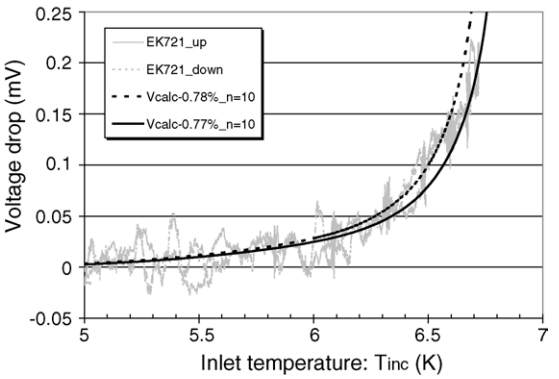


Fig. 5.16. Comparisons of ENSIC simulations (Vcalc, with values of $\varepsilon_o$ and $n$) with experimental DP1.2 voltage drop EK721 for the 80/16 kA run (up is for increasing $T_{in}$, down is for decreasing $T_{in}$), $T_{inc}$ is corrected inlet temperature (see text).

*5.4.2.3. Results.* Because of the low frequency noise remaining after filtering (moving average) in the experimental signals, the definition of a best fit computed curve turns out to be not so obvious, particularly the voltage signal offset (at the accuracy of only 10 μV) proves to have a big impact on the value of the $n_{strand}$ parameter and on $T_{CS}$. On the other hand, the value of $\varepsilon_o$ looks less sensitive to these inaccuracies (see Fig. 5.16).

Once a given set of parameters has been retained, it is easy to extract with the code the distribution of the

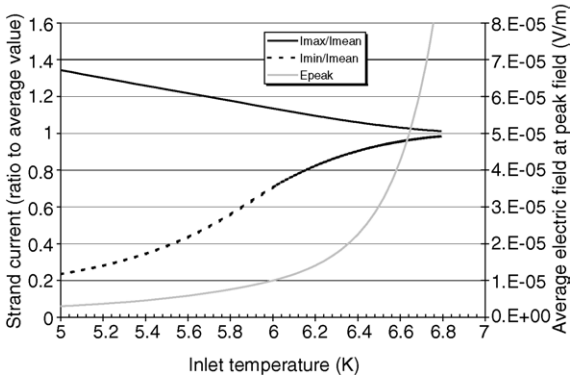


Fig. 5.17. Computed (ENSIC) evolutions of maximum ($I_{max}$) and minimum ($I_{min}$) strand currents with respect to average value ($I_{mean}$), and average electric field at peak field (Epeak) for the 80/16 kA run, with $\varepsilon_o = -0.77\%$ and $n = 10$.

annular region temperature, and of the electric field, along the conductor length. Then one can define a local temperature of current sharing $T_{CS}$ at which the local electric field is 10 μV/m. The first occurrence of this level of field is at the peak magnetic field location (see Figs. 5.1 and 5.2). Note again that the averaging over one cable twist pitch length gives a physical meaning to this definition. The results have been reported in Table 5.2. The error bars take into account uncertainties in voltage signals (offset, noise), and inlet temperature measurement (<0.02 K), in relation with the sensitivity of the calculation.

Since the ENSIC code aims at calculating the current distribution among strands, it looks interesting to check the evolution of this distribution during a $T_{CS}$ experiment. Fig. 5.17 gives the evolutions of the maximum and minimum strand currents, respectively, $I_{max}$ and $I_{min}$ (with respect to average value $I_{mean}$), as well as the value of the average electric field $E_{peak}$ at peak magnetic field, during such an experiment (80/16 kA run). It can be seen in this figure that the unbalance remains low but not quite negligible ($I_{max}/I_{mean} = 1.14$, $I_{min}/I_{mean} = 0.70$) at current sharing temperature ($E_{peak} = 10$ μV/m), while it becomes negligible at $E_{peak} = 50$ μV/m ($I_{max}/I_{mean} = 1.03$, $I_{min}/I_{mean} = 0.96$). The unbalance is lower at lower TFMC currents ($I_{max}/I_{mean} = 1.09$, $I_{min}/I_{mean} = 0.87$, at 10 μV/m for the 49/11 kA run) due to a higher longitudinal resistance at the same electric field.

### 5.5. Assessment of the operation limits of the TFMC conductor

#### 5.5.1. Comparison with strand performance

The assessment of the TFMC performance is made by comparing the behaviour of the coil to that measured on the isolated single strands. However, this exercise turns out to be not so easy because the strain state (i.e., $\varepsilon$) of the $Nb_3Sn$ filaments cannot be the same in the conductor and in an isolated strand. When using strand characteristics as given in Section 5.1, the strain in the isolated strand has been already "removed" and the exercise thus leads to determine $\varepsilon$ in the TFMC conductor (see above). The problem is then restricted to correlate this value of $\varepsilon$ with expectations. It is well known that the differential thermal contraction of the materials composing the conductor (copper, bronze, $Nb_3Sn$, steel) from the heat treatment down to the operating temperature will lead to residual strains in all these components, this is the origin of $\varepsilon_{th}$ in Eq. (5.9). Up to recently, it was considered that $\varepsilon_{th}$ could be estimated using the so-called relaxed fully bonded model [76,92], reducing by 10% the strain given by the fully bonded model (all components bonded) which led in the TFMC case to: $\varepsilon_{th} = 0.90 \times (-0.68)\% = -0.61\%$. This somewhat arbitrary value was recommended for use in the predictive analysis and has been kept as reference also here. As already explained, the operating strain $\varepsilon_{op}$ is calculated from the coil deformation FE analysis, assuming that the jacket deformation is fully transmitted to the $Nb_sSn$ filaments which is slightly inconsistent with the thermal model. Then the entire unknown is reported on $\varepsilon_{extra}$. It is also obvious that local strand deformations such as bending strain [95] and transverse strain due to the electromagnetic forces are not taken into account in ($\varepsilon_{th} + \varepsilon_{op}$), although as already pointed out, formally $\varepsilon_{extra}$ should be incorporated in $\varepsilon_{op}$. In view of such effects, $\varepsilon_{extra}$ has been plotted in Fig. 5.18a) as a function of $I \times B_{max}$, where $I$ is the TFMC current and $B_{max}$ is the maximum field at peak field (see Section 5.5.1.1 for Durham scaling). It can be seen first in this figure that both ENSIC and M&M gives similar results, then that there is roughly a linear decrease of $\varepsilon_{extra}$ (i.e., a degradation of the strand performances) with $I \times B_{max}$. The linear extrapolation to $I \times B_{max} = 0$ is $\varepsilon_{extra\_o} = -0.03\%$, which shows that the design value of $\varepsilon_{th}$ was not unrealistic.

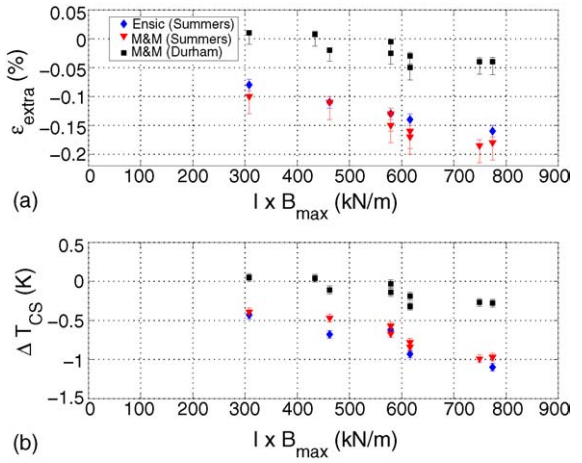


Fig. 5.18. Summary of performance assessment of the TFMC in Phase 2. M&M results computed using the Durham scaling [108] results (squares), M&M results computed using the Summers scaling (triangles), ENSIC results computed using the Summers scaling (diamonds), all assuming $\varepsilon_{th} = -0.61\%$. The error bars for the results computed using the Summers scaling are also reported (M&M error bars were assessed for the highest $I \times B$ and then assumed constant for the other points). (a) $\varepsilon_{extra}$ vs. $I \times B_{max}$ and (b) $\Delta T_{cs} = (T_{cs}^{TFMC} - T_{cs}^{strand})$ vs. $I \times B_{max}$ (see text for details).

A simplified (and conservative) way to estimate the conductor behaviour is to calculate the current sharing temperature at peak field and at: $\varepsilon = \varepsilon_{th} + \varepsilon_{op}$, this method is classically used in superconducting magnet designs [93,76]. However, when the field non-uniformity is high across the cable cross-section and when the strand $n$ value is low as measured in the TFMC, this method may be found too conservative (for a design) or too optimistic (for a performance analysis), and it is better considering the average magnetic field across the cable cross-section, which was roughly taken equal to $B_{center}$ (see Figs. 5.1 and 5.2) in our analysis (see [73] on this subject). The difference $\Delta T_{CS}$ between the $T_{CS}$ measured on the TFMC (P1.2), and the strand $T_{CS}$ evaluated at $B_{center}$ at the location where $T_{CS}$ is actually reached is given in Fig. 5.18b. It can be seen in this figure again the good agreement between the ENSIC and M&M results, as well as a significant degradation of the current sharing temperature as $I \times B_{max}$ increases which has to be related with the evolution of $\varepsilon_{extra}$ with $I \times B_{max}$ as shown in Fig. 5.18a).

The other key parameter for the characterisation of the conductor behaviour is the $n$ index. In Table 5.2 are given both the $T_{CS}$ measured on the coil and the value of the fitting parameter $n$ (with M&M) or $n_{strand}$ (with ENSIC). It can be seen that the values by M&M are in agreement with the values by ENSIC for low TFMC currents ($\leq$61 kA) while ENSIC gives higher values at higher currents due to the non-uniform current distribution among strands (see Section 5.4.2.3). These values can be compared with $n_{strand} \sim 12$–25 (increasing with current) measured on isolated strands [94], showing that the $n$ of the strands in the conductor is significantly smaller (by a factor of $\sim$2) than that of the isolated strand, which cannot be explained by the non-uniformity of the current distribution among strands, and that also $n$ increases with the TFMC current. Such a result could be also explained by local and periodic stress effects [95]. It should be also noted here that the low conductor $n$ index allowed a stable operation of the coil well above $T_{CS}$, although of course this requires additional cooling power to remove the corresponding resistive losses.

*5.5.1.1. Critical re-assessment of the EM strand database.* The TFMC conductor uses a strand produced by Europa Metalli (EM) in Italy.

Until very recently, the characterisation of this strand was mainly performed without mechanically applied compressive strain [75,96], or within a limited or a not assessed range of compressive strain [97,98]. So far, see, e.g. [76,78,83,86,99], the Summers scaling [77] was adopted to extrapolate to the strain conditions relevant to the TFMC, using recommended values of the critical parameters [76].

During the last months, an extensive campaign of characterisation of an isolated EM (TFMC) strand under applied strain has been performed at the University of Durham, UK [100], and the data have been preliminarily fitted using a different parameterization [101] than Summers, as it was not possible to reproduce them with sufficient accuracy using that functional form, see Fig. 5.19. Furthermore, the Summers extrapolation with the recommended parameter values [76] used so far in the TFMC analysis ("historical" fit in Fig. 5.19) significantly overestimates the measured $I_C$ at large compressive strain, while by construction a very good agreement is obtained with the new proposed fit, at all temperatures. Note that the Durham data are consistent with experimental data from other laboratories at zero applied strain (including average cable data), all taken on the so-called ITER barrel [102].

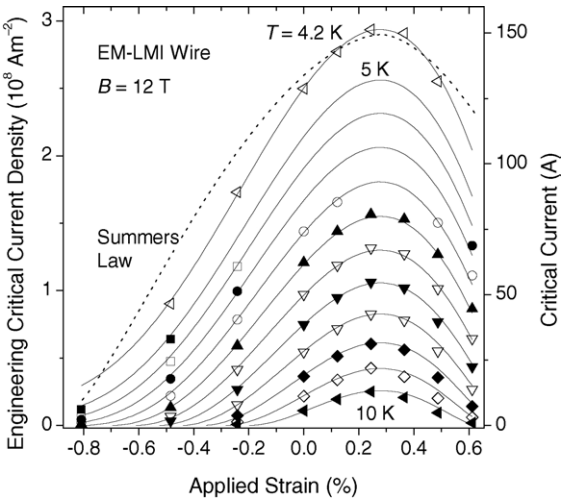


Fig. 5.19. Strand $I_C$ at 4.2 K from [83] (dashed line) and Durham proposed fit (solid lines) as a function of Durham experimental results on mechanical applied strain at 12 T and different temperatures. Electric field criterion at 10 μV/m.

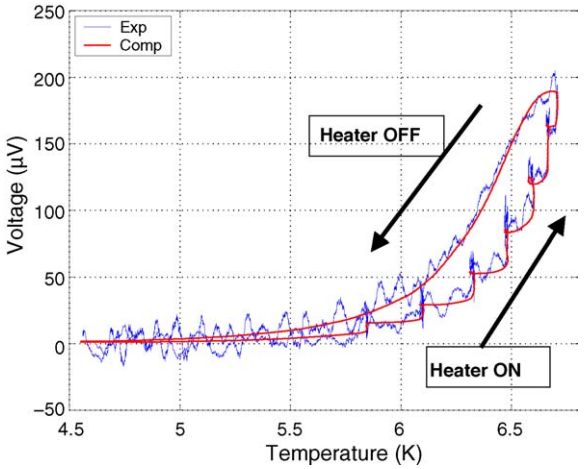


Fig. 5.20. Comparison between measured and M&M computed $V$–$T_{in}$ characteristics of P1.2 using Durham scaling law. Complete transient at 80/16 kA; increasing voltage as the heater is ramped-up, decreasing voltage after heater turn-off.

In Fig. 5.20, results of simulation with M&M, using the Durham scaling, have been plotted versus experimental curves showing the possibility to get also good agreement with this scaling. In Fig. 5.18a, for the sake of comparison, the results based on the Durham scaling are given (taken from [54]). The conductor performance looks then closer to expectations from strand measurements (i.e., $\varepsilon_{extra}$ is closer to 0) than in the analysis using the Summers scaling, although a $I \times B_{max}$ dependence of $\varepsilon_{extra}$ is still there (slope ∼1/2 of that with Summers scaling). However, now the positive values of $\varepsilon_{extra}$ must be related to a too low (compressive) $\varepsilon_{th}$ implicitly assumed here. As a matter of fact, if a linear extrapolation would hold back to $I \times B_{max} = 0$, then one should assume $\varepsilon_{th} \sim -0.5\%$. This value would then imply a large relaxation of strain (minimum 30%) as compared to the fully bonded model, which is not yet understood. Also for Fig. 5.18b similar considerations can be made as for Fig. 5.18a. Note however the discrepancy observed between the points at $\varepsilon_{extra} = 0$ and at $\Delta T_{CS} = 0$ (i.e., they should be equal) which is related to the use of $B_{center}$ as an approximation of the effective magnetic field for calculating $\Delta T_{CS}$ (see [72]). Finally, it should be noted that the $T_{CS}$ measured on the coil and the value of the fitting parameter $n$, as calculated by M&M and reported in Table 5.3, essentially do not depend on the strand scaling.

Based on the implication of the above differences as concerns the knowledge of the strain state of the $Nb_3Sn$

Table 5.3
Summary of M&M results (Phase 2) for the conductor $n$ and $T_{CS}$ at different combinations $I_{TFMC}/I_{LCT}$ using either Summers or Durham parameterization

| Date | $I_{TFMC}$ [kA] | $I_{LCT}$ [kA] | M&M (Summers) | | M&M (Durham) | |
|---|---|---|---|---|---|---|
| | | | $T_{CS}$ [K] | $n$ | $T_{CS}$ [K] | $n$ |
| 9/11/2002 | 60.6 | 13.9 | 8.6 | 6 | 8.5 | 7 |
| 11/11/2002 | 49.5 | 11.3 | 10.0 | 5 | 10.0 | 6 |
| 18/11/2002 | 80 | 14 | 6.3 | 7 | – | – |
| 19/11/2002 | 80 | 0 | 8.3 | 7 | 8.2 | 7 |
| 20/11/2002 | 70 | 16 | 7.2 | 7 | – | – |
| 21/11/2002 | 80 | 16 | 6.0 | 8 | 6.0 | 9 |

filaments in the TFMC (and similar) conductor and as concerns the impact on the ITER coil design, it is clear that an independent confirmation of the Durham data will be desirable since they appear in contradiction with previous experimental results [97,98].

*5.5.1.2. The possible role of bending.* Recent analysis linked to ITER model coils experimental results has suggested that the rough formula used for ITER design were too simple to describe the situation in a CICC and that bending strain can explain at the same time:

- the larger effective compressive strain in CICC;
- the dependency of $\varepsilon_0$ on $I \times B$ even more pronounced in case of low expansion materials like incoloy or titanium;
- the low '$n$' observed in $Nb_3Sn$ CICC.

Mitchell has pioneered this reflection and a review concerning this analysis can be found in [95]. Bending strain in $Nb_3Sn$ has been studied extensively 20 years ago by Ekin [104] at a time when react and wind coils were envisaged. In this study, strands were bent after reaction on mandrels, creating a bending strain, which depends on the mandrel radius. In this situation, the strain over the strand cross-section is no longer uniform but classically presents a gradient around a neutral zone. On the external radius the compressive strain is decreased while it is increased on the internal radius. The results of this academic study are still valid and show that the specific combination of thermal strain and bending strain plays a very important role. Thus, samples with high thermal strain are less sensitive to bending strain. The high thermal compressive strain can be seen even like a protection preventing the strain to go into the tensile region where permanent degradation is expected.

This sensitivity is also linked to the ability of current redistribution inside a strand within a twist pitch to face the strain gradient. The low '$n$' value could be an indication of this process. This ability is very dependent on the strand twist pitch and on the effective matrix electrical resistivity.

In the analysis presented in [95], bending strain is not originated like in Ekin's experiment by the react and wind method.

The twist of the strands in the cable creates a wave whose amplitude is dependent on the overall cabling angle ($\cos\varphi = 0.95$ typically for an ITER cable) and the strands are no longer aligned with the jacket. Due to this wave, even without mechanical loading, the thermal compression originates a complex system of bending strain in a CICC, which is very different from the bonded model. This strain can vary across the strand cross-section and along the strand with a wavelength of typically 5–10 mm. The magnetic forces generate an additional source of bending strain.

A finite element model has been developed to simulate these phenomena [95], which can indicate useful tracks for the cable design. However, this model can only deliver a range of possible performances, which is quite wide, without quantitative dependency, as a complete representative description of such a complex system is hardly possible. Indeed, many mechanical and thermal properties are not sufficiently explored. The role of the void fraction, which is probably important, does not appear explicitly in the model. There is even a doubt about the exact value of differential thermal expansion between steel and $Nb_3Sn$, which is a well-identified factor of the degradation.

The optimum would be to predict the CICC behaviour from the mechanical behaviour of one strand. A code is being developed: a first application has been the successful prediction of the residual thermal strain of the VAC strand [105]. A tendency now is more in favour of a systemic approach: by comparing experimental observation with code prediction of CICC's measured critical current at various tensile loads [99]. This approach will be used in a new R&D programme using the FBI facility to be launched in Europe and can help to identify the driving parameters of the collective behaviour.

In that sense the results obtained on the TFMC were very precious. They brought direct representative information for ITER and allowed to adjust the conductor design in a pragmatic way.

### *5.5.2. Extrapolation to the ITER TF coils*

The ITER TF coils will use a conductor similar to the one of the TFMC but slightly larger (1350 strands instead of 1080 strands). This conductor will operate at a higher maximum magnetic field (11.8 T) than the TFMC one (10.0 and 9.68 T at 80/16 kA on pancake P3.1 and P2.1, respectively) and at a lower current

(68 kA instead of 80 kA). The maximum electromagnetic force on the cable $I \times B_{max}$ will be 802 kN/m against 800 kN/m (on pancake P3.1), and 774 kN/m (on tested pancake P1.2).

One cannot make a direct application of the TFMC results to the ITER TF coils because of the lower level of the operating field, however one can use the results of the analysis (see Fig. 5.20) because the level of $I \times B_{max}$ requires only a short extrapolation (from P1.2). Thus, the value of $(\varepsilon_{th} + \varepsilon_{extra})$ can be (slightly) extrapolated to be about −0.81% (Summers scaling) in the ITER TF coils. In the same way, the conductor $n$ value can be taken conservatively to 7 (see Table 5.3). Also, to be more realistic (but less conservative), it was seen that the average electric field along the conductor should take into account the magnetic field gradient over the cable cross-section [106].

All these considerations have led to modify the original design of the ITER TF coil conductor with the conclusion that a higher performance (critical current density) strand is needed to keep the size of the conductor identical [107]. These performances look quite accessible for the present $Nb_3Sn$ strands and an R&D program has been launched with industrial companies and laboratories to fabricate and qualify such strands.

### 5.6. Summary

The Phase 2 $T_{CS}$ tests of the TFMC DP1.2 conductor were successfully performed at several combinations of $I_{TFMC}$ and $I_{LCT}$, including conditions very close to the cable peak electro-mechanical load, which will be encountered in the full-size coil.

The analysis shows that an equivalent compressive strain (up to −0.18% at full load), possibly due to take into account the strand bending, has to be invoked in order to reconcile the conductor performance with the one of the isolated single strand, evaluated using the Summers scaling. The level of this additional strain is obviously dependent on the expected (or design) strain, which is −0.61% and the scaling law adopted. However, the (linear) extrapolation of the results at zero electromagnetic load $I \times B$ leads to a thermal strain of −0.64% which is close to the expected value given above. Thanks to the design of the TFMC conductor at maximum peak field, the current sharing temperature of the coil was first found to be only slightly degraded compared to the expectations [76,86]. However, considering more realistically an average magnetic field over the cable cross-section, one can show that a remarkable reduction of the temperature margin, more than 1 K at the highest electromechanical load, has been found, which has to be related to an additional compressive strain on the $Nb_3Sn$ filaments. Also the $n$ index of the conductor, which can be deduced from the $V$–$T_{in}$ characteristic, turns out to be more than a factor of 2 smaller than the strand $n$, which cannot be explained by the expected non-uniform current distribution among the strands. This $n$ index still increases with $I_C$ (as in the isolated strand) in spite of the increase of the electromagnetic load.

Recent preliminary data show that the dependence of the TFMC strand critical current on strain could be stronger than expected from Summers scaling. Taking this into account, the analysis of the $T_{CS}$ tests with the M&M code shows that the TFMC performed closer to strand performance than evaluated with Summers (with $\varepsilon = -0.61\%$). An $I \times B$ dependent "degradation" is still present, although about half lower than in previous assessments. However, the extrapolated strain at zero electromagnetic load is then −0.50%, which looks quite low (in absolute value). Therefore, such a result leads to stress the importance of the bending stresses and of the $Nb_3Sn$ strain state in the CICC conductors, as well in the TFMC conductor as in subsize jacketed conductors tested several years ago [97]. In any case, the analysis of the TFMC current sharing temperature tests has confirmed the need to redesign the ITER TF conductor.

Symbols used in equations:

| Symbols | Explanation |
|---|---|
| $a$ | Coefficient used to calculate the influence of the strain $\varepsilon$ on $C_0$, $T_{c0}$ and $B_{c20}$ |
| $A_{nc}$ | Non-copper area in strand ($m^2$) |
| $B$ | Magnetic field modulus (T) |
| $B_\perp$ | Magnetic field component perpendicular to strand (T) |
| $B_{center}$ | Magnetic field at conductor center (T) |
| $B_{max}$ | Maximum magnetic field in cable cross-section (T) |
| $B_{peak}$ | Peak magnetic field on cable in a pancake (T) |
| $B_{c20m}$ | Second critical magnetic field[a] at 0 K and zero strain (T) |
| $B_{c20}$ | Second critical magnetic field[a] at 0 K and strain $\varepsilon$ (T) |
| $B_{c2}$ | Second critical magnetic field[a] at temperature $T$ and strain $\varepsilon$ (T) |

| Symbols | Explanation |
|---|---|
| $C_{00}$ | Coefficient for critical current density calculation at zero strain ($(A/m^2) \times T^{0.5}$) |
| $C_0$ | Coefficient for critical current density calculation at strain $\varepsilon$ ($(A/m^2) \times T^{0.5}$) |
| $E$ | Electric field (V/m) |
| $E_c$ | Electric field at critical current or current sharing temperature (V/m) |
| $E_{peak}$ | Average (among strands) electric field at peak magnetic field (V/m) |
| $E_s$ | Electric field along strand (V/m) |
| $I$ | Current through TFMC coil (A) |
| $I_s$ | Strand current (A) |
| $I_{max}$ | Maximum strand current (A) |
| $I_{mean}$ | Average strand current (A) |
| $I_{min}$ | Minimum strand current (A) |
| $J_c$ | Non-copper critical current density ($A/m^2$) |
| $J_{c00}$ | Non-copper critical current density at zero field and 0 K ($A/m^2$) |
| $J_{c0}$ | Non-copper critical current density at zero field and temperature T ($A/m^2$) |
| $J_{c1}$ | Non-copper critical current density as given by Summers formula ($A/m^2$) |
| $J_s$ | Non-copper operating current density ($A/m^2$) |
| $n$ | Strand $n$ index (cable index in M&M) |
| $n_{strand}$ | Strand $n$ index in ENSIC |
| $t$ | Time (s) |
| $t_d$ | Average helium travel time from inlet to peak field region of P1.2 (s) |
| $T$ | Operating temperature (K) |
| $T_{c0m}$ | Critical temperature at zero field and zero strain (K) |
| $T_{c0}$ | Critical temperature at zero field and strain $\varepsilon$ (K) |
| $T_{CS}$ | Current sharing temperature (K) |
| $T_{in}$ | Helium inlet temperature (K) |
| $T_{inc}$ | Corrected helium inlet temperature versus time to account for helium travel time $t_d$ (K) |
| $V$ | Voltage drop (V) |
| $\varepsilon$ | Longitudinal strain in $Nb_3Sn$ filaments |
| $\varepsilon_{extra}$ | Extra strain in $Nb_3Sn$ filaments (depends on electromagnetic load) |
| $\varepsilon_{extra\_o}$ | Extrapolation of "experimental" $\varepsilon_{extra}$ to zero electromagnetic load |
| $\varepsilon_{op}$ | Operating strain in $Nb_3Sn$ filaments as calculated from coil winding deformation |
| $\varepsilon_o$ | $=\varepsilon - \varepsilon_{op}$: part of the strain in $Nb_3Sn$ filaments to be added to $\varepsilon_{op}$ |
| $\varepsilon_{th}$ | Thermal strain in $Nb_3Sn$ filaments (i.e., strain at zero current) |
| $\rho_{t\_cond}$ | Interstrand resistivity in conductor as used in ENSIC ($\Omega$ m) |

General acronyms, abbreviations, and initialisms are explained in Glossary.

[a] As extrapolated to 0 from critical current curve.

## 6. Electrical losses and thermal-hydraulic properties

### 6.1. Electrical losses

In the TFMC, loss power arises in steady state mainly from thermal losses ($P_{thermal}$), joint resistance losses ($P_{joints}$), but also ripple losses ($P_{ripple}$) due to voltage ripple of the power supply that induces eddy currents in the radial plates. In transient regimes, such as magnet cycling current ramps or safety discharges, electrical losses ($P_{electrical}$) are generated. They include hysteresis losses ($P_{hl}$) and coupling losses ($P_{cl}$) in the conductor, and eddy current losses ($P_{ec}$) generated in the radial plates and in the coil case.

For a given type of transients, the total loss power ($P_{total}$) can be written:

$$P_{total} = P_{thermal} + P_{joints} + P_{electrical} + P_{ripple} \quad (6.1)$$

The various tests performed to measure and discriminate all the categories of losses will be described in the following sections.

Models taking into account the exact shape of the field have been developed to calculate electrical losses in the superconductor as well as those due to eddy currents in the radial plates [108,109].

In the following, all the equations are presented in the international system units (SI), unless differently specified.

#### 6.1.1. Estimation of loss components

In this section, the main attention is given to the three components of $P_{electrical}$. The equations given thereafter are valid only for the TFMC alone carrying a current $I$ without the LCT coil.

##### 6.1.1.1. Hysteresis losses.

$$P_{hl} = \frac{2}{3\pi} d_{eff} S_{nonCu} \int J_{nonCu}(x,t) \frac{dB(x)}{dt} dx = \alpha(I_{max}) \frac{dI}{dt} \quad (6.2)$$

See Table 6.1 for $\alpha$ as a function of $I$.

Integration of (6.2) with time leads to a general equation for hysteresis energy $E_{hl}$, dissipated during a current variation in the coil from 0 to $I_{max}$ or from

Table 6.1
Characteristics for losses in the conductor [142,96]

| Data for $P_{hl}$ and $P_{cl}$ estimation | |
|---|---|
| Non-copper section in the conductor $S_{nonCu}$ [mm$^2$] | 148 |
| Strand section in the conductor $S_{strand}$ [mm$^2$] | 371 |
| Cable time constant ($n\tau$) [ms] | 100 |
| Filament effective diameter $d_{eff}$ [μm] | 36 |
| $\alpha(I)$, respectively, for $I = 25, 40, 80$ kA | 0.44, 0.37, 0.27 |

$I_{max}$ to 0.

$$E_{hl} = \alpha(I_{max})I_{max}$$

*6.1.1.2. Coupling losses in the cable.* The definition of variables in the following equation can be found in Table 6.1.

$$P_{cl} = \frac{1}{\mu_0}(n\tau)S_{strand}\int\left(\frac{dB}{dt}(x)\right)^2 dx = 1.0210^{-4}\left(\frac{dI}{dt}\right)^2 \quad (6.3)$$

A general equation for the coupling loss energy $E_{cl}$, dissipated in the two most frequently encountered cases, is obtained by integrating (6.3):

- an exponential discharge of current from $I_{max}$ to 0 with a time constant $t_d$

$$E_{cl} = \frac{1.0210^{-4}I_{max}^2}{2t_d} \quad (6.4)$$

This equation is valid when $t_d$ is far larger than the time constant $n\tau$ of the cable (about 100 ms)

- a linear increase of current at ($dI/dt$), a plateau at $I_{max}$ and a linear decrease of current at $-(dI/dt)$ (trapezoidal run):

$$E_d = 2.0410^{-4}I_{max}\frac{dI}{dt} \quad (6.5)$$

*6.1.1.3. Eddy current losses in the structure material.* Eddy current loss power is dissipated in the radial plates ($P_p$) and in the casing ($P_c$). It can be given with some approximation by the following simplified equation

Table 6.2
Characteristics for losses in the radial plates and in the case

| Data for $P_p$ and $P_c$ estimation | |
|---|---|
| Mutual inductance $M_{wp}$ | |
| One TFMC turn/total radial plates circuit [μH] | 2.88 |
| Total resistance of radial plates $R_p$ [μΩ] | 27.993 |
| Mutual inductance $M_{wc}$ | |
| One TFMC turn/total case circuit [μH] | 2.055 |
| Total resistance of case $R_c$ [μΩ] | 19.045 |
| Number of turns in the TFMC $N$ | 98 |

(using Table 6.2):

$$P_p = \frac{N^2M_{wp}^2}{R_p}\left(\frac{dI}{dt}\right)^2 = 0.00284\left(\frac{dI}{dt}\right)^2 \quad (6.6a)$$

$$P_c = \frac{N^2M_{wc}^2}{R_c}\left(\frac{dI}{dt}\right)^2 = 0.00213\left(\frac{dI}{dt}\right)^2 \quad (6.6b)$$

Integrating (6.6a,b) it is possible to derive a general equation for the energies $E_p$ and $E_c$, dissipated in the two most encountered cases:

- an exponential discharge of current from $I_{max}$ to 0 with a time constant $t_d$

$$E_p = \frac{2.84 \times 10^{-3}I_{max}^2}{2t_d}$$

$$E_c = \frac{2.13 \times 10^{-3}I_{max}^2}{2t_d} \quad (6.7a,b)$$

This equation is valid when $t_d$ is far larger than the time constant of the radial plates (about 100 ms).

- a linear increase of current at ($dI/dt$), a plateau at $I_{max}$ and a linear decrease of current at $-(dI/dt)$ (trapezoidal run):

$$E_p = 5.68 \times 10^{-3}I_{max}\frac{dI}{dt},$$

$$E_c = 4.26 \times 10^{-3}I_{max}\frac{dI}{dt} \quad (6.8a,b)$$

*6.1.2. Calorimetric measurements*

The scheme of the cooling circuit of the TFMC is illustrated in Section 3 (Fig. 3.13). During the coil operation in the ITER relevant cooling conditions, a supercritical helium circulation pump provided helium

Table 6.3
Loss power in the most important coil components

| Coil component | Name of the virtual channel that stores the related loss power (units: W) | Short-form notation used in the text |
|---|---|---|
| TFMC winding pack | QMFI700A | $W_{wp}$ |
| Pancake P1.1 | QMFI710 | $W_{1.1}$ |
| Pancake P1.2 | QMFI712 | $W_{1.2}$ |
| Pancake P2.1 | QMFI720 | $W_{2.1}$ |
| TFMC case | QMFI800 | $W_{case}$ |

at about 0.3–0.6 MPa and 4.5 K to the coil and the structure. The 10 pancakes (designated Pi.1, Pi.2, $i = 1–5$) and the two bus bars are cooled in parallel.

Taking into account the available sensors (inlet mass-flow, inlet and outlet temperature, pressure), and multiplying the enthalpy variation of helium from inlet to outlet by the mass-flow, it is possible to calculate the apparent dissipated power in the circuit under consideration.

These data are stored by the DAS as virtual channels. Table 6.3 shows the nomenclature of the most important virtual channels (and the short-form notation used in the text) and the related coil component.

Calorimetric calculations are difficult on P1.1 that is instrumented with sensors for measurement of the inlet mass flow, the inlet and outlet temperatures but whose outlet temperature sensor does not reflect the pancake outlet temperature because the latter is measured beyond the joint with the bus bar where substantial heat exchange takes place. As a matter of fact, this bus bar is cooled by fresh helium (see Section 6.1.2.2 for more details). For that reason, most calculations and evaluations have been done on pancake P1.2 because it is similarly instrumented and is not affected by heat exchange at the bus bar joint.

*6.1.2.1. Methodology to be applied to calorimetric measurements.* The virtual loss power channels (QMFI) on the DAS do not provide a perfect image of the instantaneous power dissipated in the coil except in steady state. In transient regimes, a large amount of energy is stored in the helium contained in the cable and in the radial plates. It has also to be taken into account that the circulation time in a pancake at 8 g/s is typically in the range of 500–600 s depending on the temperature.

For a given transient event (e.g., ramping, safety discharge), it is possible to calculate the corresponding dissipated energy by integrating the loss power received from the virtual loss power channels. Note that the initial and final states have to be thermally similar; otherwise some energy can be hidden in a part of the coil.

For instance, for a given transient in current, the method to be applied is to start the integration of the loss power in steady thermal state before current increase and stop it when the thermal situation has come back to the initial one.

*6.1.2.2. Correction to be applied to the virtual loss power $W_{wp}$, due to heat exchange of the side pancakes with the bus bars (BB).*

*6.1.2.2.1. General experimental observations.* As illustrated earlier (Section 6.1.2), the winding pack virtual loss power $W_{wp}$ underestimates the total TFMC loss power because some heat escapes through the P1.1 joint with the BB (and through the P5.2 joint with its BB) since the bus bars are cooled by a separate circuit. In addition, some heat exchange with the case certainly takes place for the side pancakes P1.1 and P5.2. It is not possible to make a direct measurement of this heat on the bus bar circuit, but the amount of lost energy can be evaluated as follows.

It can be observed (Fig. 6.1) that, as expected, at any time, the value of the P1.1 heat load is appreciably smaller than that of P1.2. This difference (DQ) changes continuously during the run because the coil temperature (and the heat transferred to the BB and the coil case) changes according to the heat generated during the various phases of the current evolution. By integrating DQ one obtains the energy lost at each of the two extreme joints to be added to the integral of $W_{wp}$.

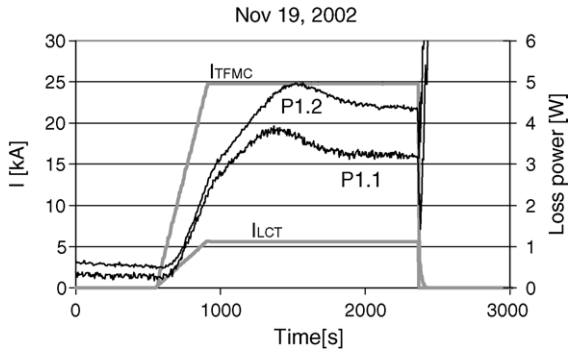


Fig. 6.1. Standard safety discharge No. 2 of Phase 2. Time evolution of the current in the two coils (grey lines) and of the loss power of the pancakes P1.1 and P1.2.

This correction is of the order of some percent (about 7% for runs with a current plateau of 25 kA). It can be expressed as a multiplying factor $K$ of $W_{wp}$:

$$K = \frac{W_{wp} + 2(W_{1.2} - W_{1.1})}{W_{wp}} \tag{6.9}$$

The evolution of $K$ during a typical run is shown in Fig. 6.2. It changes continuously, starting from 1 before the ramp-up, reaching 1.07 on the plateau and finishing at 1 at the end.

To compare runs at different currents, $K$ had to be evaluated at the plateaus of the runs during which the current was kept constant for a long time. The results are shown in Fig. 6.3. The slight increase of $K$ at 80 kA can be attributed to the higher value of the joint resistances of pancake P1.2 in comparison with P1.1 (see

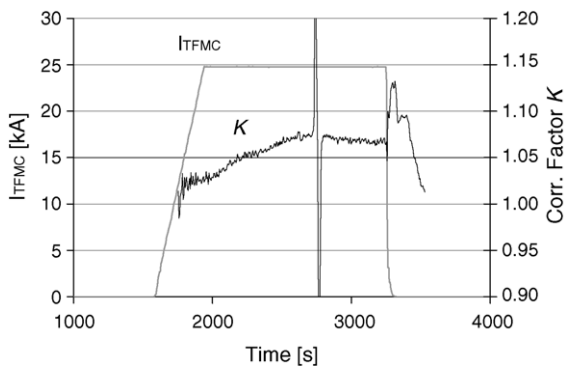


Fig. 6.2. Evolution of the correcting factor $K$ as related to the TFMC current. The spike at about 2700 s is due to a sudden and limited cryogenic instability.

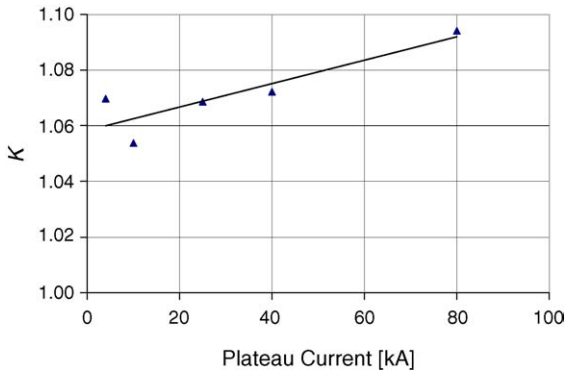


Fig. 6.3. The correcting factor $K$ vs. the TFMC plateau current. The straight line is a linear fit to the data.

Section 6.1.2.4). In practice, $K$ has been taken equal to 1.07 for the calorimetric experiments.

Another way to calculate the correction factor $K$, which is valid if the power is distributed uniformly among the pancakes is:

$$K = \frac{10W_{1.2}}{8W_{1.2} + 2W_{1.1}} \tag{6.10}$$

The two expressions of $K$ give numerically very similar results.

*6.1.2.2.2. Particular case of the heat exchange between P1.2 and P2.1.* The heat exchange at the joint between two pancakes has been also evaluated during a heater scenario test for the $T_{CS}$ measurements at zero current, where only P1.1 and P1.2 were heated by resistors at the pancake inlets. As can be seen in Fig. 6.4, some loss power appears in P2.1 ($W_{2.1}$) because of the heat exchange between P1.2 and P2.1 at

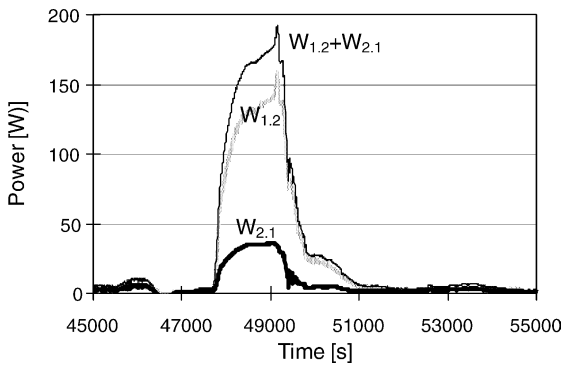


Fig. 6.4. Loss power in pancakes P1.2 ($W_{1.2}$) and P2.1 ($W_{2.1}$) during heating scenario test (05/11/2002).

the outer joint outlet. This heat exchange is similar to the heat exchange between P1.1 and the bus bar (and P5.2 and the other bus bar).

Using the data of Fig. 6.4, a ratio $\chi$ can be defined:

$$\chi = \frac{W_{2.1}}{W_{1.2} + W_{2.1}} = \frac{35W}{172W} \cong 20\% \tag{6.11}$$

which gives an estimation of the power transferred at the joint. Assuming this value for the heat exchange at the P1.1–bus bar joint, and that the power is distributed uniformly among the pancakes, one can evaluate:

$$W_{1.1} = (1 - \chi)W_{1.2} \tag{6.12}$$

and from Eq. (6.10) is obtained:

$$K = 1.04 \tag{6.13}$$

The heat exchange with the TFMC case is probably higher for the side pancakes, which can explain the higher values of $K$ in Section 6.1.2.2.1.

*6.1.2.3. Thermal losses $P_{thermal}$.* Even at zero current, some loss power is visible in the virtual channels of $W_{wp}$ and $W_{1.2}$.

This loss power can be due to the thermal loss power (radiative and conductive) imposed on the coil because it is not perfectly insulated from the exterior. It is not perfectly constant with time and some fluctuation is visible (see Fig. 6.5).

A typical value of the thermal loss power is about 15 W for steady state winding pack loss power ($W_{wp}$) and 0.6 W for pancake P1.2 loss power ($W_{1.2}$). It should be noted that there is more than a factor of 10 difference between the two values. A more detailed analysis shows a large variation between the loss power of the different pancakes at zero current. It can therefore be concluded that this loss power is not a perfect image of the thermal losses due to lack of precision in the estimation of the very small temperature increase. This power loss will be subtracted in the following analysis.

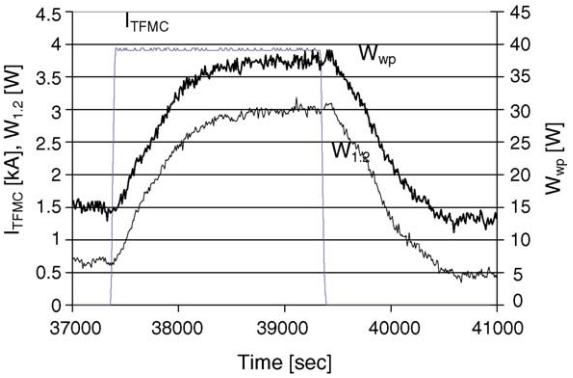


Fig. 6.5. Loss power of pancake P1.2 ($W_{1.2}$) and winding pack ($W_{wp}$) due to the ripple of the power supply as a function of time (31/07/2001 experiment).

*6.1.2.4. Resistive losses $P_{joint}$.* A detailed description of the joints behaviour is given in Section 7.1.

It can be considered for this section that the resistive loss power due to the joints at a given current $I_{TFMC}$ in the coil reads as follows:

$$P_{pancake} = R_{pancake} \cdot (I_{TFMC})^2 \tag{6.14}$$

$$R_{pancake} = \frac{R_{inner} + R_{outer}}{2} \tag{6.15}$$

$R_{inner}$ and $R_{outer}$ are the inner and the outer joint resistances, respectively, for a given pancake such as P1.2. The total resistance of the coil $R_{TFMC}$ is the sum of all joint resistances of the 10 pancakes.

Values of the pancakes joint resistance, estimated by calorimetry, are reported in Section 7. In accordance with the heat exchange effect described in Section 6.1.2.2, the amplification coefficient 1.07 has been applied to correct the resistance of P1.1 and P5.2.

The following values are used in the analysis:

$$R_{P1.1} = 1.19\,n\Omega \tag{6.16}$$

$$R_{P1.2} = 1.62\,n\Omega \tag{6.17}$$

$$R_{TFMC} = 13.12\,n\Omega \tag{6.18}$$

*6.1.3. Losses due to the ripple of the power supply*

The power supply used for the tests of the TFMC is a 12-pulse thyristor converter. Oscillations at 600 Hz are present in the supply voltage and this ripple induces eddy currents in the radial plates, generating heat that is transferred to the conductor.

This phenomenon was not known beforehand and was discovered at the beginning of the TFMC experiment.

It was confirmed in an experiment performed at a very low current (4 kA) and presented in Fig. 6.5.

As soon as the power supply is connected, the temperature of the plates starts rising. This rise continues

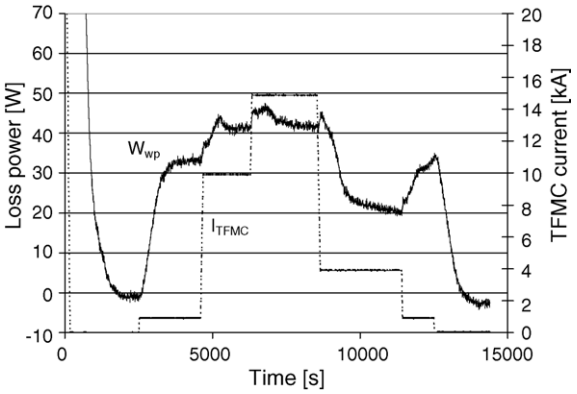


Fig. 6.6. Loss power of the TFMC winding pack due to the ripple of the power supply in the low current range.

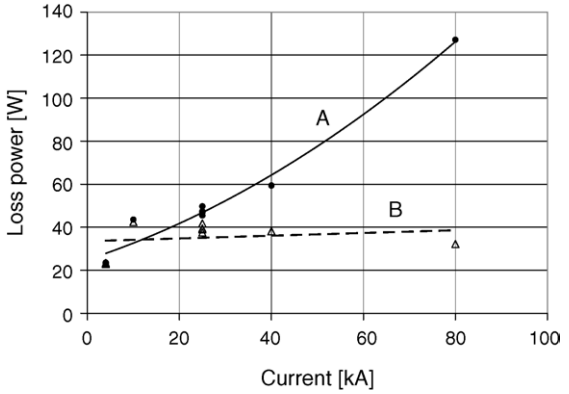


Fig. 6.7. Loss power in the winding pack ($W_{wp}$) in steady conditions vs. plateau current. (A) Corrected $W_{wp}$ (see text, Section 6.1.3.1). (B) Calculated contribution due to the ripple of the power supply.

until an equilibrium is reached (at a temperature $T_{max}$ that is unknown since there are no temperature sensors placed in the plates) at which the heat produced equals that transferred to the coolant.

Up to 15 kA, the heat produced by the joints resistance is negligible (<3 W for all the joints of the coil). Thus, in this range of current, after a thermal transient associated with the circulating time of helium along the pancakes, the ripple loss power is visible (Fig. 6.6) associated with a plateau in power. The ripple loss power varies slightly as a function of the current in a way which is not understood and probably linked to the power supply thyristors regulation. Thus, the ripple power at 1 kA is around 32 W and the ripple power at 4 kA is lower around 20 W

*6.1.3.1. Impact of ripple on calorimetric measurements at different currents.* As described in Section 6.1.2, the measured loss power of the winding pack ($W_{wp}$) must be corrected by subtracting $P_{thermal}$ (thermal losses due to conduction and radiation, Section 6.1.2.3) and the heat transferred by conduction to the bus bars. In steady state conditions (current plateau, after ramping up) this corrected loss power is the sum of heat generated by the joints resistance and that due to the ripple of the power supply. The resistance of the joints has been separately measured and its dependence on the magnetic field is known (Section 7.1) hence the heat generated at any current can be calculated. By subtracting this value from the total, the contribution of the ripple can be evaluated. Fig. 6.7 shows the corrected value of $W_{wp}$ measured on the plateau of runs at different coil currents up to 80 kA and the calculated loss power due to the ripple. It can be seen that the loss power due to the ripple is roughly constant (around 40 W) in the range of current between 10 and 80 kA.

*6.1.4. Trapezoidal pulses and cycling*

*6.1.4.1. Trapezoidal pulses.* For trapezoidal pulses, practical equations for the dissipated energy have been given in Section 6.1.1:

- by eddy current losses in the radial plates $E_p$;
- by hysteretic losses in the conductor $E_{hl}$;
- by coupling losses in the conductor $E_{cl}$.

Trapezoidal pulses at 40 kA plateau have been carried out on the TFMC at different current rates (100–1000 A/s) to discriminate the various categories of losses.

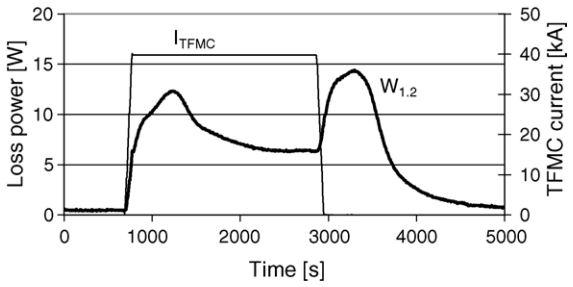


Fig. 6.8. Apparent loss power dissipated in pancake P1.2 ($W_{1.2}$) during a trapezoidal shot run at 500 A/s (30/07/2001 experiment).

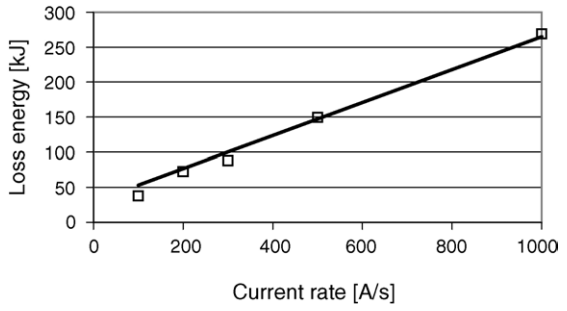


Fig. 6.9. Loss energy of the TFMC winding pack during trapezoidal runs performed at different current ramp rates. Squares: experimental points; line: model.

The apparent loss power is presented in Fig. 6.8. Comparison between the model and experimental results are presented in Figs. 6.9 and 6.10.

According to Table 6.4, it can be seen that the coupling losses are very small in comparison with radial plate eddy current losses. No information can therefore be obtained from this experiment about the conductor time constant $n\tau$. Radial plate losses and hysteretic losses are in good agreement with the models.

*6.1.4.2. Behaviour of TFMC during cycling.* The continuous triangular cycling of the TFMC at different current levels and different current ramp rates brought a confirmation of the fact that the model was quite efficient in describing the loss power mechanism in the winding pack as well as in the case.

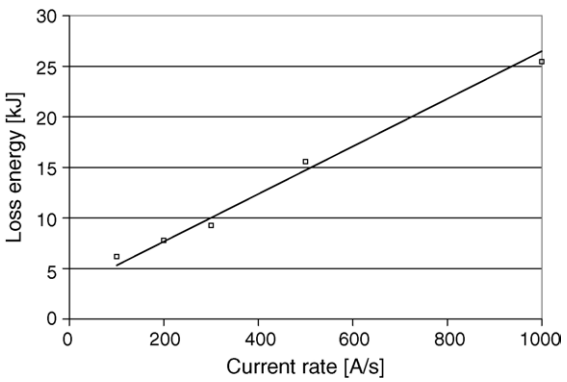


Fig. 6.10. Loss energy of pancake P1.2 during trapezoidal runs performed at different current ramp rates. Squares: experimental points; line: model.

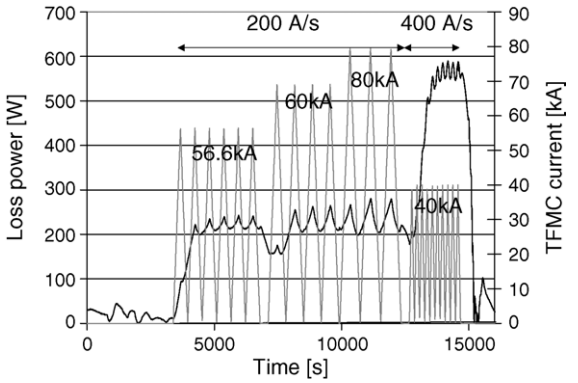


Fig. 6.11. Loss power in TFMC winding pack ($W_{wp}$) during cycling (15/09/2001 experiment); black line: $W_{wp}$; grey line: TFMC current.

*6.1.4.2.1. Winding pack losses.* Fig. 6.11 shows a run during which the TFMC current was cycled at 200 A/s for three different values of the current (time up to about 13000 s) and then at 400 A/s at a current of 40 kA. The cycles are triangular in shape. The AC components shown by the measured loss power are in phase with the current and the amplitudes are proportional to $I^2$. They can be attributed to the Joule losses at the outer joints, whose dissipation is immediately visible on the apparent loss power because they are situated hydraulically at the outlet of the circuit. The measured loss power is practically independent of the current value. Its dominant component $P_p$ is proportional to $(dI/dt)^2$.

At 40 kA plateau and 400 A/s, the respective calculated contributions of $P_{joint}$ (average), $P_{ripple}$, $P_{hl}$ and $P_p$ are 10.5 (average), 40, 148 and 454 W giving a total of 653 W, that is typically 10% higher than the measured loss power. The $P_p$ contribution is dominant and the coupling losses contribution is negligible.

*6.1.4.2.2. Case losses.* The measured loss power in the coil casing ($P_c$) during the TFMC cycling, presented in Fig. 6.12 (test of 25th September 2001, without LCT coil), are in good agreement with the equations. In steady state loss power is eliminated by the He mass flow circulation in the case channels. In the case the corresponding thermal flux is linked to a thermal gradient through the case thickness. The time constant $\tau$ to establish the steady state is associated with the necessary time to heat the edge of the case (temperature $T_{edge}$) and establish the relevant temperature gradient through the case steel thickness.

Table 6.4
Losses decomposition according to model for a trapezoidal run at 1000 A/s and a plateau of 40 kA

| | Hysteretic losses [kJ] | Coupling losses [kJ] | Radial plates losses [kJ] | Total [kJ] |
|---|---|---|---|---|
| TFMC | 29.6 | 8.2 | 227.2 | 265 |
| P1.2 | 2.96 | 0.82 | 22.7 | 26.5 |

$\tau$ is a function of $P_c$, and the steady state has not been reached as visible at 400 A/s in Fig. 6.12. This time constant is larger than that for the winding pack.

$m_{ss}$ is the mass of the case. $C_{p,ss}$ is the case specific heat. The corresponding equation driving $\tau$ is the following, but no complete calculation has been done.

$$P_c\tau = m_{ss}\int_{T_0}^{T_{edge}} C_{p,ss}(T_{ss})\mathrm{d}T_{ss} \quad (6.19)$$

At 200 A/s, the measurement gives 65 W for the minimum value that has to be compared to the prediction of 85 W.

Peaks in the loss power signals are again visible like those for the winding pack (but this time they are not in phase with the current), which is surprising because in the casing there is no loss power contribution that is immediately visible as in the winding pack. Helium in the winding pack and in the casing is circulating in parallel, there therefore can be no link between conductor losses and casing losses.

### 6.1.5. Losses at high field ramp rate

The field ramp rate d$B$/d$t$ during the trapezoidal pulses is relatively low. As a consequence the amount of coupling losses (CL) is negligible with respect to the hysteresis (HL) and eddy current losses in the radial plates (ECL). For a global validation of the losses models, described in Section 6.1.1 and in [110], it is therefore necessary to perform tests at higher d$B$/d$t$, during which the CL are at least comparable to the HL. This can be achieved by discharging the stored magnetic energy into the protection resistor with an exponential current decay of time constant $\tau$. In this case, the highest value of d$B$/d$t$ is generated at the beginning of the discharge and can be calculated as: $(\mathrm{d}B/\mathrm{d}t)_{max.} = B_{plateau}/\tau$. There is a limit for these tests because of the large amount of heat generated which becomes unacceptable for the helium pumps cooling system. At currents higher than this limit (25 kA), the valves that connect the coil to the pumps cooling system were automatically closed before initiating the discharge and the expelled He was relieved in a cold storage vessel. The measurement of the losses power, which is performed calorimetrically, is then impossible. As a typical value of $\tau$ is 4 s, the maximum value of d$B$/d$t$ is about 0.6 T/s.

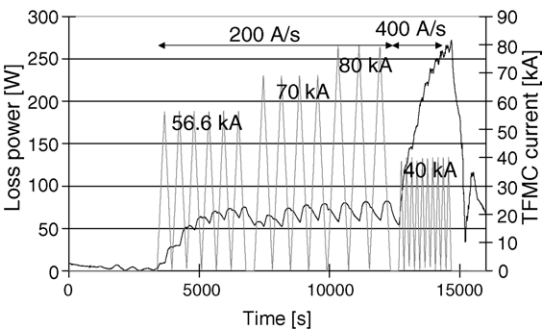


Fig. 6.12. Loss power in TFMC case ($W_{case}$) during cycling (25/09/2001 experiment); black line: $W_{case}$; grey line: TFMC current.

Unfortunately, the increase of d$B$/d$t$ results also in bigger ECL (both CL and ECL are proportional to the square of d$B$/d$t$), which remain at least one order of magnitude higher than the HL and CL.

From these tests, it is not possible to obtain separately the values of HL, CL and ECL. The comparison with the model can then be done only on the basis of the total heat generated. However, the next section describes how this type of measurement allows the study of the CL evolution during the test campaign.

*6.1.5.1. The 25 kA "standard safety discharge".* Some years ago, pulsed tests of a relatively large coil [111] demonstrated that the amount of coupling losses in the CIC conductor was not constant, but was a decreasing function of the number of the coil charges. The decrease was rather large (a factor 3) and saturated after many cycles.

This phenomenon was attributed to the Lorentz force that compresses the cable at each charge as it was described in [112–114]. This continuous little move-

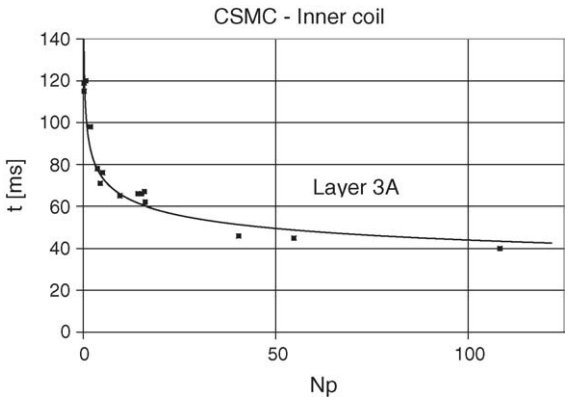


Fig. 6.13. Evolution of the coupling loss time constant $\tau$ of the layer 3A of the CSMC during the test campaign.

ment increases the inter-strands resistivity and consequently the coupling losses decrease.

Also the tests of the ITER CS Model Coil (Naka, Japan) showed very clearly that the coupling losses decreased monotonically during the test campaign [115,116]. The different layers of the coil showed, in the virgin state, quite different values of the coupling loss constant $\tau$, ranging from about 100 to about 300 ms. After a number of charges of the order of 15–30, all of them tend to saturate to a value close to 50 ms. An example is shown in Fig. 6.13. These results are consistent with measurements of the AC loss and inter-strand contact resistance on short samples [113].

In the case of the TFMC, the detection of this phenomenon is much more difficult because, as illustrated previously, the coupling losses are expected to be only 3–4% of the total. For this reason, the concept of "standard safety discharge" was developed. The idea is that of repeating exactly the same safety discharge from time to time during the test campaign. As the losses due to the HL in the conductor and the ECL in the radial plates remain the same, if a change in the total energy is detected, it can be attributed to a change in the conductor coupling losses. Only by using identical SSD this small change can be detected, as these runs can be compared relatively to each other, without involving absolute values of the different parameters, which would produce unacceptable errors. The comparison is affected only by the reproducibility error of a few sensors ($T$, $P$, mass flow and current).

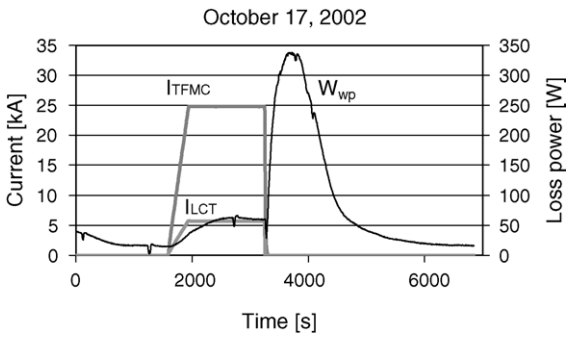


Fig. 6.14. Standard safety discharge No. 1 of Phase 2. Time evolution of the current in the two coils (grey lines) and of the total TFMC winding pack loss power ($W_{wp}$).

*6.1.5.2. Calorimetric measurements.* Fig. 6.14 shows the evolution of the currents in the coils during a run of Phase 2 and the related total TFMC loss power $W_{wp}$. According to what was discussed in the Section 6.1.2, the following procedure has been applied (details in [117]).

(a) Subtraction of the constant power due to conduction and radiation.
(b) Integration of $W_{wp}$ from the start of the current ramp to the end of the run which is normally chosen to be long enough (typically 3600 s after the dump) to guarantee that all the heat has come out of the coil. Actually, it was calculated [118] that the time constant for the transfer of heat between the radial plates and the conductor through the thick insulation is about 200 s. A value of energy $E_{wp}$ is thus obtained.
(c) Correction of $E_{wp}$ by the multiplying factor $K$, to account for the heat exchange to the bus bars.
(d) Subtraction of the heat generated by the joints (including the half joints between the coil and the bus bars) that can be calculated since the resistance of the joints is known.
(e) Subtraction of the heat generated in the radial plates by the ripple of the power supply (see Section 6.1.3). When the dump is initiated (and the noise of the power supply disappears) all the heat accumulated in the radial plates is transferred to the coolant with a time constant of 200 s.

What remains is the sum of the loss energy $E_{tot}$ due to HL, CL and ECL (total AC losses) and can be compared to the results of the theoretical calculations.

Table 6.5
Results of the total AC losses energy measurements and calculations

| | Run # | Date | $N_p$ | $E_{tot}$ [kJ] |
|---|---|---|---|---|
| Phase 1 | 60 | August 02, 2001 | 16.1 | 245 |
| Phase 1 | 78 | September 14, 2001 | 21.4 | 236 |
| Phase 1 | 111 | September 24, 2001 | 34.9 | 235 |
| Phase 1 | 120 | September 26, 2001 | 49.1 | 236 |
| Phase 2 | 172 | October 17, 2002 | 56.1 | 319 |
| Phase 2 | 216 | November 19, 2002 | 94.8 | 316 |
| Calculated values [115]: | | | | |
| Phase 1 | | | | 232 |
| Phase 2 | | | | 335 |

*6.1.5.3. Results.* As mentioned previously, the tests of the TFMC were performed in two phases.

In Phase 1, the SSD consisted of a safety discharge of the TFMC alone from 25 kA [119]. In Phase 2, the TFMC was still discharged from 25 kA, but simultaneously the LCT coil was discharged from 5.77 kA. The total field as well as the field rate were then appreciably higher than in Phase 1 and larger losses were produced. This gave the opportunity to compare the results and the calculations in two different conditions.

The results are reported in Table 6.5 and in Fig. 6.15. The total measured and calculated energy due to AC losses is plotted as a function of the number of coil charges $N_p$. This is calculated as the summation, over all the coil charges, of the normalized Lorentz force:

$$N_p(i) = N_p(i-1) + \frac{B_i \cdot I_i}{B_{max} \cdot I_{max}} \tag{6.20}$$

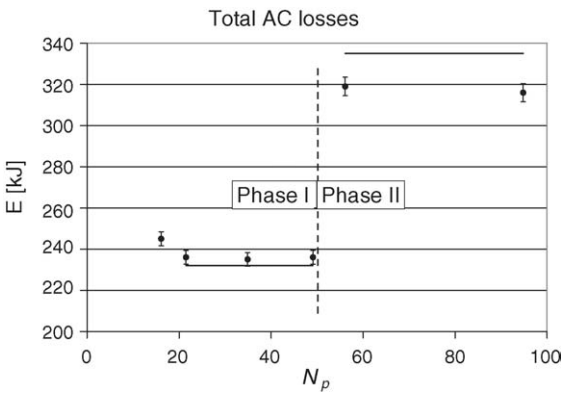


Fig. 6.15. Total AC loss energy $E_{tot}$ in the TFMC superconducting cable. Experimental (dots) and theoretical data (full lines).

where $i$ indicated the $i$-th run, $I_i$ is the corresponding current in the TFMC and $B_i$ is the corresponding flux density experienced by the TFMC (self-field in Phase 1, field due to the two coils in Phase 2).

It can be seen that, for the total loss energy, the agreement between calculations and experimental data is good: within 1.7% for Phase 1 and 5–6% for Phase 2.

*6.1.5.4. Coupling loss evolution.* Examining in detail the experimental points of Fig. 6.15 (Phase 1), one can see that the first point is appreciably higher than the other three, which are very well aligned. This seems to confirm the usual decrease of the CL during the test campaign, followed by saturation (Section 6.1.5.1). Unfortunately, it was not possible for the TFMC campaign to start this type of measurements at values of $N_p$ lower than 16, where, according to the previous experiences, the difference with respect to the plateau should have been much more evident.

The two points of Phase 2 are aligned within the error bar, despite of the large difference in $N_p$, and this confirms that no further evolution has occurred.

These conclusions are supported by the short sample measurements that have been performed on a piece of TFMC conductor, that clearly show the increase of the inter-strand contact resistance and associated decrease of the coupling loss from the virgin state towards saturation during the first several tens of cycles [114].

*6.1.6. Summary*

During the operation of the TFMC at low temperature the coolant must remove from the coil an appreciable amount of heat, which is either conducted to it or generated in the coil itself by several different sources. During both Phase 1 and Phase 2 different tests have been performed to discriminate and measure, by the calorimetric method, the various contributions to these losses. The three main components are developed during transient regimes: those due to eddy currents generated in the structure (radial plates; coil case) and those generated inside the superconducting cable itself: coupling and hysteresis losses. Models have been developed to calculate these contributions and a good agreement was found between measurements and calculations for all the different transient regimes during Phase 1 (within 1.7% in the case of safety discharges)

and during Phase 2 (within 6%). The tests of the TFMC allowed the characterisation of another source of loss, unidentified beforehand, due to the current ripple of the power supply. Also in this case the measurements are in good agreement with calculations (within 15%). These results confirm that the available models can be confidently applied to predict the behaviour of the ITER TF magnets.

### 6.2. Thermal-hydraulic properties

#### 6.2.1. Pressure drop

*6.2.1.1. General behaviour.* Thermal-hydraulics has played a major role in the ITER TFMC test and analysis [120]. The two test campaigns of Phases 1 and 2 resulted in the fact that a significant amount of ITER-relevant information, ranging from the current sharing temperature to AC losses, could be extracted from the analysis of the TFMC performance. To make this possible, notwithstanding the fact that all diagnostics were located outside the coil, a suitable understanding of the thermal-hydraulics in the coil was needed [83,78,122,123].

Besides the issues considered in this section, other items of relevant thermal-hydraulic interest have already been considered elsewhere (e.g., the issue of heat generation and exchange in the joints [124,80], or the effects of the resistive heaters on the helium dynamics in the coil [125]). Details about the major thermal-hydraulic issues (pressure drop and quench in particular) in the TFMC are given in [53].

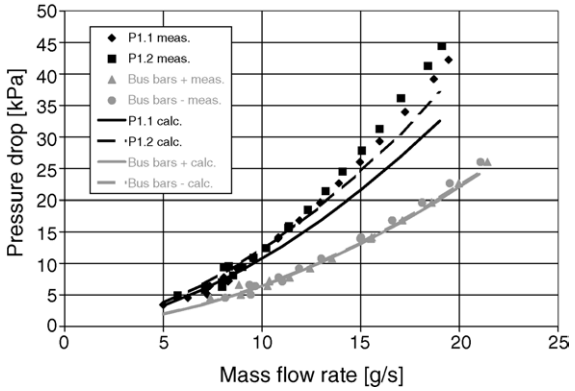


Fig. 6.16. Pressure drop for the TFMC pancakes P1.1 and P1.2 and positive and negative side bus bars.

Fig. 3.13 shows a schematic cooling circuit of the TFMC. The hydraulic resistance measurements method is presented in more details in [127]. Mass flow rate measurements were performed on the pancakes P1.1 and P1.2 of DP1, the double pancakes DP2, DP3, DP4 and DP5 and in the two superconducting bus bars ((+) and (−)). Pressure drop measurements were performed on P1.1 and P1.2. Differential pressure transducer across the pancakes and temperature sensors at the inlet and outlet of the conductor in the cooling path are installed. The major hydraulic parameters for the different TFMC conductors are summarised in Table 6.6.

The pressure drop measurements are presented for the pancakes P1.1 and P1.2 in Fig. 6.16 and compared

Table 6.6
TFMC DP1, bus bars CS-type (NbTi) and TFMC bus bar joint conductor hydraulic parameters

| | TFMC DP1 conductor | Bus bars CS-type conductor | TFMC bus bar joint |
|---|---|---|---|
| Cable cross-section without jacket [mm$^2$] | 1097.2 | 1176.3 | 893.7 |
| Total strands section ($S_{strands}$)[a] [mm$^2$] | 579.11 | 593.62 | 579.11 |
| Bundle region helium cross-section ($S_{heb}$)[a] [mm$^2$] | 355.2 | 366.34 | 201.5 |
| Void fraction [%] | 36.85 | 35.36 | 25.8 |
| Bundle wetted perimeter (the whole strands) (Ub)[a] [m] | 3.193 | 3.149 | 3.137 |
| Bundle hydraulic diameter ($D_{hb}$)[a] [mm] | 0.445 | 0.465 | 0.257 |
| Hole hydraulic diameter ($D_{hh}$)[s] [mm], inner/outer diameter | 12, spiral 10/12 | 12, spiral 10/12 | 6, tube 6/12 |
| Diameter of quench detection wire [mm] | No | 3.5 (1 and 2) | 3.5 |
| Helium section in the central hole ($S_{heh}$)[a] [mm$^2$] | 113.1 | 103.47 | 18.65 |
| Conductor length $L$ [m] for bus bars type 1 and 2: positive side (+), negative side (−) | 72.2 for P1.1; 82 for P1.2 | 7.57(1+), 8.07 (1−), 2.627 (2+ and 2−) | 0.595 |

[a] Parameter names for the GANDALF input.

to calculations performed with models using friction factor correlation defined in Eq. (6.21). The bundle region friction factor is expressed in [128] and previous experiments [129] give a very similar expression (6.22). The central channel friction factor was determined in [130,131]: Eq. (6.23) gives the central channel friction factor for the Showa spiral, which is used as the central channel envelope in double pancakes DP1 and DP5; Eq. (6.24) gives the central channel friction factor for the Cortaillod spiral, which is used in double pancakes DP2, DP3 and DP4. The joints regions give no significant contribution to the global pressure drop [131]. These correlations (6.22)–(6.24) are those presented in the ITER design criteria [132] (note that the relation for the wetted perimeter in the ITER design criteria includes a factor 5/6, instead of 1 which is the correct value [91]). For spirals as envelopes of central channels, an implicit correlation of friction factor is given in [133] as a function of dimensionless combinations of all relevant geometrical parameters (helix gap, thickness, gap length to thickness ratio). This correlation was applied/validated in [135,136]. The main difference between the two pancakes P1.1 and P1.2 comes from different conductor lengths. The central channel geometry as well as the test conditions has an important effect on the hydraulic resistance of the conductor and its mass flow rate distribution.

$$\Delta P_{\mathrm{He}} = f_{\mathrm{EU}} \frac{\rho v^2}{2} \frac{L}{Dh} \tag{6.21}$$

Bundle channel :

$$4 f_{\mathrm{US}} = f_{\mathrm{EU}} = \left(\frac{1}{\mathrm{void}}\right)^{0.742} \times (0.0231 + 19.5/Re^{0.7953}) \tag{6.22}$$

$$\text{Showa spiral}: \quad f_{\mathrm{EU,SHO}} = 0.3024 Re^{-0.0707} \tag{6.23}$$

$$\text{Cortaillod spiral}: \quad f_{\mathrm{EU,COR}} = 0.7391 Re^{-0.1083} \tag{6.24}$$

$$\text{Smooth tube}: \quad f_{\mathrm{EU,ST}} = 0.184 Re^{-0.2} \tag{6.25}$$

Note that the friction factor definitions used in EU and US differ by a factor of 4! This is important if comparing friction factor relations from different sources.

Fig. 6.16 also shows the pressure drop measurements of pancakes P1.1, P1.2 and the superconducting bus bars in comparison with calculated values. The hydraulic circuit model of the superconducting bus bars (BB) (see Fig. 3.13) comprises in series: pancake terminal/BB1 first joint, BB1 conductor, BB1/BB2 second joint, BB2 conductor, and BB2/currents leads third joint. The thermal-hydraulic parameters of pancakes P1.1 and P1.2 and BB conductors are summarised in Table 6.6. The smooth tube correlation (6.25) is used for the bus bars where the quench detection wires induce a drastic helium cross-section reduction: for the negative side, at a mass flow rate of 20 g/s, the pressure drops are measured to be 5370 Pa in BB1 and 1845 Pa in BB2. The mean value of the calculated pressure drop is about 4200 Pa in each BB joint. In the ITER relevant cooling conditions at 4.5 K, 43.6% of the helium circulates in the bundle channel in case of bus bar conductor and 49.4% in the bus bar joints.

The agreement between the measurements and the calculated values (Fig. 6.16) is good for the bus bars and reasonable for the coil pancakes and confirms that the developed hydraulic models are suitable. The pressure drop at extended mass flow conditions, i.e., at 18 g/s, is underestimated by about 25%. On the other hand, for ITER conditions, i.e., at 10 g/s, the agreement is good.

As opposed to, e.g., the case of the central solenoid insert coils (CSIC) or the central solenoid model coil (CSMC) where a relatively large fraction of the conductor is at high field, and therefore subject to a high electromechanical load, which could deform the cable [136,113], the peak field region in the TFMC is only 1–2 m long, i.e., much shorter than a pancake length (∼70–80 m). It is therefore to be expected that operation with transport current should not significantly affect the hydraulic characteristic as it was confirmed, within error bars, during the tests.

*6.2.1.2. Further investigations.* More detailed investigations have shown [53] that the use of the relationships given in the ITER design criteria might not be sufficient to describe the friction factors of the ITER type conductors for both the cable space and the central channel. For example, the global friction data may indicate some effect of curvature. Qualitatively, this should be relevant for the hole and irrelevant for the bundle, but a quantitative assessment is difficult. On the

other hand, if using the central channel friction factor $f_H$ deduced from the spiral tests [133] (already successfully applied/validated for the case of the CSMC straight sample [136]) for the analysis of the TFMC Phases 1 and 2 data, those data can then be fitted with very good agreement, see [53], over a wide range of mass flow rates by using the Katheder correlation [128] for the bundle friction with an ad-hoc multiplier (∼2.4). Such a large multiplier cannot be explained from first principles (a much smaller multiplier, ∼1.35, was needed for the CSMC straight sample [133]). It could be related to a number of presently not quantified effects, as seen above: wrappings, conductor curvature, etc. In conclusion, it is clear, however, that the agreement between the present ITER design criteria (the bundle region friction factor $f_B$ deduced from the TFMC straight sample data, $f_H$ from the spiral data) and the TFMC data can certainly be improved, and that the predictions of the design criteria are not conservative (actual pressure gradient underestimated by ∼25%).

### 6.2.2. *Thermal-hydraulics of quench and safety discharge*

*6.2.2.1. Quench behaviour.* In test Phase 1, the quench behaviour of the TFMC was clearer because only one coil was installed in the TOSKA vacuum vessel. Compared to the expectations the first observation was that the discharge time constant of the coil at nominal current was not 4 s but about 3 s. The reason is that during the energy dump of the coil, the dump resistor heats up leading to a higher resistance. At lower currents, the effect was smaller because the heating was less. Fig. 6.17 shows the measured coil current versus time during the discharge for different current plateau levels.

As already presented in Section 5, 10 quenches have been produced in P1.2 during test Phase 1 and 3 quenches during test Phase 2 during the $T_{CS}$ measurements at different current levels. If looking to the compensated voltage signals along the pancake, a large spread of its maximum at 80 kA was observed. During the exponential current decay of the safety discharge, the compensated voltage is composed of the normal zone resistive voltage and a small inductive voltage (about 0.2 V maximum, caused by small a residual inductance), which can be neglected. In a first approximation, the voltage level is a function of the normal zone length (resistance). The compensated voltage trace shows large fluctuations, at least for the same current, which means that the quench evolution was not reproducible.

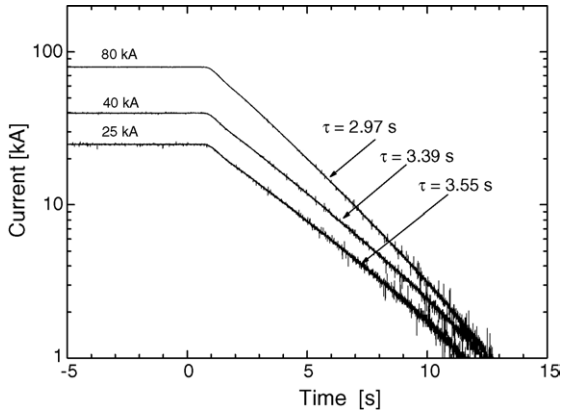


Fig. 6.17. TFMC current vs. time during coil discharge for different current plateaus.

Fig. 6.18 shows the measured compensated voltage versus time. The top figure shows the evolution with time including the safety discharge for selected quenches produced during test Phases 1 and 2 whereas the bottom one shows the voltage traces for the same quenches performed but only at the beginning of the quench before the triggering of the safety discharge ($t = 0$). The maximum voltage occurred always at the same time after the quench trigger was set. The maximum temperature at the inlet of P1.2 occurred about 5–10 s after triggering of the safety discharge. If looking at the data for the 80 kA runs, the maximum voltages did not correlate with the maximum inlet temperature of P1.2, which means that the different quench propagations did not affect the hot spot temperature. Comparing the compensated voltages along P1.2 for single- and two-coil operations during test Phase 2, the voltage increase for 69.3 and 70/16 kA are similar (TFMC dominated) whereas later on, the single- and two-coil operations grouped together.

As a consequence of this large spread of the maximum and also of the different slopes of the voltage with time, the quench propagation should be also different. The total quench propagation velocity can be estimated from the slope of the compensated voltage signals as a function of time considering the definition of the resistive voltage ($V = I\rho_{Cu}^{el}x_{norm}/A_{cu}$) and differentiating it

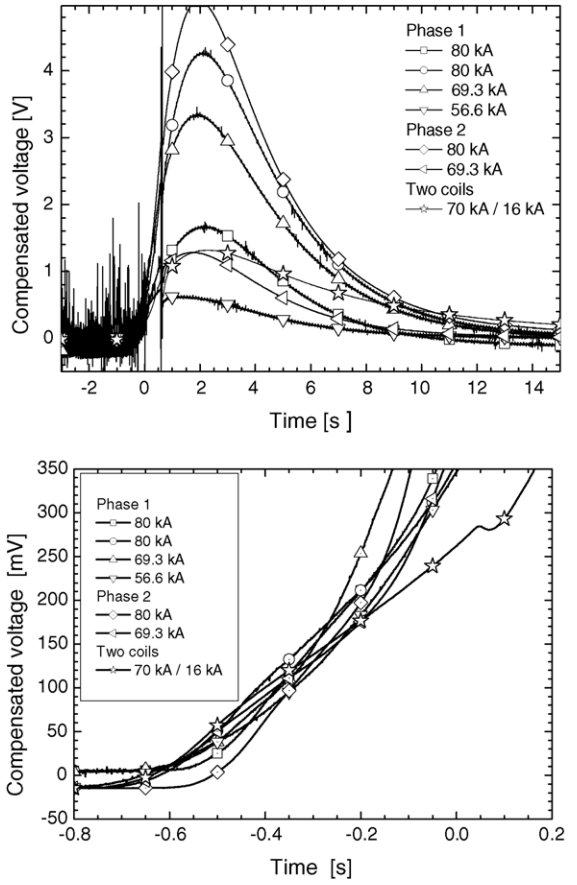


Fig. 6.18. Compensated voltages of selected runs along pancake P1.2 vs. time during quench. Top: total evolution (test Phase 1); bottom: evolution at the beginning (test Phases 1 and 2).

with respect to time

$$\frac{\partial \rho_{\mathrm{Cu}}^{\mathrm{el}}}{\partial T}\frac{\mathrm{d}T}{\mathrm{d}t}\frac{x_{\mathrm{norm}}}{A_{\mathrm{Cu}}}I + \frac{\rho_{\mathrm{Cu}}^{\mathrm{el}} v_q}{A_{\mathrm{Cu}}}I = \frac{\mathrm{d}V}{\mathrm{d}t} \tag{6.26}$$

The first term in (6.26) can be neglected because $T \sim 25$–$30$ K in the first tenths of second, so that $\frac{\partial \rho_{\mathrm{Cu}}^{\mathrm{el}}}{\partial T}$ is negligible (as confirmed by the quasi linear slope of $V(t)$).

In Fig. 6.19, the quench propagation velocity is plotted versus time for the selected quenches. The characteristic is unique for all quenches: after a quench initiation, there is nearly a constant velocity for 0.2–0.4 s followed by a non-linear increase. In Fig. 6.20 top, the average quench propagation velocity at the beginning is plotted as a function of the conductor current. All the

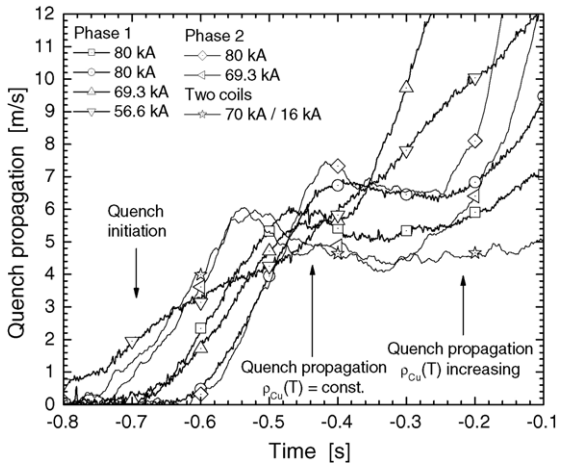


Fig. 6.19. Quench propagation velocity vs. time for selected quenches during test Phase 1 (80, 69.3 and 56.6 kA) plus the 80/0 and 70/16 kA quenches during test Phase 2.

velocities fit a power law of the form $I^b$ with $b = 1.27$, i.e., slightly larger that linear.

One 80 kA quench, indicated with (*) in Fig. 6.20 does not fit the others. This is due to the fact that the corresponding $T_{\mathrm{CS}}$ heater scenario was completely different (linear ramp-up in about 60 s and subsequent plateau instead of multi-step heating) and the initial quench location and length may be different to those of all the other initiated quenches [134].

All quenches were the termination of the current sharing temperature $T_{\mathrm{CS}}$ measurements. The conductor is filled with heated helium near $T_{\mathrm{CS}}$. This will have an impact on the quench propagation compared to spontaneous quench propagation. Since the maximum temperature during quench is not much affected by the maximum voltage, it is concluded that the different maximum voltage levels are due to different initial normal zones (INZ) and different quench lengths.

This argument is confirmed by the fact that it was not possible to simulate the quench performance of the TFMC using the code GANDALF [137] successfully. At first, a simulation of the quench propagation was difficult without exact modelling of quench initiation because the temperature distribution along the conductor, the mass flow rate and the pressure depend on history. Taking the measured pressure, temperature and mass flow just before the quench of the conductor as initial conditions for the GANDALF simulations,

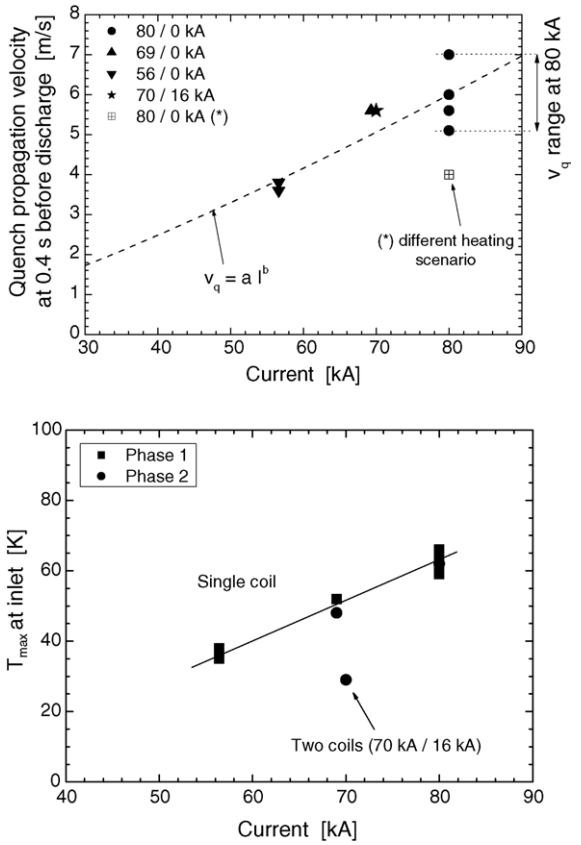


Fig. 6.20. Top: quench propagation velocity vs. current. *A different heating scenario (see text). Bottom: maximum temperature at inlet of pancake P1.2 vs. current.

leads to results that strongly depend on the amount of energy needed to produce an INZ. The maximum temperature was reasonably simulated, but the voltage was not. Also, the maximum pressure was much too high, but this was due to the simple hydraulic model used.

If comparing the quench propagation in the TFMC P1.2 for test Phases 1 and 2 during single-coil operation, no difference was observed. On the other hand, a different behaviour was found for the quench of the TFMC in the two-coil operation (but only one quench was produced). Especially, the maximum temperature of the 70/16 kA run was significantly lower than for the 69/0 kA run which scales very well with current (see Fig. 6.20, bottom). This may be explained by the shorter high field region in P1.2 in the two-coil compared to single-coil operation.

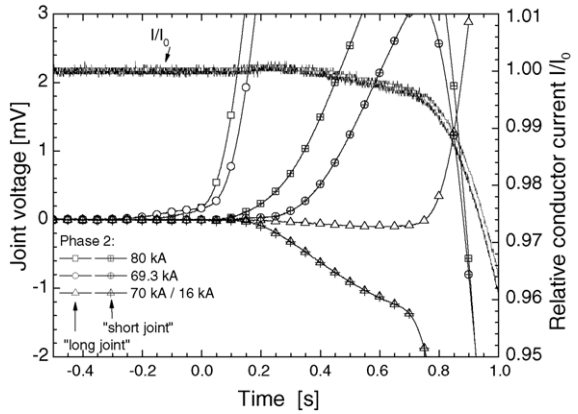


Fig. 6.21. Resistive voltage propagation of the joint voltage taps ("short joint" = across joint length, "long joint" = across joint + 2 × 600 mm conductor each including current transfer voltage for current distribution in cable) for measurement of the upstream quench propagation.

Besides the total quench propagation, which was mainly derived from the compensated voltage, the attempt was made to determine also the upstream quench propagation by the evaluation of two voltage taps, which were applied for measurement of the joint resistance [53]. One pair was directly assembled across the length of the joint while the other pair included 600 mm conductor on each side. From the time of flight of the resistive voltage the upstream quench propagation was determined (Fig. 6.21). For the two-coil test TFMC 70 kA/LCT 16 kA, the quenching high field region is farer away from the joint and a negative voltage value indicated already an inductive voltage caused by the starting safety discharge. Therefore, the upstream propagation was not evaluated. In Table 6.7, the quench propagation velocities as well as the measured peak temperature at the pancake P1.2 inlet are given. A quantitative simulation with the Multi Mithrandir (M&M) code has not been performed yet, so no estimations about the maximum pressures and temperatures in the conductor can be given. The numbers presented in Table 6.7 are measured values at the inlet of pancake P1.2.

*6.2.2.2. Safety discharge.* During a safety discharge (specially 25 kA fast discharge with 3.55 s time constant) of the magnet, eddy currents and associated heat generation are induced in the radial plates and the case. The power generated in radial plates is transferred

Table 6.7
Quench characteristics

| | $v_q$ [m/s] | $v_q^{up}$ [m/s] | $T_{max}$ [K] | $V_{max}$ [V] |
|---|---|---|---|---|
| 80/0 kA (all quenches of Phases 1 and 2) | $6.7 \pm 1$ | $2.7 \pm 0.3$ | $63 \pm 2$ | 1.4–5 |
| 69.3/0 kA (all quenches of Phases 1 and 2) | $5.3 \pm 1$ | $2.0 \pm 0.2$ | 50 | 1.3–3.3 |
| 56.6/0 kA (all quenches) | $3.6 \pm 4.4$ | $1.6 \pm 0.1$ | 39 | 0.6–0.8 |
| 70/16 kA | $5.0 \pm 1$ | See text | 30 | 1.3 |

into the conductor helium channels by a diffusion process through the conductor steel jacket and insulation, which is presented in details in [123]. The behaviour of the case during transient regimes is described in [138].

*6.2.2.2.1. GANDALF Radial Heat Diffusion Model (GRDM) and Specific Energy Model (SEM).* To perform the study of heat diffusion, two concentric zones are modelled with the GANDALF code [137] coupled with a 1D Radial Diffusion Model (GRDM). The volumetric heat source $P_{pv}$ in the radial plates is determined from a transformer model [139] and the power dissipated in the conductor [109] comprises the hysteretic losses and the coupling losses. The heat equations (6.27) for each zone are solved using a finite difference method with a fully implicit scheme in time (neglecting the radial dependency of $\lambda$).

$$\rho c_p(T)\left(\frac{\partial T(r,t)}{\partial t}\right) = \left(\frac{\partial \lambda(r)}{\partial r} + \frac{\lambda(r)}{r}\right)\frac{\partial T}{\partial r} + \lambda(r)\frac{\partial^2 T}{\partial r^2} + P_{pv}(r,t) \tag{6.27}$$

In addition, a more simple approach can be used: the Specific Energy Model, which considers that the energy deposited in stainless steel $E_{SS}$ is instantaneous and the maximal temperature $T_{SS,max}$ (6.28) can be estimated.

$$E_{SS} = m_{SS}\int_{T_0}^{T_{SS,max}} c_{p,SS}(T_{SS})\,\mathrm{d}T_{SS} \tag{6.28}$$

*6.2.2.2.2. Conductor and radial plates during a 25 kA safety discharge with 3.55 s time constant.* The total energy deposited due to the eddy currents is expressed in (6.29) and is equal to 23.9 kJ per pancake [108].

$$E_p = \int_0^\infty P_{v0} e^{2t/\tau_d} V_p\,\mathrm{d}t = \frac{P_v \tau_d}{2} V_p \tag{6.29}$$

Fig. 6.22 presents the experimental inlet and outlet conductor temperatures for the pancake P1.2 of the first double pancake.

Considering the helium in the conductor being static, in a first approximation, the radial plates and helium in the conductor reach a thermal equilibrium at temperature $T_f$ (6.30) after the heat diffusion time delay $\tau$ (6.31) induced by the insulation [118].

$$E_p = \int_{T_0}^{T_f} \rho_{SS} V_p c_{p,SS}\mathrm{d}T_p + \int_{T_0}^{T_f} \rho_{He}(P_{He}, T_{He}) V_{He,CICC}\mathrm{d}h_{He}(P_{He}, T_{He}) \tag{6.30}$$

$$\tau = \frac{\rho_{He} c_{v,He} S_{He,CICC} e_{ins,CICC}}{\lambda_{ins} U_{He,CICC}} \tag{6.31}$$

with $T_0$ = 4.5 K, $P_{He}$ = 0.53 MPa, $\rho_{He}$ = 137.7 kg/m$^3$, $c_{v,He}$ = 2500 J/kg K, $e_{ins,CICC}$ = 2 mm and $\lambda_{ins}$ = 0.0166 W/m K, which is the insulation thermal conductivity [140] for fibreglass divided by a fitting-factor of 6 [123]. $T_f$ is then equal to 5.4 K and $\tau$ = 206 s: these cal-

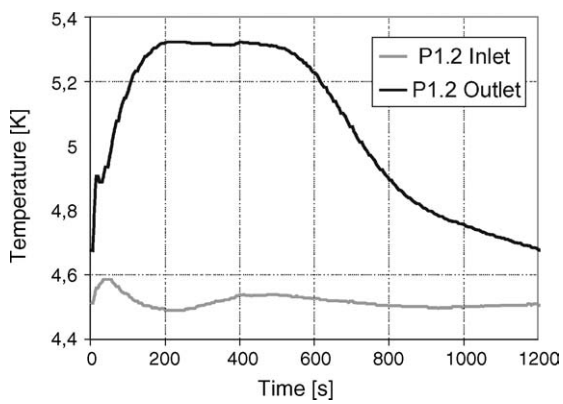


Fig. 6.22. The TFMC P1.2 measured conductor inlet and outlet temperature during a 25 kA fast discharge.

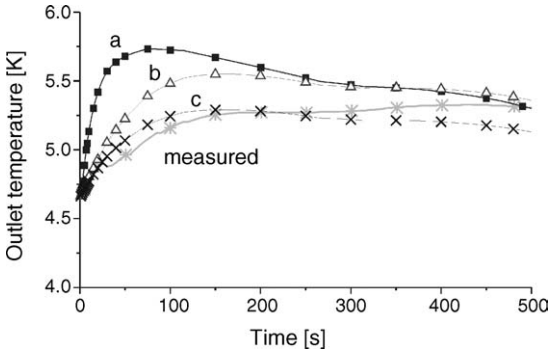


Fig. 6.23. Measured (multi star) and calculated conductor outlet temperatures of the TFMC pancake P1.2 during a 25 kA fast discharge. a–c denote different models: (a) original thermal conductivity of the conductor insulation, $\lambda_{ins}$; (b) best-fit of $\lambda_{ins}$; (c) best-fit of $\lambda_{ins}$ and improved eddy-current model [130].

culations are in good agreement with the experimental value (plateau at 5.35 K near 200 s).

A similar result was obtained with the computer code MAGS where also the thermal conductivity of the conductor insulation had to be (drastically) reduced by a factor of 8 compared to the nominal material data [122]. This is shown in Fig. 6.23 where the measured and computed outlet temperatures are plotted versus time.

This important phenomenon of heat transfer from plates to conductor has to be validated and verified for the toroidal field coil of ITER and thus argues for cold tests of coils, to guaranty their performances, prior to their installation [141].

With the Specific Energy Model, and taking into account the total energy deposited equal to 238 kJ for the 10 pancakes, the maximal radial plates temperature $T_{SS,p}$ is estimated to 10.1 K.

In Fig. 6.24, the temperature evolution computed with the GANDALF Radial Heat Diffusion Model is presented at four different radial locations: conductor side insulation, radial plate side insulation, insulation side plate, and case side plates. The maximum radial plate temperature calculated with GRDM is 9.7 K and is in good agreement with the 10.1 K value estimated with SEM: this validates both of the models used.

*6.2.2.3. Efficiency of energy transfer.* To verify the efficiency of the transfer of the stored magnetic energy to the external dump resistor in case of a safety discharge, the stored energy was related to the re-cooling

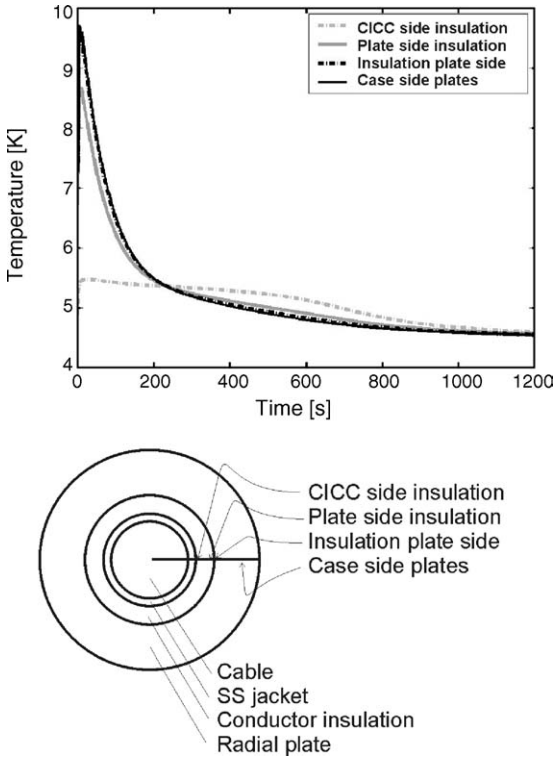


Fig. 6.24. Top: TFMC radial plates and different insulation temperatures at different radial locations calculated with the GANDALF Radial Diffusion Model (GRDM) during a 25 kA fast discharge. Bottom: Schematic of the GRDM and locations where the temperatures are calculated.

energy of the cryogenic system. The latter one is equivalent to the energy dissipated in the winding and in the structure. Table 6.8 summarises the results of the re-cooling energy of the winding(s) for various quenches analysed, both for single coil and twin coils operation. The re-cooling energy of the casing and of the ICS was

Table 6.8
Energy efficiency during safety discharge

| Current [kA] | Stored energy [MJ] | Re-cooling energy [MJ] |
|---|---|---|
| Phase 1 (TFMC without LCT) | | |
| 80 (Q) | 86.4 | 4.68 (5.4%) |
| 80 (Q) | 86.4 | 4.72 (5.5%) |
| Phase 2 (TFMC + LCT) | | |
| 70/16 (Q) | 337 | 9.09 (2.7%) |
| 49.5/11.6 | 174.3 | 3.63 (2.1%) |
| 25/5.7 | 42.73 | 0.514 (1.2%) |

Q, safety discharge after quench.

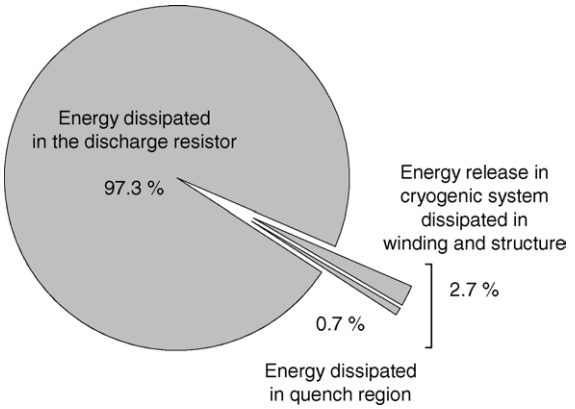


Fig. 6.25. Efficiency of energy transfer.

not taken into account because their cooling circuits were connected in series to the windings. The higher efficiency of the energy extraction in case of the two-coil operation is due to the fact that the LCT coil has no radial plates leading to a higher efficiency. Moreover, the LCT coil has a much larger stored energy than the TFMC, so the higher efficiency has a substantial impact on the total energy efficiency.

Fig. 6.25 shows the efficiency of the energy transfer for the two-coil operation (70/16 kA).

### *6.2.3. Summary*

From the two test campaigns of Phases 1 and 2 ITER-relevant information was extracted from the analysis of the TFMC performance. The pressure drop could be modelled using friction factor correlations for both the bundle and the central channel regions with two types of spirals acting as an envelope for the central channel. At extended mass flow rate conditions of 18 g/s for each pancake, the models underestimate the pressure drop data by about 20% whereas at 10 g/s the agreement is quite good. On the other side, there is also a spread in the pressure drop data in the order of ±10% for pancakes having the same spiral.

Because the critical current of the TFMC was much higher than the highest possible operating current, all quenches were forced by the heating scenario to evaluate the current sharing temperature. So the quench behaviour of the coil was strongly influenced by the quench initiation, which results in a large spread of the maximum voltage along the quenched pancake even at the same conductor current. On the other hand, the corresponding maximum He-temperature $T_{max}$ after a quench was rather constant. It could be shown that at the very beginning of the quench all the quench velocities (single coil and two-coil operation) fit to a power law. For single-coil operation, $T_{max}$ scaled very well with the conductor current whereas the only quench performed during the two-coil operation does not fit. A quantitative investigation of the quench propagation was not done by a more advanced code than GANDALF so far and so there is no information available for both the $T_{max}$ and the maximum pressure inside the conductor.

During the safety discharge of the TFMC, eddy currents and associated heat generation are induced in the radial plates and the coil case. The diffusion process of the generated heat from the plates to the conductor helium was described by different models. The experimental data could be well reproduced by modelling if the thermal conductivity of the conductor insulation was reduced by a factor of 6–8 compared to the material data of fibreglass reinforced epoxy.

The efficiency of the transfer of the stored magnetic energy to the external discharge resistor in case of a safety discharge was demonstrated. The dissipated energy in the TFMC was about 5.5% relative to the stored magnetic energy but a significant amount of heat was generated by the eddy currents in the radial plates and coil case.

List of symbols used in the equations:

| | |
|---|---|
| $A_{Cu}$ | Copper cross-section |
| $c_p$ | Heat capacity of helium at constant pressure |
| $c_{p,SS}$ | Heat capacity of stainless steel |
| $c_{v,He}$ | Helium heat capacity at constant volume |
| $D_h$ | Hydraulic diameter |
| $D_{hb}$ | Bundle hydraulic diameter (GANDALF input parameter) |
| $D_{hh}$ | Central hole hydraulic diameter (GANDALF input parameter) |
| $d_{eff}$ | Effective filament diameter |
| DQ | Difference in the instantaneous power of pancakes P1.1 and P1.2 |
| $E_c$ | Loss energy in the coil case |
| $E_{cl}$ | Loss energy due to coupling losses |
| $E_{hl}$ | Loss energy due to hysteresis losses |
| $e_{ins,CICC}$ | Conductor insulation thickness |
| $E_p$ | Loss energy due to eddy currents in the radial plates |
| $E_{SS}$ | Deposited energy in stainless steel |
| $E_{tot}$ | Total loss energy of the superconducting cable |
| $E_{wp}$ | Loss energy winding pack |

| | |
|---|---|
| $f_B$ | Friction factor of the bundle region |
| $f_H$ | Friction factor of the central channel (hole) |
| $f_{EU}, f_{US}$ | Friction factor, European convention, Friction factor, US convention |
| $h_{He}$ | Helium enthalpy |
| HL | Hysteresis losses |
| $I_{max}$ | Maximum TFMC current |
| $I_{TFMC}$ | Current of the TFMC |
| $I$ | Coil current |
| $J_{nonCu}$ | Non-copper current density |
| $K$ | Amplification factor |
| $L$ | Length of hydraulic channel |
| $M_{wp}$ | Mutual inductance between one TFMC winding turn and all radial plates |
| $M_{wc}$ | Mutual inductance between one TFMC winding turn and the coil case |
| $m_{SS}$ | Mass of stainless steel |
| $N$ | Number of turns of the TFMC |
| $N_p$ | Number of coil charges |
| $(n\tau)$ | Cable time constant for coupling losses |
| $P_{pancake}$ | Loss power of one pancake due to joint resistance |
| $P_{He}$ | Helium pressure |
| $P_{hl}$ | Hysteresis loss power |
| $P_{pv}$ | Volumetric heat source |
| $P_{cl}$ | Coupling loss power |
| $P_{v0}$ | Initial power |
| $P_{ripple}$ | Losses caused by the ripple of the coil current |
| $P_p$ | Loss power of radial plates |
| $P_{joint}$ | Total joint losses of the TFMC |
| $P_c$ | Loss power of coil case |
| QMFI700A | DAS virtual channel; Heat load (loss power) of the whole TFMC coil |
| QMFI710 | DAS virtual channel; Heat load (loss power) of the pancake P1.1 |
| QMFI712 | DAS virtual channel; Heat load (loss power) of the pancake P1.2 |
| QMFI800 | DAS virtual channel; Heat load (loss power) of the TFMC case |
| $r$ | Radial coordinate |
| $R_{pancake}$ | Joint resistance regarding one pancake |
| $R_p$ | Resistance of radial plate |
| $R_c$ | Resistance of coil case |
| $R_{inner}$ | Resistance of inner joint |
| $R_{outer}$ | Resistance of outer joint |
| $R_{P1.1}$ | Joint resistance regarding pancake P1.1 |
| $R_{P1.2}$ | Joint resistance regarding pancake P1.2 |
| $R_{TFMC}$ | Total joint resistance of the TFMC |
| $Re$ | Reynolds number |
| $S_{He,CICC}$ | Helium cross-section |
| $S_{heb}$ | Bundle helium cross-section (GANDALF input parameter) |
| $S_{heh}$ | Central hole helium cross-section (GANDALF input parameter) |
| $S_{strands}$ | Total strands cross-section (GANDALF input parameter) |
| $S_{nonCu}$ | Non-Cu cross-section |
| $T$ | Temperature |
| $t$ | Time |
| $T_{CS}$ | Current sharing temperature |
| $t_d$ | Time constant for exponential current decay |
| $T_0$ | Initial temperature |
| $T_{He}$ | Helium temperature |
| $T_{max}$ | Maximum temperature during quench |
| $T_{edge}$ | Temperature at the coil case edge |
| $T_{SS}$ | Temperature of stainless steel |
| Ub | Bundle wetted perimeter (GANDALF input parameter) |
| $U_{He,CICC}$ | Helium perimeter |
| $v$ | Helium velocity |
| $V$ | Resistive voltage |
| $V$ | Volume |
| $V_{He,CICC}$ | Helium volume in cable |
| $V_{max}$ | Maximum pancake voltage during quench |
| Void | Void fraction of cable |
| $V_p$ | Volume radial plate |
| $W_{1.1}$ | Loss power of the pancake P1.1 |
| $x$ | Local coordinate |
| $W_{1.2}$ | Loss power of the pancake P1.2 |
| $W_{2.1}$ | Loss power of the pancake P2.1 |
| $W_{case}$ | Loss power of the TFMC case |
| $W_{wp}$ | Loss power of the TFMC winding pack |
| $x_{norm}$ | Normal conducting (resistive) length |
| $\Delta P_{He}$ | Helium pressure drop |
| $\alpha$ | Special function |
| $\lambda$ | Thermal conductivity of specific material |
| $\lambda_{ins}$ | Thermal conductivity of conductor insulation |
| $\nu_q$ | Quench propagation velocity |
| $\nu_q^{up}$ | Upstream quench velocity |
| $\rho$ | Helium density |
| $\rho_{Cu}^{el}$ | Electrical resistivity of copper |
| $\tau_d$ | Discharge time constant for exponential current decay (safety discharge) |
| $\tau$ | Time constant to establish a steady state heat flow |
| $\chi$ | Loss power ratio |

General acronyms, abbreviations and initialisms are explained in Glossary.

## 7. Properties of special components

### 7.1. Joints

A scheme of the general TFMC electrical network is presented in Fig. 7.1, where all the joints are shown and numbered. The different types of joint to be considered are listed in Table 7.1. All these joints are overlap joints (see Fig. 3.5) of the shaking-hand type (conductors on opposite sides of the joint, see Fig. 7.2), except TFMC-bus bar type 1 positive pole (BB1+) joint (#3) which

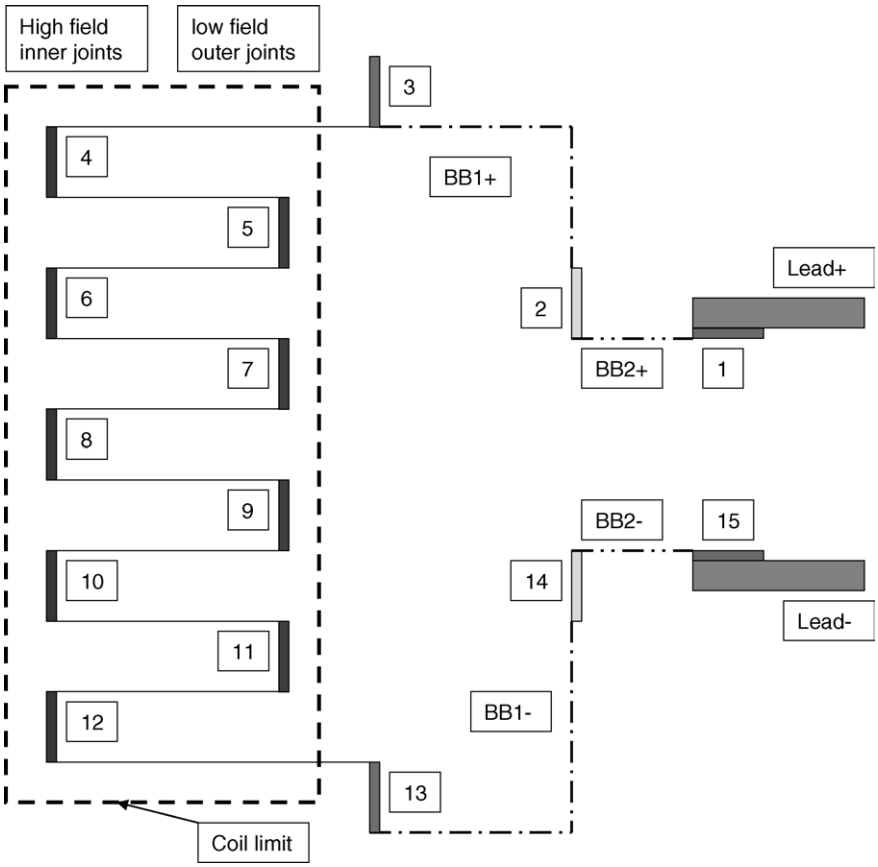


Fig. 7.1. Electrical network (with joints) of TFMC.

is of the praying-hand or hair-pin type (conductors on the same side of the joint).

### *7.1.1. Joints in the winding pack of TFMC*

The joints located in the winding pack of TFMC (#4–12) are composed of the five inner joints (inter pancake joints, each of them can be associated with a double pancake, e.g., joint #4 associated to DP1), and the four outer joints (inter double pancake joints, e.g., joint #5 connecting DP1–DP2). Due to their locations, the inner joints are operating under higher magnetic field compared to the outer joints.

*7.1.1.1. Electrical measurements.* The most demanding joints (i.e., the inner joints operating under high field) have been equipped with voltage taps to measure their resistances (see Fig. 3.14). Two kinds of measurement have been used: a “short length” mea-

Table 7.1
List of joints involved in the TFMC experiments

| Type (joint #) | Number | Conductors | Jointing technique |
|---|---|---|---|
| TFMC inner joint (#4, 6, 8, 10, 12) | 5 | $Nb_3Sn$–$Nb_3Sn$ | Soldered with PbSn |
| TFMC outer joint (#5, 7, 9, 11) | 4 | $Nb_3Sn$–$Nb_3Sn$ | EB weld of copper pins |
| TFMC–BB1 (#3, 13) | 2 | $Nb_3Sn$–NbTi | Soldered with PbSn |
| BB1–BB2 (#2, 14) | 2 | NbTi–NbTi | Pressed indium wires |
| BB2–leads (#1, 15) | 2 | NbTi–$Nb_3Sn$ inserts | Pressed indium foil |

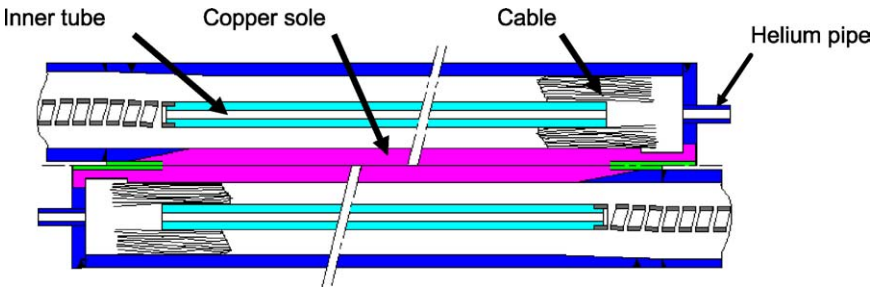


Fig. 7.2. Sketch of TFMC inner joint longitudinal cut.

surement with voltage taps located on the helium pipes of the joint boxes (see Fig. 7.2), and a "long length" measurement with taps located 600 mm apart from the joint, on the conductor jacket. Because of a high resistance between the cable and the jacket (or the steel joint box), the "short length" measurement should lead to underestimate the joint resistance by picking an electric potential lying in between the cable and the copper sole potentials, as in a voltage divider. On the other hand, far enough (>500 mm) from the joint, the electric potential on the steel jacket is equal to the one of the cable, and the joint resistance measurement is therefore more accurate [144].

During the TFMC Phase I experiment, an odd phenomenon was observed, which remained unexplained during several weeks, and which was erroneously attributed in the beginning to a measurement problem. Indeed, a reverse of polarity was observed on all the "short length "voltage drops between normal state and superconducting state, which was not observed on the "long length" voltage drops. A model was developed which explained this real phenomenon [144], coming from the fact that the "short length" voltage drop is indeed negative when the longitudinal resistance along the cable is much larger than the joint resistance itself.

Among the 10 inner joint measurements, DP5_long length (#12, long distanced voltage taps) had to be rejected because of erratic results. The other measurements appear quite trustable, with a slight increase of resistance with current, and so with field (see Fig. 7.3). The joint resistances at 80 kA are given in Table 7.2 where it can be seen that, as expected, the "short length" resistances are generally lower (by about 30%) than the "long length" resistances. Note also that two outer joint resistances (#9 and 11) were measured directly using quench detection wiring.

*7.1.1.2. Calorimetric measurements.* The Joule power $P_j$ dissipated in each pancake is calculated through the helium enthalpy variation between outlet and inlet, using measured outlet temperature $T_{outlet}$, inlet temperature $T_{inlet}$, mass flow rate $\dot{m}$, and pressure $p$ (see Eq. (7.1)). This calculation is only valid under steady operation and more details can be found in Section 6 (see also [145]).

$$P_j = \dot{m}(h_{outlet} - h_{inlet}) \tag{7.1}$$

where $h_{outlet}(p, T_{outlet})$ and $h_{inlet}(p, T_{inlet})$ are the helium enthalpies at outlet and inlet, respectively.

The TFMC hydraulic network is shown in Fig. 3.13 where it can be seen that the first two pancakes (P1.1 and P1.2 of DP1) are fully equipped and independent, while the other pancakes are coupled either for mass flow measurement or for temperature measurement.

In order to calculate $P_j$ in every pancake, the following rules have been used (except for DP1 obviously): $T_{inlet}$ is assumed equal for all pancakes to the value measured on P1.2, a common $T_{outlet}$ is assumed to be

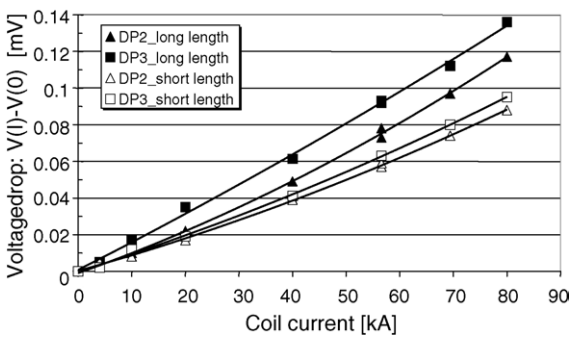


Fig. 7.3. Typical voltage drops across TFMC inner joints (symbol height = error bar = ±2.5 μV, including point at 0).

Table 7.2
TFMC joint resistances during Phase I

| Type | Current [kA] | Location (joint #) | Short length [nΩ] | Long length [nΩ] |
|---|---|---|---|---|
| Inner | 80 | DP1 (#4) | $1.19 \pm 0.06$ | $1.68 \pm 0.06$ |
| Inner | 80 | DP2 (#6) | $1.10 \pm 0.06$ | $1.46 \pm 0.06$ |
| Inner | 80 | DP3 (#8) | $1.19 \pm 0.06$ | $1.70 \pm 0.06$ |
| Inner | 80 | DP4 (#10) | $1.13 \pm 0.06$ | $1.65 \pm 0.06$ |
| Inner | 80 | DP5 (#12) | $1.15 \pm 0.06$ | $1.62 \pm 0.15$[a] |
| Outer | 56.6 | DP3–DP4 (#9) | – | $1.31 \pm 0.07$ |
| Outer | 56.6 | DP4–DP5 (#11) | – | $1.24 \pm 0.07$ |

[a] Extrapolated from short length value.

the value relative to each pancake, mass flow is assumed equally shared among pancakes for DP2, DP3 and DP4, while for DP5, the same mass flow repartition as measured in DP1 has been assumed. Pressure $p$ is measured inlet pressure.

Besides these rules, the final accuracy for the Joule heating (and so for the pancake resistance) is limited by the temperature difference accuracy $\Delta T$ ($=\pm 5\,\text{mK} \rightarrow \Delta P_j \approx \pm 0.2\,\text{W}$) and the mass flow rate accuracy $\Delta \dot{m}$ ($=\pm 5\% \rightarrow \Delta P_j = \pm 5\%$).

The results are presented in the form of $P_j(I^2)$ curves, where $I$ is the current flowing through the TFMC conductor. As shown in Fig. 7.4, the curves are roughly linear, the slopes of these curves being the pancake "resistances". The points close to $I = 0$ correspond in fact to $I = 4\,\text{kA}$, they show the so-called residual steady power, which is attributed to eddy currents produced in the radial plates by the power supply voltage ripple at 600 Hz (see Section 6.1.3). However, the side pancakes (P1.1 and P5.2) have different behaviours, the curves are less linear (or the origin points are shifted)

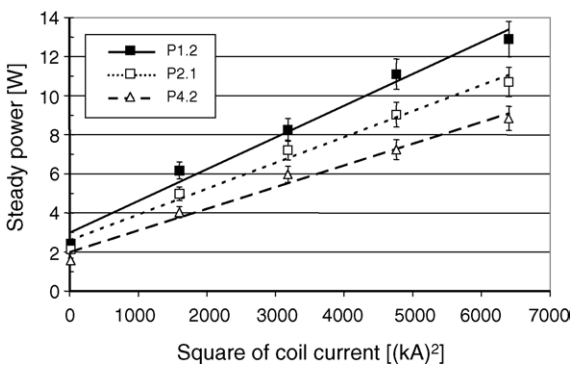


Fig. 7.4. Steady state power dissipated in some TFMC pancakes (error bars = $\pm 0.2\,\text{W} \pm 5\%$).

and the slopes are much lower (50–60%). This result has been attributed to the heat exchange in the coil terminal joints with the bus bars (corresponding to helium inlet for the bus bars) and also possibly to heat exchange with the casing (see Section 6.1), leading to underestimate the real Joule heating. From the work presented in Section 6.1.2.2 (see Fig. 6.3), the correction to be applied to the measurements *on each side pancake* can be evaluated to lie within the 1.4–1.7 W range (average = 1.55 W).

There is a good linearity of the Joule power versus $I^2$, which means apparently a constant resistance, in contradiction with Section 7.1.1.1. However, one must first note that the magneto-resistance effect should be lower on the outer joints (compared to the inner joints) because the magnetic field is lower. Second, that plotting a curve as function of $I^2$ tends to mitigate the apparent effect of a linear increase of resistance with $I$. Last, that the residual steady power may not be constant from 4 to 40 kA (see Section 6.1.3).

A summary is given in Table 7.3. The values of the pancake resistances were calculated from the slope of the $P_j(I^2)$ curves. The resistance of a given pancake contains in fact the resistance of the half inner joint plus the resistance of the half outer joint of this pancake (see Fig. 7.1).

*7.1.1.3. Cross checking and extrapolations.* As illustrated in Table 7.3, a pancake resistance $R_{pancake}$ is the sum of the resistance of the half inner joint ($R_{inner}$) plus the resistance of the half outer joint ($R_{outer}$) of this pancake. For two pancakes (P3.2 and P4.1), it was possible to crosscheck the electric measurements and the calorimetric measurements. In order to improve the comparisons, the Joule heating was calculated in these pancakes using the associated inner and outer joint volt-

Table 7.3
TFMC pancake (joint) resistances (Phase I)

| Double pancake | Pancake (joint numbers) | Resistance [nΩ] |
|---|---|---|
| DP1 | P1.1 (1/2 of #3 + 1/2 of #4) | $1.25 \pm 0.25$[a] |
| | P1.2 (1/2 of #4 + 1/2 of #5) | $1.62 \pm 0.14$ |
| DP2 | P2.1 (1/2 of #5 + 1/2 of #6) | $1.33 \pm 0.13$ |
| | P2.2 (1/2 of #6 + 1/2 of #7) | $1.27 \pm 0.12$ |
| DP3 | P3.1 (1/2 of #7 + 1/2 of #8) | $1.28 \pm 0.12$ |
| | P3.2 (1/2 of #8 + 1/2 of #9) | $1.35 \pm 0.13$ |
| DP4 | P4.1 (1/2 of #9 + 1/2 of #10) | $1.26 \pm 0.12$ |
| | P4.2 (1/2 of #10 + 1/2 of #11) | $1.11 \pm 0.12$ |
| DP5 | P5.1 (1/2 of #11 + 1/2 of #12) | $1.43 \pm 0.13$ |
| | P5.2 (1/2 of #12 + 1/2 of #13) | $1.35 \pm 0.30$[a] |

[a] Corrective coefficient applied due to heat exchange by the helium cooling of the bus bars in joints #3 and 13 (see Section 7.1.1.2).

Table 7.4
TFMC pancake (joint) resistance

| Pancake | Calorimetry [nΩ] | Voltage drops [nΩ] | Overlapping range [nΩ] |
|---|---|---|---|
| P3.2 | $1.35 \pm 0.13$ | $1.46 \pm 0.07$ | 1.39–1.48 |
| P4.1 | $1.26 \pm 0.13$ | $1.39 \pm 0.07$ | 1.32–1.39 |

age drops. Then the power as function of $I^2$ was plotted and the slope of the linear fit was calculated to be compared with the values given in Table 7.3 [144].

In Table 7.4, the pancake resistance values given by the calorimetric method are presented and compared to the values given by the electrical method. The agreement is good, i.e., within the measurement accuracies. The last column of this table gives the overlapping range.

The same process can be used to calculate $R_{\text{outer}}$, knowing $R_{\text{pancake}}$ by calorimetry and $R_{\text{inner}}$ by voltage drops. This allows to estimate the "missing" outer joint resistances #5 and 7, not directly measured (see Section 7.1.1.1). Obviously the final accuracy is poor because in fact $R_{\text{outer}}/2$ is calculated. Since values by the calorimetric method were used, it is convenient to calculate here $R_{\text{inner}}$ by the slope of the linear fit of the Joule power calculated from the voltage drop.

It can be noticed that each outer joint can be calculated using two different pancakes. The results are presented in Table 7.5. The agreement is good, i.e., within the accuracies. The last column of the table gives the overlapping range. The final accuracy is poor, however the low values of the outer joint resistances are confirmed (see Table 7.5).

*7.1.1.4. Comparisons with joint samples.* Within the framework of the TFMC fabrication program, three full-size joint samples were fabricated and tested by the EU Home Team [146]. The DC resistances of the joints of these samples were measured under high magnetic field (up to 8 T), with high transport currents (up to 80 kA) [147,148]. Two of these samples used exactly the same cable as the TFMC but different jackets. One of them (called TFMC–FSJS) used exactly the same conductor as the TFMC and had a joint similar to the outer joints of the TFMC (i.e., facing copper soles connected with EB welding of copper pins) [149]. The other sample (called TF–FSJS), although using an incoloy-jacketed conductor and incoloy–copper joint boxes, can be considered as relevant to the TFMC inner joints (i.e., facing copper soles connected with PbSn solder) [149].

The resistances of these joints were found to be given by the following laws, independent of current when far from critical current [149]:

$$R_{\text{joint}} = R_{\text{o}} + \beta \mathbf{B} \tag{7.2}$$

where $\mathbf{B}$ is the local magnetic field modulus (in $T$) on the joint (i.e., applied field plus self field).

Note that the field (vector) $\mathbf{B}$ was oriented perpendicular to the current lines in the copper soles ($=\mathbf{B}_{\perp}$).

Table 7.5
Estimation of missing outer joint resistances

| Joint # | Pancake | $R_{\text{inner}}/2$ [nΩ] | $R_{\text{pancake}}$ [nΩ] | $R_{\text{outer}}$ [nΩ] | Overlapping range [nΩ] |
|---|---|---|---|---|---|
| 5 | P1.2 | $0.83 \pm 0.03$ | $1.62 \pm 0.14$ | $1.58 \pm 0.34$ | 1.24–1.54 |
| 5 | P2.1 | $0.72 \pm 0.03$ | $1.33 \pm 0.13$ | $1.22 \pm 0.32$ | |
| 7 | P2.2 | $0.83 \pm 0.03$ | $1.27 \pm 0.12$ | $0.87 \pm 0.30$ | 0.65–1.17 |
| 7 | P3.1 | $0.81 \pm 0.03$ | $1.28 \pm 0.12$ | $0.95 \pm 0.30$ | |

In addition, measurements performed on sub size joints have given the ratio $\gamma$ of the magneto-resistance effect of a parallel field $\mathbf{B}_{//}$ compared to the effect of a perpendicular field $\mathbf{B}_{\perp}$ by: $\gamma = 0.58$ [150].

The values of $R_o$ and $\beta$ for the two samples are reported in Table 7.6. It can be seen that $\beta$ is almost the same for the two samples, while $R_o$ (which is representative of the strand–copper contacts) is much higher in the TFMC–FSJS, which was attributed to the effect of the EB welding.

It should be also noted that the tested sample joints were of the praying hand type, while the TFMC joints are of the shaking hand type. However, in superconducting state, no difference should be expected in DC operation.

In the TFMC joints the magnetic field has any orientation with regard to the current lines in copper soles, the radial field component $B_x$ (with respect to the coil) is a $\mathbf{B}_{\perp}$ for the joints, while the axial field component $B_y$ (with respect to the coil) is a $\mathbf{B}_{//}$ for the joints.

Without any data on the effect of any field orientation, and without any theoretical model available, the following empirical formula has been used to calculate the TFMC joint resistances:

$$R_{\text{joint}} = R_o + \beta\sqrt{B_x^2 + \gamma^2 B_y^2} \tag{7.3}$$

where $R_o$ and $\beta$ are given in Table 7.6.

This simple law has been used because it enables to recover the correct values with $B_x = 0$, or with $B_y = 0$, as well as it gives a monotonous decrease from perpendicular field to parallel field. Note that other calculations, assuming a linear decrease of the magneto-resistance effect with field angle, gave similar results on the TFMC joints.

The values of the magnetic field on the TFMC joints are reported in Table 7.7, for the maximum current of 80 kA (no current in LCT coil). Note that during Phase I (test of TFMC alone), the field is symmetric with respect to coil mid-plane.

It was already noted that $R_o$ is characteristic of the strand–copper contacts (quality, surface, number), while $\beta$ has almost the same value since it depends mainly on the copper sole. It was then tempting to try to fit the experimental voltage drop curves $V(I)$, playing only with $R_o$ while using Eq. (7.3). This analysis was only possible on joints having full reliable characteristics $V(I)$ (see Section 7.1.1.1). The results were quite good as well for the inner joints as for the outer joints (see Fig. 7.5 as an example) [144].

The good fits obtained by playing only with $R_o$ prove the validity of the magneto-resistance formula (associated with an accurate field calculation). Finally, the qualities of the joints can be compared using only $R_o$ as the effect of magnetic field (and so of joint location) has been eliminated. The values of $R_o$ are reported in Table 7.8, compared to the FSJS values.

The values of the inner joint resistances measured in the Phase II experiment (with current in the LCT coil) were found quite in agreement with the values calculated using Eq. (7.2) associated with values of $\beta$ in Table 7.6, and with values of $R_o$ in Table 7.8 (see Fig. 7.6 as an example). The local magnetic field on the joints was accurately computed for this purpose.

Table 7.6
Values of characteristic parameters for EU FSJS joints

| Sample | TFMC joint type | $R_0$ [nΩ] | $\beta$ [nΩ/T] |
|---|---|---|---|
| TF–FSJS | Inner | 0.922 | 0.119 |
| TFMC–FSJS | Outer | 1.63 | 0.111 |

Table 7.7
Magnetic field components on TFMC joints at 80 kA (Phase I)

| Location | Joint # | Type | $B_x$ [T] | $B_y$ [T] |
|---|---|---|---|---|
| DP1–BB1+ | 3 | Terminal/bus bar | 1.29 | 1.37 |
| DP1 | 4 | Inner | 2.13 | 4.96 |
| DP1–DP2 | 5 | Outer | 1.75 | 2.24 |
| DP2 | 6 | Inner | 1.07 | 5.65 |
| DP2–DP3 | 7 | Outer | 0.60 | 2.64 |
| DP3 | 8 | Inner | 0.11 | 5.85 |

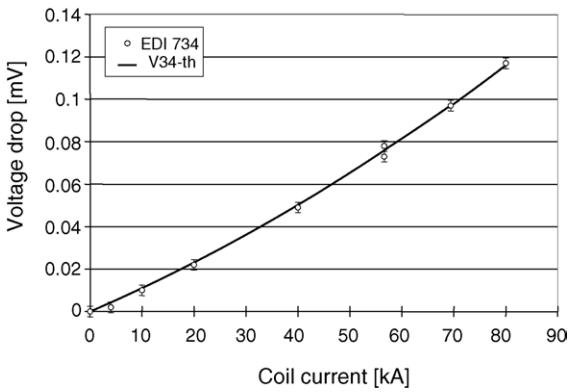


Fig. 7.5. Experimental (dots with error bars) and theoretical (line) voltage drops of DP2 inner joint.

Table 7.8
Values of TFMC and FSJS joint origin resistances

| Joint type | Location | Joint # | $R_o$ [nΩ] |
|---|---|---|---|
| Inner | DP1 | 4 | 1.31 |
| Inner | DP2 | 6 | 1.04 |
| Inner | DP3 | 8 | 1.32 |
| Inner | DP4 | 10 | 1.25 |
| Outer | DP3–DP4 | 9 | 1.20 |
| Outer | DP4–DP5 | 11 | 1.08 |
| TF–FSJS | – | – | 0.92 |
| TFMC–FSJS | – | – | 1.63 |

*7.1.1.5. Comparisons with models.* Neglecting the PbSn solder resistance (two thin layers, about 0.1 mm thick each, accounting for less than 0.05 nΩ), the joint resistance $R_{joint}$ can be expressed in a rough and general way as follows (at better than 5% compared to a FE calculation):

$$R_{joint} = 2\frac{\rho_b e_b}{P_c L} + 2\frac{\rho_{cu} e_{cu}}{P_c L} \quad (7.4)$$

where "$\rho_b e_b$" is the overall barrier resistance (per unit contact area) between cable and copper sole, $\rho_{cu}$ the copper sole resistivity (RRR = 320), $e_{cu}$ (≈10 mm) the average copper sole thickness, $P_c$ (≈38 mm) the geometrical contact perimeter of cable on copper sole and $L$ = 440 mm is the joint overlapping length (see Fig. 3.5). Note that the barrier resistance includes not only the contact resistance but also internal barriers in strands.

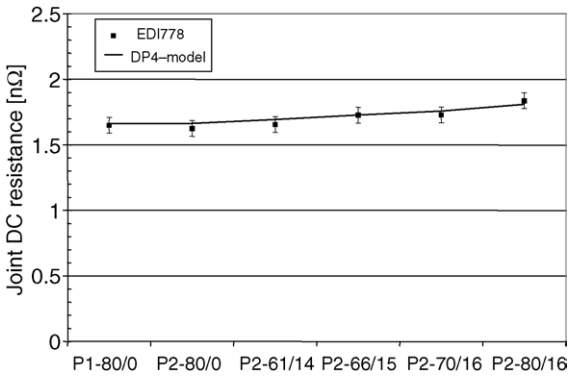


Fig. 7.6. TFMC DP4 inner joint (#10) resistance in Phase I and Phase II experiments (abscissa is Phase no_$I_{TFMC}$[kA]_$I_{LCT}$[kA]). Measured values (dot + error bars), and model (line).

Using Eq. (7.4) for an average inner joint resistance $R_o$ (at 0 T) of 1.20 nΩ (see Table 7.8), one gets:

$$\rho_b e_b \approx 9.5 \times 10^{-12}\ \Omega\,m^2 \quad (7.5a)$$

Eq. (7.4) also shows that the contribution of the copper soles is negligible at 0 T (about 0.064 nΩ).

Taking into account the fact that only two-third of the strands are superconducting, the value of "$\rho_b e_b$" given in Eq. (7.5a) has to be corrected accordingly for a better relevance and easier comparisons with other joints. Then one gets:

$$\rho_b e_b \approx 6.3 \times 10^{-12}\ \Omega\,m^2 \quad (7.5b)$$

This value is in agreement with experimental results obtained on subsize joints used for the qualification of the joint design, taking into account the 25% cable void fraction in the TFMC joints. Indeed, values of "$\rho_b e_b$" ranging from 2 to $3 \times 10^{-12}\ \Omega\,m^2$ were found at 20% void, and about $8 \times 10^{-12}\ \Omega\,m^2$ was found at 30% void [151].

Note also that the real barrier resistances are lower than these values because the real contact perimeter is lower than the geometrical contact perimeter $P_c$. As a matter of fact, measurements performed on a full size joint mock-up have given an effective contact perimeter at the strand scale of about 28% of $P_c$.

Eq. (7.4) also shows that the theoretical magneto-resistance coming from the copper soles is: $\beta_{th} \approx 0.054$ nΩ/T. The magneto-resistance coefficient $\beta_{th}$ should be also affected by the proportion of superconducting strands but in a less straightforward and a much less significant manner than "$\rho_b e_b$", as observed on full-size joint samples [148]. The observed magneto-resistance coefficient (accurately measured on samples and confirmed by the TFMC results) $\beta \approx 0.12$ nΩ/T, is about twice the calculated value. This has been understood as the effect of current paths through the copper sheath of the strands and thus is integrated in the "$\rho_b e_b$" of the model (i.e., a "$\rho_b e_b$" value increasing with field).

*7.1.1.6. Comparison with ITER specifications.* When the TFMC was designed, the ITER TF coil design was considering a single pancake winding with internal and external joints. Then the internal joints (also helium inlets) were key components and the maximum joint resistance was limited by the effect of the Joule heat-

ing in the joint on the operating temperature of the conductor at peak field. The DC power in the joint was limited so as not to increase the helium temperature by more than 0.05 K, which at the end led to impose a joint resistance: $R_{TF} \leq 2.5\,n\Omega$. From the first results obtained on subsize joints, a target value $R_{target} = 2n\Omega$ looked quite reachable.

At the time of the TFMC design, the maximum magnetic field on the ITER TF coil inner joints was about 6.5 T. Taking conservatively the field to be normal to the current lines leads to a magneto-resistance coefficient of 0.12 nΩ/T (as measured on samples under $\mathbf{B}_{\perp}$, see Table 7.6). Then one gets the following specification for the $R_o$ value of the ITER TF coil joints: $R_o \leq 1.7\,n\Omega$, with a target at 1.2 nΩ. It can be seen in Table 7.8 that the TFMC joints are quite at the level of the ITER target.

The present ITER design is considering double-pancake winding without internal joints and the specifications for the joint resistances can be relaxed because of no more impact on the conductor operating conditions. However, lower joint resistances still offer the interest to decrease the thermal load of the TF coils which operate in DC mode.

*7.1.1.7. Summary.* From the values given in Table 7.8, the following can be derived: the values of $R_o$ are low (1–1.3 nΩ range) and lie in the lower half range between the TF–FSJS and the TFMC–FSJS values, no difference is visible between inner and outer joint resistances, the total dispersion among the TFMC joints is within ±11%.

Finally, these results are rather unexpected taking into account the test results of the two FSJS, and lead to the following comments: neglecting a possible effect of incoloy, the TF–FSJS sample had a very good joint (lower boundary), the industrial fabrication of the TFMC joints has led to a rather good uniformity of the joint resistances certainly due to well defined and repetitive processes, the quality of the outer joints (strand–copper interface) has been significantly improved compared to the TFMC–FSJS joint, to be attributed to an improvement of the copper pins EB welding.

The resistances of the TFMC inner joints are lower than the specifications for the ITER TF coils and are at the level of the ITER target (as defined at the time of the TFMC design).

*7.1.2. TFMC terminals*

In contrary to the inner and outer conductor terminations, the terminals of the coil were fabricated at the elongated ends of the conductor of DP1 and DP5. A piece of conductor of about 1 m length is standing out of the radial plate. The end of this conductor is welded to the terminal joint piece.

The design of the terminal is identical to the inner joint, however, the outer contour of the termination box is shaped to a rectangular cross-section. The manufacturing procedures for fabricating the termination is used unchanged as for the manufacture of the inner and outer terminations. The conductor is insulated up to the welding seam of the conductor jacket to the stainless steel part of the termination box.

DP1 carries the terminal connected to the positive pole of the power supply, DP5 carries the terminal connected to the negative pole of the power supply. The "bus bar 1 positive" forms a "praying hands" configuration when being joined to the coil terminal. This is important, because the insulation thickness of both the conductor end of DP5 and of the bus bar necessitated the introduction of a copper shim piece in order to bridge the geometrical distance between the copper soles. Therefore, there are two soldered connections at this joint. The "bus bar 1 negative" is connected to the terminal in the same configuration as all inner joints are made ("shaking hands"). Also the soldering technique used was identical to that of the inner joints. The reason for the difference of "praying hands" and "shaking hands" configuration lays in the routing of the bus bars arriving from the same side to the winding terminals.

*7.1.3. TFMC bus bar joints*

*7.1.3.1. TFMC bus bar termination.* The terminations of the bus bars were fabricated to an identical design except the one to be connected to the superconductive shunted copper connection bar at the cold end of the heat exchanger of the current lead (joints #1 and 15).

As the bus bar conductor is made of NbTi strands, one could profit from the fact that a heat treatment is not required and therefore a low melting interlayer between the strands and the inner surface of the copper sole was used: the copper sole was indium coated by a melting process at a thickness of a few microns. The NbTi strands were pressed into the indium-coated surface thus increasing the contact surface between strands and copper sole. Moreover, during the soldering pro-

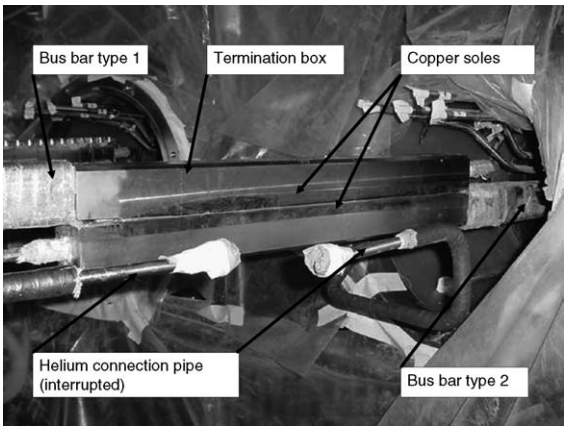


Fig. 7.7. The insulated bus bar type 1 arriving from left connected to bus bar type 2 emerging from the TOSKA cryostat extension to the right, just before being disassembled after end of test Phase I, the clamps are removed, the copper soles are aligned face to face.

cess for the fabrication of the joint, this indium layer was re-melted, thereby reducing the contact resistance of the strands to the copper sole.

The manufacturing procedure regarding the preparation of the cable end to be pressed into the groove of the termination box was used unchanged as for the inner and outer terminations. The shape of the termination box was identical to the shape of the termination box of the coil terminals.

*7.1.3.2. Bus bar type 1 to bus bar type 2 joints.* Due to the fact that the test of the TFMC was planned to be performed in two phases, these joints needed to be opened and remade in order to allow the extraction of the TFMC from the TOSKA vessel between the two test phases (see Fig. 7.7). The connections between the TFMC bus bars and the current lead system were realised by very similar joints as between bus bars type 1 and bus bars type 2: the copper soles of both parts, the termination of bus bar type 2 and the cold termination of the current lead were pressed together as described in Section 4.4.3. A special clamping system was used in order to fit with the half circular cross-section of the cold termination of the current lead and the square cross-section of the bus bar type 2.

Ten indium wires of 1.5 mm diameter were placed on the surface of the gold-coated copper sole of bus bar type 2 termination box which was facing upwards. The silver-coated copper sole of bus bar type 1 was positioned on top and pressed down using the clamping system equivalent to that of the joints between coil terminals and bus bars. A torque of 15 Nm on each of the 40 bolts (M8), which was repeatedly applied during about 10 working days (two weeks), and an elevated temperature of about 60 °C brought the creeping of the indium practically to an end.

The thickness of the squeezed indium wires remains to $0.13 \pm 0.02$ mm. The coverage of the surface by the indium is $77 \pm 2\%$, which was checked after undoing the joint during the disassembly of the TFMC for the preparation of Phase II.

*7.1.3.3. Bus bar to current lead joints.* The current lead system consists of two components: running from room temperature area to cryogenic area, there is

- a flexible water cooled bus bar;
- a helium gas cooled heat exchanger (copper rod with cooling fins, shunted by superconductive $Nb_3Sn$ inserts and a cold gas return flow at the cold end (see Section 4.4).

The connections between the TFMC bus bars and the current lead system were realised by very similar joints as between bus bars type 1 and bus bars type 2: the copper soles of both parts, the termination of bus bar type 2 and the cold termination of the current lead were gold plated, an indium foil was placed in between and the two terminations were pressed together with a pressure of about 25 MPa. A special clamping system was used in order to fit to the half circular cross-section of the cold termination of the current lead.

*7.1.3.4. Quench detection system of the bus bars.* Similar to the TFMC double pancakes, the bus bars were equipped with voltage taps providing signals for the quench protection system. The voltage taps were connected to the ends of the 2 bus bar types (see Fig. 7.8): one voltage tap was connected to the copper sole of the joint of bus bar type 1 at the winding terminal, the other voltage tap was connected to the helium outlet pipe of bus bar type 2. The wire coming from the helium inlet pipe of bus bar type 1 was placed in the central cooling channel of the bus bars. It passed the joint connecting bus bar type 1 to bus bar type 2 inside the helium pipe which connects the exit pipe of bus bar type 1 to the inlet pipe of bus bar type 2. The voltage signal therefore includes part of the ohmic resistance of the joint

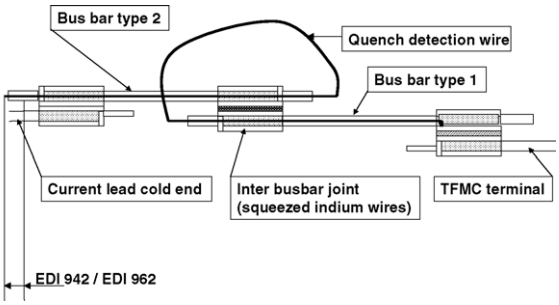


Fig. 7.8. Layout of the quench detection voltage taps of the bus bars.

"copper sole–superconducting cable of bus bar type 1", the joint between bus bar type 1 and bus bar type 2 and the ohmic resistance of "superconducting cable-copper sole of bus bar type 2". Summing up these resistances, it is estimated to be in the order of 1.5 times of a single joint between two bus bars.

In addition, the joint connecting bus bar type 1 to bus bar type 2 being designed with squeezed indium wires was expected to have a higher resistance compared to the soldered inner joints.

The helium inlet to the bus bar system was made at both coil terminals where the outlet helium from the winding terminals arrives at the other side of the joint. Due to this fact it is not possible to do any assessment of the thermal losses of the ohmic resistance of the bus bare joints: the temperature of the helium entering the cooling channels of the bus bar cables is not known, because there is an unknown heat transfer in the soldered joint of the TFMC terminals to the bus bar terminals.

The voltage drop across the bus bar system was measured using the voltage taps. Using all experiments of constant current operation of the model coil, the resistance of the bus bar system shows a small dependence to the transport current. There was no significant change of the bus bar system detected when the intermediate joint between type 1 and type 2 bus bars were opened and remade.

Fig. 7.9 shows the results calculated from the measurements of EDI942 and EDI962 voltage drops (see Fig. 7.8) as function of operating current (above 4 kA) for both bus bar systems during Phase I and Phase II operations (to improve the signal to noise ratio 7 Hz filters have been installed between phase I and phase II).

Expressing these measurements into linear trend lines, the results become:

$$R\mathrm{pos},1\,[\mathrm{n}\Omega] = 2.21\,[\mathrm{n}\Omega] - 1.25\times10^{-4}\,[\mathrm{n}\Omega/\mathrm{kA}]\times I\,[\mathrm{kA}]$$

$$R\mathrm{pos},2\,[\mathrm{n}\Omega] = 1.82\,[\mathrm{n}\Omega] + 6.88\times10^{-3}\,[\mathrm{n}\Omega/\mathrm{kA}]\times I\,[\mathrm{kA}]$$

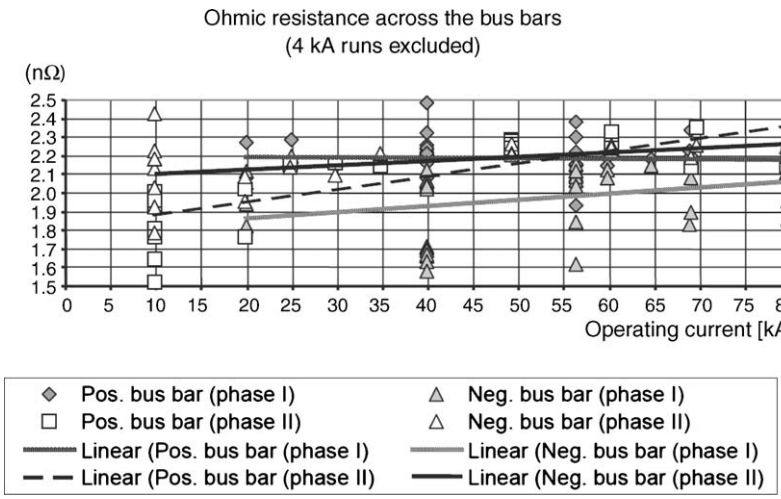


Fig. 7.9. Resistance of the bus bar system vs. operating current level.

$$R\text{neg, 1}\,[\text{n}\Omega] = 1.77\,[\text{n}\Omega] + 3.75 \times 10^{-3}\,[\text{n}\Omega/\text{kA}] \times I\,[\text{kA}]$$

$$R\text{neg, 2}\,[\text{n}\Omega] = 2.08\,[\text{n}\Omega] + 2.31 \times 10^{-3}[\text{n}\Omega/\text{kA}] \times I\,[\text{kA}]$$

Except for the positive bus bar system in test Phase 1, there is a small dependency of the resistance on the current.

As already mentioned, the resistance across the bus bar system includes not only one joint. A rough assessment gives that the resistance of a joint is composed of three main parts. Parts 1 and 3 are the resistances of the current transfer from the filaments to the copper sole contributing about 40% of the total resistance. Part 2 is the resistance of the current transfer between the two copper soles contributing to about 20% of the total resistance. Taking this partition of the joint resistance into account, the resistance of the inter bus bar joint is about 72% of the total resistance of the bus bar system. The average value therefore is

$$R\text{pos, inter} = 1.55 + 0.32/-0.64\,[\text{n}\Omega]$$

$$R\text{neg, inter} = 1.58 + 0.36/-0.48\,[\text{n}\Omega].$$

*7.1.3.5. Summary.* Although originally the twin box joint technology was developed for conductors based on $Nb_3Sn$ strands, the results of joint resistances of NbTi-based conductors are of the same magnitude. Only a few joints of this kind are manufactured by industry, however, the reproducibility was acceptable.

## *7.2. NbTi bus bars*

### *7.2.1. Bus bar characteristics*

The bus bar systems are each divided into two sections. Section 1 (bus bar type 1) was soldered to the TFMC terminals bringing the ends of the coil conductor to the entrance point of the current lead system into the TOSKA vessel. Section 2 (bus bar type 2) was part of the so-called TOSKA cryostat extensions containing the current lead system. A demountable joint connects bus bar type 1 and 2 to each other as explained in Section 7.1.3 [152].

The maximum local induction taking into account the self-field of the conductor reached 3.61 T. This gives a safety margin to the operating point of about 3 K (see Fig. 7.10).

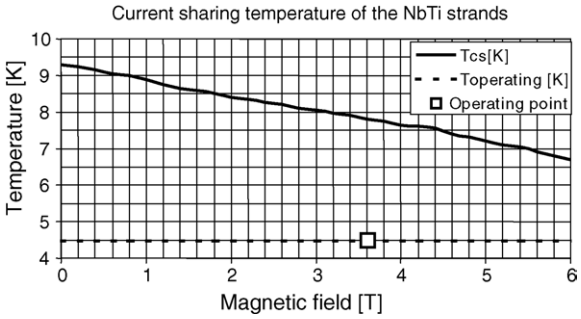


Fig. 7.10. Current sharing temperature of TFMC bus bar conductor.

The bus bars were not specifically tested, however, during the experiments with heated helium, the temperature of the positive bus bar system was elevated, because of the heat exchanging property of the TFMC terminal joint to the bus. The safety margin was reduced down to 2 K in the most extreme case. Fig. 7.11 shows the helium exit temperatures of positive and negative bus bar system during the $T_{CS}$ experiments at 80 kA with heated helium entering the inner joint of pancake P1.1 and exiting at the coil terminal joint to the positive bus bar system. However, the bus bars could be operated without any problem during both test phases.

### *7.2.2. Current distribution in bus bar type 1 positive (BB1+) and BB1−*

*7.2.2.1. Experimental set-ups.* Two different set-ups using both Hall probes have been installed on the NbTi bus bars of the TFMC. The aim of these systems was to evaluate the current distribution among the strands

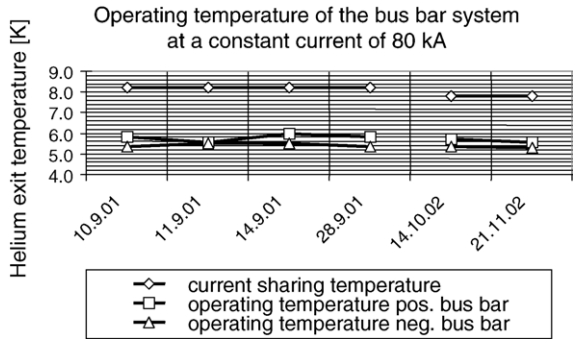


Fig. 7.11. Helium exit temperature of the bus bar system in relation to the current sharing temperature of the NbTi strands.

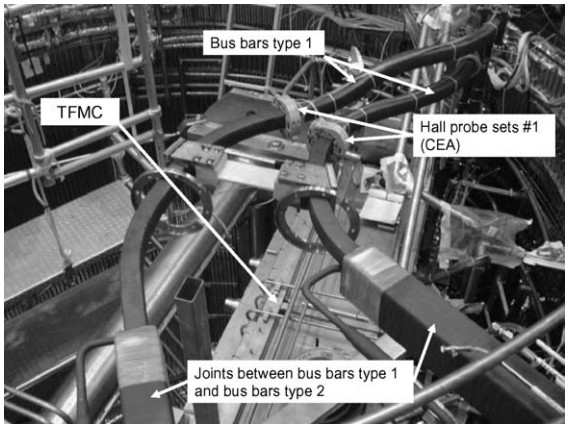


Fig. 7.12. The CEA Hall probe sets are located between the BB1–BB2 joints (at the figure bottom) and the coil terminals.

of the cables. Due to fabrication constraints and time schedule, it was not possible to install them on the TFMC conductor itself, therefore the bus bars were chosen since they use the same joint technology (i.e., twin-box concept) as the coil (see above).

A first simple set-up (#1) was installed by CEA for the Phase I experiment (single coil test) in 2001. A second more sophisticated set-up (#2) was installed on one bus bar by ENEA to be operational during the Phase II campaign (test with LCT coil) in 2002.

A simple but powerful set-up was retained for Phase I, based on the equipment already installed on the ITER CS Insert, tested at JAERI (Naka, Japan) [153,161]. Each of the BB1 leg was equipped with a four-quadrant head, measuring the tangential field component with respect to the cable (see Fig. 7.12). Four flat Hall probes are mounted into a rigid frame composed of two bolted half-moon structures [154]. This frame is then fixed and wedged onto the insulated conductor. The relative positions and orientations of the probes are thus precisely determined by the frame, while the relative position of the frame with respect to the conductor center is only roughly known due to the insulation thickness.

During the 2002 test campaign, two additional measuring heads (set-up #2), each provided with 12 Hall probes, were installed on the BB1 positive distanced by a quarter of the cable pitch. One of the heads was provided with six “tangential” probes and six “radial” ones, the other head with ten radial and two tangential probes [155].

The Hall probes were all fabricated and calibrated at the Institute of Electrical Engineering of Bratislava (Slovak Republic); the chosen type is HHP-NP, with a maximum control current of 150 mA, and a sensitivity higher than 100 mV/T (active area 0.625 $mm^2$).

All the sensors of set-up #1 were individually calibrated at 4.2 K, under magnetic field ranging from −5 to +5 T. Only 5 mA power supplies were available in Phase I, which limited the signal accuracy.

The Hall probes of set-up #2 were individually calibrated at room temperature (from −0.4 to +0.4 T), at 77 K (from −0.4 to +0.4 T), and at 4.2 K (from −2 to +2 T). In order to evaluate the effect of positioning inaccuracies, the measuring heads were first tested in laboratory, mounted on a resistive bus bar in a coaxial arrangement (i.e., the return current was flowing in an external concentric cylindrical conductor) to eliminate the influence of the return current. This provided a good indication of the inaccuracy of the Hall probes positioning and alignment in comparison to the nominal sensing direction. This latter figure was found to be in the range of 2°–3° at worst. The heads were fabricated and mounted by IEE of Bratislava. The experimental set-up included a dedicated data acquisition system based on National Instruments components and software. The accuracy of the DAS was estimated to be better than 0.1% with a sensitivity of about 1.2 μV.

*7.2.2.2. Signal analysis and reconstruction.* A systematic offset correction has been applied to every Hall probe signal by setting a zero output value when the TFMC current is zero (in Phase I experiment), this corrects both for a possible remaining stray field and for amplifier offsets.

For checking the sensors accuracy and linearity, the average value of the four sensors mounted on each bar was computed and compared to the field value given by the Ampere’s law (assuming the current uniformly distributed over the cable cross-section). If the current density in the cable cross-section does not vary over a very small geometric scale, then it can be shown, using the harmonic analysis [144], that the two values must be equal. Practically, this equality is helped by the multi-twisted structure of the cable and by the finite relative distance between sensors and cable which both mitigate the effects of small scale inhomogeneities in the cable. The agreement between the probe signals and the corresponding values derived with the Ampere’s

law actually is good (better than ±1.5% for both BB1− and BB1+ with set-up #1), which gives confidence in the values given by the probes. On the other hand, the individual signal given by each probe is highly perturbed by the stray field of TFMC and by the field produced by one bus bar leg on the other one, these two fields being proportional to the bus bar current. The main effects of these perturbations can be checked qualitatively on the signals (i.e., polarity, order of magnitude), however the exact locations and orientations of the sensors are not known with enough accuracy to allow quantitative evaluations. At the end, without the accurate knowledge of the perturbing effects, only evolution from one situation to another can be measured. However, there are conditions under which the current distribution can be assumed uniform, and which can be used as references. They are the normal state (or resistive) operation, the full quench of bus bars, and the purely inductive regime. Among these three possibilities, only the third one was used in the Phase I experiment. It should be finally noticed that these referencing methods may be even more powerful than the pure calculation of the perturbing fields, because they cope with the inaccuracy of the location of the sensors with respect to the cable itself (insulation thickness, jacket wall thickness). Only the relative locations and orientations of the sensors, one with respect to the other ones, need then to be accurately known.

There are two main ways to analyse the Hall probe signals in order to get an idea of the current distribution in the cable [144,155,159,161]. The calculation of the current barycentre location is the easiest analysis to be performed with this kind of sensors, it provides useful information such as barycentre motion, easily understandable data, but it does not give a direct information of the current unbalance responsible for a deviation from the geometrical cable centre. The calculation of the individual petal currents requires more sensors and a more complex analysis, it relies on the hypothesis of a uniform current distribution inside each petal, and it is also more sensitive to (geometrical, electrical) inaccuracies.[4] However, interesting estimations can be made using only four probes with the so-called four-quadrant model. The two analysis methods used by CEA can be found in [155] and in more details (with a third method) in [144], they will therefore not be treated here.

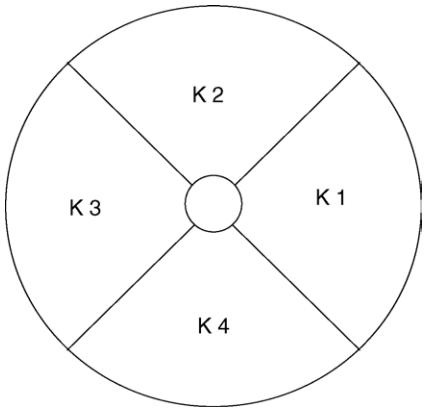


Fig. 7.13. The CEA four-quadrant model used for the bus bar cable.

The four-quadrant model simply corresponds to the division of the cable cross-section into four quadrants instead of six real petals (see Fig. 7.13). This model assumes a uniform current distribution within each quadrant. In order to get absolute values, for each leg the steady state current distributions were compared with the inductive current distribution (best determined at the end of ramp-up at 40 kA, with 300 A/s). The differences between steady state distribution and inductive distribution in BB1+ (relative deviation of quadrant currents with respect to average value: $\delta K/K_{ave}$) are plotted in Fig. 7.14. Similar results are found in BB1− [155]. Then, assuming the inductive distributions to be uniform, the non-uniformity of the steady state distri-

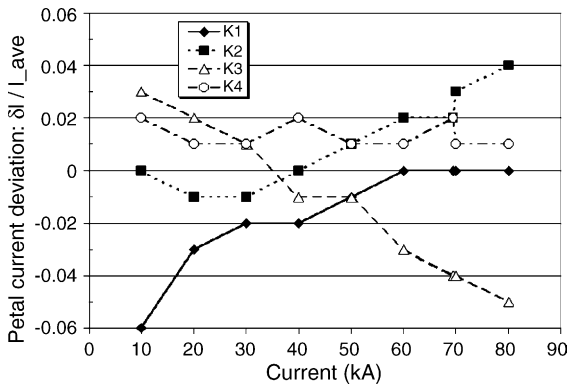


Fig. 7.14. Evolution of BB1+ steady current distribution with total current (set-up #1).

[4] The calculation of the individual petal currents may also be misleading in case of a real cable deformation.

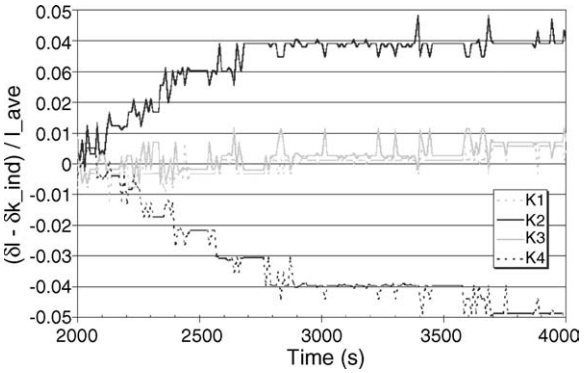


Fig. 7.15. Evolution of current distribution among petals in BB1− during flat top at 40 kA following a ramp at 300 A/s (set-up #1).

butions remains quite low (better than ±6%), although a slightly higher scattering should be expected among the real six petals. This is within the range expected from the TFMC bus bar joints geometrical analysis (≈±10%) [156]. It can also be seen that the uniformity of the current distribution among the petals does not necessarily improve as the transport current increases. Note that the accuracy is ±0.5% on $\delta K/K_{ave}$, once the inductive distribution is assumed uniform.

After having removed the inductive current distribution from the transient distribution, the evolutions of the quadrant currents during a plateau current at 40 kA, following a ramp at 300 A/s, were plotted in Fig. 7.15. Particularly, one can see that there is a small loop current (about 5% of $K_{ave}$) flowing mainly through two opposite quadrants (corresponding to K2 and K4, see Fig. 7.14), and which is due to unbalanced current sharing in the steady state regime as compared to the inductive regime (assumed uniform). The time constant for current redistribution is about 400–500 s. This whole transient can be well modelled by considering a relative resistance unbalance of 5% (in the joints) between two opposite petals [155]. The same kind of phenomenon exists in BB1+, with a lower loop current (about 3% of $K_{ave}$), different quadrant locations, and about the same time constant [144].

Set-up #2 is more sophisticated and leads theoretically to more accurate results, although it requires a more complex analysis and needs more accuracy on the measurements. From the mathematical point of view, the reconstruction of the current profile falls into the class of inverse problems. The actual number of Hall probes available in measuring systems (12 for each Hall probe head) is very small compared to the number of current carrying strands (1152) in the considered cable (a full ITER cable), whose last stage is composed of six groups of s/c strands (the “petals”), helicoidally twisted with a pitch of 450 mm. A simplifying assumption of uniform current distribution inside each petal allows reducing the number of unknowns to six. The degrees of freedom are therefore the “equivalent” current amplitudes in each petal. The choice of over determining the system of equations guarantees better smoothness properties also in the case of ill-conditioning, and higher robustness with respect to measurement inaccuracies and model uncertainties. As discussed above, the ill-conditioning of the equations system makes the solution extremely sensitive either to inaccuracies in the model parameters and to measurement noise [157–159]. To limit the errors in the reconstructed currents, instead of considering the total currents in each petal as model unknowns, the system was reformulated in terms of “petal current unbalances” with respect to the resistive (i.e., not superconductive) current profile, assumed here uniform. The advantage of such a formulation is that the evenly distributed current contribution can be measured in a situation, in which the cable is in the normal state, and then scaled, for each experiment, to the actual total current in the cable. Such an approach requires of course an experiment dedicated to the measurement of the field map under controlled conditions [155]. For the evaluation of the self-field profile, the model takes into account a spatial (3D) geometry of the bus-bars and the geometrical details of the six petals twisting in the vicinity of the Hall probes and position of the cable inside the conduit [157], An example of current re-construction at 69 kA TFMC current is shown in Fig. 7.16. A spread of approximately ±25% around the average petal current value can be seen in the re-constructed currents.

A similar result, indicating a spread in the petal currents up to ±30% from the average current per petal, was found also in the case of another somewhat simplified model introduced by the University of Twente [159], where six petals are assumed to be straight and infinitively long pieces and not being twisted. An example of a current reconstruction at 10 kA TFMC current is shown in Fig. 7.17, where the currents in the six petals are evaluated at the instant just before the cur-

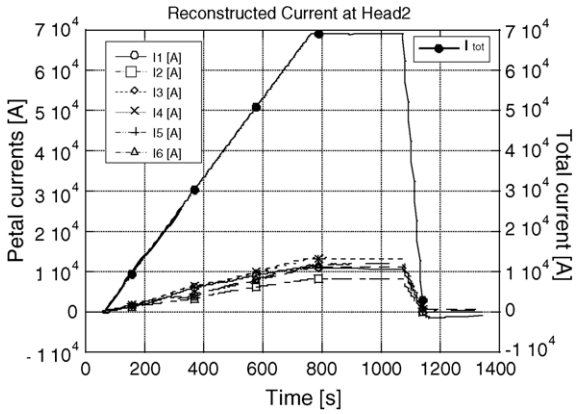


Fig. 7.16. Current in the petals reconstructed from measurements at Head 2 (set-up #2).

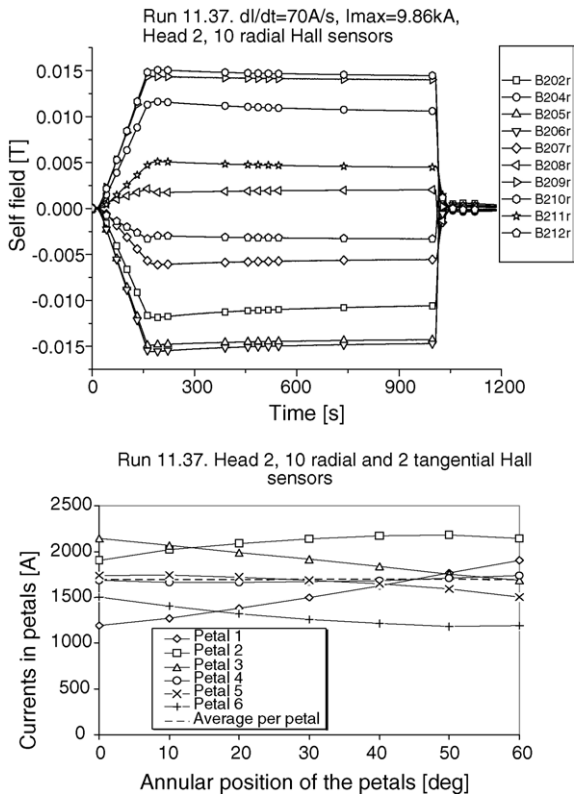


Fig. 7.17. An experimental run and current in the petals reconstructed from measurements at Head 2 (set-up #2) using simplified model.

rent ramp down and as a function of the angle between the Hall probes and the petals array orientation [160]. The ±30% unbalance calculated by the Twente model is based on the resistive (i.e., non-superconducting) distribution as a reference. The solution is practically similar to the one presented in [157], in spite of the fact that the Twente model is basically simpler. The similarity of the results obtained by the two models points toward the conclusion that the result of the current reconstruction is hardly coherent with the accuracy in the geometrical parameters knowledge. The proposed model gives an acceptable solution for currents in sub-bundles or petals of the cable with an accuracy of about ±10% but only if their exact geometry and location is known and all experimental errors are minimized. For this reason it is attractive to subdivide the cable into sub-bundles but as a consequence it is still required to assume that the current in a defined bundle is homogeneously distributed. However, when the geometry and position of the petals inside the conductor is not well-known, as for the TFMC, the accuracy decreases to at about ±30%. Unfortunately, this variation is of the same range as the error of reconstruction [159]. Therefore, it is impossible to distinguish between a uniform and non-uniform current distribution in absolute sense for this TFMC test, only relative changes can be quantified more accurately.

In a number of experiments with TFMC powered alone, after the current shutdown, a persistence of signals from Hall probes has been observed in spite of the fact that the total current in the coil had been extinguished. This could indicate the presence of some currents in the petals, although without any net transport current in the conductor. This could be explained by postulating “current loops” involving inductive paths closing on inter-strand (or inter-bundles) contact resistances or at the joints.

The effect was observed in several experiments. The currents, reconstructed on the basis of the measurements from Head 2 and Head 4, in an experiment with flat top current of 10 kA and current ramp-up of 70 A/s (no current in the LCT coil) are shown in Figs. 7.18 and 7.19. After the total transport current goes to zero, some currents of a couple of hundreds ampere of maximum amplitude, and whose sum is zero, remain in the six petals both with positive and negative sign, slowly decaying on the time scales of a few hundreds of seconds.

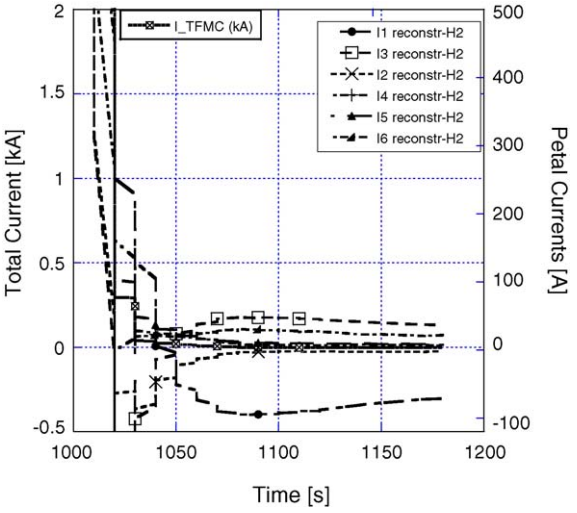


Fig. 7.18. Petal "persistent" currents at the end of the pulse (from Head 2 of set-up #2).

All methods of current reconstruction based on self-field measurements can give solutions with even larger uncertainty when local non-uniformities are present inside the bundles. This is possible for instance if the probes are located on a short distance from the joints at the extremities of a cable. The current distribution within a petal is not necessarily homogeneous when

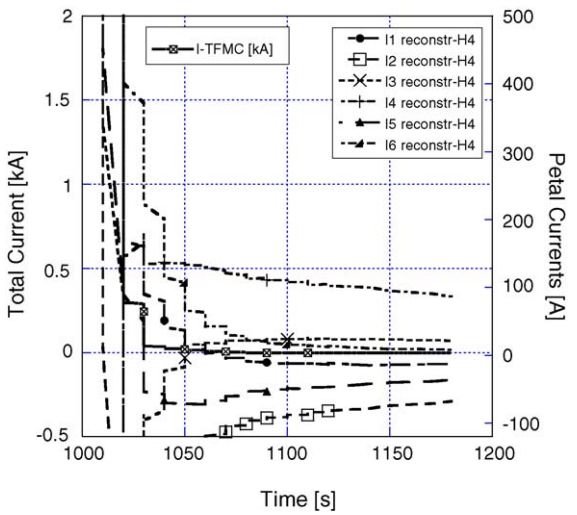


Fig. 7.19. Petal "persistent" currents at the end of the pulse (from Head 4 of set-up #2).

arrived in the "resistive" regime (current plateau) coming from the mainly inductive regime (current ramp), as it is then determined by the variation in joint connection resistances between strands. A cable having the size of a petal has no homogeneous current distribution by definition, even when all the strands are connected by very low resistance at the joint. This has been demonstrated with the analysis of the self-field measurements on the so-called SeCRETS conductors in SULTAN [162]. In principle, the TFMC conductor can be considered as having six of such conductors in parallel, although the variation in connection resistance between strands in the joints is likely worse. Moreover, a certain level of current unbalance can even occur for the "normal state reference" in non-superconducting state representing the homogeneous calibration of the method.

Also the alternative method for calibration by using the inductive regime, supposing homogeneous petal currents distribution, may be less advantageous as the time frame required to charge such a large magnet as the TFMC, is in the same range or even larger than the time constants involved in the redistribution of currents. This means that redistribution of currents already starts at the beginning of the ramp although the impact of the redistribution depends on the ramp rate. Obviously this method can only be used when the initial strand currents, at the start of the current ramp, are all set to zero [154].

*7.2.2.3. Summary.* The Hall probe set-up (#1) installed on the TFMC bus bars BB1− and BB1+ during Phase I operation (single coil test) has proved to be a sensitive tool for estimating current unbalance among the conductor petals through the four-quadrant model. A slight evolution (without improving uniformity) of petal currents with steady transport current has been found. Assuming the inductive current distribution to be uniform, one could get absolute values for the steady state current distributions, which then turn out to deviate only by less than 6% from the uniform current distribution for both bus bars, in agreement with expectations from geometrical measurements (about ±10% expected). However, the capability to get absolute values for petal current deviations relies on an assumed reference for perfectly uniform current distribution, which cannot be checked in a different way. The inaccuracy linked to this refer-

ence may exceed the inaccuracy of the measurement itself.

The encouraging results obtained from the measurements with set-up #2 during Phase II campaign indicates that the detection of current unbalances in ITER type conductors is possible using measuring heads composed of Hall probes. On the other hand, the actual quantitative assessment of the reliability of the current re-constructions was extremely hard to obtain due to the lack of independent and dependable measuring systems.

The apparent discrepancy between the quantitative results obtained with the two different set-ups can be explained by the following arguments:

- set-up #1 results concern Phase I experiment only while set-up #2 is dealing with Phase II, and the inter-bus bar joints were dismantled and rebuilt in between the two phases;
- the four-quadrant model leads to a better apparent uniformity than six real petals by principle (there is a kind of averaging in each quadrant);
- the hypothesis of uniform current distribution among the strands of a sub-structure (i.e., a petal or a quadrant), which is used in all models, may be not fully valid and its impact on the final results may be different for the three models;
- the reference of uniformity is not the same for the three models: resistive state (#2) or inductive distribution (#1), and maybe none of them is really uniform at a few percents.

Note finally that the expected value of ±10% comes from some discrepancies among the final twist pitches of the cables observed during the fabrication of the bus bar joints, which led to mismatch in the joints. Although the overlapping lengths have been calculated in order to minimize the effect on petal current non-uniformity, it was not possible to avoid a final non-uniformity of about 10% as computed.

### 7.3. Summary and conclusions

The resistances of all the TFMC joints were found to be as low as expected (i.e., below 1.8 nΩ) in spite of the high magnetic field applied on the inner joints. The extrapolations to zero magnetic field have produced quite low and homogeneous values (within the 1–1.3 nΩ range) for all the inner and outer joints. These values lie within the lower half range between the relevant full-size joint samples tested in the SULTAN facility. The industrial fabrication of the TFMC joints has led to a rather good uniformity of the joint resistances certainly due to well defined and repetitive processes, the quality of the outer joints (strand–copper interface) has been significantly improved compared to the relevant SULTAN joint sample.

The resistances of the two dismountable joints between the NbTi bus bars were found to be also low (i.e., about 1.5 nΩ) and to be reproducible after dismantling and rebuilding of these joints.

The measurements of the current distribution among the conductor petals of the NbTi bus bars was performed using Hall probes, first in simple four-quadrant set-ups (Phase I), then in more sophisticated set-ups (Phase II). These tools have proved to be very sensitive although the interpretation of the results has appeared rather difficult because of the stray field produced by the TFMC on the sensors. The results then rely on the hypotheses about conditions used as references for uniform distribution (inductive regime, resistive state) as well as on the uniformity of the current distribution inside each petal. The discrepancy between the two set-up analyses (6% of petal current deviation by the first one against 25% by the second) has not been yet fully understood although tracks have been identified.Symbols used in equations:

| Symbol | Explanation |
|---|---|
| $\mathbf{B}$ | Magnetic field (vector) [T] |
| $\mathbf{B}_{\perp}$ | Magnetic field component perpendicular to current lines (vector) [T] |
| $\mathbf{B}_{//}$ | Magnetic field component parallel to current lines (vector) [T] |
| $B_x$ | Radial magnetic field component (with respect to TFMC) [T] |
| $B_y$ | Axial magnetic field component (with respect to TFMC) [T] |
| $I$ | Current through TFMC coil [A] |
| $K_{\mathrm{ave}}$ | Average value of quadrant current (CEA four-quadrant model) [A] |
| Kn | Current in quadrant #$n$ (CEA four-quadrant model) [A] |
| $p$ | Inlet helium pressure [Pa] |
| $P_{\mathrm{j}}$ | Joule power dissipated along a pancake [W] |
| Pnq | Pancake #$q$ (1 or 2) of double pancake #$n$ (1–5) |
| $q$ | Helium mass flow rate through a pancake [kg/s] |
| Rneg,1 | Negative (pole) bus bar resistance in Phase I (including joints) [Ω] |

| Symbol | Explanation |
|---|---|
| Rneg,2 | Negative (pole) bus bar resistance in Phase II (including joints) [Ω] |
| Rneg,inter | Negative (pole) inter-bus bar joint resistance [Ω] |
| Rpos,1 | Positive (pole) bus bar resistance in Phase I (including joints) [Ω] |
| Rpos,2 | Positive (pole) bus bar resistance in Phase II (including joints) [Ω] |
| Rpos,inter | Positive (pole) inter-bus bar joint resistance [Ω] |
| $R_o$ | Electrical resistance of a joint extrapolated at zero magnetic field [Ω] |
| $R_{inner}$ | Electrical resistance of a TFMC inner joint [Ω] |
| $R_{joint}$ | Electrical resistance of a joint (TFMC or FSJS) [Ω] |
| $R_{outer}$ | Electrical resistance of a TFMC outer joint [Ω] |
| $R_{pancake}$ | Electrical resistance of a TFMC pancake (including the joints) [Ω] |
| $T_{CS}$ | Current sharing temperature [K] |
| $T_{inlet}$ | Helium inlet temperature [K] |
| $T_{outlet}$ | Helium outlet temperature [K] |

General acronyms, abbreviations, and initialisms are explained in Section 8.

## 8. Mechanical properties

Concerning the mechanical properties the aim was to test the model coil under ITER relevant stress and deformation conditions. The test was performed in two phases. In the first phase the TFMC was tested as a single coil up to 80 kA. Under these conditions only 'in-plane' stresses and deformations take place. In the second phase the TFMC was tested in the background field of the EURATOM LCT coil, in nearly parallel positions (4.5° angle) with the interposed inter-coil structure transferring the forces between the two coils. The combined operation of the TFMC and the LCT coil, with the ultimate attainable limit of 80 and 16 kA, respectively, causes 'out-of-plane' load and bending in the TFMC, as well as significant increase in the 'in-plane' stresses. In order to adjust the level of stresses in the winding pack and casing to the ITER TF coil level, an initial gap was introduced in wedge L4 (LCT coil side) transmitting the TFMC load to the ICS. The status of bonding between casing and winding pack and, in addition, frictional behaviour between other test rig components including opening or closing of gaps between the contact surfaces, determine the relative loading and stresses which can lead to highly non-linear mechanical behaviour.

### 8.1. Mechanical instrumentation

The TFMC was instrumented with potentiometric displacement sensors (GDI), 'rosette' strain gauges (GRI) and uni-axial strain gauges (GEI), where each strain gauge was temperature and magnetic field compensated by operation in half bridge circuit with one unstrained nearby gauge. The position of sensors is shown in Fig. 8.1.

Six displacement sensors (GDI830–GDI835) measure the horizontal expansion of the coil aperture, three on each side in symmetrical positions; two (GDI820–GDI821) determine the vertical elongation on the coil mid-plane, and four (GDI770–GDI773) the coil vertical elongation at the joints leg.

The digital conversion of the signal has an accuracy of 0.04 mm (40 μm), which should be considered as the error bar. In some cases, the most noticeable being GDI773, the signal is affected by noise during the current ramp up/down phases, but it is reliable under steady state current.

All strain gauges are located on the main planes of symmetry on the horizontal and vertical axes of the racetrack. Ten 'rosette 45°' strain gauges are used to measure the strains on the surface of the coil case at the following locations: four on the coil inner bore ring surface on the vertical plane, two at the top (GRI830–GRI831) and two at the bottom (GRI820–GRI821) in nearly out-of-plane symmetrical positions, at the location where maximum stresses are expected. On the horizontal plane four gauges are on the TFMC front side (the side that is not facing the LCT coil), two on the coils 'joint leg' (GRI836–GRI838), and two on the coil front leg (GRI828–GRI826). Two gauges are on the TFMC LCT coil side (the side that is facing the LCT coil and the ICS), one on the coils 'joint leg' (GRI835) and one on the front leg (GRI825). Each of the three channels (three half bridges a–c) is recorded. The signal at zero current is assumed to be an offset, equivalent to zero forces. This allows to reconstruct the principal stresses and the stress intensity (Tresca stress).

Fourteen uniaxial gauges are located around the coil cross-sections on the main planes of coil symmetry orientated along symmetry planes, to provide information on the case wall deformation.

Additional instrumentation was installed on the ICS as shown in Fig. 8.2 to allow for the observation of the highly loaded ICS and the coil configuration.

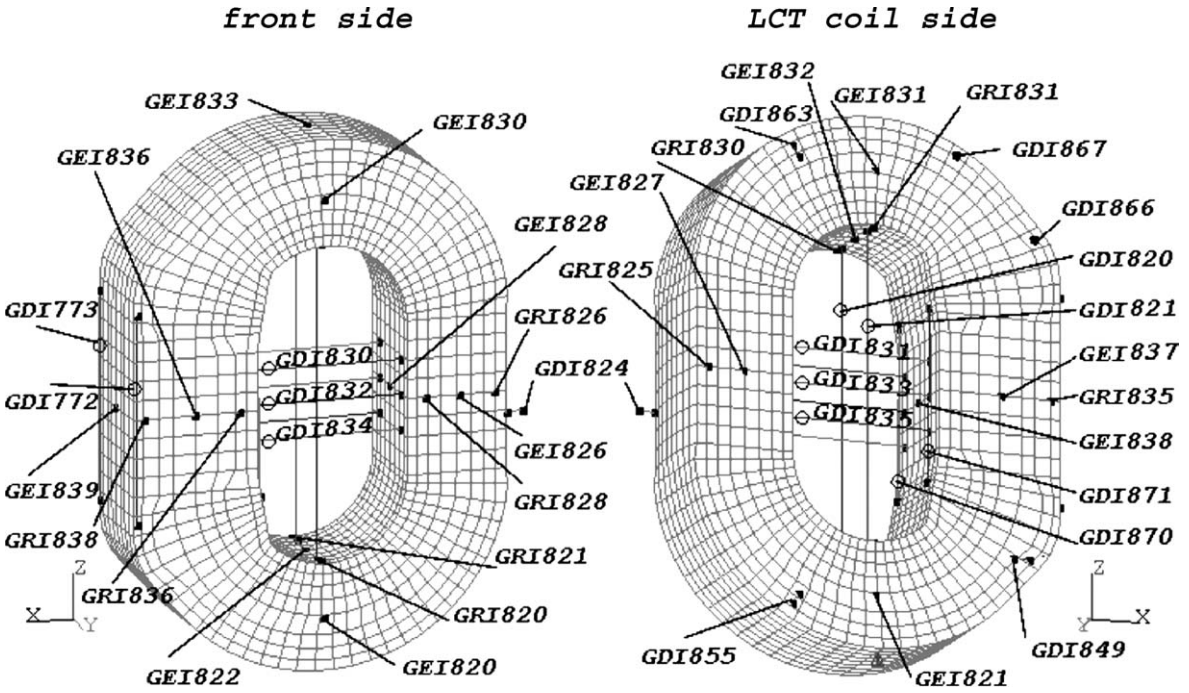


Fig. 8.1. Mechanical sensors on the TFMC (GDI, displacement transducer; GEI, strain gauge; GRI, 45° strain gauge rosette).

Nine GDI sensors allow to measurement of the gross ICS deformation (GDI890–GDI891), the gap closure at the side wedges (GDI866–GDI867) during loading, the relative in- and out-of-plane displacements between TFMC and ICS (GDI849, GDI855, GDI863) and the relative change of distance between the attracting coils under load (GDI845, GDI865).

The stress level and load distribution of the highest loaded side wedge is observed by one GRI sensor (GRI845) and four GEI sensors (GEI845–GDI848) sitting on the supporting ribs.

Sixteen GEI sensors give information of the load transfer between the ICS and the LCT coil near the supporting areas.

### *8.2. The FE model and predictive calculations*

The predictions for the whole test rig behaviour were obtained using the FE model described in [163,164] and shown in Fig. 8.3. The TFMC is fixed in the ICS by four side wedges L1–L4 and a front wedge (shown also in Fig. 8.2). The ICS is supported on the LCT coil side plate by ribs (horizontal plates) pads and hooks (shown in Fig. 8.2) forming the desired two coil configuration. The TFMC is modelled as a winding pack with orthotropic material properties simulating the conductors in the radial plates with insulation material surrounded by the coil case (Fig. 8.4). The contact behaviour (force transfer) between the winding pack and the coil case is simulated by contact elements that are also used at all contact surfaces between various test components. This contact behaviour, together with assumed friction, results in non-linear mechanical response. The Lorentz forces for the two coils are determined in a separate electro magnetic FE analysis using the FE grid of the two winding packs. The FE model, built with the ANSYS code [165] includes 15465 eight-node brick elements, 11710 four-node shell elements, 2990 four-node surface-to-surface contact elements and 481 two-node beam and link elements.

The test procedure for the determination of the mechanical behaviour was a linear ramping up of the currents in the coils up to maximum load, a subsequent hold at maximum current and a subsequent ramping down with the same ramp rate. To assure thermal equilibrium and thus avoid temperature effects of the strain

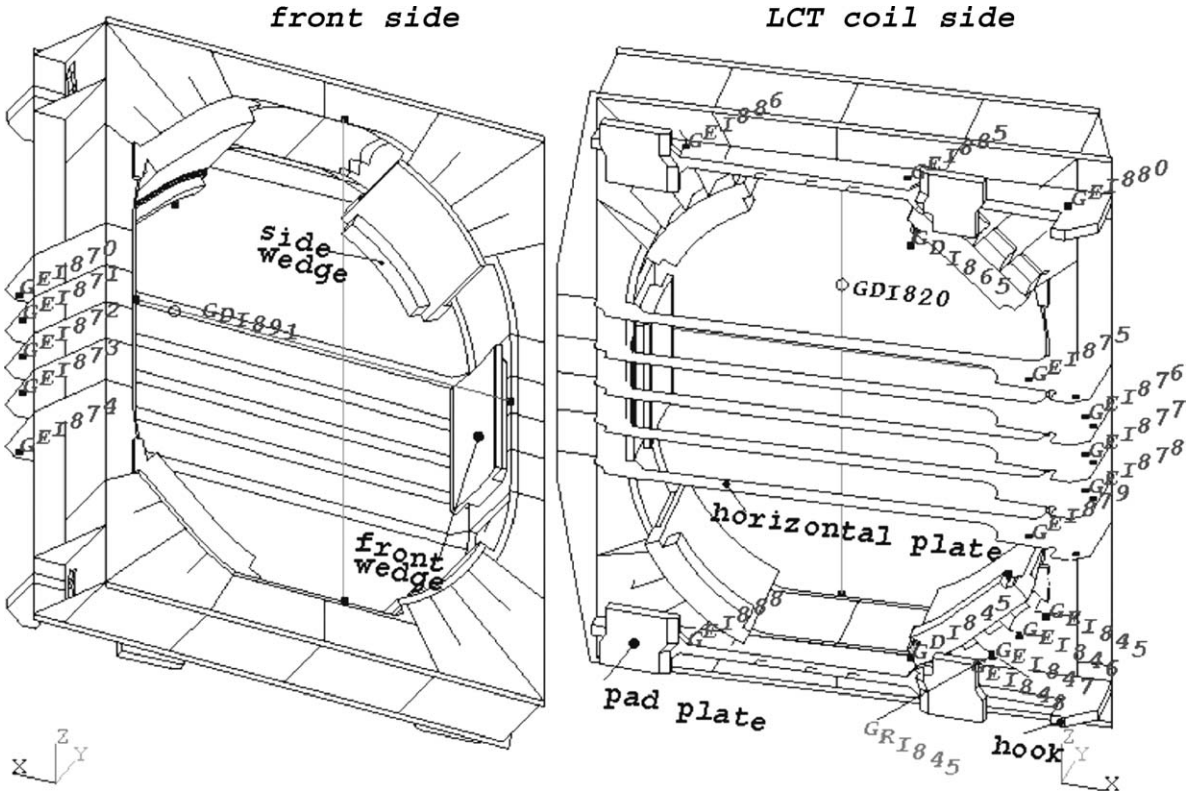


Fig. 8.2. Mechanical sensors on the ICS (GDI, displacement transducer; GEI, strain gauge; GRI, 45° strain gauge rosette).

gauges the ramp rate was chosen to be <70 A/s. FE calculations were performed to simulate such current ramp loadings. For comparison, calculated and measured values are plotted against the percentage of the load, which is proportional to the square of current in the single coil test and the product of the currents in the two-coil test, respectively. A linear mechanical behaviour should result in a linear rise and fall of stress, strain and deformation. Non-linear behaviour will result in non-linear curves and/or some hysteretic behaviour. An example is shown in Fig. 8.5 for the out-of-plane sliding of the TFMC in the front wedge measured by GDI824. In this example the FE model prediction can only reproduce the mean behaviour but not the strong hysteretic behaviour due to friction.

The accuracy of the simulation results depends on the accuracy of the model details and the fineness of the chosen mesh. In addition, the unknown friction behaviour at various contact surfaces creates some uncertainty in the model predictions. Therefore, the coefficient of friction was varied in the FE analysis. A further contribution to the model discrepancy comes again from the model mesh since for the prediction of a sensor reading the value of the node nearest to the sensor position is used without further interpolation.

### 8.3. Mechanical data evaluation

#### 8.3.1. Supporting structure

Due to the space limitation in the TOSKA vessel the ICS could not be designed as stiff as desired. The predictions showed, e.g., that in some parts (highly loaded side wedge L2 (Fig. 8.3)) the stresses at maximum load were at the limit of the allowable. In addition, some imperfections caused in the ICS in the course of fabrication and during test rig assembly required a diligent observation of some sensor readings throughout the test to guarantee the safety of the test rig. Concerning the model coil behaviour it was important to check the supporting stiffness of the ICS and the LCT coil, which

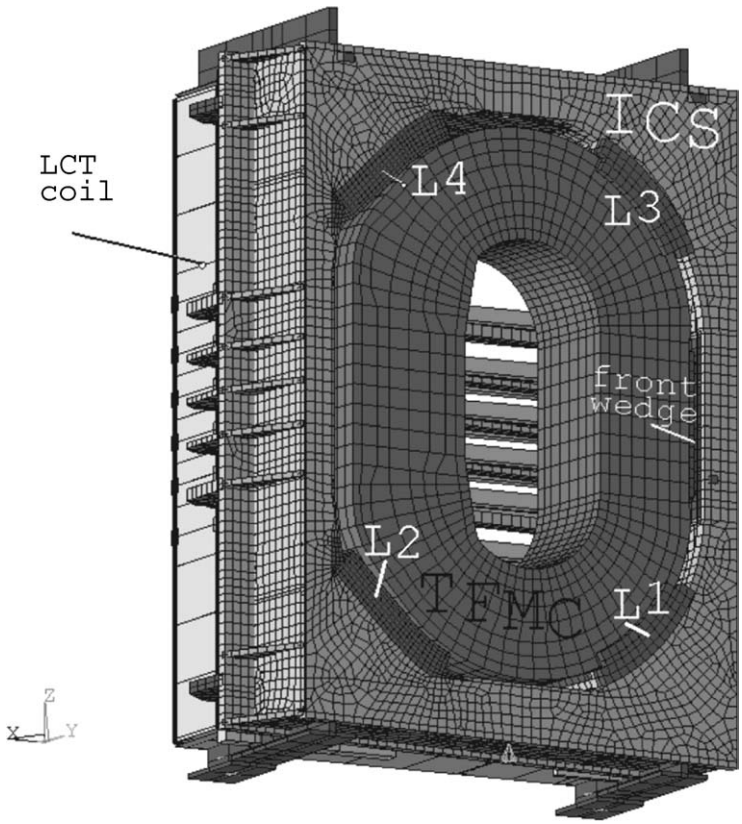


Fig. 8.3. FE model of the coil assembly.

provided support to the coil and therefore had some influence on the coil loading.

For the test rig integrity, the observation of side wedge L2 (Fig. 8.3) was important. In the analysis local plasticity was predicted for the rated load case (70/16) (70 kA in the TFMC, 16 kA in the LCT coil). During the test the stress level of the side wedge was observed by GRI845 mounted on a stiffener of the high loaded side wedge (Fig. 8.2) and compared to the FE predictions for that load case. Due to the fact that this stress (Fig. 8.6) was only 20% higher than predicted, the safety margin of the structure determined in the aforementioned plastic analysis allowed performing the originally planned loading case (80/16) (extended case) and thus allowed reaching the stress level of the ITER TF coils.

The quality of the supporting stiffness simulation can be seen at the contact behaviour of the rear side wedges L2 and L4. As mentioned above, an initial gap was introduced at L4 to increase the coil stress by additional out-of-plane bending. In addition, to allow for a smoother stress distribution, some wedge shaped supporting sheets have been introduced on all side wedge supporting surfaces in the design. They allow control of the contact behaviour in such a way that the contact first occurs at the inner sides of the wedges and after some coil deformation the supporting contact surfaces spread over the whole length of the side wedge. Fig. 8.7 shows this behaviour during the coil loading up to 100%. In that detail the test object behaves as predicted. It seems that the distance between the coil and the wedge is about 1 mm less than designed. The relative change of distance between the two attracting coils is shown in Fig. 8.8 measured by the two sensors between the LCT coil and the rear side wedges. The relative displacement at the upper side wedge was predicted rather well. At the lower side wedge, the measured displacement is 30% higher than predicted. The discrepancy is mainly due to lesser stiffness

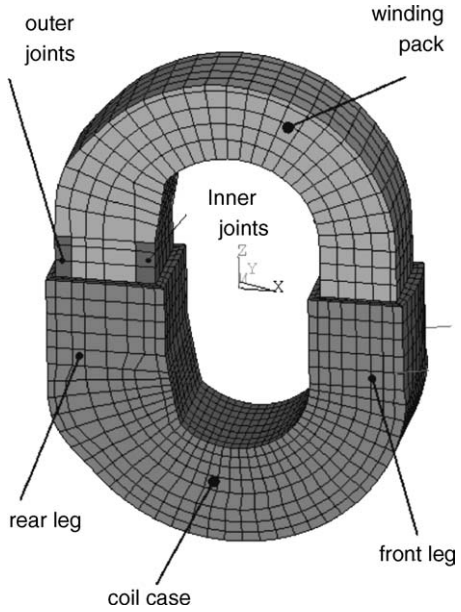


Fig. 8.4. FE model of the TFMC.

observed at loads less than 10%. Unfortunately, all the displacements between different parts of the test rig are relative measurements and it is not possible to separate the contribution of each component.

Concerning the load transfer between the ICS and the LCT coil measured by single strain gauges some discrepancy between measurement and prediction occurred. In the out-of-plane direction more load is transferred on the rear side and by the horizontal plates than predicted. In the in-plane direction the load transfer is more concentrated at the hooks of the pads than at the hooks of the horizontal plates. As mentioned above the fabrication of the ICS lead to strong imperfections caused by welding that could not be modelled analytically. In addition to the geometry imperfections, the structure is supposed to be strongly pre-stressed because it was not possible to anneal it after welding. In addition, during the assembly of the components it was difficult to control the contact surfaces where sheets had to be adapted to get initial contact between the ICS and the LCT coil. Therefore, some imperfections at the contacting surfaces may also have some influence on the load transfer and stiffness behaviour.

### *8.3.2. TFMC*

The questions, which the mechanical data evaluation intended to answer, are the following. Does the FE model adequately represent the TFMC behaviour:

(a) Operating as single coil?
(b) In combined operation under the effect of the LCT coil background field?

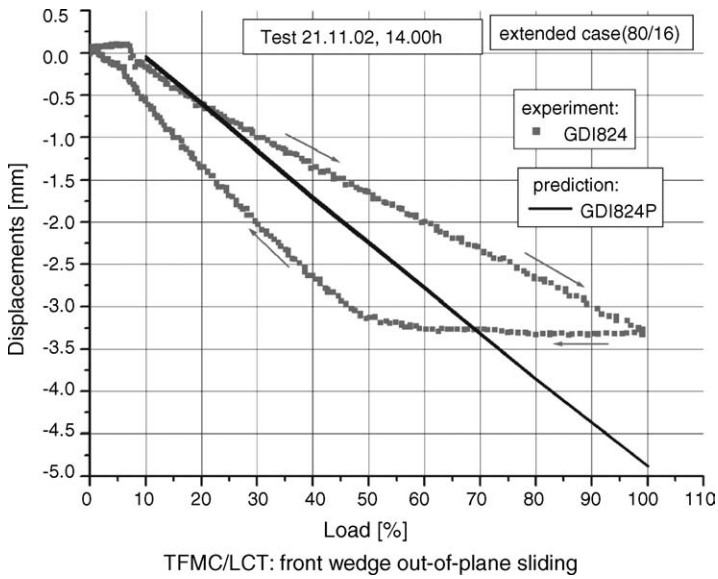


Fig. 8.5. Non-linear and hysteretic behaviour during up and down ramps.

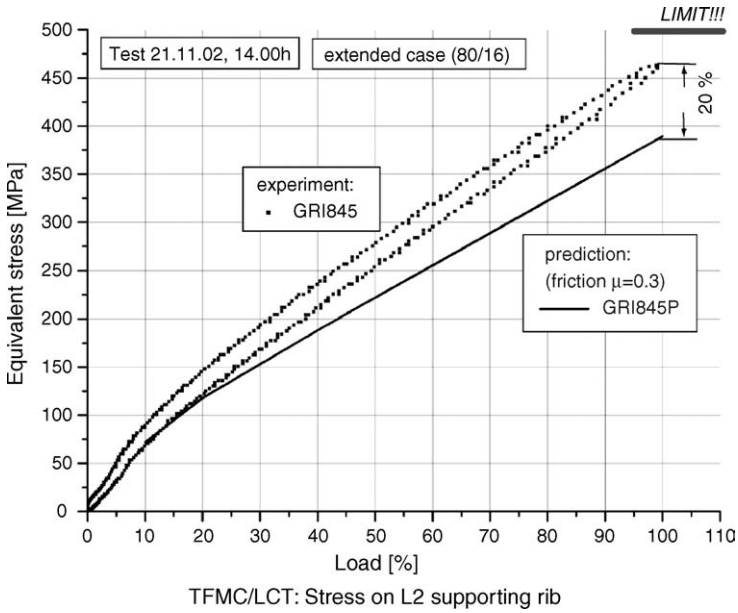


Fig. 8.6. Stress on side wedge L2 supporting rib.

(c) The best fit in relation to the assumed friction coefficient?
(d) Did the TFMC behaviour change in any respect after the cycled operation tests (TFMC 70 kA–LCT 16 kA) indicating degradation and/or setting effects?

The main results are just given in [166]. In the following some more details are presented.

*8.3.2.1. Single-coil operation of the TFMC up to 80 kA.* Concerning the FE calculations these tests allowed checking the TFMC model without interfer-

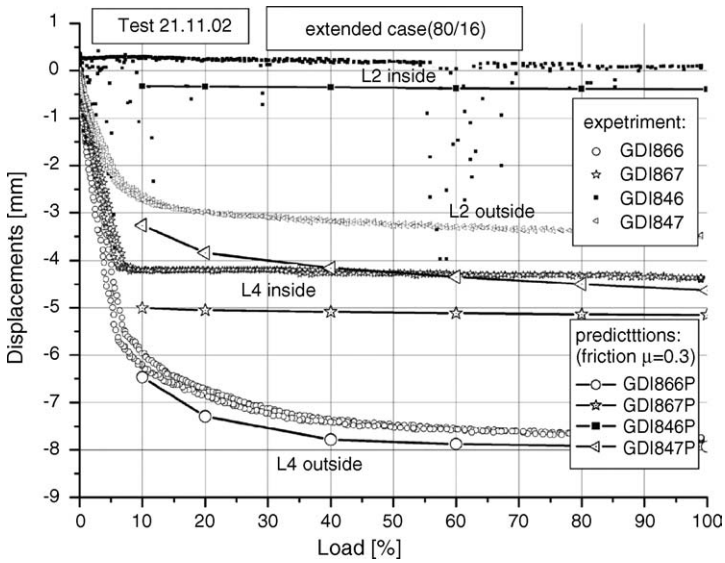


Fig. 8.7. Gap closure at side wedges L2 and L4.

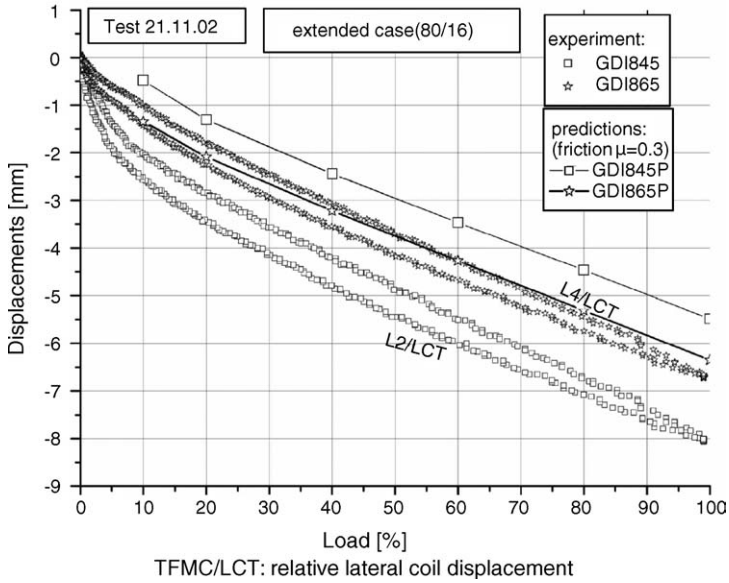


Fig. 8.8. Relative lateral displacement between TFMC and LCT coil.

ence of the ICS and LCT coil since only the TFMC was loaded. With regard to the instrumentation checks of sensors could be performed owing to symmetric positioning in the out-of-plane direction.

As the coil shape tends to deform from a racetrack into a circular shape, the coil inner bore tends to contract vertically and expand horizontally. The coil is subjected to hoop stress and in-plane bending. Maximum stresses are at the top and bottom inner ring on the vertical symmetry plane.

In principle, the displacement sensors GDI demonstrate linear behaviour, but as shown in Fig. 8.9 for three selected sensors measuring the main TFMC deformations some stick–slip and hysteretic effects occur indicating some friction behaviour. The following results were concluded from Fig. 8.10, showing the values for maximum current and all sensors:

The horizontal displacement signals correlate well with the predictions and have the expected symmetry due to the sensors location; GDI830–GDI831–GDI834–GDI835 all measure +1.5 mm and GDI832–GDI833 both measure +1.6 mm. Predictions overestimate by +15%.

The vertical displacement measurements are within ±20% of the predictions, although with no such clear cut tendency to over or underestimate as for the horizontal displacements. The signals, in the ‘joint leg’ of the coil are not as symmetrical as one might expect, possibly due to the real complexity of this leg, which contains the pancake joints, and local frictional effects.

The results for Tresca stress evaluation at the maximum load gained from the GRI sensors are shown in Fig. 8.11. On the inner ring (Fig. 8.11, left hand side) the predictions fit the measured values within 10%. Less agreement is found for the stress values on the cover plate and bottom plate of the case (Fig. 8.11, right hand side). A closer look at the individual strain gauge signals showed that this is an effect of the level of the signals [163]. Low level signals are highly disturbed showing rather non-linear behaviour and give relatively poor agreement with the predictions whereas high level signals demonstrate fairly linear behaviour and are in good agreement with the predictions. For the rosettes on the inner ring, all three strain gauges show nearly equal high values but for the other rosettes one strain gauge has the major strain and the other only small components.

The GEI sensors were intended to give information about the local case wall deformations in the equatorial and vertical cross-sections. For example, Fig. 8.12, shows the deformed case wall in the upper vertical cross-section and a path plot around the coil case cross-

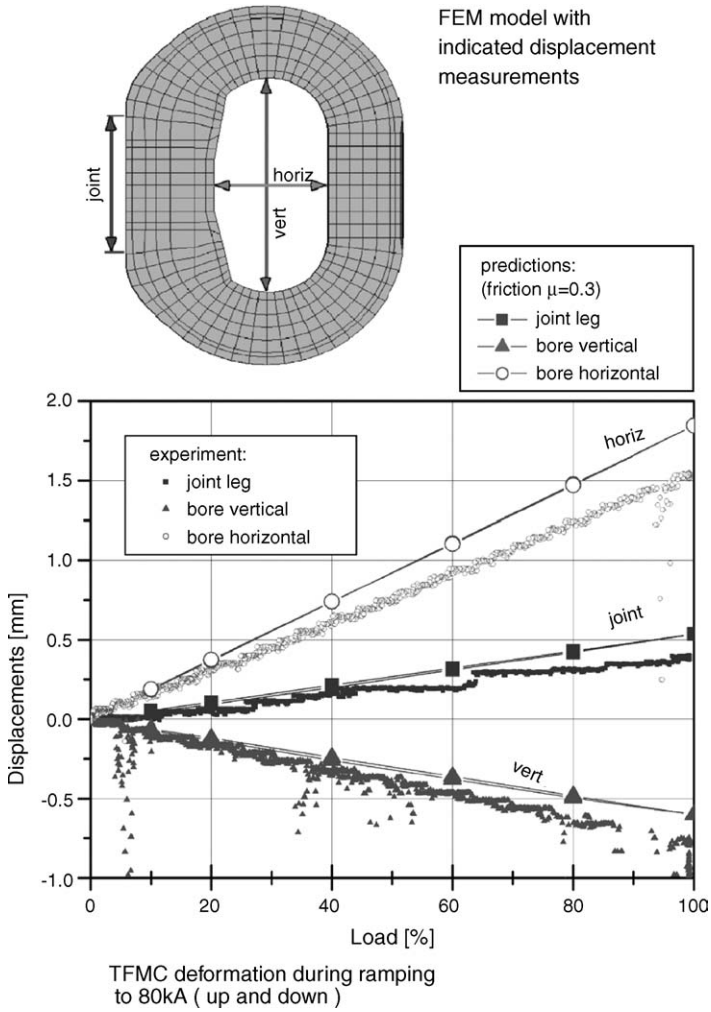


Fig. 8.9. Main TFMC deformation during ramping to 80 kA (up and down).

section for the strains in the path direction. The deviation of the two sensors (GEI832, GEI833) is quite acceptable, for the other two sensors (GEI830, GEI831) it is not. On the sides, where the latter are sitting, a change of sign of the strain occurs near the sensor location. In the FE analysis the location of zero value will be rather sensible to the mesh of the casing and the contact behaviour. In the actual calculation the mesh may be too coarse to describe the detailed case behaviour properly. In addition, the local wall deformation behaviour may be disturbed by unpredictable pre-stresses due to welding of the case cover.

*8.3.2.2. Two-coil operation.* The TFMC is exposed to out-of-plane bending and torsion while at the same time the in-plane forces and bending are increased. Fig. 8.13 shows the rear part of the deformed coil.

Fig. 8.14 shows the main coil deformations for the test ramp and allows a comparison with the single coil test shown in Fig. 8.9. The out-of-plane bending effects can be seen in the differences of the displacements between each side of the coil.

All sensor values in Fig. 8.15 are shown at full load:

The horizontal displacements, signals GDI830–GDI831–GDI834–GDI835, clearly show the effect of

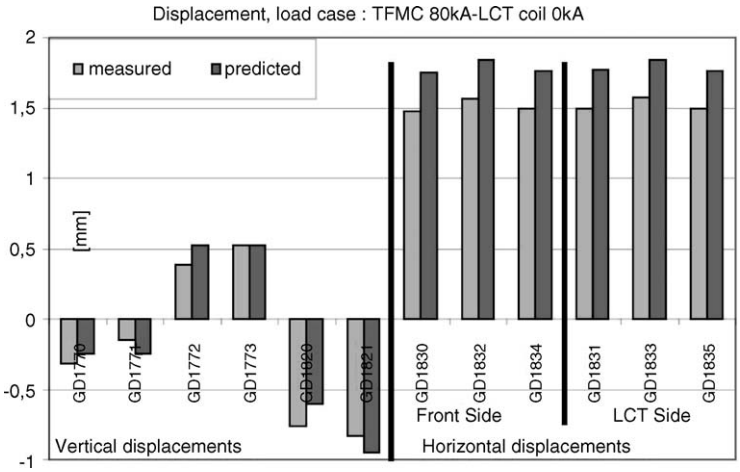


Fig. 8.10. TFMC displacements in the single coil test at 80 kA.

out-of-plane bending and correlate well with the predictions. Predictions are underestimating by +10% the signals on the LCT coil side where the bore opens more than on the front side.

The vertical displacement signals GDI820–GDI821 (on the vertical symmetry plane) correlate well with predictions with the same trend as the horizontal displacement predictions. Concerning the joint leg elongation (GDI770–GDI771–GDI772–GDI773) similar to the single coil test the predictions for GDI770 and GDI773 correlate rather well with the measurements but for the sensors GDI771 and GDI772 the correlation is worse.

The stress evaluation for the GRI sensors on the inner ring during the test operation is shown in Fig. 8.16. The non-linear behaviour during the initial loading up to 20–30% reflects the coil out-of-plane bending until the gap at the upper rear side wedge (L4, Fig. 8.3) is closed. The further stress increase is nearly linear. The model reflects this behaviour too but with some systematic underestimate. Fig. 8.17 shows all values at the maximum load. On the inner ring all three GRI channels tend to produce a signal of similar level. The prediction trends fit the measurements with a tendency to underestimate up to 30% in some cases.

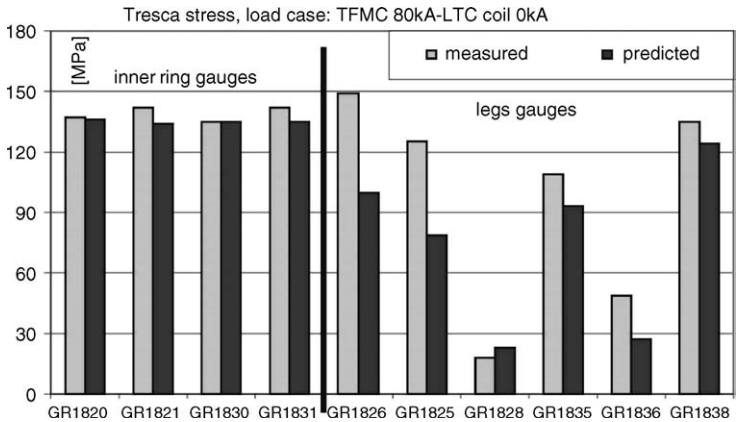


Fig. 8.11. TFMC stresses in the single coil test at 80 kA (The inner ring gauges lie on the inner ring in the vertical mid plane, the leg gauges on the bottom and cover plate on the horizontal cross-section).

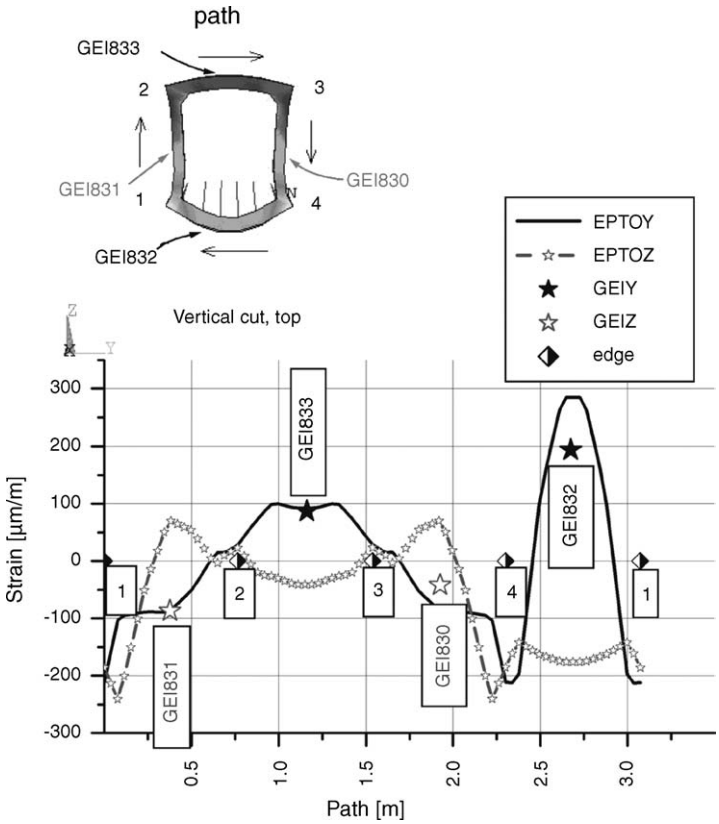


Fig. 8.12. Strain along the path of the vertical upper coil cross-section (EPTOY, strain in out-of-plain direction; EPTOZ, strain in vertical direction).

On the coil legs – LCT coil side and front side – again one channel signal (in the direction of circumferential stress) is prevalent compared to the other channels. As in the single coil test the predictions for the dominant strain gauge of the rosette tend to fit the measurement, whereas the error for the other strain gauges of the rosette is much larger. But, according to the displacement results, the out-of-plane bending stress is underestimated by the model by about 10–20%.

Concerning the detailed case wall behaviour similar comments as for the single coil test can be given. Fig. 8.18 shows that the strains along the path around the coil cross-section in the upper part partially fit quite well and partially (GEI831) not. The wall deformation seems to be simulated rather well. But the exact bending behaviour may be rather sensitive to such effects as edge stiffness, the contact conditions between the winding pack and the case and to unpredictable internal welding stresses due to manufacturing.

*8.3.3. Comparison of the test results with predictions using various friction coefficients*

Several structural parts of the test rig are connected by contacting surfaces under friction:

(a) winding pack and case of both coils with a material pairing of steel/filled epoxy;
(b) ICS and LCT coil also with pairing of steel/filled epoxy;
(c) TFMC and ICS wedges with a pairing of steel/steel (plasma nitride coated).

The actual friction behaviour of the structure after manufacturing was not very well known. The predictions used so far have been calculated with a friction coefficient $\mu = 0.3$ at all material pairings.

In general, increased friction increases the stiffness of the structures, especially the coils, but also the whole compound test rig. To evaluate the possible amount of stiffness variation a parametric study was performed

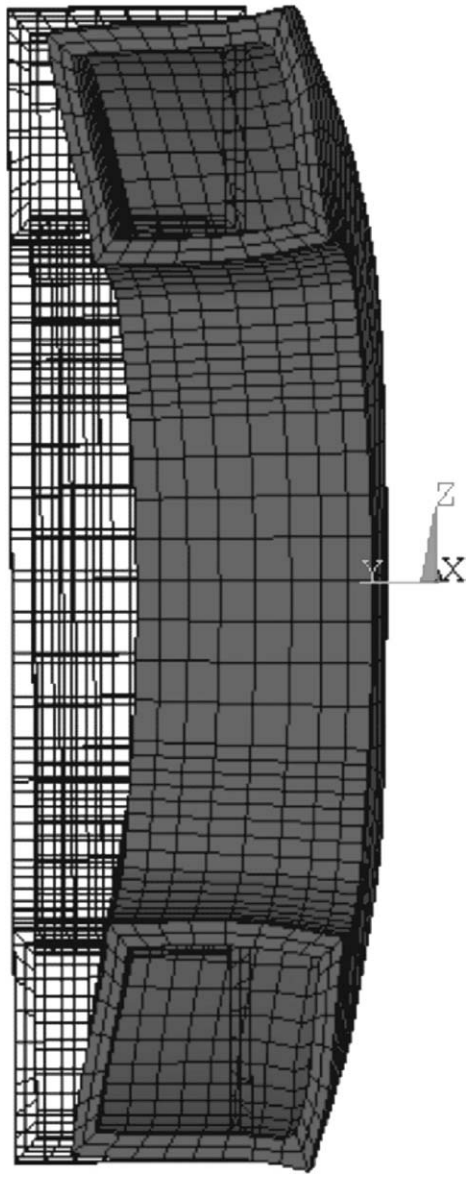


Fig. 8.13. Deformation of the rear coil half in the two coils test (displacement magnification factor 50).

using zero friction and high friction ($\mu = 1.0$) The hope was that these values would give the upper and lower bounds for the measured sensor values. In the case of the single coil test, where only friction between the winding pack and the case applies, there is some indication [163] that $\mu = 0.3$ is a good assumption. But in the two-coil test, where friction occurs at different contact surfaces, the measured values were outside of the bounds given by the above extreme friction values and therefore no conclusions concerning friction could be made.

It should be mentioned that the static friction (Coulomb) model used in the FE analysis seems not to be able to simulate the hysteretic behaviour adequately (see, e.g., Figs. 8.5 and 8.8). For simulation of this effect more work using extended friction models available in the ANSYS code will be required.

### *8.3.4. Behaviour of the TFMC after cycling tests*

The two-coil operation TFMC 70 kA–LCT coil 16 kA has been used as reference as this was performed before and after the cycling test. The data of the runs performed on the dates of 30/10/2002, 15/11/2002 and 20/11/2002 were compared to see if any significant change in the mechanical signals was detectable. The three runs vary depending on the ramp up rate and the way the run is terminated, by controlled current ramp down or by a safety discharge. However, they do not display any significant change in the results and the conclusion is that the mechanical behaviour of the TFMC is unchanged after performing the cycling test, i.e., no degradation or setting effects could be observed.

## *8.4. Evaluation of conductor strains*

After having assessed the global coil behaviour by sensors on the outside coil case surface satisfactorily it can be also concluded that the internal coil behaviour is modelled sufficiently accurately. As far as the operation limits of the $Nb_3Sn$ conductor are concerned the conductor strain is an important quantity (see Section 5). Although the winding pack was modelled as a homogeneous material with orthotropic mechanical properties the strain evaluation gave some useful mean values. Fig. 8.19 shows the strain along the path of the conductor of pancake P1.2 for the load case (80/16). Due to in-plane bending the strain increases on the inner side of the curved coil sections and due to out-of-plane bending increased strain occurs in the outside parts of the straight legs. For further evaluations (Section 5), some correction in the joint regions have to be introduced taking into account the effects of the stiff joint box and the neighbouring free conductor pieces not embedded in the radial plate.

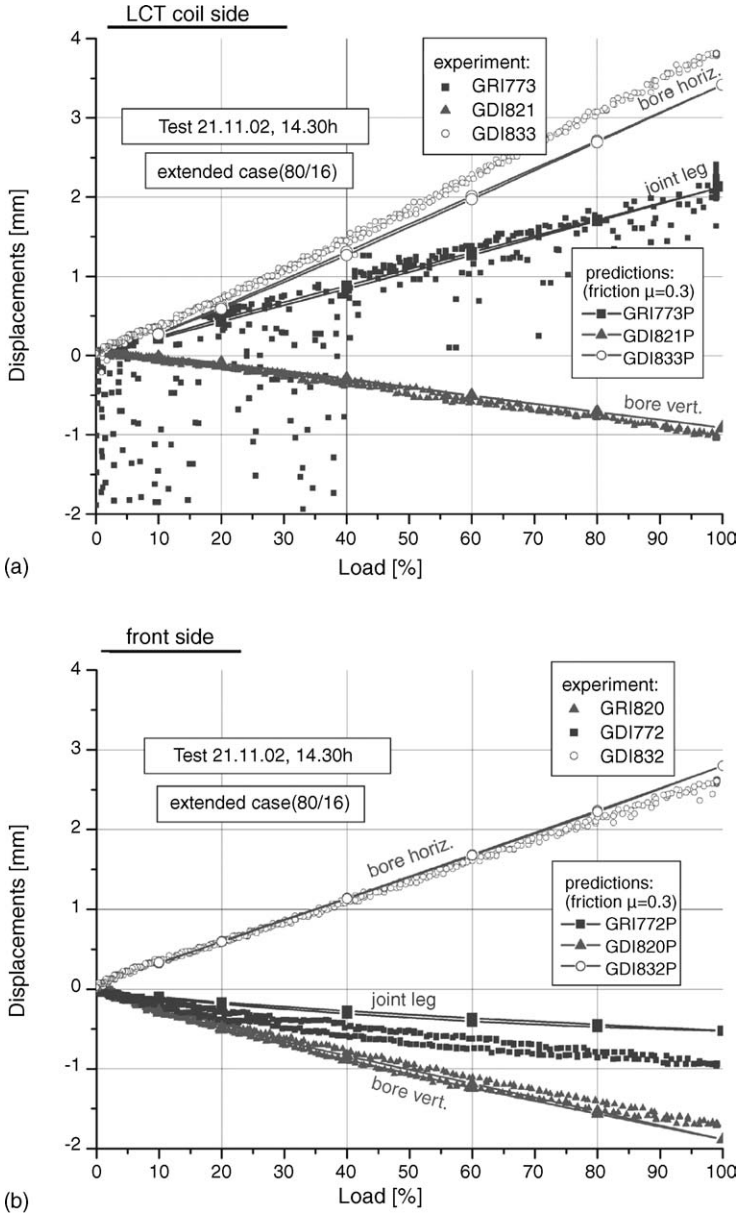


Fig. 8.14. Main TFMC deformations in the two coils test.

### *8.5. Comparison to ITER TF coil stresses*

Finally the question arises whether the TFMC could reach ITER TF relevant stresses in winding pack and case. As shown in Fig. 8.20 the design of the TFMC is quite relevant to that of the TF coil: the conductor size, the insulation system, the radial plate design are either exactly that of the TF coil or show very small differences (e.g., the TFMC conductor diameter is 40.6 mm instead of 43.7 mm for the present TF conductor, the radial plate thickness is 121 mm instead of 118.4 mm). In the FE model, the differences are reflected in some differences of the orthotropic winding pack material properties. The ITER turn insulation will be applied in

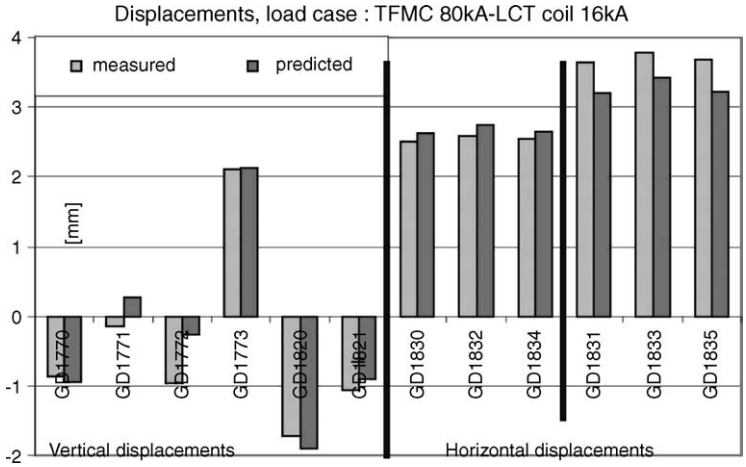


Fig. 8.15. Displacements of the TFMC in the two coils test.

a similar way as done at the TFMC and the materials basically will be the same. Therefore, the bonding will be rather similar.

In Table 8.1 a comparison of FE model predictions between the TFMC single coil test with 80 kA, the two coil test with the TFMC at 80 kA and the LCT coil at 16 kA and the ITER TF [167] coil is given. The table is a revised and extended version of that given earlier [168] using the latest values of ITER and TFMC predictions. Since both FE models are rather comparable (same FE code ANSYS, similar elements and grid) also the stresses are comparable. Using the correct detailed material properties also local stresses can be compared.

The result is that the two coil configuration could essentially increase the values of the TFMC alone and the predictions essentially reach the ITER TF coil stress level. In addition, the predictability of the TFMC results by the ANSYS model presented in the paper shows that the used FEM model give reliable results for the ITER TF coil, too.

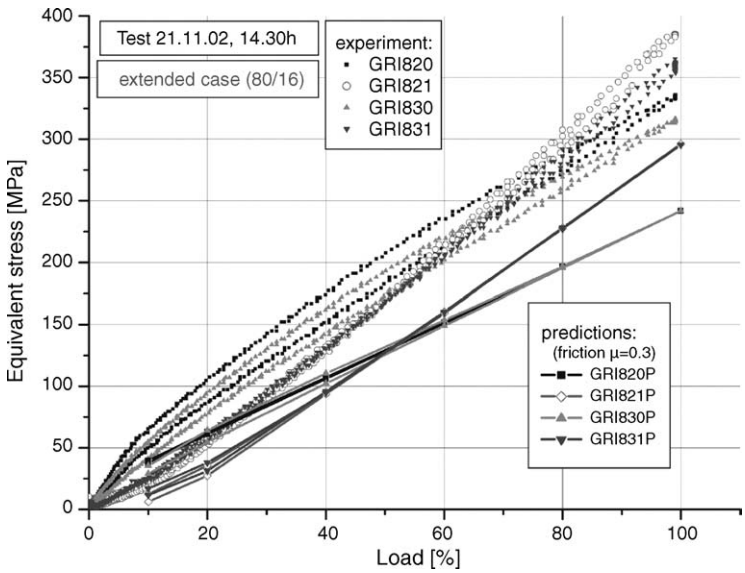


Fig. 8.16. TFMC equivalent stresses on the inner ring for a ramp up and down test.

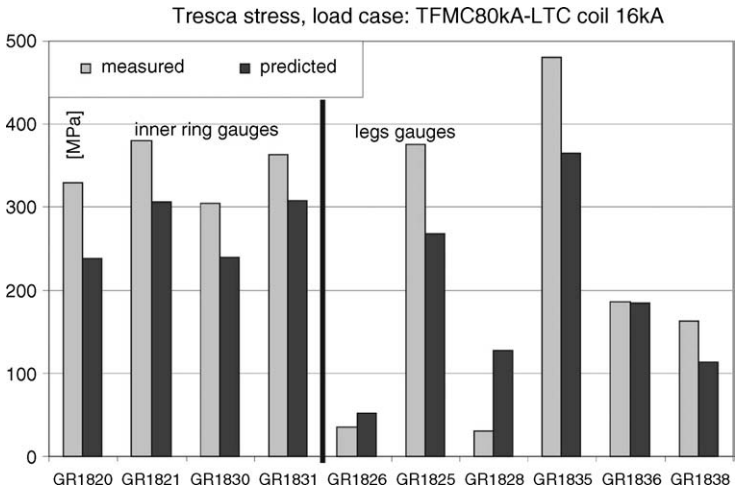


Fig. 8.17. Tresca stresses on the TFMC in the two coils test.

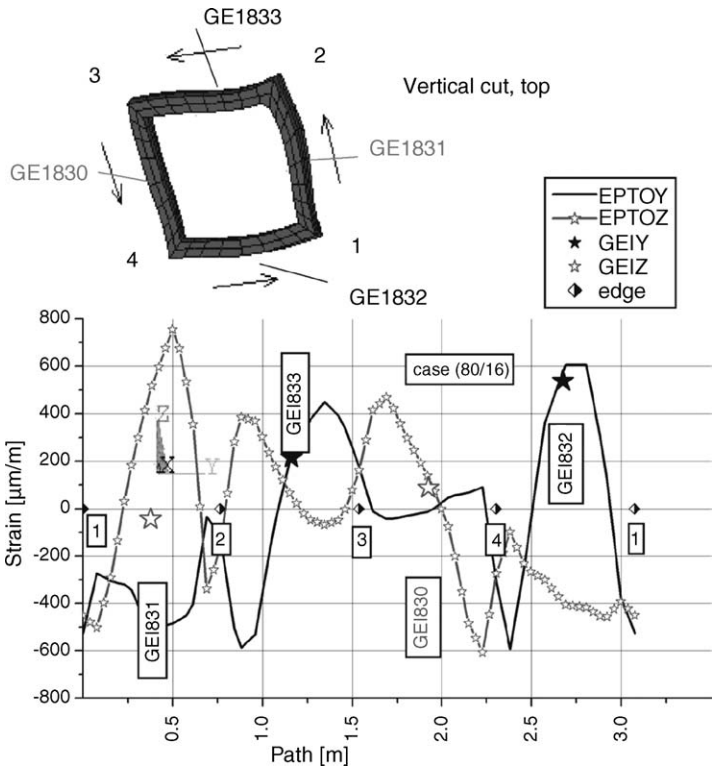


Fig. 8.18. Strains along the upper vertical case cross-section.

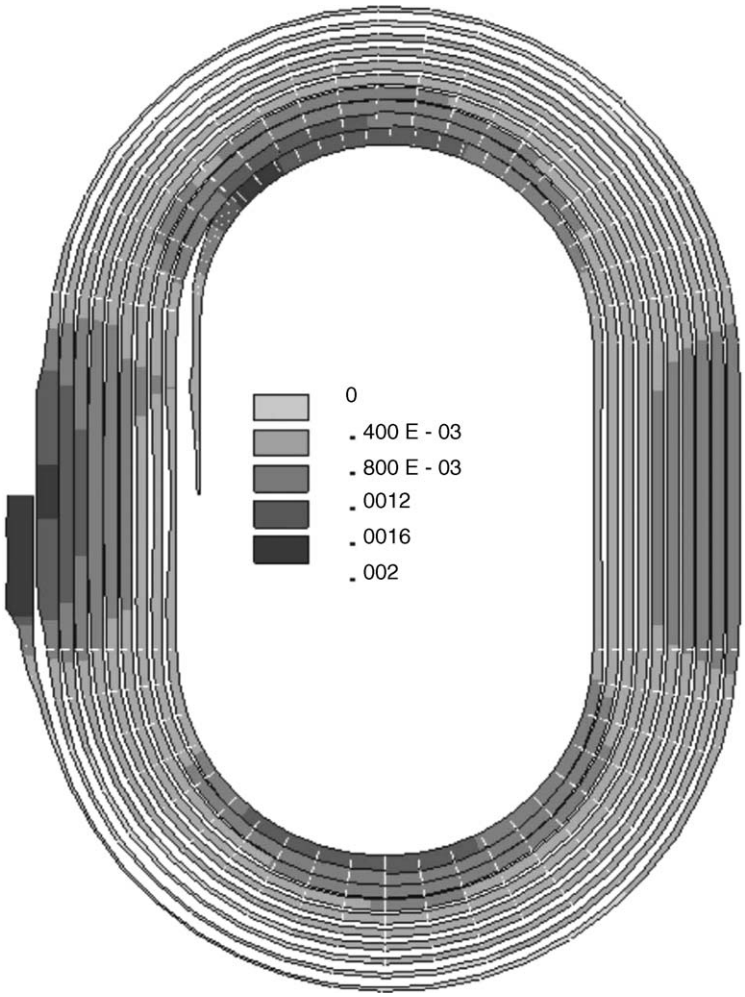


Fig. 8.19. Strain (m/m) along the conductor of pancake P1.2 (load case (80/16), friction $\mu = 0.3$).

### 8.6. Summary

Due to the mechanical sensors it was possible to some extend to compare the test rig and the TFMC behaviour to predictions made by FE calculations. The mechanical sensors worked rather well. The high stressed inter-coil structure in the critical parts behaved as predicted. Therefore, also the extended load case

Table 8.1
Relevance of the TFMC testing in the chosen arrangement with respect to the ITER TF coil loading

| Stress type | ITER TF | TFMC alone | TFMC + LCT |
|---|---|---|---|
| Max. winding hoop stresses [MPa] | 203 | 104 (51%) | 250 (123%) |
| Max. inter-pancake shear stresses [MPa] | 24 | 10 (41%) | 45 (187%) |
| Max. radial pressure [MPa] | −172 | −30 (17%) | −130 (76%) |
| Max. out-of-plane pressure [MPa] | −130 | | −155 (119%) |
| Max. case Tresca stress [MPa] | 675 | 174 (26%) | 800 (119%) |

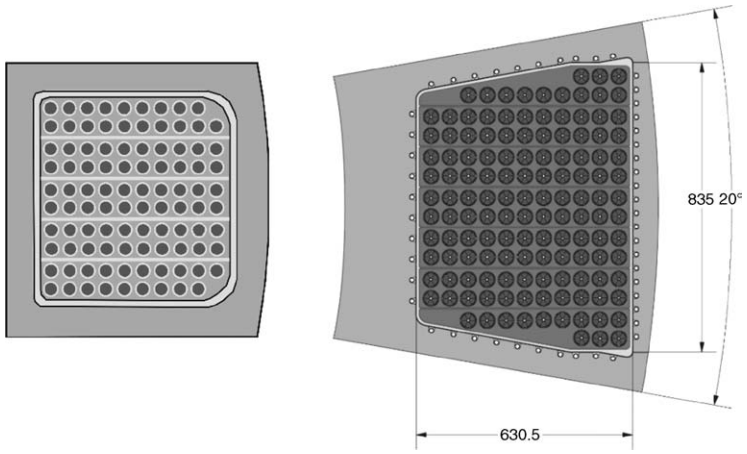


Fig. 8.20. Similarity of TFMC (left) and ITER TF coil (right) cross-section.

with 80 kA in the TFMC and 16 kA in the LCT coil could have been performed so that the stress level of the ITER TF coils was essentially reached. Probably due to some imperfections in the inter-coil structure caused by the manufacturing its behaviour in some respects deviates from the predictions. In a single coil test, the TFMC displacement and stress levels are in relatively good agreement with the predictions within deviations of 10 to 20%. The predictions for the detailed case wall behaviour were partly not satisfactory, probably due to model deficiencies but also due to unpredictable welding stresses. For the two-coil operation, whereas a similar agreement is still found for the displacements, the deviations of the predictions for the TFMC stresses are higher (∼25%). This could be explainable due to the more complex system. However, the evaluation reveals the clear trend that the model is underestimating the coil bending due to out-of-plane forces by 10–20%. Improved results may be possible with some higher resolutions in the FE model for the TFMC, e.g., modelling the radial plates in the winding pack.

Some amount of uncertainty may be contributed by friction. On the one hand, the friction coefficients are not known very well; on the other hand, more analysis using progressed friction models is required.

Finally, the comparison of the test results before and after cycling showed that in the mechanical behaviour, detected by the sensors on the TFMC case, no degradation occurred.

## 9. Dielectric properties

Discharging of the large magnet system of a future fusion reactor within a given time range is indispensable for the safe operation. In fast discharge mode, the stored energy of the TF magnets (40 GJ) is dissipated in nine resistors interleaved with each pair of TF coils which leads to a high voltage stress of several kilovolts across the coil and from coil to ground [169]. Accordingly, the ITER TF model coil was designed to withstand a test voltage of 10 kV to ground and for a fast discharge with +5/−5 kV to ground.

### *9.1. High voltage insulation concept and test strategy*

The design concept of the ITER TFMC [170] is based on the embedding of the electrical insulated conductor with a circular cross-section in five radial plates made of stainless steel (Fig. 9.1) (Section 3.1). Every radial plate comprises a double pancake and is surrounded with its own insulation. After stacking the five radial plates and connecting the conductor of each pancake with the adjacent one, the ground insulation is fabricated around the stack of the double pancakes. The insulated winding pack is inserted in the stainless steel coil case and fixed by quartz sand filled epoxy resin for force transmission. The terminals of the coil are connected to superconducting bus bars (Section 3.4.7) that lead to the cold ends of the 80 kA current leads

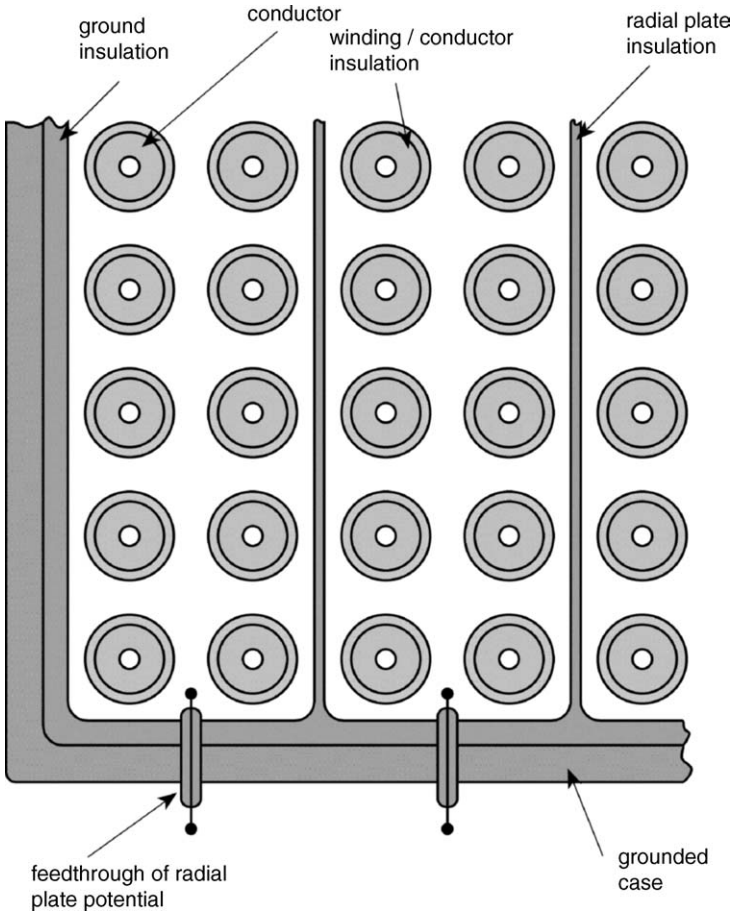


Fig. 9.1. Insulation design of ITER TFMC (Table 3.1).

(Sections 4.4 and 7.2). The heat exchanger of each current lead is surrounded by a commercially available capacitor bushing. The warm ends of the current leads are connected to the normal conductive bus bars of the electrical high current supply system. The potentials of each inner pancake joint and each radial plate are accessible for high voltage measurements via screened high voltage instrumentation cables.

Thus, the insulation system of the coil consists of three different main types:

- conductor insulation between the conductor and the surrounding radial plates;
- radial plate insulation between two neighbouring radial plates;
- ground insulation between the radial plates and the grounded coil case.

The rated terminal-to-terminal voltage of 10 kV (9.8 kV ± 2%) for a symmetrical grounding, means that the voltage at the plus terminal is −5 kV and at the minus terminal is +5 kV (Fig. 9.2). In order to minimise the electrical stress of the conductor insulation during current operation each inner pancake joint potential is connected with the potential of its own radial plate [171]. During current operation resistors of 1.2 MΩ were put in all connections between radial plates and inner pancake joints to limit the current in case of a fault in the conductor insulation. For a linear voltage distribution, this kind of connection leads to a voltage drop of 2 kV between two adjacent radial plates. For a linear distribution of the conductor voltage, the voltage drop is 2 kV along each of the five double pancakes, too. In this ideal linear case, the maximum potential difference between the conductor and the surrounding radial

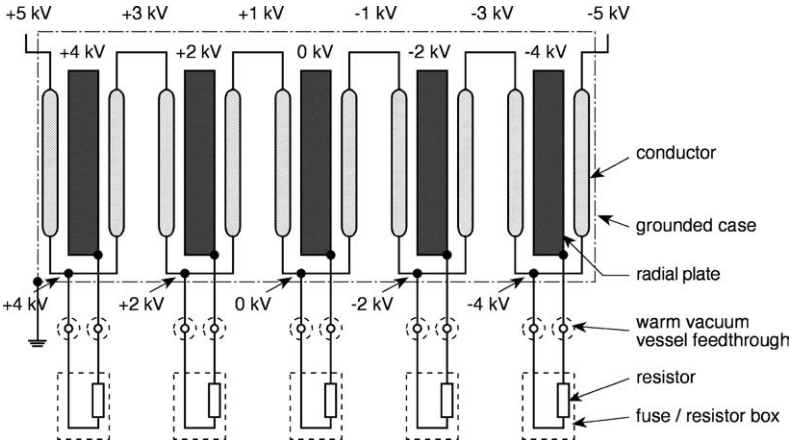


Fig. 9.2. Ideal voltage distribution for a symmetrical discharge with ±5 kV. The conductor is embedded in the radial plates, but it is drawn outside the radial plates for better visibility. The real voltage distribution is only linear for slow voltage changes. The steel case of the coil is grounded.

plate would be 1 kV. For a non-oscillating system, the maximum voltage between the grounded case and any high potential component is 5 kV.

To verify the soundness of the dielectric properties over the complete operation time, the coil was tested after each important manufacturing and test step. All typical high voltage test series consist of a number of different tests. A 9.8 kV impulse test with a rise time of about 10 μs is the most important high voltage test because it produces a high stress with a similar distribution as during a fast discharge. Due to a detection of a defect in the ground insulation at the plus terminal side a symmetrical operation of the coil was not possible. During impulse testing, the coil was therefore grounded at one terminal and the impulse voltage was applied to the other terminal. The ideal voltage distribution for a 0 V/10 kV impulse can be obtained if 5 kV were added for every voltage value given in Fig. 9.2. During the high voltage tests, direct connections between radial plates and their inner pancake joints were used for the examination of the ground insulation (Fig. 9.3). In this case, the DC or AC voltage was applied to only one terminal and the other terminal was open (or short circuited with the other terminal), so that all active parts have the full applied potential to the grounded case.

For the examination of the insulation of an individual radial plate, the connection of this radial plate to the belonging inner pancake joint was disconnected and the radial plate was grounded. By grounding radial plates number 2 and 4 and applying the test voltage to radial plates number 1, 3 and 5, all radial plate insulations can be examined simultaneously (Fig. 9.4). Comparison with the dielectric properties of the conductor insulation would have been necessary in case of failure (or partial discharge activity) during a measurement with this configuration because the voltage was also applied to the conductor insulation of the two grounded radial plates.

The conductor insulation within all radial plates can be examined simultaneously by grounding all radial plates and applying the test voltage to the conductor (Fig. 9.5).

The change of the connection between the radial plate and the inner pancake joint is possible at the high voltage instrumentation feedthrough chamber (Fig. 9.6). For all kinds of connections, a set of connectors were preassembled. One connector was also prepared for the connection to the detection impedance of the partial discharge measurement system.

The examinations after impulse testing were performed in a succession that minimises the assembly work. Therefore, the complete test sequence was:

- ground insulation, DC;
- impulse test;
- ground insulation, DC;
- ground insulation, AC, partial discharge test;
- ground insulation, Schering bridge measurement;
- radial plate insulation, DC;
- radial plate insulation, AC, partial discharge test;

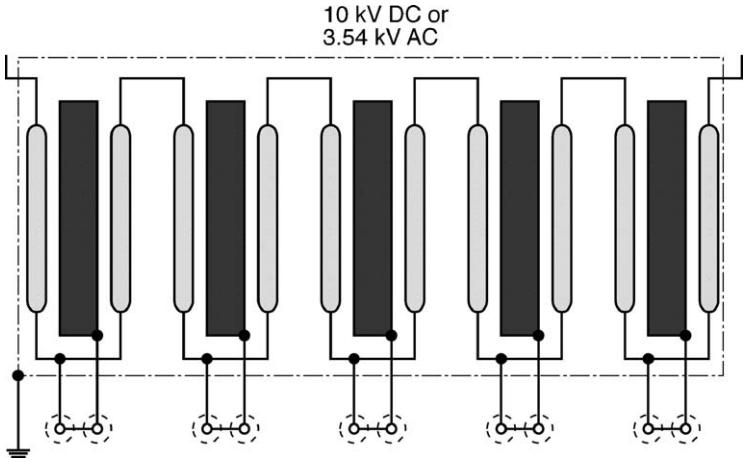


Fig. 9.3. Voltage during DC and AC testing of ground insulation. All electrical active parts (conductor, radial plates) are on the same potential. The steel case of the coil is grounded.

- conductor insulation, DC;
- conductor insulation, AC, partial discharge test.

The encapsulation of all electrical active parts with solid insulation and covering of insulated parts with conductive paint would make an ITER TFMC with no insulation fault independent of the surrounding conditions in the cryostat vessel (which is important in the case of a vacuum breakdown). The pressure values of the non-solid insulation within the coil system (some inner areas of current leads and radial potential breaks) were controlled during the high voltage tests to ensure sufficient dielectric strength.

All high voltage tests under ambient conditions were successfully carried out after fabrication although a mistake during the manufacturing process of the ground insulation (remaining Tedlar tapes from vacuum impregnation) had been recorded. It was therefore assumed that the low voltage discharge (Section 9.5.1) at 80 kA can be performed under cryogenic conditions

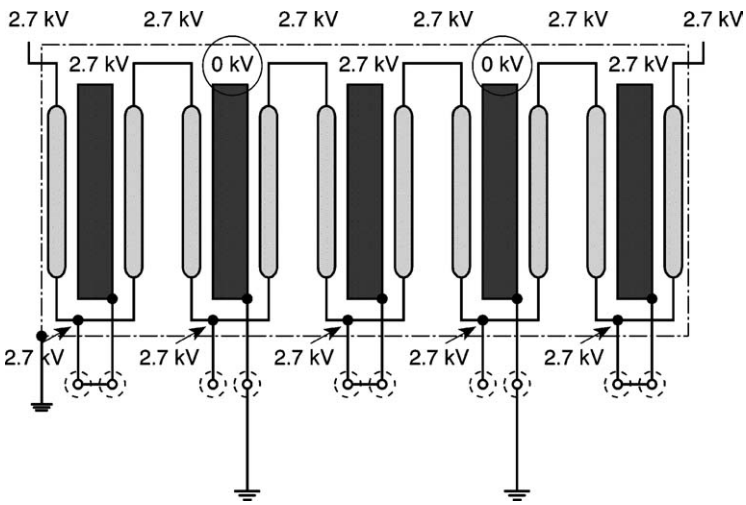


Fig. 9.4. Voltage distribution during DC testing of radial plate insulation. Radial plates number 2 and 4 are grounded.

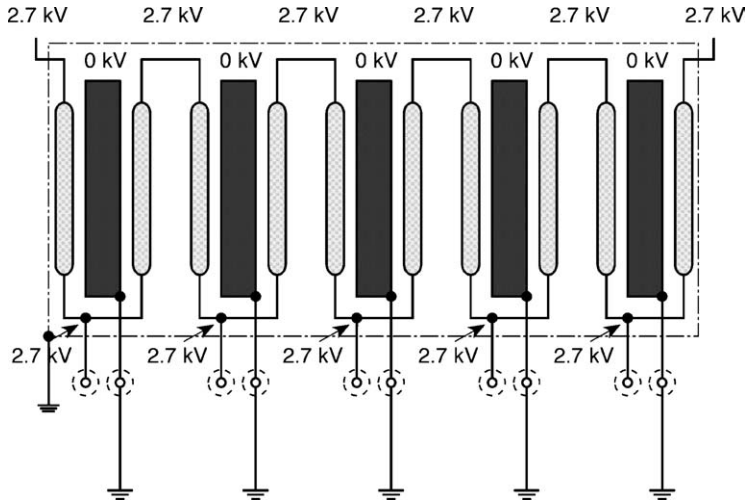


Fig. 9.5. Voltage distribution during DC testing of conductor insulation. All radial plates are grounded and the conductor is connected with high voltage.

with a sufficient safety margin. Hence the decision was taken by the project management to go ahead with the TFMC testing and to check the insulation level instead of having a delay of 4 months, which would have been required for a repair.

### *9.2. DC tests*

The DC tests were performed with 10 kV for ground insulation and 2.7 kV for radial plate and conductor insulation with a test time of 1 min.

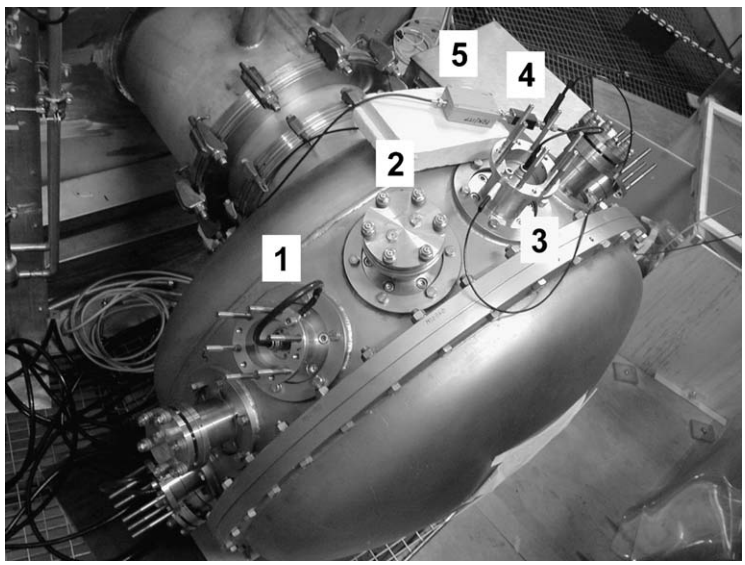


Fig. 9.6. High voltage instrumentation feedthrough chamber with vacuum tight instrumentation cable sockets during partial discharge measurement on conductor insulation (similar to arrangement of Fig. 9.5). The radial plates are grounded with radial plate to ground connectors (1) or over the preamplifier (5) and detection impedance (4) of the partial discharge measurement system with the radial plate to detection impedance connector (3). The plugs for the connection to the TOSKA data acquisition during high current operation are disconnected from the sockets of the feedthrough chamber and not shown.

The specification of the insulation resistances was >200 MΩ for all three insulation types. The tests at ambient conditions (air at 1 bar around the coil, room temperature) were passed successfully with values above 20 GΩ for ground insulation, values above 3 GΩ for radial plate insulation and values above 2 GΩ for conductor insulation. But after completion of installation in the TOSKA facility and performing the high voltage tests at a reduced pressure around the coil, the ground insulation showed pressure dependent breakdown behaviour. The minima were found at about 0.9 kV at pressures between 0.6 and 0.8 mbar air. After evacuation of the cryostat and cool down of the coil all DC withstand tests were successfully performed without a breakdown. The measurement of the insulation resistance of the coil was not possible under cryogenic conditions because the water-cooling circuit cannot be interrupted and the insulation resistance of the water within the hoses is only in the range of some MΩ.

After the first warm up of the coil a detailed inspection of the insulation fault was performed. The best method was found to be an observation of the coil in the pressure range between 0.06 and 500 mbar by CCD cameras. Intensive light effects were detected in the feedthrough areas of the helium inlet and outlet tubes, in the cut outs of the coil case side plate and at the clamps of the bend at the lower end of plus bus bar type I. Visual inspection of the helium tubes identified the position of the manufacturing mistake as one fault location, where some Tedlar tapes were not removed at intermediate ends of the pipe insulation before completing the insulation up to the axial insulation breaks. A breakdown path between parts on high voltage potential and the grounded case (or conductive paint) is therefore likely. For a possible degradation at the plus bus bar type I no explanation has been found until now.

No evident insulation degradation was found within both test phases. At the end of Phase II the coil withstood all specified voltage values under ambient conditions. An increasing of the test time to 15 min delivers values above 40 GΩ for ground insulation.

### *9.3. AC tests*

#### *9.3.1. Withstand tests*

The AC withstand tests were performed with 3.54 kV rms (10 kV peak-to-peak) on ground insulation and 955 V rms (2.7 kV peak-to-peak) on radial plate and conductor insulation. The test time was 1 min. The withstand tests were only performed if the preceding DC-test was performed without a breakdown. During the AC tests the current was measured on the high voltage side. A constant reactive current during the test time was a criterion for the quality of the insulation. Current limiting resistors are used for the protection of the coil during the AC tests.

AC withstand tests in air at atmospheric pressure were successfully performed without a breakdown. But during one of the AC tests under operating conditions some breakdowns were found at 3.5 kV rms (before second warm up) although the coil could withstand a 10 kV DC test. This behaviour is caused by a well known effect called “sliding discharge”, which can lower the breakdown voltage for AC and impulse tests compared with DC voltage depending on the capacitive arrangement around the breakdown area. Although the breakdown occurred only during the last test under cryogenic conditions, it cannot be clearly stated that degradation occurred because the statistical number of tests is not sufficient and the breakdown behaviour shows often a wide scattering.

#### *9.3.2. Partial discharge measurement*

Partial discharges do not bridge the electrodes completely. At least under good vacuum corona discharges can be excluded so for the ITER TFMC only surface and internal discharge appear under cryogenic conditions. Partial discharge activity starts if a certain inception voltage is reached in internal voids within the insulating material and at delaminations to the electrodes. The partial discharge activity stops after decreasing under a certain voltage level, called extinction voltage.

Because partial discharge measurement can be performed at rated voltage it is a non-destructive test method. Although the shape of the voltage pulse during a fast discharge has no sinus waveform an AC voltage was used for the partial discharge measurement for practical reasons. The peak-to-peak value of the AC waveform was chosen to be the same as during high voltage discharge with symmetrical grounding and with ideal voltage distribution, i.e. for ground insulation the rms value was $U = 5\,\text{kV}/(2\cdot\text{sqrt}(2)) = 1.77\,\text{kV}$. For conductor insulation it was $1\,\text{kV}/(2\cdot\text{sqrt}(2)) = 0.354\,\text{kV}$. The radial plate insulation is measured at the same voltage instead of the

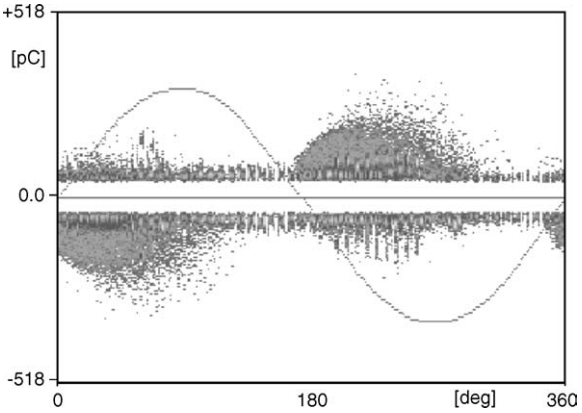


Fig. 9.7. Partial discharge activity of the ITER TFMC during 1 min with 3.52 kV and ambient conditions at the end of test phase II.

double voltage as the conductor insulation to avoid too high stress of the conductor insulation in the grounded plate.

External disturbances interfered with the partial discharge detection of the TFMC. Especially during the cold tests this disturbances were rather high. No partial discharge above the noise level was found under the partial discharge measuring voltage. The partial discharge equipment was also used during the AC tests at higher voltage levels (e.g. ground insulation: $U = 3.54$ kV). Partial discharge activity was detected only for the ground insulation. The last examination (Fig. 9.7) showed void activity with a maximum apparent charge of 0.35 nC at 3.52 kV, but no accurate localisation of the insulation defect was possible with this method.

### 9.3.3. Schering bridge measurements

The dissipation factor can be measured by a Schering bridge. In the presence of increasing losses, e.g. caused by partial discharge, the dissipation factor is increasing.

For the ITER TFMC, the target has only been the demonstration of the feasibility of a Schering bridge measurement at 1.77 kV; no dissipation factor limit was specified.

A Wagner auxiliary branch was used to eliminate the influence of the stray capacitances within the measurement circuit of the grounded coil. A compressed gas standard capacitor of 1000.6 pF was applied as comparison capacitor. For cryogenic operation, the water hoses cannot be removed. The measured values of the dissipation factor are therefore not significant for the coil at operation conditions. At room temperature the last measurement was performed after disconnecting the water hoses and delivered a dissipation factor of 0.011. The balanced Schering bridge delivered also the capacitance value of 119.04 nF. For comparison a low voltage LCR meter indicated a capacitance value of 119.8 nF, which is a difference of less than 0.7%.

## 9.4. Tests for the determination of the transient behaviour

Fast voltage excitations in large electrical devices may cause local overvoltages, which are considerable higher than for the ideal voltage distribution. The electrical transient behaviour is therefore an essential topic of the dielectric properties of the TF model coil. A network calculation [172] delivered the basis for the choice of the preferable measurement points within the electrical system of the coil.

### 9.4.1. Measurements in the frequency domain

In the frequency domain low voltage measurements were performed to determine the first resonance frequency of the coil. According to [173] the measurement confirms the results of the calculation of this frequency that was found to be in the range of 300 kHz. The rise time for a high voltage discharge with ITER TF had been expected in the range of 35 μs [175]. Hence no relevant component of the excitation voltage of the coil is expected around the first resonance frequency. A safe operation during the high voltage discharge was therefore predicted from this point of view.

### 9.4.2. Impulse tests

The purpose of the impulse tests is the generation of a voltage distribution similar to the electrical voltage stress under high voltage discharge with a reduced amount of energy. The energy of the impulse was delivered by a capacitor bank of the POLO switching circuit [174]. The impulse was started by firing of ignitrons. The rise time was adjusted with the damping resistor to about 10 μs which ensures on one hand a relevant test for the expected high voltage discharge rise time of about 35 μs and, on the other hand, is slow enough to avoid high overvoltages caused by resonances. The maximum voltage on the high voltage

side of the coil was 9.8 kV. The other terminal of the coil was grounded.

Under ambient conditions, no breakdown appeared during all impulse tests. Breakdowns occurred under cryogenic conditions after increasing the impulse voltage above 4 kV at the high voltage plus terminal, although sufficient dielectric strength of 10 kV DC was proven before all impulse test series. When the high voltage connection was on the minus terminal, the coil withstood most of the 9.8 kV tests but there was one breakdown at 9.73 kV after cool down in test Phase II.

During high current operation the plus terminal is connected to the high voltage side and the minus terminal is grounded over the 80 kA switching circuit. Hence it is evident that a reliable high current operation of the coil with discharge voltages above 1 kV was not possible assuming a safety factor of 4 for the design value of an insulation fault. (A safety factor between breakdown voltage and operation voltage must be higher than a safety factor between test voltage and operation voltage.)

### 9.5. Current operation

Two different discharge modes over resistors were possible during the test of the TF model coil: a safety discharge up to currents of 80 kA and voltages < 1 kV and a fast discharge mode with voltages > 1 kV. The low voltage safety discharge is sufficient to protect the ITER TFMC for the 80 kA current operation. The intended high voltage discharge is more representative for the dielectric stress during the fast discharge and some calculated fault cases of ITER TF.

#### 9.5.1. Low voltage discharge (safety discharge)

The safety discharge up to 80 kA was performed with the 80 kA switching circuit containing a 6.7 mΩ dump resistor. An arc chute breaker commutates the current from the freewheeling short circuit into the resistor path. The PTC characteristic of the resistor and the switching process of the arc chute breaker caused higher voltages than the simple rule $U = R_{\text{room temperature}} \times I$. Especially for currents till 40 kA the overvoltage reached more than 100% of $U = R_{\text{room temperature}} \times I$. The highest voltage value of a safety discharge with 80 kA was measured as 960 V (Fig. 9.8) which is an overvoltage of 80% but still acceptable under safety aspects (see Section 9.4.2). The time constant for the discharge of ITER TFMC ($L = 28$ mH) in this mode was 4 s (Fig. 4.31).

#### 9.5.2. High voltage discharge

The POLO switching circuit in the TOSKA facility allows high voltage discharges with forced commutation with voltages up to 23 kV and currents of 21 kA.

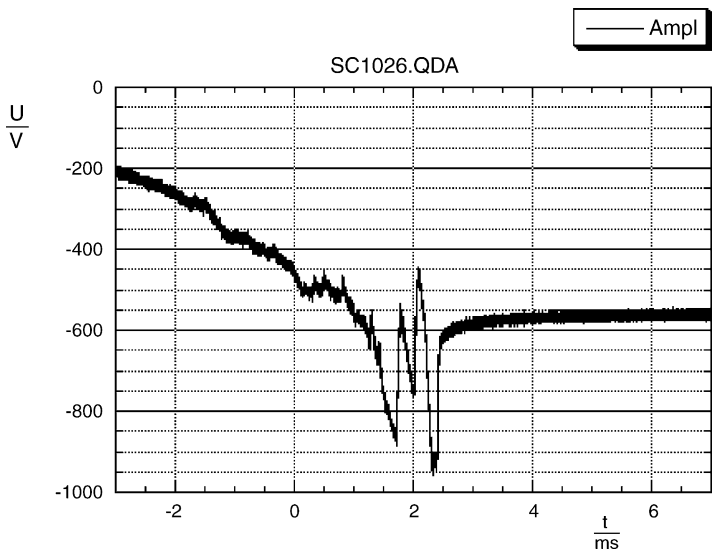


Fig. 9.8. Voltage maximum between the plus terminal and vacuum vessel (ground) during a safety discharge with 80 kA.

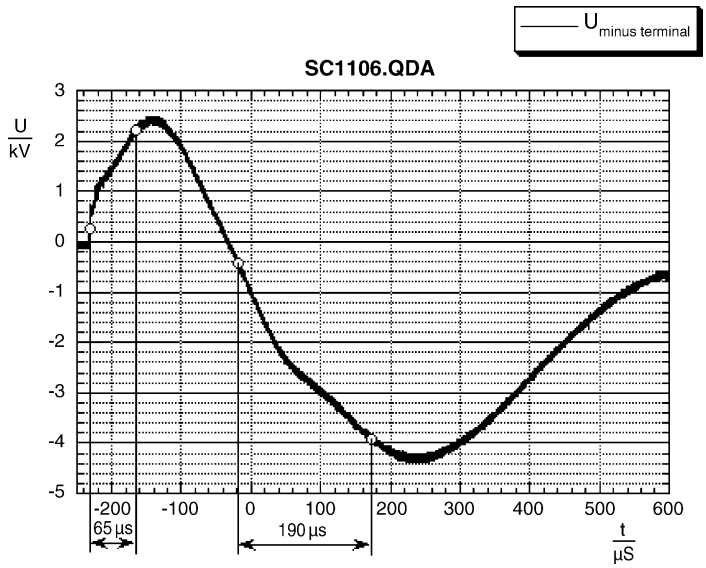


Fig. 9.9. Voltage between minus terminal and vacuum vessel (ground) during a high voltage discharge with 6.3 kA.

The specified high voltage discharge with a voltage of ±5 kV to ground was not practicable due to the insulation defects detected during the high voltage tests, especially the impulse tests. A modified fast discharge was prepared with a voltage of 0 V/−4.4 kV. The modification to a non-symmetrical discharge is not a disadvantage compared to the relevance for a fast discharge without a fault of the ITER TF coil system because in this case all TF coils have only one terminal on high voltage potential. A 1 Ω discharge resistor was used for the high voltage discharge of ITER TFMC which allows to reach −4.4 kV with a modest coil current to

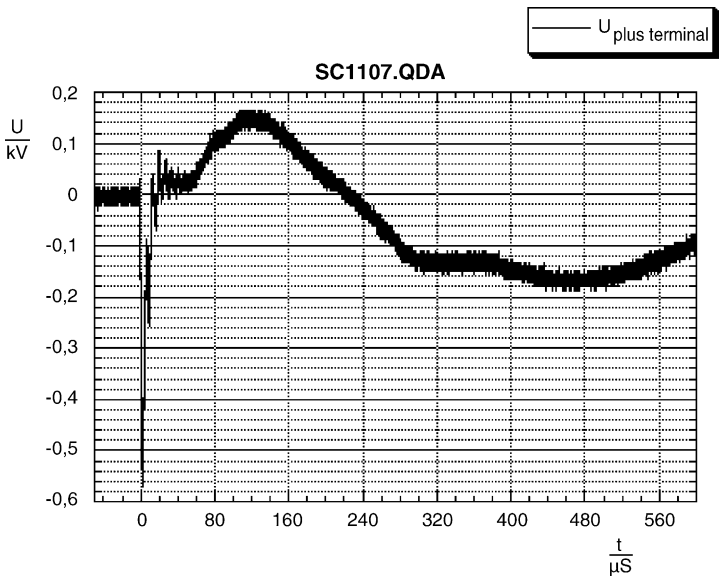


Fig. 9.10. Voltage between plus terminal and vacuum vessel (ground) during a high voltage discharge with 6.3 kA. (Trigger time is not the same as for Fig. 9.9).

minimise possible hazards in case of an unexpected failure of the insulation.

Five modified fast discharges were performed with a current of 6.3 kA and a minimum voltage of −4.4 kV. The voltage was measured with a high voltage divider: three times on the minus terminal, one time on plus terminal and one time on the radial plate number 5, which is adjacent to the minus terminal. All these five potentials were measured to the vacuum vessel ground (foot point of the high voltage divider).

The voltage between minus terminal and vacuum vessel ground (Fig. 9.9) shows an increasing to a maximum of 2.5 kV caused by the discharging of the capacitor bank for the current commutation in the short circuit path. The rise time for this impulse increases with increasing current. A rise time of 65 μs was measured for the maximum current of 6.3 kA. The rise time for the minimum voltage was 190 μs independent of the current value (related to the zero transition). The minimum voltage at the radial plate number 5 was about 10% less compared with the ideal voltage distribution. The internal measurement system of TOSKA showed no deviation for the pancake voltages from the ideal voltage values. The voltage between vacuum vessel ground and plus terminal (Fig. 9.10) showed a short time impulse with a rise time of only 2.2 μs and a minimum of −570 V at the beginning of the discharge process. This potential difference to vacuum vessel ground was already known by prior investigations during impulse tests. It is caused by capacitive currents through the grounding resistor of the POLO switching circuit after the activation of the capacitor bank.

### *9.6. Summary*

- Detailed dielectric investigations were performed on the ITER TFMC and are relevant for the ITER project. Preparatory calculations have shown that, for this coil, no transient oscillations are expected during fast discharge.
- High voltage DC, AC and especially impulse tests have shown that the coil does not fulfil the specifications of the dielectric strength completely under rated conditions due to a manufacturing defect but a safety discharge with 80 kA and voltages < 1 kV was still possible.
- A modified high voltage discharge with a reduced minimum voltage of −4.4 kV proved the assumption of a linear voltage distribution along the conductor but demonstrated a non-linear distribution of the radial plates voltages caused by the current limiting resistors in the connection to the pancake joints.
- Two probable fault areas were localised at the end of test phase I.
- For future superconducting fusion magnets, the transient behaviour has to be taken into account for the electrical insulation integration.

More extended high voltage testing is indispensable for the quality assurance of the dielectric insulation system. High voltage tests under atmospheric pressure are not sufficient. AC withstand tests should be performed with the peak voltage value referenced to the DC value. DC, AC and impulse tests with the coils embedded in conductive liquid or Paschen minimum conditions are also strongly recommended in order to ensure reliable dielectric strength under operation conditions.

## 10. Summary and conclusions

The ITER tokamak, with a plasma volume of about 840 $m^3$, presents a major challenge for the design and construction of large superconducting magnet systems at field levels of about 12–13 T. Special design principles and new technologies have been applied for mastering the huge Lorentz forces in these types of magnet systems. The feasibility of these technologies were demonstrated by the successful completion of the ITER model coil programs, in which two model coils namely a central solenoid model coil, CSMC, and a toroidal field model coil, TFMC, have been designed, constructed and tested. The description of the TFMC project and its results has been the subject of this publication.

The design, construction and testing of the TFMC required an international collaboration between research organisations, industry and the international ITER Team. This well working international collaboration can be considered as an excellent example for the future construction of ITER.

### *10.1. Industrial fabrication*

A representative length of about 1000 m thin walled, stainless-steel-jacketed $Nb_3Sn$ cable with

circular cross-section and central cooling channel was produced for the TFMC. By application of a "wind–react–insulate–transfer" technique, 10 pancakes were fabricated with conductors of about 100 m resting in grooves located in both sides of five radial plates. The winding pack was built up by stacking and the application of vacuum impregnation technique with epoxy resin. To achieve a high stiffness against bending, the winding pack was enclosed in a thick (80–100 mm) stainless steel case where the gap between the winding pack and the case was vacuum impregnated with quartz sand filled epoxy resin for force transmission. All components such as conductor joints, electrical insulation system, and instrumentation were developed separately and tested as needed. A detailed quality assurance program accompanied the fabrication procedure. The design and fabrication was a well-coordinated collaboration and interaction between the industry consortium AGAN, EFDA and the European superconducting research laboratories.

The feasibility of the industrial production of large superconducting $Nb_3Sn$ coils was successfully demonstrated by the fabrication of ITER TF model coil.

### *10.2. Test and test facility*

A suitable test rig consisting of the TFMC and the LCT coil linked by a stainless steel structure for force transmission was designed and constructed. Torus relevant forces were generated and ITER TF coil relevant stress levels in the ITER TFMC winding pack and structure were achieved.

The components of the existing TOSKA facility were extended regarding the electrical and cryogenic supply systems and the data acquisition and control systems were renewed to match the needs of the TFMC tests. One pair of 80 kA forced-flow-cooled current leads was developed in line with the design principles used for current leads in former projects.

The careful preparation and performance of pretests and tuning of the interfaces led to a smooth running installation work and test program within the schedule. No leak appeared during the test in the TFMC hydraulic system.

The facility fulfilled all requirements of the test program over a running time of 2 years. For the challenging determination of the operation limits of the TFMC, the cryogenic system was operated stably far outside its rated cooling power by the use of stored liquid helium and skilled handling of the cooling system.

All safety discharges without and including TFMC quenches were handled without problems by the cryogenic and electric system up to 370 MJ total stored magnetic energy at TFMC current levels of 80 kA.

In parallel to the extension of the facility for the TFMC test, the TOSKA facility was used for other projects (forced-flow He II test of the EURATOM LCT coil and test of the W 7-X DEMO coil). Thus, the continuous improvement of facility components resulted finally in a facility availability of 98% for the TFMC test.

### *10.3. Test results*

The analysis of the TFMC test was preceeded by code development and experiments. The required database for this analysis was developed by the European superconducting research laboratories and the international ITER collaboration.

To reduce both the installation time as well as the risk of schedule delays and to be able to obtain the experimental results before the end of the ITER EDA, the test was performed in two phases, one without (Phase 1) and one with the LCT coil (Phase 2). He leaks, which are poorly accessible in the two coil configuration and of which repair requires removal from the vacuum vessel and disassembly, would cause heavy schedule delays.

#### *10.3.1. Operation limits of the magnet*

The operation limits of the TFMC were determined by the measurement of the current sharing temperature $T_{CS}$ at different current levels without and with the LCT coil. For the complex experimental boundary conditions, a suitable stepwise helium gas heating strategy was elaborated by the computer code M&M, which was developed for computing thermal-hydraulic behaviour. Various tests were evaluated by the codes M&M and ENSIC. The results were reproducible and consistent. When comparing the measured $T_{CS}$ with the one extrapolated from single strand data by using Summer's law, it turned out that there is a discrepancy, which can be balanced by an additional conductor strain which probably has its origin in the cable structure under compressive Lorentz force. When taking the maximum magnetic field as parameter which is

according to the ITER design criteria, the current sharing temperature $T_{CS}$ is only slightly reduced. When using the more realistic averaged field across the conductor cross-section, this leads to a larger reduction of the designed temperature margin of 1 K. The temperature margin was mainly assigned to withstand magnetic field transients stably. But it has been a fact that the TFMC was stably operated in the resistive region up to 0.5 K above $T_{CS}$. These tests were determining to select stainless steel as jacket material for all the ITER conductors. In addition, higher strand critical current densities, which can be achieved now with advanced strands, will give sufficient flexibility and confidence for reliable operation of the ITER TF magnets.

*10.3.2. Electrical losses and thermal-hydraulic behaviour*

The thermal-hydraulic behaviour of the TFMC is determined by the substantial quantity of structural material used in the coil and by the dual cooling channel design of the ITER TF conductor.

The massive structural material integrated in the winding pack and the enclosure in a thick-walled stainless steel case cause eddy current losses during the magnetic field changes required when the magnet is operated. A calculation model was developed and compared with the measurements gained during the runs in the test program. The dominant losses are the eddy current losses of the structural material. The common conductor losses (hysteresis and coupling) are small (3–4%) compared to the total loss power. The losses were determined by calorimetric measurements. They were in fair agreement with the expectations derived from the model with <5%.

As a curiosity it was found that the current ripple of the thyristorised 12-pulse high current rectifier caused a continuous background loss power of 40 W.

During the safety discharge about 95–99% of the stored magnetic energy of the TFMC was dissipated in the external discharge resistors depending on the operation mode (Table 6.8). The remaining energy was dissipated mainly in the structural material (radial plates, coil case) by eddy current loss power.

The heat diffusion from the radial plate to the conductor was investigated by numerical codes. The experimental and calculated results fitted if the thermal conductivity of the fibreglass reinforced epoxy conductor insulation was reduced by a factor 6–8 from its initially assumed value.

For the communicating dual cooling channel system of the TFMC conductor, friction factors were elaborated for the central cooling channel and the cable bundle region. The central channel friction factor depends on the geometrical parameters of the spiral which forms the central channel. For pancakes with one spiral type, the scattering of the measured pressure drop is within ±10%. The measured pressure drop for rated mass flow is about 20% higher than expected. The conductor showed a good thermal-hydraulic behaviour. The thermal-hydraulic models indicate that the reduction of the diameter of the central cooling channel causes a considerable increase of the friction factor and should be avoided as much as possible for future designs.

In general it can be concluded that the electrical losses met the expectations, the thermal conductivity of the conductor insulation has to be checked and the friction factors have to be improved by cross checks with experimental data. For the thermal-hydraulic analysis of the quench, the accuracy achieved by the numerical code GANDALF is only in the range of 30%, thus a more complex code has to be applied describing temperature and pressure behaviour.

*10.3.3. Properties of special components*

A compact joining technique was developed for the TFMC conductor. This technique has been applicable joining conductor ends by soft soldering, electron beam welding and dismountable clamping with indium in between. The joining techniques were developed and tested in the frame of the conductor short sample test program. It has been demonstrated that joints were reliably fabricated under industrial conditions. A total of fifteen joints including the joints of the NbTi bus bars were applied in the TFMC test. All joints achieved a resistance about 1.5 nΩ or better determined by electrical resistance measurement or calorimetry and met therefore the ITER specification < 2 nΩ.

The NbTi superconducting bus bars connecting the TFMC terminals and the cold end current lead terminals worked very well. Intermediate joints in the bus bar system were needed for assembly reasons. There were no major problems to adapt the TFMC joining technique to the NbTi conductor.

The bus bar system served also as test object for the determination of the current distribution by applying

two different sets of Hall probe arrangements (simplest arrangement four tangential Hall probes used in Phase 1 up to 10 tangential plus six radial probes used in Phase 2).

The evaluation of the data of Phase 1 with a suitable model resulted in a deviation from homogeneous current distribution of less than 6%.

In Phase 2, the more sophisticated Hall probe arrangement was applied. The investigations showed that such arrangements of the Hall probes can analyse the current distribution in the ITER like superconducting cables. A direct comparison of results of Phases 1 and 2 was not possible because the bus bar joints were opened in between. Also the reference of homogeneity for calibration was different.

The developed joint technology is applicable for the ITER TF coils. Superconducting NbTi bus bars with a cable cross-section comparable to the ITER TF conductor can be used for the ITER current feeders.

*10.3.4. Mechanical properties*

For design and evaluation purposes a FEM model of the test configuration was developed. For high loaded regions, detailed FEM models were applied taking the boundary conditions from the global model. To cover the uncertainty of friction between winding pack and case and also between the different test rig components, different friction coefficients were used in the model. The results were compared with the measurements of global deformation and displacements as well as local equivalent stresses and local strain on structure. The main results were in fair agreement with the expectations from the model. The impact from the friction coefficient was not as strong as expected. Some local coil case behaviour seems to be unpredictable due to welding stresses caused by manufacture without annealing. A closer look on the model deviations shows that the model underestimates the out-of-plane and overestimates the in-plane coil bending. This could be caused by the orthotropic material data assumed for the winding pack, which probably does not reflect the true behaviour of the stack of radial plates housing the conductor.

Under cyclic loading (15 cycles for currents > 75% of rated current) the configuration showed no mechanical degradation.

The measured results allowed an up-scaling by the FEM model above the rated load case (TFMC 70 kA, LCT 16 kA) without the risk of damage. The extended load case (TFMC 80 kA, LCT 16 kA) achieved the Lorentz body force of about 800 kN/m, which was equivalent to the ITER TF coil conditions. Thus, it was demonstrated that the used test configuration is capable to generate ITER TF coil relevant mechanical stresses in structure and conductor.

*10.3.5. Dielectric properties*

The dielectric properties of the TFMC were investigated by DC, AC, and pulse voltage at the specified voltage levels. The special configuration of the winding pack required the treatment of an electrical network, which can be excited by switching transients causing internal oscillations with voltages above the linear distribution of the rated voltage across the winding. The measured TFMC resonance frequency of 300 kHz was in good agreement with that derived from a network model.

The systematic investigation by three kinds of voltages during the different stages of the test program helped to find, localise and assess insulation faults, which appeared in the Paschen minimum even though the TFMC passed before successfully all tests at the rated voltage of 10 kV. Since the fault occurred above 4 kV the high current operation with a safety discharge voltage < 1 kV could be performed without any risk. The problems were identified as a defect in the electrical insulation of the helium supply pipes detected and documented during fabrication.

The developed and applied testing methods have been a powerful tool for investigation and quality assurance of the electrical insulation system of superconducting magnets for fusion during fabrication, acceptance, and operation. The test voltage levels have been selected according to the analysis of the electrical network under possible transient voltages. The worst boundary conditions, which can appear, have to be taken into account for testing.

*10.4. Final conclusions*

The design principles, manufacturing methods and developed components are applicable under industrial conditions for the ITER TF coils.

The test configuration and test facility were fully capable of achieving ITER TF coil relevant operation conditions.

The ITER EDA design criteria were demonstrated to be suitable for the design of the TFMC and the ITER TF coils. The presently proposed ITER TF coils are feasible assuming the use of advanced superconducting strands with higher critical current density. These higher critical current density strands are presently being qualified.

The electrical and thermal-hydraulic properties have been mastered successfully; some improvement and clarification are needed in the ITER design criteria.

The electrical insulation properties have to be monitored carefully during fabrication, acceptance, installation, and operation. They are one of the most critical items determining the lifetime of the magnet.

## Acknowledgements

The TFMC Project was funded by European Fusion Technology Program within the frame of the ITER Research and Development Program. The authors acknowledge the effort of their colleagues and the European industry making substantial contributions to the success of the project by preparing the test facility and fabrication of the TFMC.

## Appendix A

The linear differential Eq. (4.1) written in terms of the circuit currents, is transformed in terms of state variables $x_i$, where $x_i = I_i$, $i = 1, 2, \ldots, 5$ in order to be integrated with SIMULINK. Defining with $u$ the $2 \times 1$ input vector, coinciding with the forcing voltage $V$ with simple algebraic manipulations it is possible to express this equation in the following state variable

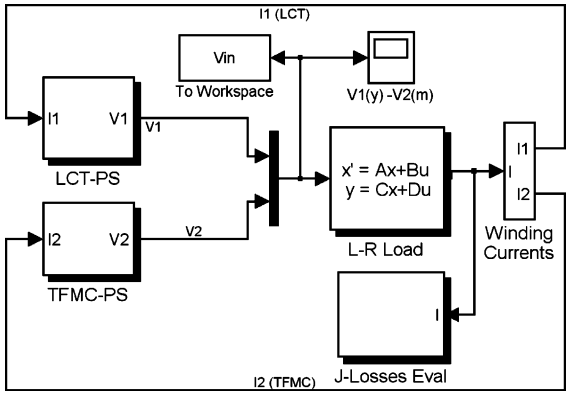


Fig. A.1. SIMULINK model of the LCT–TFMC power circuit for phase II.

matrix form:

$$\frac{dx}{dt} = -L^{-1}Rx + L^{-1}u \tag{A.1}$$

where the $5 \times 5$ inductance matrix $L$, in $H$, is given by:

$$L = \begin{bmatrix} 1.56 & 62.6e-3 & 18.69e-4 & 63.88e-5 & 63.88e-5 \\ 62.6e-3 & 28.02e-3 & 10.65e-5 & 28.20e-5 & 20.14e-5 \\ 18.69e-4 & 10.65e-5 & 3.07e-6 & 1.086e-6 & 1.086e-6 \\ 63.88e-5 & 28.20e-5 & 20.14e-5 & 2.843e-6 & 2.055e-6 \\ 63.88e-5 & 20.14e-5 & 1.086e-6 & 2.055e-6 & 1.985e-6 \end{bmatrix}$$

and the $5 \times 5$ resistance matrix $R$, in $\Omega$, is given by:

$$R = \begin{bmatrix} R_{11} & 0 & 0 & 0 & 0 \\ 0 & R_{22} & 0 & 0 & 0 \\ 0 & 0 & 43.3e-6 & 0 & 0 \\ 0 & 0 & 0 & 27.9e-6 & 0 \\ 0 & 0 & 0 & 0 & 19.1e-6 \end{bmatrix}$$

The method for the calculation of the inductance matrix $L$ and resistances in the passive structures (i.e., $R_{33}$, $R_{44}$ and $R_{55}$)[5] is reported in [62]. The resistance of the LCT coil and TFMC windings (i.e., $R_{11}$ and $R_{22}$) are mostly due to the conventional bus bar system external to the vacuum vessel (i.e., Al bus bar and flexible cables). The circuit Eq. (A.1) is represented in the SIMULINK model by the following state space

[5] Kept constant to the values shown.

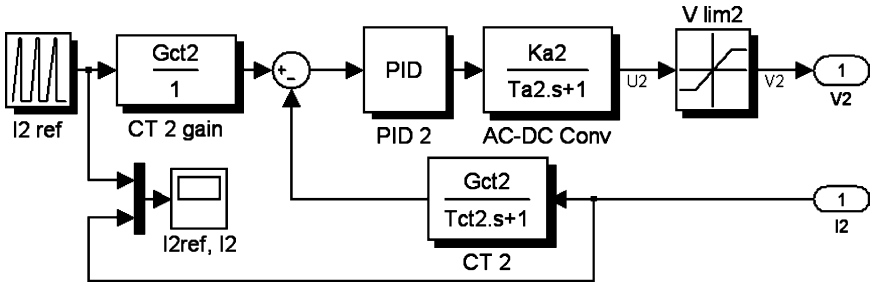


Fig. A.2. SIMULINK model of TFMC power supply (TFMC-PS).

equation:

$$\frac{dx}{dt} = Ax + Bu$$
$$y = Cx + Du \quad (A.2)$$

where $y$ is the output, $A = -L^{-1}R$, $B = L^{-1}$, $C = \text{diag}(1;1;1;1;1)$ and $D = \text{zeroes}(5, 2)$ and $D$ is a $5 \times 2$ matrix with all elements equal to zero.

The state-space model of the coil system represents the main building block of the SIMULINK model shown in Fig. A.1. Other important blocks to simulate the dynamic of the system are the two power supplies models (LCT-PS and TFMC-PS). The dynamic of the 30/50 kA power supply, based on two 12-pulse thyristor converters connected in parallel, is simulated with the SIMULINK model shown in Fig. A.2. The thyristor converters are simulated simply with a first order transfer function with gain $K_{a2}$ and a time constant $T_{a2}$ and a voltage limiter ($\pm 35$ V). A first order transfer function with gain $G_{ct2}$ and a time constant $T_{ct2}$ simulates the current transducer. The current control module is implemented with a conventional PID, of which only the proportional and integral terms are used. The current reference $I_{2ref}$, defined as a series of time–amplitude pairs, allows the implementation of the desired current waveform. The 20 kA power supply, simulated with a similar schema, is also a thyristor converter made of two 6-pulse bridge converters ($\Delta$ and Y) of 10 kA each connected in parallel to yield a 12-pulse converter. The LCT coil power supply feedback controls the sum of the current in the LCT coil and the current in the dump resistor which was permanently connected. This is simulated with an additional block with gain $1/R_{d1}$, where $R_{d1} = 125\,\text{m}\Omega$ is the resistance of the LCT coil dump circuit at room temperature.

An integration method with variable step, called *ode23tb*, and a relative tolerance of 1.e−3 allows simulation times, with a 1.7 GHz Pentium, between 2 and 3 orders of magnitude faster than the real time.

## References

[1] M.S. Lubell, W.F. Gauster, K.R. Jefferson, A.P. Fraas, H.M. Long, J.N. Luton, C.E. Parker, D. Steiner, W.C.T. Stoddart, Engineering design studies on the superconducting magnet system of a tokamak fusion reactor, in: Plasma Physics and Controlled Nuclear Fusion Research, vol. III, IAEA, Vienna, 1971, pp. 433–446.

[2] D.S. Beard, W. Klose, S. Shimamoto, G. Vecsey, The IEA Large Coil Task, Fusion Eng. Des. 7 (1 and 2) (1988) 1–230.

[3] G.H. Miley (Ed.), Next European Torus (NET), Fusion Technol. 14 (July (1)) (1988).

[4] Next European Torus—Predesign Report Fusion Eng. Des. 21 (1993).

[5] B. Blau, I. Rohleder, G. Vecsey, G. Pasotti, M.V. Ricci, N. Sacchetti, et al., Testing of fullsize high current superconductors in SULTAN III, IEEE Trans. Magn. 30 (4) (1994) 1934–1937.

[6] K. Okuno, H. Tsuji, Y. Takahashi, H. Nakajima, K. Kawano, T. Ando, et al., The first experiment of the 30 kA NbTi DEMO POLOIDAL COILS (DPC-U1 and -U2), in: Proceedings of the MT-11, vol. 2, Tsukuba, Japan, August 28–September 1, 1989, pp. 812–817.

[7] M.M. Steeves, M. Takayasu, T.A. Painter, M.O. Hoenig, T. Kato, K. Okuno, H. Nakajima, H. Tsuji, Test results from the $Nb_3Sn$ US-demonstration poloidal field coil, Adv. Cryo. Eng. 37A (1992) 345–354.

[8] M.M. Steeves, M. Takayasu, T.A. Painter, J.V. Minervini, J.H. Schultz, D.B. Montgomery, Applicability of the US-DPC to the ITER model poloidal coil, in: Proceedings of the 14th IEEE/NPSS Symposium Fusion Engineering 91CH3035-3, 1991, pp. 459–464.

[9] M. Darweschsad, G. Friesinger, R. Heller, M. Irmisch, H. Kathol, P. Komarek, W. Maurer, G. Nöther, G. Schleinkofer, C. Schmidt, C. Sihler, M. Süßer, A. Ulbricht, F. Wüchner, Development and test of the poloidal field prototype coil POLO at

Forschungszentrum Karlsruhe, Fusion Eng. Des. 36 (1997) 227–250.
[10] K. Bauer, S. Fink, G. Friesinger, A. Ulbricht, F. Wüchner, The electrical insulation system of a forced-flow-cooled superconducting (sc) magnet, Cryogenics 38 (1998) 1123–1134.
[11] V.A. Alhimovch, I.O. Anashkin, A.N. Vertiporokh, A.N. Volobuev, V.F. Zhulkin, D.P. Ivanov, et al., First tests of T-15 toroidal field superconducting system, in: Proceedings of the MT-11, vol. 2, Tsukuba, Japan, August 28–September 1, 1989, pp. 773–776.
[12] B. Turck, Six years operating experience with Tore Supra, the largest tokamak with superconducting coils, IEEE Trans. Magn. MAG-32 (4) (1996) 2264–2267.
[13] Y. Nakamura, A. Nagao, N. Hiraki, S. Itoh, Reliable and stable operation on the high-field superconducting tokamak TRIAM-1M, in: Proceedings of the MT-11, vol. 2, Tsukuba, Japan, August 28–September 1, 1989, pp. 767–772.
[14] P.-H. Rebut, D. Boucher, D.J. Gambier, B.E. Keen, M.L. Watkins, The ITER challenge, Fusion Eng. Des. 22 (1993) 7–18.
[15] M. Huguet, The ITER magnet system, Fusion Eng. Des. 36 (1997) 23–32.
[16] H. Tsuji, K. Okuno, R. Thome, E. Salpietro, S. Egorov, N. Martovetsky, M. Ricci, R. Zanino, G. Zahn, A. Martinez, G. Vecsey, K. Arai, T. Ishigooka, T. Kato, T. Ando, Y. Takahashi, H. Nakajima, T. Hiyama, M. Sugimoto, N. Hosogane, M. Matsukawa, Y. Kawano, M. Oshikiri, Y. Nunoya, K. Matsui, Y. Tsuchiya, G. Nishijima, H. Kubo, T. Shimba, E. Hara, K. Imahashi, Y. Uno, T. Ohuchi, K. Ohtsu, J. Okayama, T. Kawasaki, M. Kawabe, S. Seki, K. Takano, Y. Takaya, F. Tajiri, G. Tsutsumi, T. Nakamura, H. Hanawa, H. Wakabayashi, T. Shimizu, K. Karamochi, T. Omine, T. Tamiya, J. Harada, K. Nishii, M. Huguet, N. Mitchell, D. Bessette, J. Minervinvi, R. Vieira, P. Michael, M. Takayasu, B. Bevilacqua, R.K. Maix, R. Manahan, R.J. Jayakumar, L. Savoldi, W. Herz, A. Ninomiya, Progress of the ITER central soleniod model coil programme, Nucl. Fusion 41 (2001) 645–651.
[17] N. Martovetsy, P. Michael, J. Minervini, A. Radovinski, M. Takayasu, C.Y. Gung, R. Thome, T. Ando, T. Isono, K. Hamada, T. Kato, K. Kawano, N. Koizumi, H. Nakajima, G. Nishijima, Y. Nunoya, M. Sugimoto, Y. Takahashi, H. Tsuji, D. Bessette, K. Okuno, N. Mitchell, M. Ricci, R. Zanini, L. Savoldi, K. Arai, A. Niomiya, Test of the ITER central solenoid model coil and CS insert, IEEE Trans. Appl. Supercond. 12 (2002) 600–605.
[18] C. Marinucci, L. Bottura, P. Bruzzone, N. Mitchell, B. Stepanov, R. Wesche, Analysis and interpretation of $T_{CS}$ tests of the ITER toroidal field conductor insert coil, IEEE Trans. Appl. Supercond. 14 (2) (2004) 1523–1526.
[19] K. Okuno, N. Martovetsky, N. Koizumi, M. Sugimoto, T. Isono, K. Hamada, et al., Test of the $Nb_3Al$ insert and ITER central solenoid model coil, IEEE Trans. Appl. Supercond. 13 (2) (2003) 1437–1440.
[20] A. Ulbricht, the ITER L2 Project Team, Test results of the ITER toroidal field model coil experiment in the TOSKA facility of the Forschungszentrum Karlsruhe, Fusion Eng. Des. 66–68 (2003) 103–118.
[21] M. Huguet, the ITER Joint Central Team, Key engineering features of the ITER–FEAT magnet system and implication for the R&D programme, in: Proceedings of the 18th IAEA Fusion Energy Conference, 2000.
[22] G. Bevilacqua, l. Borin, G. Drurix, F. Fusari, M. Huguet, R. Kind, G. Malavasi, N. Mitchell, A. Nyilas, G. Poltronieri, E. Salpietro, A. Scardua, C. Sborchia, Manufacture of full scale models of the ITER toroidal field coil cases, Fusion Eng. Des. 58–59 (2001) 281–287.
[23] Belleli Report, Fabrication and Quality Assurance R&D for the TF Coil Cases and Radial Plates (Contract No. NET/96-911), EFDA/CSU IPP-Garching, Germany (unpublished).
[24] The ITER EU Home Team: ITER TF Model Coil—Rationale and Conceptual Design, Naka, April, 1995.
[25] The ITER EU Home Team: Technical Specification for the Manufacture of a TF Model Coil for the ITER Tokamak, Document No. EFDA 0821/S/27E, 15 November 1995, Rev.E 8. December 1999. EFDA-CSU, IPP Garching.
[26] P. Libeyre, B. Bertrand, P. Decool, B. Turck, P. Komarek, W. Maurer, A. Ulbricht, G. Zahn, M. Spadoni, E. Salpietro, Conceptual design of the ITER TF model coil, IEEE Trans. Magn. 32 (4) (1996) 2260–2263.
[27] E. Salpietro, R. Maix, G. Bevilacqua, N. Mitchell, B. Turck, A. Ulbricht, M. Spadoni, The ITER toroidal field model coil development programme, in: Proceedings of the 17th IAEA Fusion Eng. Conference, Yokohama, Japan, 19–24 October, 1998.
[28] P. Komarek, E. Salpietro, The test facility for the ITER TF model coil, Fusion Eng. Des. 41 (1998) 213–221.
[29] Y. Shimomura, R. Aymar, V. Chuyanov, M. Huguet, ITER overview, in: Proceedings of the 17th IAEA Fusion Eng. Conference, Yokohama, Japan, 19–24 October, 1998.
[30] R. Maix, G. di Bartolo, G. Bevilacqua, P. Libeyre, P. Decool, A. Ulbricht, B. Schellong, A. Bourquard, B. Crepel, N. Valle, P. Pesenti, E. Theisen, Manufacture of the ITER TF model coil, in: Proceedings of the 20th SOFT, Marseille, France, 7–11 September, 1998, pp. 833–836.
[31] R. Maix, A. Bourquard, D. Bresson, P. Decool, A. della corte, H. Fillunger, R. Garré, F. Hurd, A. Laurenti, P. Libeyre, N. Mitchell, J. Palmer, E. Salpietro, B. Schellong, E. Theisen, A. Ulbricht, N. Valle, G. Zahn, Manufacture, assembly and QA of the ITER toroidal field model coil, IEEE Trans. Appl. Supercond. 10 (2000) 584–587.
[32] P. Libeyre, B. Crepel, P. Decool, H. Fillunger, B. Glassl, U. Hoeck, R. Kreutz, R. Maix, R. Meyer, R. Penco, S. Raff, E. Theisen, N. Valle, From conceptual to engineering design of the ITER TFMC, in: B. Beaumont, et al. (Eds.), Proceedings of the 20th Symposium on Fusion Technology (SOFT), Marseille, France, 1998, Fusion Technology 1998: Proc. of the 20th Symposium on Fusion Technology, Marseille, France, 7–11 September 1998, pp. 767–770.
[33] R. Maix, H. Fillunger, F. Hurd, E. Salpietro, N. Mitchell, P. Libeyre, P. Decool, A. Ulbricht, G. Zahn, D. Bresson, A. Bourquard, J. Baudet, B. Schellong, E. Theisen, N. Valle, Completion of the ITER toroidal field model coil (TFMC), Fusion Eng. Design 58–59 (2001) 159–216.

[34] E. Salpietro, R. Maix, G. Bevilacqua, N. Mitchell, B. Turck, A. Ulbricht, M. Spadoni, The ITER Toroidal Field Model Coil Development Programme, Fusion Energy 1998, vol. 3, IAEA, Vienna, 1999, p. 1041.

[35] R. Maix, A. della Corte, H. Fillunger, M. Ricci, ITER Toroidal Field Model Coil (TFMC), Test and Analysis Summary Report, Chapter 4: TFMC Manufacturing and Related Quality Control Data, EFDA/CSU Garching, No. EFDA-MS-RE-34.0, 2002.

[36] S. Conti, R. Garre', S. Rossi, A. della Corte, M.V. Ricci, M. Spadoni, G. Bevilacqua, R.K. Maix, E. Salpietro, Fabrication of prototype conductors for ITER TF model coil, in: Proceedings of the 19th Symposium on Fusion Technology (SOFT96), Lisbon, September, Elsevier Science Publ. B.V., 1996, p. 1047.

[37] A. della Corte, M. Ricci, M. Spadoni, G. Bevilacqua, R. Maix, E. Salpietro, S. Conti, R. Garrè, S. Rossi, Successful completion of the conductor manufacture for the ITER TF model coil, in: Proceedings of the Symposium on Fusion Technology (SOFT98), Marseille (F), September, 1998, p. 841.

[38] D. Ciazynski, J.L. Duchateau, T. Schild, A.M. Fuchs, Test results and analysis of two European full-size conductor samples for ITER, IEEE Trans. Appl. Supercond. 10 (2000) 1058–1061.

[39] P. Decool, D. Ciazynski, A. Nobili, S. Parodi, P. Pesenti, A. Bourquard, F. Beaudet, Joints for large superconducting conductors, Fusion Eng. Des. 58–59 (2001) 123–127.

[40] P. Libeyre, P. Decool, J.L. Duchateau, H. Cloez, A. Kienzler, A. Lingor, H. Fillunger, R. Maix, A. Bourquard, F. Beaudet, NbTi superconducting busbars for the ITER TFMC, Fusion Eng. Des. 58–59 (2001) 117–122.

[41] H. Fillunger, F. Hurd, R.K. Maix, E. Salpietro, D. Ciazynsky, J.-L. Duchateau, P. Libeyre, A. Martinez, E. Bobrov, W. Herz, V. Marchese, M. Süßer, A. Ulbricht, F. Wüchner, G. Zahn, A. della Corte, M. Ricci, E. Theisen, G. Kraft, A. Bourquard, F. Beaudet, B. Schellong, R. Zanino, L. Savoldi, Assembly in the test facility, acceptance and first test results of the ITER TF model coil, IEEE Trans. Appl. Supercond. 12 (2002) 595–599.

[42] F.H. Hurd, H. Fillunger, G. Zahn, A. Ulbricht, P. Libeyre, E. Theissen, F. Beaudet, The ITER TF model coil assembly, commissioning and instrumentation, Fusion Eng. Des. 58–59 (2001) 171–176.

[43] H. Fillunger, S. Raff, M. Süßer, F. Wüchner, G. Zahn, ITER Toroidal Field Model Coil (TFMC), Test and Analysis Summary Report, Chapter 2: Sensors, EFDA/CSU Garching, No. N/C/0821/63/889/R/1/A, October 2001.

[44] H. Tsuji, S. Shimamoto, A. Ulbricht, P. Komarek, H. Katheder, F. Wüchner, G. Zahn, Experimental results of domestic testing of the pool-boiling cooled Japanese coil and the forced-flow cooled EURATOM LCT coil, Cryogenics 25 (1985) 539–551.

[45] M. Darweschsad, S. Fink, G. Friesinger, A. Grünhagen, R. Heller, A. Hofmann, W. Herz, P. Komarek, W. Maurer, G. Nöther, K. Rietzschel, G. Schleinkofer, M. Süßer, A. Ulbricht, F. Wüchner, G. Zahn, Test of the EURATOM LCT coil (NbTi conductor) with forced flow He II, Fusion Eng. Des. 45 (1999) 361–375.

[46] R. Heller, W. Maurer, A. Ulbricht, I. Schoenwolf, F. Wüchner, G. Zahn, Abschlußbericht zum Test der Wendelstein 7-X Demonstrationsspule in TOSKA, Wissenschaftliche Berichte, FZKA 6486, Juli 2000.

[47] G. Zahn, M. Darweschsad, G. Dittrich, S. Fink, G. Friesinger, A. Götz, R. Heller, W. Herz, P. Komarek, O. Langhans, W. Lehmann, W. Maurer, I. Meyer, H. Neumann, G. Nöther, W. Ratajczak, J. Sapper, H.P. Schittenhelm, G. Schleinkofer, I. Schoenewolf, R. Singer, E. Specht, H.J. Spiegel, M. Süßer, A. Ulbricht, M. Wanner, F. Werner, F. Wüchner, Cryogenic Experience and Test Results of the Wendelstein 7-X (W7-X) Demo Coil Test in TOSKA, in: Proceedings of the 18th ICEC, Mumbai, India, February 21–25, 2000, pp. 139–142.

[48] G.R. Zahn, M. Bagnasco, M. Darweschsad, G. Dittrich, J.L. Duchateau, H. Fillunger, W.H. Fietz, S. Fink, U. Fuhrman, R. Heger, R. Heller, W. Herz, P. Komarek, A. Kienzler, O. Langhans, W. Lehmann, A. Lingor, I. Meyer, H. Neumann, S. Nicollet, G. Noether, M. Roehrling, L. Savoldi-Richard, E. Specht, M. Süsser, A. Ulbricht, F. Wuechner, R. Zanino, Cryogenic test results of the ITER TF model coil test in TOSKA, in: Proceedings of the CEC, Anchorage, USA, September 22–26, Adv. Cryo. Eng., vol. 49A, 2004, pp. 675–684.

[49] W.H. Fietz, E. Bobrov, ITER Toroidal Field Model Coil Test Program, Outline of the Test Procedure Phase 2, Version 3.2, July 23, 2002. ITP/Forschungszentrum Karlsruhe, unpublished.

[50] F. Spath, R. Heil, J. Lesser, H. Schimmer, J. Weber, A. Gray, et al., A 2 kW He refrigerator for SC magnet tests down to 3.3 K, in: Proceedings of the 14th ICEC, Kiev, Ukraine, June 8–12, 1992, pp. 56–59.

[51] S. Nicollet, J.L. Duchateau, R. Heller, G. Zahn, L. Savoldi, R. Zanino, H. Fillunger, R. Maix, Hydraulic resistance of the ITER toroidal field model coil dual channel cable-in-conduit pancakes, in: Proceedings of the 19th ICEC, Grenoble, France, July 22–26, 2002, pp. 161–164.

[52] R. Zanino, M. Bagnasco, H. Fillunger, R. Heller, L. Savoldi Richard, M. Suesser, G. Zahn, Thermal-hydraulic issues in the ITER toroidal field model coil (TFMC) test and analysis, in: Proceedings of the CEC, Anchorage, USA, September 22–26, Adv. Cryo. Eng., vol. 49A, 2004, pp. 685–692.

[53] G. Zahn, M. Darweschsad, G. Dittrich, S. Fink, G. Friesinger, A. Götz, R. Heller, W. Herz, A. Hofmann, P. Komarek, O. Langhans, W. Lehmann, W. Maurer, I. Meyer, G. Nöther, G. Perinic, W. Ratajczak, H.P. Schittenhelm, G. Schleinkofer, E. Specht, H.J. Spiegel, M. Süsser, A. Ulbricht, F. Wüchner, Experiences with 1.8 K forced flow HeII cooling of a large superconducting magnetdkjdot, in: Proceedings of the 17th ICEC, Bournemouth, UK, July 14–17, 1998, pp. 883–886.

[54] R. Zanino, M. Bagnasco, G. Dittrich, W.H. Fietz, H. Fillunger, D.P. Hampshire, et al., $T_{CS}$ tests and performance assessment of the ITER toroidal field model coil (phase II), IEEE Trans. Appl. Supercond. 14 (2) (2004) 1519–1522.

[55] R. Heller, S. Fink, G. Friesinger, A. Kienzler, A. Lingor, G. Schleinkofer, M. Süsser, A. Ulbricht, F. Wüchner, G. Zahn, Development of forced flow cooled current leads for fusion magnets, Cryogenics 41 (2001) 201–211.

[56] R. Heller, G. Friesinger, A. Kienzler, P. Komarek, A. Lingor, A. Ulbricht, G. Zahn, Construction and operation performance of the 80 kA current leads used for the test of the ITER toroidal

field model coil in the TOSKA facility, IEEE Trans. Appl. Supercond. 13 (2) (2003) 1918–1921.
[57] G. Friesinger, R. Heller, Use of $Nb_3Sn$ inserts in a forced flow cooled 30 kA current lead, Appl. Supercond. 2 (1) (1994) 21–27.
[58] R. Heller, Numerical Calculation of Current Leads for Fusion Magnets, KfK Report KfK 4608, 1989.
[59] A. Ulbricht, M.S. Darweschsad, S. fink, G. Friesinger, R. Heller, W. Herz, A. Kienzler, A. Lingor, V. Marchese, I. Meyer, G. Nöther, G. Schleinkofer, M. Süßer, F. Wüchner, G. Zahn, ITER Toroidal Field Model Coil (TFMC), Test and Analysis Summary Report, Chapter 3: TOSKA Facility, Forschungszentrum Karlsruhe, Wissenschaftliche Berichte FZKA 6614, Mai 2001, pp. 67–143.
[60] V. Marchese, S.M. Darweschsad, G. Nöther, A. Ulbricht, F. Wüchner, Circuit analysis and control of the power supply system for the testing of ITER TF model coil, Fusion Eng. Des. 58–59 (2002) 69–73.
[61] V. Marchese, Circuit analysis and operation experience with power supplies and 80 kA dump circuit for TFMC, Minutes of the Thirdrd TFMC Test Group Meeting, Presentation of the TFMC Test Results of Phase I, Forschungszentrum Karlsruhe, 22–23 January, 2002, unpublished.
[62] P. Hertout, J.-L. Duchateau, A. Martinez, Eddy current and thermal analysis of the TF Model Coil during safety discharges, IEEE Trans. Appl. Supercond. 11 (1) (2001) 1534–1537.
[63] J.-L. Duchateau, D. Ciazynski, P. Hertout, S. Nicollet, M. Rebai, M. Ricci, R. Heller, ITER toroidal field model coil test: analysis of heat transfer from plates to conductor, Fusion Eng. Des. 66–68 (2003) 1007–1011.
[64] A. Augenstein, H. Barthel, I. Donner, H. Frankrone, G. Gruber, G. Hellmann, et al., A data acquisition, control and visualization system for the upgraded TOSKA facility at FZK, Proceedings of the 19th SOFT, Lisbon, Portugal, September 16–20, 1996, pp. 921–924.
[65] G. Nöther, S. Gauß, W. Maurer, L. Siewerdt, A. Ulbricht, F. Wüchner, Quench detection system of the EURATOM coil for the Large Coil Task, Cryogenics 29 (December) (1989) 1148–1153.
[66] A. Hofmann, P. Komarek, W. Maurer, G. Ries, B. Rzezonka, H. Salzburger, Ch. Schnapper, A. Ulbricht, G. Zahn, Further use of the EURATOM LCT coil, in: Proceedings of the 15th SOFT, Utrecht, Netherlande, 19–23 September, 1988, pp. 1556–1802.
[67] R. Heller, M. Darweschsad, S. Fink, G. Friesinger, W. Herz, W. Maurer, G. Nöther, G. Schleinkofer, M. Süßer, A. Ulbricht, F. Wüchner, G. Zahn, Operation limits of the EURATOM LCT coil at forced flow He II temperature, Cryogenics 38 (1998) 519–524.
[68] A. Grünhagen, Detailed analysis of the LCT coil with input displacements (version no. 4) taken from the global model of the configuration wit the TFMC, Wiss. Berichte FZKA 6776, November 2002. Forschungszentrum Karlsruhe.
[69] T. Schild, D. Ciazynski, S. Court, Effect of actual cabling pattern on the critical current of a multistage CIC, Adv. Cryo. Eng. 46B (2000) 1051.
[70] D. Ciazynski, J.L. Duchateau, Validation of the CEA electrical network model for the ITER coils, IEEE Trans. Appl. Supercond. 11 (1) (2001) 1530.
[71] V. Galindo, D. Ciazynski, J.L. Duchateau, G. Nishijima, N. Koizumi, Y. Takahashi, T. Ando, Current distribution and strain influence on the electromagnetic performance of the CS insert, IEEE Trans. Appl. Supercond. 11 (1) (2001) 1538.
[72] J.L. Duchateau, D. Ciazynski, O. Guerber, S.H. Park, W.H. Fietz, A. Ulbricht, G. Zahn, L. Zani, Exploring the limits of a very large $Nb_3Sn$ conductor: the 80 kA conductor of the ITER toroidal field model coil, Supercond. Sci. Technol. 17 (2004) 241–249.
[73] P. Hertout, Magnetic field calculations for the TFMC tests, CEA Internal Note AIM/NTT-2000.010, March 17, 2000, unpublished.
[74] S. Raff, Stress analysis for the TFMC tests in TOSKA: conductor strain in pancake P1, Internal Note IRS 04/02, Fusion 187, May 2002, unpublished.
[75] A. Martinez, J.L. Duchateau, Field and temperature dependencies of critical current on industrial $Nb_3Sn$ strands, Cryogenics 37 (12) (1997) 865.
[76] J.L. Duchateau, D. Ciazynski, P. Hertout, M. Spadoni, W. Specking, Electromagnetic evaluation of the collective behaviour of 720 twisted strands for the TFMC, IEEE Trans. Appl. Supercond. 11 (1) (2001) 2026.
[77] L.T. Summers, M.W. Guinan, J.R. Miller, P.A. Hahn, A model for the prediction of $Nb_3Sn$ critical current as a function of field, temperature, strain and radiation damage, IEEE Trans. Mag. 27 (1991) 2041.
[78] R. Zanino, L. Savoldi Richard, Performance evaluation of the ITER toroidal field model coil phase I. Part 2: M&M analysis and interpretation, Cryogenics 43 (2003) 91–100.
[79] R. Zanino, N. Mitchell, L. Savoldi Richard, Analysis and interpretation of the full set (2000–2002) of $T_{CS}$ tests in conductor 1A of the ITER central solenoid model coil, Cryogenics 43 (2003) 179–197.
[80] L. Savoldi, R. Zanino, M&M: multi-conductor mithrandir code for the simulation of thermal-hydraulic transients in superconducting magnets, Cryogenics 40 (2000) 179–189.
[81] L. Savoldi, R. Zanino, Predictive study of current sharing temperature test in the toroidal field model coil without LCT coil using the M&M code, Cryogenics 40 (2000) 539–548.
[83] R. Zanino, L. Savoldi Richard, the TFMC Testing Group, Performance evaluation of the ITER toroidal field model coil phase I. Part 1: Current sharing temperature measurement, Cryogenics 43 (2003) 79–90.
[84] L. Savoldi, R. Zanino, V. Marchese, N. Martovetsky, M. Suesser, A. Ulbricht, F. Wuechner, G. Zahn, First measurement of the current sharing temperature at 80 kA in the ITER toroidal field model coil (TFMC), IEEE Trans. Appl. Supercond. 12 (2002) 635–638.
[85] M. Bagnasco, L. Savoldi Richard, R. Zanino, Effect of a resistive heater on the supercritical helium dynamics in the ITER superconducting toroidal field model coil experiments, in: Proceedings of the 21st Meeting of the Italian Thermal-Hydraulics Union, 2003, pp. 483–488.

[86] R. Heller, D. Ciazynski, J.L. Duchateau, V. Marchese, L. Savoldi-Richard, R. Zanino, Evaluation of the current sharing temperature of the ITER toroidal field model coil, IEEE Trans. Appl. Supercond. 13 (2003) 1447–1451.
[87] R. Zanino, M. Bagnasco, L. Savoldi Richard, the TFMC Testing Group, Preliminary analysis of TFMC $T_{CS}$ tests phase II, November 24, 2002 (Available from: http://staff.polito.it/∼zanino/ep/titles/PSTTT.pdf).
[88] D. Ciazynski, Tests of PF–FSJS in SULTAN: thermohydraulics and calibrations, Presented at the CRPP Meeting on Fifteen months of NbTi CICC Results in SULTAN, Gstaad, Switzerland, 22–24 January, 2003, CRPP, Villigen (Switzerland), unpublished.
[89] S. Nicollet and J.L. Duchateau, ITER Task CODES: Cable-in-conduit Conductor central spiral characterization and influence of new correlation on heat transfer coefficient, CEA Internal Report DRFC/STEP AIM/NTT-2002.029, 25 April, 2002, unpublished.
[90] D. Ciazynski, Analysis of TFMC current sharing tests: comparisons with new analyses of TFMC–FSJS and TF–FSJS tests in SULTAN, 16th TFMC Test Analysis Meeting, Karlsruhe, 28 May, 2002. unpublished.
[91] D. Bessette, private communication (2003).
[92] N. Mitchell, D. Bessette, K. Okuno, H. Takigami, E. Zapretilina, P. Bruzzone, Annex to DRG1: Superconducting Material Database Article 2. Strand Strain in Nb3Sn Jacketed Conductors, ITER Report N 11 FDR 39 01-07-04 R 0.1, 2001, unpublished.
[93] ITER JCT Naka, Magnet Superconducting and Electrical Design Criteria—Annex to Design Requirements and Guidelines Level 1 (DRG1), ITER Document N 11 FDR 12 01-07-02 R 0.1, 2001, unpublished.
[94] A. Godeke, H.G. Knoopers, A. Nijhuis, H.J.G. Krooshoop, B. ten Haken, H.H.J. ten Kate, Characterization of ITER strands in the frame of the third benchmark tests, Internal Report University of Twente, UT-NET 98-5, 1998, unpublished.
[95] N. Mitchell, Mechanical and magnetic load effects in $Nb_3Sn$ cable-in-conduit conductors, Cryogenics 43 (2003) 255–270.
[96] J.-L. Duchateau, M. Spadoni, E. Salpietro, D. Ciazynski, M. Ricci, P. Libeyre, A. Della Corte, et al., Development of high current high field conductors in Europe for fusion application, Supercond. Sci. Technol. 15 (2002) R17–R29.
[97] W. Specking, J.L. Duchateau, P. Decool, First results of strain effects on critical current of incoloy jacketed $Nb_3Sn$ CICC's, in: Proceedings of MT-15 Conference (Beijing), 1998, pp. 1210–1213.
[98] A. Godeke, B. ten Haken, H.H.J. ten Kate, Scaling of the critical current in ITER type niobium-tin superconductors in relation to the applied field, temperature and uni-axial applied strain, IEEE Trans. Appl. Supercond. 9 (2) (1999) 161–164.
[99] R. Zanino, M. Bagnasco, L. Savoldi Richard, Assessment of the model coil and insert coil results, ITER Magnet Meeting, Garching, Germany, 6–9 May, 2003, unpublished.
[100] D.M.J. Taylor, D.P. Hampshire, Comparison of the E-T and E-J characteristics and parameterisation of the critical current density of an EM-LMI niobium-tin superconducting wire as a function of magnetic field, temperature and strain, Cryogenics, submitted for publication.
[101] S.A. Keys, D.P. Hampshire, A scaling law for the critical current density of weakly and strongly-coupled superconductors, used to parameterise data from a technological Nb3Sn strand, Supercond. Sci. Technol. 16 (2003) 1097–1108.
[102] D.M.J. Taylor, D.P. Hampshire, EM-LMI Strand Parameterisation, private communication, 2003.
[104] W. Ekin, Mechanical, properties and strain effects in superconductors, in: Superconductor Material Science, Plenum Press, New York, 1981, p. 455.
[105] D.P. Boso, M. Lefik, B.A. Schreffler, A multilevel homogenised model for superconducting strands, Cryogenics 45 (4) (2005) 259–271.
[106] N. Mitchell, Summary, assessment and implications of the ITER model coil test results, Fusion Eng. Des. 66–68 (2003) 971–983.
[107] D. Bessette, Sensitivity of $Nb_3Sn$ ITER conductor design to selected parameters, IEEE Trans. Appl. Supercond. 13 (June (2)) (2003) 1433–1436.
[108] P. Hertout, J.L. Duchateau, A. Martinez, Eddy current and thermal analysis of the TF model coil during safety discharge, IEEE Trans. Appl. Supercond. 11 (1) (2001) 1534–1537.
[109] J.L. Duchateau, P. Hertout, S. Nicollet, M. Ricci, A. Ulbricht, G. Zahn, AC losses in the ITER TF model coil: a comparison between model and experimental results, in: Proceedings of the 19th International Cryogenic Engineering Conference (ICEC 19), Grenoble, France, 2002, pp. 285–288.
[110] P. Hertout, Presentation of the TFMC Model for Field Calculations. Evaluation of Incertitudes, 17th Tests and Analysis Meeting, Cadarache 04–05/02/2003, unpublished.
[111] E.P. Balsamo, D. Ciazynski, O. Cicchelli, P. Gislon, G. Pasotti, M.V. Ricci, M. Spadoni, Direct measurement of the AC loss of an ITER relevant coil, in: International Cryogenic Material Conference (ICMC98), Topical Conference on AC Loss and Stability, Physica C, vol. 310, University of Twente (NL), May, 1998, p. 258.
[112] A. Nijhuis, H.H.J. ten Kate, P. Bruzzone, The influence of Lorentz force on the AC loss in sub-size CIC conductors for ITER, IEEE Trans. Appl. Supercond. 7 (June (2)) (1997) 262–265.
[113] A. Nijhuis, Yu. Ilyin, W. Abbas, B. ten Haken, H.H.J. ten Kate, Performance of an ITER CS1 model coil conductor under transverse cyclic loading up to 40,000 cycles, IEEE Trans. Appl. Supercond. 14 (2) (2004) 1489–1494.
[114] A. Nijhuis, N.H.W. Noordman, N. Mitchell, H.H.J. ten Kate, Electromagnetic and mechanical AC loss of an ITER TF model coil conductor (DP4) under transverse cyclic loading, IEEE Trans. Appl. Supercond. 10 (March (1)) (2000) 588–591, ISSN 1051-8223.
[115] M. Ricci, Deliverable #3 of the Task GB8-M12: Report on CS Model Coil Test Results, May 31, 2001, ENEA, Frascati, Italy, unpublished.
[116] N. Martovetsky, P. Michael, J. Minervini, A. Radovinsky, M. Takayasu, C.Y. Gung, R. Thome, T. Ando, T. Isono, K. Hamada, T. Kato, K. Kawano, N. Koizumi, K. Matsui, H. Nakajima, G. Nishijima, Y. Nunoya, M. Sugimoto, Y. Taka-

hashi, H. Tsuji, D. Bessette, K. Okuno, N. Mitchell, M. Ricci, R. Zanino, L. Savoldi, K. Arai, A. Ninomiya, Test of the ITER central solenoid model coil and CS insert, IEEE Trans. Appl. Supercond. 12 (1) (2002) 600–605.

[117] M. Ricci, Deliverable #2 of the Task TW2-TMST-TOSKA: Installation and Testing of the TFMC + LCT Coil in TOSKA, March 25, 2003, ENEA, Frascati, Italy, unpublished.

[118] J.L. Duchateau, D. Ciazynski, P. Hertout, S. Nicollet, M. Rebaï, M. Ricci, R. Heller, ITER Toroidal Field Model Coil test: analysis of heat transfer from plates to conductors, Fusion Eng. Des. 66–68 (2003) 1007–1011.

[119] M. Ricci, Deliverable #5 of the Task GB8-M12: Report on TF Model Coil Test Results, February 19, 2002, ENEA, Frascati, Italy, unpublished.

[120] P. Libeyre, B. Bertrand, P. Decool, B. Turck, P. Komarek, W. Maurer, A. Ulbricht, G. Zahn, M. Spadoni, E. Salpietro, Conceptual design of the ITER TF model coil, IEEE Trans. Mag. 32 (1996) 2260.

[122] V. Pasler, R. Meyder, G. Schmitz, Effective thermal conductivity of the conductor insulation of the ITER toroidal field model coil at operation temperature, Cryogenics 43 (2003) 199–207.

[123] S. Nicollet, J.L. Duchateau, P. Hertout, M. Rebaï, Heat transfer from plates to conductors: from toroidal field model coil tests analysis to ITER model, Cryogenics 43 (2003) 209–214.

[124] R. Zanino, L. Savoldi, Tests and modeling of heat generation and heat exchange in the full size joint sample, in: Proceedings of the 18th ICEC, 2000, pp. 363–366.

[125] M. Bagnasco, L. Savoldi Richard, R. Zanino, Effect of a resistive heater on the supercritical helium dynamics in the ITER superconducting toroidal field model coil experiments, in: Proceedings of XXI Congresso Nazionale sulla Trasmissione del Calore, 2003, pp. 483–488.

[127] S. Nicollet, J.L. Duchateau, H. Fillunger, R. Heller, R. Maix, L. Savoldi, G. Zahn, R. Zanino, Hydraulic resistance of the ITER toroidal field model coil dual channel cable-in-conduit conductor pancakes, in: Proceedings of the 19th International Cryogenic Engineering Conference, Grenoble, France, 2002, pp. 161–164.

[128] H. Katheder, Optimum thermohydraulic operation regime for cable in conduit superconductor (CICC), in: Cryogenics and ICEC 15 Proceedings, vol. 34, 1994, pp. 589–595.

[129] S. Nicollet, H. Cloez, J.L. Duchateau, J.P. Serries, Hydraulics of the ITER toroidal field model coil cable-in-conduit conductors, in: Proceedings of the 20th Symposium on Fusion Technology, Marseille, France, 1998, pp. 771–774.

[130] S. Nicollet, J.L. Duchateau, H. Fillunger, A. Martinez, S. Parodi, Dual channel cable in conduit thermohydraulics: influence of some design parameter, IEEE Trans. Appl. Supercond. 10 (1) (2000) 1102–1105.

[131] S. Nicollet, J.L. Duchateau, H. Fillunger, A. Martinez, Calculations of pressure drop and mass flow distribution in the toroidal field model coil of the ITER project, Cryogenics 40 (2000) 569–575.

[132] ITER Joint Central Team, Magnet Superconducting and Electrical Design Criteria, Annex to Design Requirements and Guidelines Level 1 (DRG1), ITER Joint Work Site, Naka, Japan, 2002, p. 25.

[133] R. Zanino, P. Santagati, L. Savoldi, A. Martinez, S. Nicollet, Friction factor correlation with application to the central cooling channel of cable-in-conduit superconductors for fusion magnets, IEEE Trans. Appl. Supercond. 10 (1) (2000) 1066–1069.

[134] C. Marinucci, L. Bottura, P. Bruzzone, Analysis of the measurement of the current sharing temperature in the ITER TF Model Coil, Proceedings of the 22nd SOFT, Helsinki, Finland, September 19–13, 2002, Fusion Eng. Des. 66–68 (2003) 1001–1005.

[135] K. Hamada, T. Kato, K. Kawano, E. Hara, T. Ando, H. Tsuji, K. Okuno, R. Zanino, L. Savoldi, Experimental results of pressure drop measurement in ITER CS model coil tests, Adv. Cryo. Eng. 47 (2002) 407–414.

[136] R. Zanino, C.Y. Gung, K. Hamada, L. Savoldi, Pressure drop analysis in the CS insert coil, Adv. Cryo. Eng. 47 (2002) 364–437.

[137] L. Bottura, A numerical model for the simulation of quench in the ITER magnets, J. Comput. Phys. 125 (1996) 26–41.

[138] S. Nicollet, J.L. Duchateau, H. Fillunger, S.H. Park, G. Zahn, Experimental thermal behaviour of the toroidal field model coil: application to ITER TF transient regimes, Proceedings of CEC03, Anchorage, USA, 2003, Adv. Cryogen. Eng. 49A (2004) 693–700.

[139] P. Hertout, A. Bleyer, J.L. Duchateau, A. Martinez, S. Nicollet, Model of heat deposition during fast discharge tests of the ITER TFMC, IEEE Trans. Appl. Supercond. 12 (1) (2002) 1426–1429.

[140] He-Tables, Helium Properties, Version 2.1, CryoSoft 1997.

[141] P. Libeyre, D. Ciazynski, J.L. Duchateau, T. Schild, W.H. Fietz, G. Zahn, How should we test the ITER TF coils? Proceedings of the 23rd Symposium on Fusion Technology (SOFT), Venice, Italy, 2004, in press.

[142] A. Nijhuis, Yu Ilyin, W. Abbas, H.H.J. ten Kate, M.V. Ricci, A. della Corte, Impact of void fraction on mechanical properties and evolution of coupling loss in ITER $Nb_3Sn$ conductors under cyclic loading, Proceedings of the Applied Superconductivity Conference, October, 3–8, 2004, Jacksonville, USA, Trans. Appl. Supercond. 15 (2) (2005) 1633–1636.

[144] D. Ciazynski, Contributions to the electromagnetic analysis of the ITER TFMC phase I experiment, CEA Cadarache (France), Tech. Rep. AIM/NTT-2002.001, January, 2002, unpublished.

[145] D. Ciazynski, M. Ricci, J.L. Duchateau, V. Marchese, A. Ulbricht, F. Wuechner, G. Zahn, H. Fillunger, R. Maix, Resistances of electrical joints in the TF model coil of ITER: comparisons of first test results with samples results, IEEE Trans. Appl. Supercond. 12 (March (1)) (2002) 543.

[146] P. Libeyre, D. Ciazynski, P. Decool, E. Salpietro, R. Maix, H. Fillunger, A. Bonito Oliva, B. Crepel, R. Kreutz, Development of joints in Europe for the ITER TFMC, in: Proceedings of the 15th International Conference on Magnet Technology, Science Press, Bejing, 1998, p. 421.

[147] D. Ciazynski, P. Decool, M. Rubino, J.M. Verger, N. Valle, R. Maix, Fabrication of the first European full-size joint sam-

ple for ITER, IEEE Trans. Appl. Supercond. 9 (2) (1999) 648.
[148] D. Ciazynski, J.L. Duchateau, T. Schild, A.M. Fuchs, Test results and analysis of two European full-size conductor samples for ITER, IEEE Trans. Appl. Supercond. 10 (March (1)) (2000) 1028.
[149] P. Decool, D. Ciazynski, A. Nobuli, S. Parodi, P. Pesenti, A. Bourquard, F. Beaudet, Joints for large superconducting conductors, Fusion Eng. Des. 58–59 (2001) 123.
[150] D. Ciazynski, P. Decool, B. Jager, A. Martinez, Test results of the EU subsize conductor joints for ITER, in: Proceedings of the 19th SOFT Conference, Lisbon, 1996, 1996, pp. 1039–1042.
[151] D. Ciazynski, B. Bertrand, P. Decool, A. Martinez, L. Bottura, Results of the European study on conductor joints for ITER coils, IEEE Trans. Magn. 32 (July (4)) (1996) 2332–2335.
[152] P. Libeyre, P. Decool, J.L. Duchateau, H. Cloez, A. Kienzler, A. Lingor, H. Fillunger, R. Maix, A. Bourquard, F. Beaudet, NbTi superconducting bus bars for the ITER TFMC, Fusion Eng. Des. 58–59 (Part B) (2001) 117–122.
[153] P. Michael, Current redistribution estimates in the CS insert coil, MIT PSFC, Cambridge, MA, Rep. USCSMC/Conductor Properties/02.06.01/P. Michael/Ver.1, February, 2001, unpublished.
[154] D. Ciazynski, H. Cloez, P. Decool, F. Wuechner, L. Zani, Current distribution measurement in the bus bars of the ITER TF model coil, IEEE Trans. Appl. Supercond. 13 (2) (2003) 1420.
[155] F. Bellina, T. Bonicelli, M. Breschi, M. Ciotti, A. Della Corte, A. Formisano, et al., Superconductive cables current distribution analysis, Fusion Eng. Des. 66–68 (Part B) (2003) 1159–1163.
[156] P. Decool, D. Ciazynski, Analysis of the Busbars Current Distribution, CEA Internal Note DRFC/STEP_AIM/NTT-2000. 021, 26 September, 2000, unpublished.
[157] A. Formisano, R. Martone, Current profile estimation from magnetic measurements in SC cables, in: Proceedings of EUCAS 2003, Sorrento, Italy, 15–17 September, 2003.
[158] A. Formisano, R. Martone, Optimization of magnetic sensors for current reconstruction, COMPEL 22 (3) (2003) 535–548.
[159] Yu. Ilyin, A. Nijhuis, Case studies in reconstruction efficiency of current distribution in CICC's by self-field measurements, Trans. Appl. Supercond. 13 (June (2)) (2003) 1748–1751.
[160] A. Nijhuis, Y. Ilyin, H.G. Knoopers, W. Abbas, Validation of Codes, Current Distribution Measurements and Support Experimental Actions and Analysis, 1st Intermediate Report Contract No.: EFDA-02/627, August 27, 2003, unpublished.
[161] A. Nijhuis, Yu. Ilyin, H.H.J. ten Kate, Analysis of the current distribution in the ITER CS-insert model coil conductor by self field measurements, IEEE Trans. Appl. Supercond. 12 (March (1)) (2002) 1675–1679, ISSN 1051-8223.
[162] Yu. Ilyin, A. Nijhuis, H.H.J. ten Kate, B. Stephanov, P. Bruzzone, Self-field measurements by Hall sensors on the SECRETS short sample CICC's subjected to cyclic load, Trans. Appl. Supercond. 13 (June (2)) (2003) 1752–1755.
[163] S. Raff, P. Schanz, F. Wüchner, H. Fillunger, P. Libeyre, Mechanical behaviour of the ITER toroidal field model coil (TFMC) in the single coil test, Fusion Eng. Des. 66–68 (2003) 995–1000.
[164] S. Raff, P. Schanz, H. Fillunger, B. Glaßl, Structural analysis and verification of the ITER TF model coil test conditions, Fusion Eng. Des. 58–59 (2001) 247–251.
[165] ANSYS Release 7.0, ANSYS Inc., October, 2002.
[166] P. Libeyre, N. Dolgetta, P. Decool, S. Raff, P. Schanz, F. Wüchner, H. Fillunger, Mechanical tests of the ITER toroidal field model coil, in: Proceedings of the MT-18, Morioka, Japan, October 20–24, 2003.
[167] C.T.J. Jong, Non-Linear 3D Global Structural Analysis of ITER-FEAT Toroidal Field Magnet System, N11 RI 27 00-06-29 F1, Annex [1] of ITER Design Description Document, 2001.
[168] P. Komarek, Results and conclusions from the ITER TFMC testing, in: Proceedings of the 20th IEEE/NPSS Symposium on Fusion Engineering (SOFE), San Diego CA, USA, October 14–17, 2003.
[169] B. Bareyt, Assessment of the TF Coil Circuit Behaviour During Normal and Fault Conditions, ITER Final Design Report, DDD 11 Magnet, 2.4 Fault and Safety Analysis, Annex 6a, ITER International Team Naka, Japan, 2001.
[170] R. Maix, G. Di Bartolo, G. Bevilacqua, P. Libeyre, P. Decool, A. Ulbricht, et al., Manufacture of the ITER TF model coil, in: Proceedings of the 20th SOFT, Marseille, 1998, pp. 833–836.
[171] A. Miri, C. Sihler, A. Ulbricht, Reduction of transient electrical stresses in large magnet coils by optimized grounding conditions, in: Proceedings of the 10th International Conference on High Volt. Eng., Montreal, CDN, August 25–29, 1997.
[172] A. Miri et al., Transient Voltage Effects in the ITER TF Model Coil, Final Report, ITER Task No: N11TT84/SCS2, Forschungszentrum Karlsruhe, ITP, 1999.
[173] S. Fink, A. Ulbricht, H. Fillunger, A. Bourquard, M. Prevot, High voltage tests of the ITER toroidal field model coil insulation system, IEEE Trans. Appl. Supercond. 12 (1) (2002) 554–557.
[174] M. Darweschsad, G. Nöther, C. Sihler, A. Ulbricht, W. Weigand, F. Wüchner, Switching circuit generating fast field transients in superconducting coils, in: Proceedings of the 19th SOFT, Lisboa, Portugal, September 16–20, 1996, pp. 999–1002.
[175] C. Sihler, Untersuchung von transienten elektrischen, magnetischen und mechanischen Vorgängen in großen supraleitenden Magnetspulen, Forschungszentrum Karlsruhe, Wissenschaftliche Berichte FZKA 5790, 1996, pp. 61.

## Glossary

AC: alternate current
AGAN: European industry consortium for manufacturing the TFMC (Ansaldo Superconduttori; Alstom former GEC Alsthom; Accel Instruments; Babcock Noell Nuclear
ALI: JAERI's $Nb_3Al$ Insert Coil
ANSYS: finite element code
ATI: Atominstitut der Österreichischen Universitäten, Wien (Atomic Institute of the Austrian Universities, Vienna)

B: magnetic flux density
BB1, BB2: superconducting NbTi bus bars type 1 (winding terminal – joint BB1/BB2), respectively, type 2 (joint BB1/BB2 – cold end current lead) used for connecting the coil terminals with the cold end current lead terminal with an intermediate joint BB1/BB2 (for assembly of the test configuration in the TOSKA vacuum vessel) for the positive (+) and negative (−) polarity (see Figs. 4.22, 4.23, 7.1 and 7.7)
BBC: Brown Boveri Corporation now ABB (Asea Brown Boveri)
CCD: charge coupled device
CDA: Conceptual Design Activity (ITER CDA)
CEA: Commissariat à l'Energie Atomique (France)
CERNOX: ceramic oxynitride resistance temperature sensor (Lakeshore$^{TM}$)
CIC: cable-in-conduit
CICC: cable-in-conduit conductor
CL: coupling losses
CRPP: Centre Recherche en Physique du Plasma, Technologie de la Fusion, Villigen PSI, Switzerland
CS: central solenoid
CSIC: central solenoid insert coil
CSMC: central solenoid model coil
CSU: Close Support Unit
CURLEAD: Computer code for calculations of gas cooled current leads
DAS: Data acquisition system
DGEBA: diglycidylether bisphenol A (epoxy resin)
DP: double pancake
DPC: Demo Poloidal Field Coil Project, JAERI, Japan
DPn: double pancake No. $n$, $n = 1$–5
DQ: difference in the instantaneous power of pancakes P1.1 and P1.2
EB welding: electron beam welding
ECL: eddy current losses
EDA: Engineering Design Activity (ITER EDA)
EDI: voltage tap for voltage drop across the joints
EDS: voltage tap for pancake voltage, respectively, double pancake voltage
EFDA: European Fusion Development Agreement
EK: voltage tap for compensated voltage of a pancake
ENEA: Ente per le Nuove tecnologie, l'Energia e l'Ambiente—Frascati Research Center, Frascati, Italy
ENSIC: electrical-thermal-hydraulic code developed by CEA
ETHERNET: the term *Ethernet* refers to the family of local-area network (LAN) products covered by the IEEE 802.3 standard that defines what is commonly known as the CSMA/CD protocol
EU: European Union
EURATOM: European Atomic Energy Community
FBI: conductor test facility testing strands and sub-cables under axial strain up to 100 kN (F), 13 T (B), and 10 kA (I) at FZK/ITP, Karlsruhe, Germany
FCV: flow control valve
FE: finite elements
FEM: finite element method
FI: flow indicator
FSJS: full size joint sample (ITER full scale joint sample tested in the SULTAN facility)
FZK (Karlsruhe): Forschungszentrum Karlsruhe (Research Centre Karlsruhe), Germany
GANDALF: code for calculation of thermal-hydraulic properties in a one or two channel cooling system
GDI: displacement sensor
GEI: strain gauge
GRDM: GANDALF Radial Diffusion Model
GRI: strain gauge rosette
HL: hysteresis losses
HP1: high performance 1 (ITER specification for $Nb_3Sn$ strands)
HV: high voltage
ICS: inter-coil structure: structure for force transmission between the TFMC and the LCT coil
IEA: International Energy Agency, Paris
IEE: Institute of Electrical Engineering (Slovak Republic)
IMD1: inverter mode discharge with adapted ramp rates that the zero current is achieved at the same time
IMD2: inverter mode discharge with maximum possible ramp rates that the zero current is achieved at the different times
INZ: initial normal zone
ITER: International Thermonuclear Experimental Reactor
ITP: Institut für Technische Physik, Forschungszentrum Karlsruhe
JA: Japan
JAERI: Japanese Atomic Energy Research Institute, Tokyo, Japan
JET: Joint European Torus
JT-60: Japanese tokamak; JAERI
JWS: Joint Work Site (ITER)
L1, L2, L3, L4: side wedges of the inter-coil structure (ICS)
LAN: local area network
LCR meter: instrument for the measurement of inductance, capacitance and resistance
LCT: Large Coil Task: international project under the auspices of the IEA for the development of the technology for large superconducting coils for the application in fusion in the 1980s
LCT coil: coil constructed in the frame of the "Large Coil Task (LCT)" by the European Community (EURATOM LCT coil)
$LN_2$: liquid nitrogen
M&M: thermal-hydraulic-electrical code developed by Dipartimento di Energetica, Politecnico, Torino, Italy
MAG: metal active gas welding process
MAGS: code combining the calculation of thermal-hydraulic and electromagnetic properties for making predictions in superconducting magnets under various operation conditions (delayed safety discharges and other fault conditions)
MATLAB®: the name MATLAB stands for matrix laboratory. MATLAB is a high-performance language for technical computing
MIT: Massachusetts Institute of Technology, Boston, MA, USA
Nd–YAG: solid state laser: neodymium–yttrium/aluminium garnet
ORNL: Oak Ridge National Laboratory, Oak Rigde, TN, USA
PDI: differential pressure indicator
PI: pressure indicator
PLC: programmable logic controller
POLO: project for development the technology of superconducting poloidal field coils at Research Centre Karlsruhe by construction and testing of the poloidal field model coil, which was called POLO coil

PSB: Power System Blockset is a MATLAB toolbox to rapidly and easily built models that simulate power systems
PTC: positive temperature coefficient
P*X.Y*: Single pancake, $X = 1–5$, $Y = 1–2$
QA: quality assurance
QD: quench detectors
R&D: research and development
RF: Russian Federation
rms: root mean square
Rosettes: array of 3 strain gauges on object versus 3 on reference bloc
RP: radial PLATE of the ITER TF TFMC
RRR: residual resistivity ratio between 273 and 4 K
SeCRETS: Segregated Copper Ratio Experiment on Transient Stability performed in the SULTAN facility of CRPP
SE-Cu: electrolytic touched copper
SEM: Specific Energy Model
SF-Cu: Phosphorous deoxidised copper
SIMULINK®: SIMULINK is a software package, integrated with MATLAB, for modelling, simulating and analysing dynamic systems
SIN: Swiss Institute for Nuclear Research, Villigen, Switzerland—now Paul Scherer Institute (PSI)
SPARTAN: transient data acquisition system implemented on TOSKA
sqrt: square root
SS: stainless steel
SSD: standard safety discharge at 25 kA
STAR: superconducting test arrangement
SULTAN: SUpraLeiter TestANlage, test facility for testing ITER full size conductors and joints (CRPP, Villigen, Switzerland)
T10, T15: superconducting tokamaks of the I.V. Kurchatov Institute of Atomic Energy, Moscow, Russian Federation
TF: toroidal field
TFMC: toroidal field model coil (ITER)
TFTR: Tokamak of the Princeton Laboratory, Princeton, USA
TI: temperature indicator
TIG: tungsten inert gas (welding method)
TORE SUPRA: sperconducting tokamak of the CEA Cadarache, France
TOSKA: Toroidalspulen Testanlage Karlsruhe (Toroidal coils test facility Karlsruhe)
TRIAM-1M: superconducting tokamak of the Advanced Fusion Research Center, Kyushu University; Japan
TVO: glass/carbon resistance temperature sensor of Dubna (Russian Federation) origin
USA/US: United States of America